Technological and design aspects of the processing of composites and nanocomposites

Volume II

Technological and design aspects of the processing of composites and nanocomposites

Volume II

Lublin University of Technology
University of Minho
Technical University of Košice

TECHNOLOGICAL AND DESIGN ASPECTS OF THE PROCESSING OF COMPOSITES AND NANOCOMPOSITES

Volume II

Monography

edited by

Prof. **Janusz W. Sikora**, Ph.D., D.Sc.
Lublin University of Technology

Assoc. Prof. **Ľudmila Dulebová**, Ph.D., D.Sc.
Technical University of Košice

Lublin
Lublin University of Technology Publishing House
2019

Scientific-Practical International Workshop under a Project H2020-MSCA-RISE-2016-734205

This project has received funding from the European Union's Horizon 2020 research and innovation programme under the Marie Skłodowska-Curiegrant agreement No. 734205–H2020-MSCA-RISE-2016

Reviewed by:
Janette Brezinová, prof., Ph.D., D.Sc., Technical University of Košice, Slovakia
Tomasz Rydzkowski, Ph.D., D.Sc., Assoc. Prof., Koszalin University of Technology, Poland

Publisher:
Lublin University of Technology Publishing House

Production Editor:
Janusz W. Sikora, Ľudmila Dulebová

Printed by:
TOP Włocławek, Poland

ISBN: 978-83-7947-378-6

Contents

PREFACE

This publication is a free continuation of publication “Technological and design aspects of the processing of composites and nanocomposites. Part I” Publication contains further results of the research activities of participants of the NEWEX project. Solvers are representatives of universities from Poland, Slovakia and Portugal, namely Lublin University of Technology, Technical University of Kosice and University of Minho.

The publication contains a selection from a wide field of scientific issues solved by participants of the international project at their workplaces and laboratories. This monograph presents for example new concepts of a special screw and rotational barrel segment for a new generation extruder, simulation analysis of single screw extruder in Ansys Polyflow, global extruder modelling and the properties of composites and nanocomposites. Presentation of obtained results is performed at annual workshops and also in scientific publications and conferences.

We hope that this publication will serve the scientific and professional community, students and doctoral candidates in solving theses, dissertations, problems in practice and for improvement the knowledge in the field of plastic processing.

Janusz W. Sikora
Ľudmila Dulebová

Ľudmila Dulebová[1], Ján Varga[1], Emil Spišák[1]

THE STUDY INFLUENCE OF NANOFILLERS ON SELECTED PROPERTIES OF NANOCOMPOSITES

Abstract: *The requirements for the quality are increasing. Therefore, it is important to know the characteristics of a good plastic material, the possibilities and limitations resulting from them. Polyamide 6 based nanocomposites were prepared using a melt-mixing technique in this study. Organoclay (Cloisite 30B) was used as filler for samples with various percentage additions. Study of mechanical properties was performed by tensile test, Charpy impact test and hardness measurement. Mechanical properties significantly increased after addition of MMT. Scanning electron microscopy results confirmed the nano-scaled dispersion of Cloisite 30B in the composites. Differential scanning calorimetry (DSC) results indicated small changes in crystallization kinetics of PA6. TGA analysis was also used for determination the influence of high temperatures on samples.*
Keywords*: polymer nanocomposites, polyamide, montmorillonite, mechanical properties*

1. Introduction

Polymer composites are most common used among all types of composite materials. As the polymer matrix is used a wide variety of polymer materials from common types such as thermosets and thermoplastics to special engineering polymers. In terms of material engineering there are key characteristics of the basic material such as elastic modulus, tensile strength, impact strength, and others [1]. The problem with current measurements of these properties is that the obtained result is a kind of integrals contribution of all structural components in the sample. Although now in terms of conventional materials, or in terms of advanced composites begins to acquire topical need to know the mechanical properties of individual components at the phase structure. In all these materials is valid, that their destruction is initiated at the weakest point [2].

Mechanical properties of polymer materials describe their behavior under the mechanical stress. Almost all polymer materials used in practice are mechanically stressed and therefore for their usage are knowing of their mechanical properties very important. Mechanical properties are based on the internal structure of polymers, especially the shape and size of macromolecules and macromolecular chains and the degree of mobility of chains. For assessment of the mechanical properties of polymers,

[1)] *Technical University of Kosice, Faculty of Mechanical Engineering, Department of Engineering Technologies and Materials, Mäsiarska 74, 040 01 Kosice, Slovakia, ludmila.dulebova@tuke.sk*

we used testing methods, which most of are normalized. Measuring mechanical properties of materials is very important in determining the usability of materials. The importance of these measurements is increasing with the use of increasingly sophisticated materials [3, 4].

Nanocomposites (NC) are materials that comprise a dispersion of nanometer-size particles in a matrix. The matrix may be single or multi-component. It may contain additional materials that add other functionalities to the system (e.g., reinforcement, conductivity, toughness, etc.). The matrix can be either metallic, ceramic, or polymeric – only the latter type will be discussed in this review. The nano-particles are classified as lamellar, fibrillar, shell-like, spherical, and others. For the enhancement of mechanical and barrier properties, the anisometric particles are preferred [5].

From the fundamental point of view, the reinforcing effect of nano-particles is related to the aspect ratio (p = platelet diameter/thickness) and to the particle-matrix interactions. Independently of the actual dimensions, the reinforcing effect is the same for p > 500 as of an infinitely l arge particle. The anisometric particles start overlapping when the volume fraction exceeds the "maximum packing volume fraction φ_m" [6].

In consequence of these fundamentals, PNC's (polymer nanocomposites) normally require 1–3vol% of nano-particles. They behave as a single phase and single component material. PNC's exhibit transparency and low density. They may be easily modified by additives. They can be used as such or as a matrix of traditional multiphase systems (viz. blends, composites, or foams), replacing neat polymers and traditional composites. Nanometer-scale structures are frequently found in biological materials with impressive performance. For example, bone has a structure of 4 nm-thick hydroxyapatite crystals dispersed within a collagen matrix [7, 8].

2. Nanoclays

Nanoclays are clay minerals optimized for use in clay nanocomposites – multi-functional material systems with several property enhancements targeted for a particular application. Polymer-clay nanocomposites are an especially well-researched class of such materials [5]. Nanoclays are a broad class of naturally occurring inorganic minerals, of which plate-like montmorillonite is the most commonly used in materials applications. Montmorillonite consists of ~ 1 nm thick aluminosilicate layers surface-substituted with metal cations and stacked in ~ 10 μm-sized multilayer stacks. The stacks can be dispersed in a polymer matrix to form polymer-clay nanocomposite. Within the nanocomposite, individual nm-thick clay layers are fully separated to form plate-like nanoparticles with very high (nm × μm) aspect ratio. Even at low nanoclay loading (a few weight %), the entire nanocomposite consists of interfacial polymer, with majority of polymer chains residing in close contact with the clay surface. This can dramatically alter properties of a nanocomposite compared to the pure polymer. Potential benefits include increased mechanical strength, decreased gas permeability, superior flame-resistance, and even

enhanced transparency when dispersed nanoclay plates suppress polymer crystallization [8].

Idealized structure montmorillonite clay (pre-organic modification) – Figure.1, showing two tetrahedral-site sheets fused to an octahedral-site sheet. Red spheres are oxygen atoms and grey spheres are Si, Al, or Mg atoms. Purple spheres represent Na or K ions. SEM image of refined MMT is shown on Figure 2 [3].

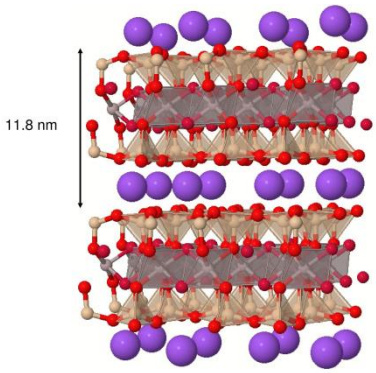

Fig. 1. Idealized structure of montmorillonite

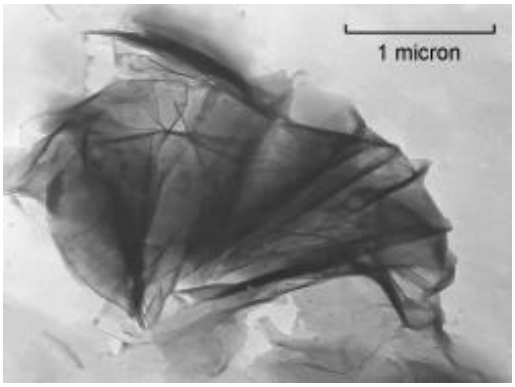

Fig. 2. SEM image of refined MMT

Since the aspect ratio of exfoliated MMT is p = 100 to 2000, the specific surface is in the order of 800 m^2g^{-1}. Thus, a small amount of anisometric particles leads to large effects. On a molecular level, the surface energy of clay particles is high. As a result, adsorbed molecules have a tendency to be strongly bonded in the layer adjacent to the clay surface. This engenders a solid-like behavior of the 2–3 nm thick surface layer and progressive reduction of viscosity with distance to the bulk liquid viscosity at about 15 nm [9].

3. Polymer-clay nanocomposite morphologies

Depending on the interfacial interactions forces between polymer matrix and silicate, three different types of nanocomposites are thermodynamically accepted (Fig. 3):

- intercalated nanocomposites: in the intercalated nanocomposites, the insertion of polymer matrix in the silicate structure occurs in a regular way, crystallographically, by alternating polymer chains and silicate layer, whose distance between each other varies from 1 to 4 nm, distance in the range of the polymer chain length;
- flocculated nanocomposites: they are the same as intercalated nanocomposites, except for the fact that some silicate layers are, sometimes, flocculated due to the interactions between hydroxyl groups of the silicate;

- exfoliated nanocomposites: in the exfoliated nanocomposites, the individual clay mineral layers are randomically separated in a continuous polymer matrix by an average distance which depends on the clay charge. Generally, the clay content in an exfoliated nanocomposite is much lower than in an intercalated nanocomposite [10].

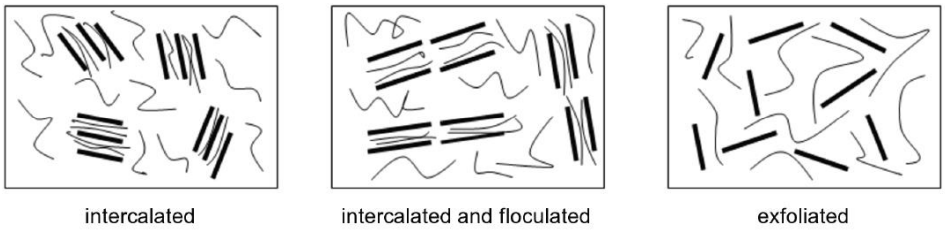

Fig. 3. Three types of thermodynamically accepted nanocomposites

4. Nanocomposite production methods

Four methods are used in nanocomposite preparation. In situ polymerization (Fig. 4) was the first method developed. In this technique, a monomer is used as a medium for the clay dispersion and favorable conditions are performed in order to carry out the polymerization between the clay mineral layers. Polymerization can be initiated by heat or radiation, by the diffusion of an adequate initiator or a fixed catalyzer inside the layers before the filling step by the monomer [11].

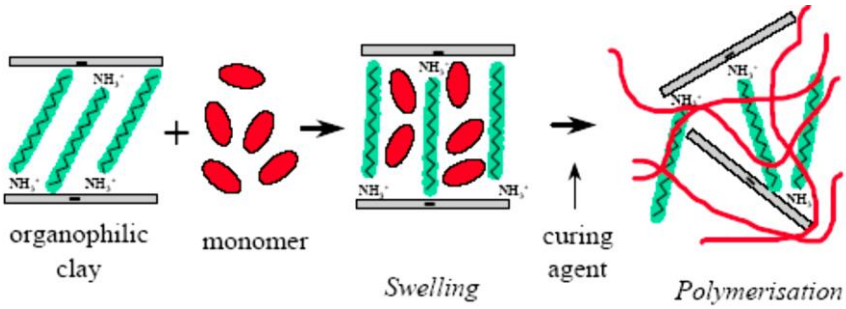

Fig. 4. The in-situ polymerization

There are cases in which complete exfoliation occurs, since the driving force for complete exfoliation is polymerization. Due to the fact that the clay mineral has high surface energy, the clay mineral layers exert attraction on the monomer units towards the inside of the galleries until equilibrium is reached. The polymerization reactions occur between the layers with lower polarities and displace the equilibrium, aiming at the diffusion of new polar specimens between the layers to progressively exfoliate the clay mineral [12].

The second method is the solution dispersion in which the silicate is exfoliated in single layers by using a solvent in which the polymer (or pre-polymer in the case of

insoluble polymers such as polyimide) is soluble. Such silicate layers, counting on weak forces that maintain the layers united can be easily dispersed in an adequate solvent by the entropy increase caused by the disorganization of the layers which exceeds the organizational entropy of the lamellas [8].

Polymer is, then, adsorbed in the delaminated layers, and when the solvent is evaporated (or the mixture is precipitated), layers are reunited, filled with polymer to form, in the best case, an ordered multilayer structure, that is, an intercalated morphology. Moreover, there is melt intercalation (Fig. 5). In this method, silicate is mixed with the thermoplastic polymer matrix in its melt state. Under these conditions and if the layer surface is sufficiently compatible with the chosen polymer, polymer chains can be dragged to the interlamellar space and form an intercalated or exfoliated nanocomposite [8, 12].

The driving force in the melt intercalation process is the enthalpic contribution of the interactions between polymer and clay. The advantage of this technique is the non-use of solvent [13].

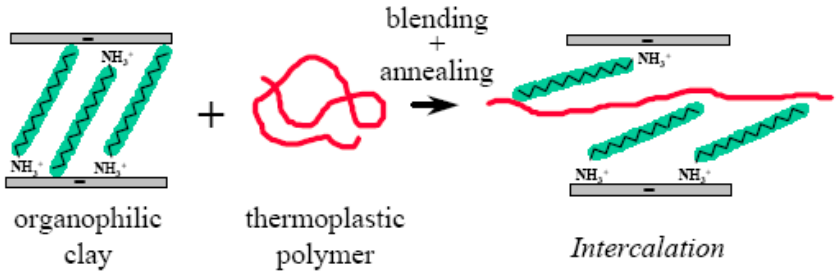

Fig. 5. The melt intercalation process

Finally, a less common method is also employed, in which clay slurry is directly mixed with the polymer. The idea of this technique consists in increasing the basal spacing of the clay in the first stage of the process, by the polymerization of the monomers or clay suspension in water/solvents and hence, the polymer matrix is intercalated in the increased basal spacing [14].

5. Experimental work

5.1 Tested material

Polyamide is an important group of the thermoplastic excellent solvent resistance and good processability. In the study was used Polyamide Durethan B30S material, manufactured by LANXESS Deutschland GmbH. Durethan B30S is non-reinforced PA6 used for injection molding with tensile modulus 3200MPa, melt volume-flow rate 100cm^3/min with easy-flow, easy-release and rapid solidification.

Cloisite 30B is alkyl quaternary ammonium salt bentonite. Cloisite 30B is an additive for plastics and rubber to improve various physical properties, such as reinforcement, CLTE, synergistic flame retardant and barrier.

Typical properties of Cloisite 30B filler:

- moisture: <3%,
- typical dry particle size: <10μm (d_{50}),
- colour: off white,
- packed bulk density: 365g/l,
- density: 1.98g/cc,
- X Ray results: d_{001} = 1.85nm.

5.2 Preparation of nanocomposite material

PA6 was dried for 48h at 80°C (to the level of ~0.1 wt.% of water content in polymer) under vacuum. The organo-montmorillonites were also dried for 4 h at 60°C before compounding. The nanocomposites were obtained in two steps in air atmosphere using co-rotating twin-screw extruder Buhler BTSK 20/40D. Rotational speed of the screws was 250 min^{-1} and temperature range was 260–280°C. In the first step the masterbatches of PA6 with one filler ZW3 in amount of 10 wt. % were prepared.

Characteristics of mixing process and extruder: configuration of screw K3, torque 32 Nm, input power 0.47 kW, temperature/pressure of polymer in head 275°C/4 bar, diameter of screws 20 mm, depth of the channel 3.75 mm, length of screws 800 mm.

Samples for tests were molded at injection molding machine type ARBURG Allrounder 370S under ISO standards in company Plaset SEZ Krompachy a.s. Labeling of used materials for test is described in Table 1.

Table 1. *Labeling of used materials for test*

Material	Label
PA Durethan B30S	PA
PA + 2% CLOISITE 30B	PA/A-2
PA + 4% CLOISITE 30B	PA/A-4
PA + 6% CLOISITE 30B	PA/A-6

5.3 Methods of testing

The mechanical properties of nanocomposites were determined according to standard EN ISO 527-1. TIRAtest 2300 tensile testing machine was used for tensile test. Five samples for each materials PA/%Cloisite 30B were used for testing. Charpy impact strength of a notched specimen was measured according to ISO 179/1eA with V-notch. Hardness was measured according to STN EN ISO 868. For addition tests, Raman spectrometry was performed using DeltaNu. Thermal properties were found

out using TGA/DSC SDT Q600. Structures of material were observed with SEM microscope.

Results of tensile test, impact strength and hardness of tested samples are processed in Figure 6 to Figure 8. Mechanical test showed that all tested mechanical properties (tensile strength, Charpy Impact strength and hardness) significantly increased after addition of Cloisite 30B nanofiller. Increase of tensile and impact strength is showed on Figure 6 and Figure 7. The test results of hardness are summarized in Figure 8. Greatest change of properties was at samples with addition of 6% of nanofiller. In Figure 9 are measured Raman spectrums of samples PA6 with various % Cloisite 30B.

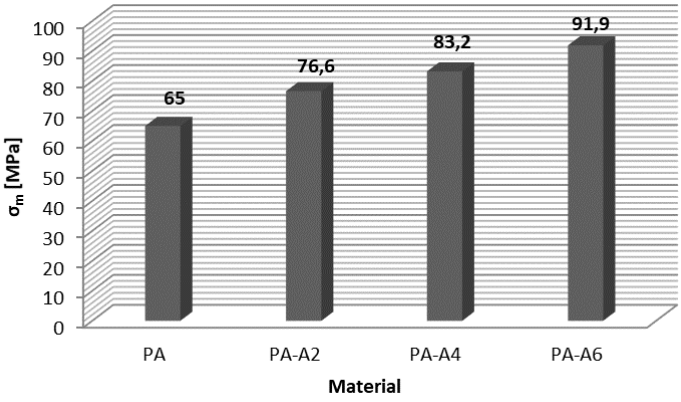

Fig. 6. Tensile strength of tested material PA/Cloisite 30B

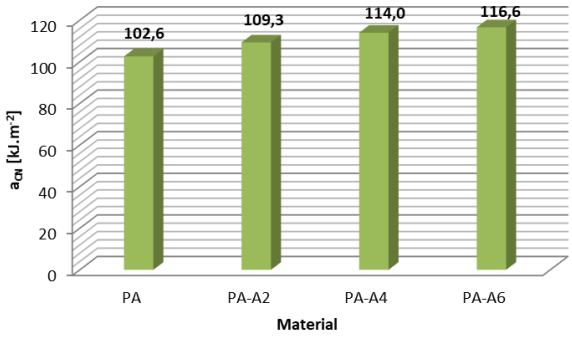

Fig. 7. Charpy impact strength of tested material PA/Cloisite 30B

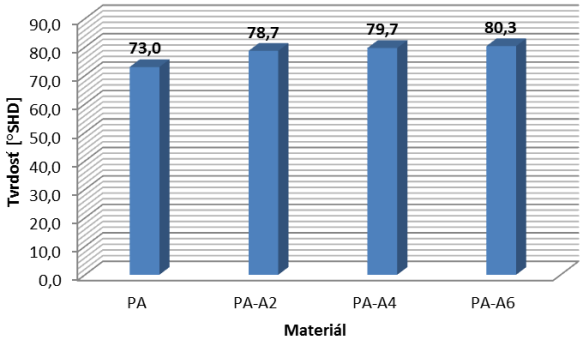

Fig. 8. Hardness of tested material PA/Cloisite 30B

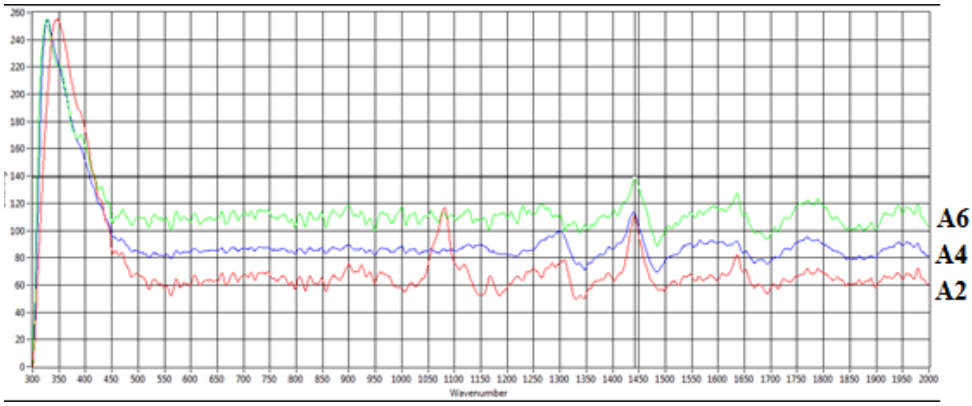

Fig. 9. Raman Spectrum–sample PA/ Cloisite 30B

A comparison of the Raman spectra of tested materials is shown in Figure 9. Each measurement was made 10x and in the NuSpec program the measurements were averaged to exclude random peaks. As can be seen from the measurements, the spectra of these materials show major peaks in the wavelength range 320–350 and 1450 cm^{-1}. The remaining peaks are not so pronounced in the spectrum.

By DSC analysis, pure PA material showed glass transition temperature at 110.48°C and melt point at 229.33°C with heat flow 2.1W/g as seen on Figure 10. PA6 polymer with addition of 6% of Cloisite 30B showed glass transition temperature at 102.74°C and melt point at 225.99°C with heat flow 1.35W/g as seen on Figure 11. DSC curves of samples from PA6 and PA/A-6 material are showed in Figure 12, where both curves were compared. TGA weight analysis showed small differences between materials, weight change of material PA6 was 1.086%, while weight change of material PA/A-6 was 1.001% as seen on Figure 13.

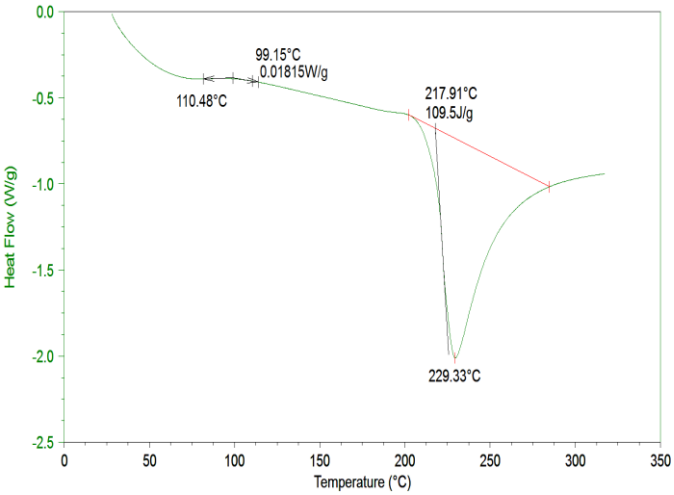

Fig. 10. DSC analyse of material PA6

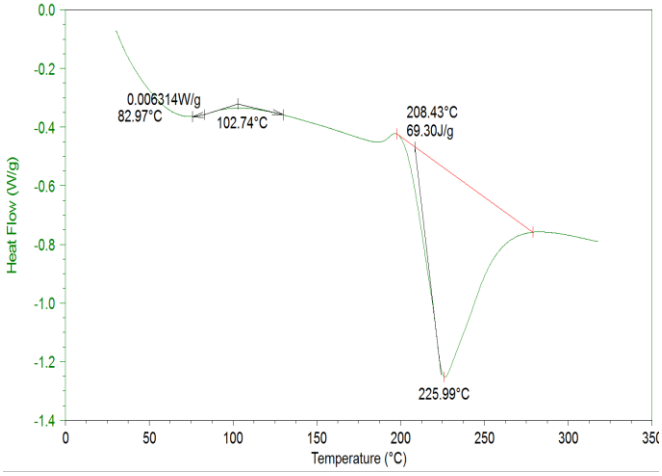

Fig. 11. DSC analyse of PA/6% Cloisite 30B

Structures of samples were observed with SEM microscope. With magnification 2500x (Fig. 14) and 5000x (Fig. 15) no aggregates of fillers were found. Filler was well-dispersed through matrix. In Figure 16 the PA/6% Cloisite 30B was observed to be partially exfoliated into a thinner multi-layered structure or even single layer, indicating a nano-scaled dispersion was achieved.

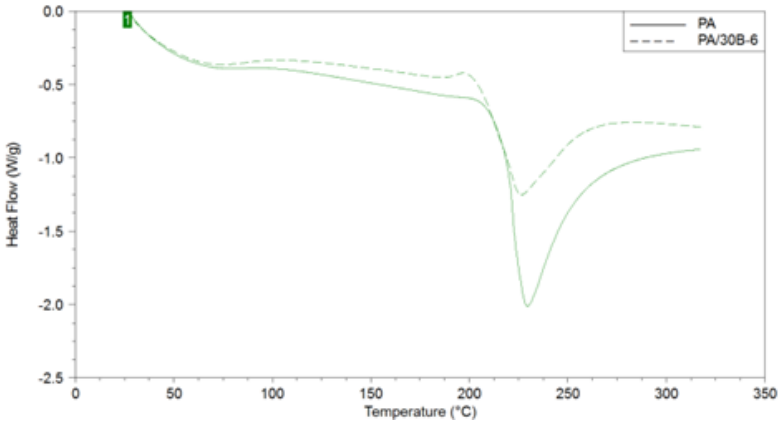

Fig. 12. Comparison of DSC curves of tested materials

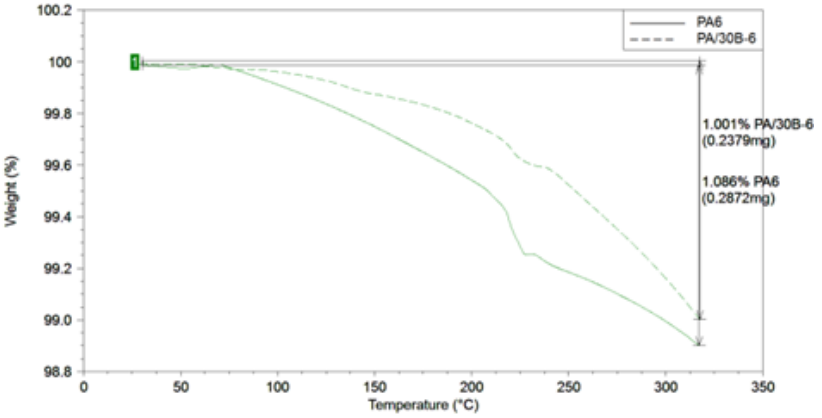

Fig. 13. TGA – Weight Change of tested materials

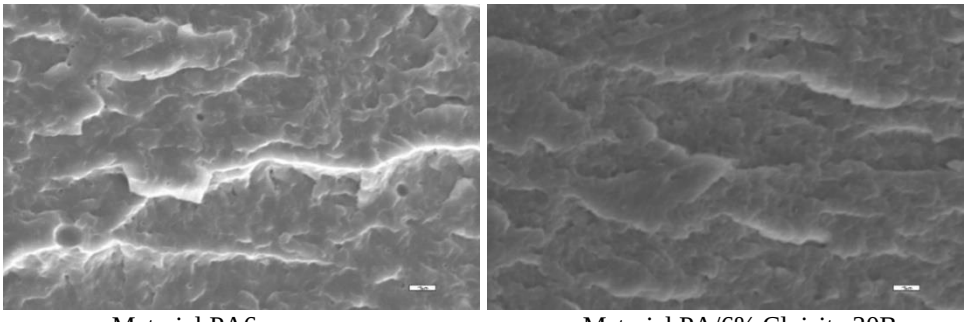

Material PA6 Material PA/6% Cloisite 30B

Fig. 14. Structures of PA/6% Cloisite 30B samples after breach, magnification 2500x

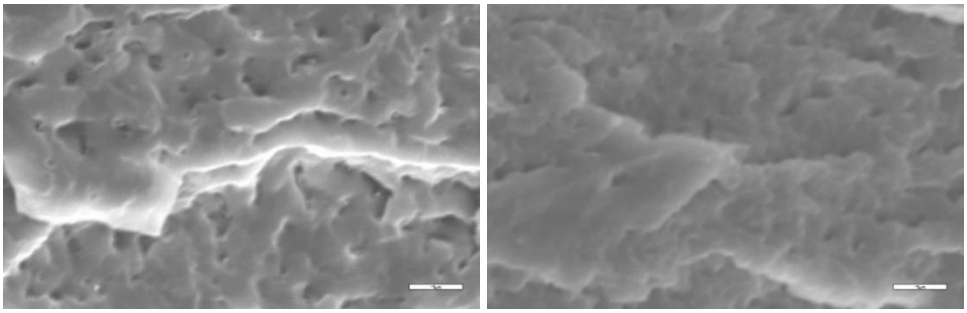

Material PA6 Material PA/6% Cloisite 30B

Fig. 15. Structures of PA/6% Cloisite 30B samples after breach, magnification 5000x

Fig. 16. TEM micrograph of PA/6% Cloisite 30B

6. Conclusion

The plastic industry has no doubt witnessed in recent years an increase in interests and demands in using nanocomposites. This study investigated the dispensability of nanofiller Cloisite 30B within a PA6 matrix. The thermal/mechanical properties of the melt-mixed samples were determined. The influence of mixing sequences on the phase morphology and thermal/mechanical properties of the PA6/Cloisite 30B composites were also evaluated. SEM and TEM results indicated that the layered Cloisite 30B was exfoliated (or at least intercalated) in the prepared composites. The PA 6-based nanocomposites were achieved irrespective of the processing sequence employed. DSC analysis showed thermal stability and differences between PA6 and PA6 nanocomposite. The TGA data confirmed the moderate thermal stability enhancement of PA6 after adding Cloisite 30B. Tensile strength of PA6 increased with the inclusion of Cloisite 30B. Greatest change of properties was at samples with addition of 6% of nanofiller Cloisite 30B: increase of tensile strength of 41.4%, increase of impact strength in 13.65% and increase of hardness in 10%.

Acknowledgement

This project has received funding from the European Union's Horizon 2020 research and innovation programme under the Marie Skłodowska-Curie grant agreement No 734205-H2020-MSCA-RISE-2016.

References

[1] Buršák, M., Bacsó, J., Skúšanie, kontrola a hodnotenie kvality materiálov. 1. vyd. Košice: TU (2008).
[2] Běhálek L, Dobranský, J., Process of cooling injection mould and quality of injection parts, Acta Technica Corviniensis: Bulletin of Engineering, 2, (2009) 19–23.
[3] Greškovič F., Dulebová Ľ., Varga J., Technológie spracovania plastov. Vstrekovanie. TU v Košiciach, (2010).
[4] Hrivňák, I., Fraktografia. STU MTF v Trnave, Bratislava, (2009).
[5] Greškovič, F., Duleba, B., Application of clay based nanofillers at polymer nanocomposites, Technological and design aspects of extrusion and injection moulding of thermoplastic polymer composites and nanocomposites, Lviv, Lviv Polytechnic Publishing House, (2013).
[6] Liu, Y., Yang, G., Non-isothermal crystallization kinetics of polyamide-6/graphite oxide nanocomposites, Thermochim. Acta, 500, (2009) 13–20.
[7] Run, M.T., Wu, S. Z., Zhang, D.Y., Wu, G., Melting behaviors and isothermal crystallization kinetics of PE/mesoporous molecular sieve composite, Polymer, 46 (14) (2005) 5308–5316.
[8] Mark, J.E., Polym. Eng. Sci., 36 (1996), p. 2905.
[9] Araújo, M. et al., Comparative Study of Membranes Obtained from PA6 and PA66/National Clay Nanocomposites, Advances in Nanocomposite Technology (2011).
[10] Ke, Y. C., Stroeve, P., Polymer-Layered Silicate and Silica Nanocomposites. Elsevier. Amsterdam, (2005).
[11] Ray, S. S., Okamoto, M., Polymer/layered silicate nanocomposites: a review from preparation to processing, Progress in Polymer Science, 28 (2003) 1539–641.
[12] Anadão, P., Clay-Containing Polysulfone Nanocomposites, Advances in Nanocomposite Technology, (2011).
[13] Souza, M.A., Pessan, L.A., Rodolfo Jr., A., Nanocompósitos de poli(cloreto de vinila) (PVC)/ argilas organofílicas, Polímeros: Cięncia e Tecnologia, 16 (2006) 257–262.
[14] Kaneko, M.L.Q.A., Torriani, I., Yoshida, I.V.P., Morphological evaluation of silicone/clay slurries by small-angle/wide-angle X-ray scattering, Journal of Brazilian Chemistry Society, 18 (2007) 765–773.

Łukasz Majewski[1], Hubert Debski[2], Ľudmila Dulebová[3]

NEW CONCEPTS OF A ROTATIONAL BARREL SEGMENT FOR A NEW GENERATION EXTRUDER

Abstract: *The work presents various design concepts of a rotational barrel segment. Different design solutions of a rotational barrel segment were presented in the form of CAD models. Next, numerical calculations were carried out aiming at strength and heat analysis of selected models. Numerical calculations were conducted using the method of finished elements. As a calculating tool ABAQUS® program was used. The special screw was loaded with the torque, the pressure, the torgue and the pressure, as well as with the temperature. Calculations have shown that the proposed constructions of the rotational barrel segment are correct, under load they operate in a safe range of stresses, and their operation at a higher temperature is stable.*
Keywords: *rotational barrel, CAD, MES, thermal and strength analysis*

1. CAD Models

The first three models present not only different solutions of a grooved, rotational barrel segment but also the possibilities of its mounting. The preliminary assumptions of the presented visualisations are the following:

- Models are made in SolidWorks system as 3D models, they are fully functional. They were tested for correctness and collision occurrence. Virtual prototypes were created in order to determine any irregularities during movement.
- In visualisations, some construction details, unimportant from the point of view of functioning, were neglected (joining elements, etc.).

The construction assumptions of the rotational barrel segment are the following:

- Rotational barrel segment is 3÷4D long, therefore it is 75÷100 mm,
- Grooves width is 4 mm,
- Grooves height is 3 mm,
- Barrel inner diameter is 25 mm,
- Temperature resistance is about 300°C,
- Pressure resistance is 200 bar,

[1)] *Lublin University of Technology, Faculty of Mechanical Engineering Department of Technology and Polymer Processing, ul. Nadbystrzycka 36, 20-618 Lublin, Poland, l.majewski@pollub.pl*

[2)] *Lublin University of Technology, Faculty of Mechanical Engineering, Department of Machine Design and Mechatronicsg, ul. Nadbystrzycka 36, 20-618 Lublin, Poland, h.debski@pollub.pl*

[3)] *Technical University of Kosice, Faculty of Mechanical Engineering, Department of Engineering Technologies and Materials, Mäsiarska 74, 040 01 Kosice, Slovakia, ludmila.dulebova@tuke.sk*

- Rotational barrel segment is heated,
- Rotational barrel segment can be co-rotating or counter-rotating,
- Rotational speed of the segment is up to 200 rev/min,
- Tightness of plasticising system connection is ensured.

Three different constructional solutions of the rotational barrel segment were presented in the form of CAD models. They are the either the developments of the existing solutions or totally new ones. There is a possibility of creating a new conception as a combination of selected elements of each conception. In all solutions, the problem of heating of the rotational barrel segment was solved by using band heating elements. They were mounted on slidable sleeves, which were made of the material resistant to high temperatures. The rotation of the heating elements is made impossible by the mountings fixed on the insulators. The problem of providing the clamping force for barrel segments was solved by threaded rods with nuts and springs. In this way a constant clamping force is ensured, independently from the temperature causing a linear elongation of elements. The whole set is mounted on the plate. Most of the suggested solutions have innovative features and can be submitted for legal protection in the form of appropriate industrial property rights.

1.1 Conception No 1

The functioning rule of the rotational barrel segment is using the additional sealing of the segment. The disadvantage of this solution is lower acceptable operation temperature equalling up to 260°C. Figure 1 presents an axonometric view of the conceptual model, while Figure 2 shows the visualisation of the longitudinal section of the extruder barrel. The particular elements are also visualised in the exploded view of the longitudinal section (Fig. 3).

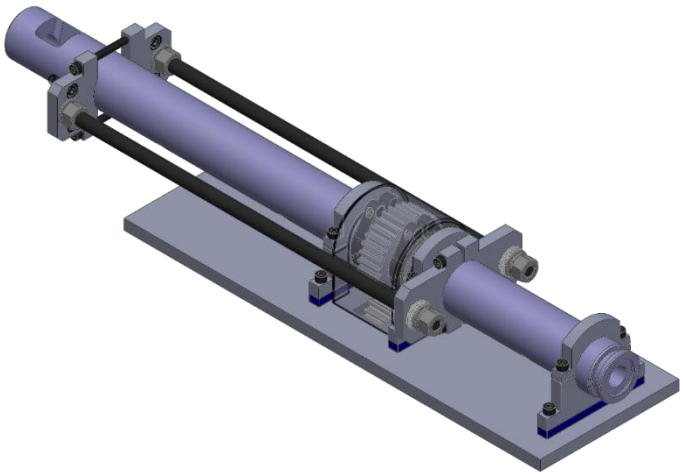

Fig. 1. Conceptual model No 1. Assembly view

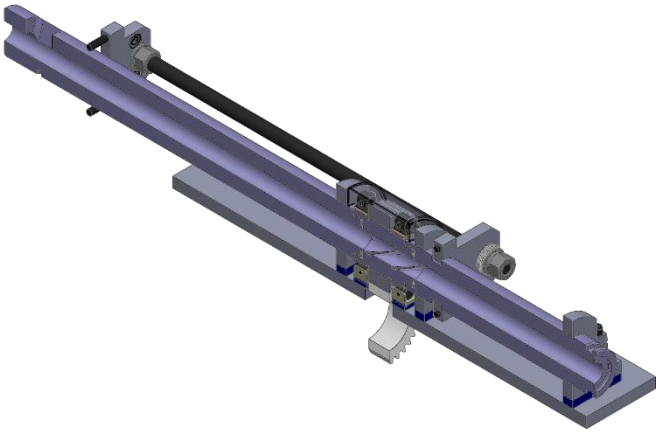

Fig. 2. Conceptual model No 1. Longitudinal section – exploded view

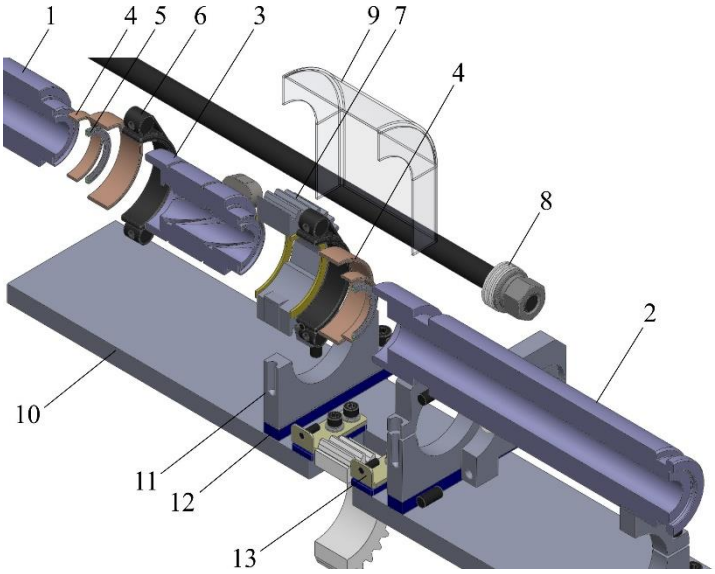

Fig. 3. Conceptual model No 1. Longitudinal section – exploded view: 1 – initial sleeve, 2 – final sleeve, 3 – rotational barrel segment, 4 – bearing bushes, 5 – sealing, 6 – band heating element, 7 – toothed wheel, 8 – fixing screw, 9 – casing, 10 – supporting plate, 11 – mounting of the barrel, 12 – insulator, 13 – mounting of the heating element

The rotational barrel segment 3 is mounted on bearing bushes 4. The rotation of the segment is made possible by a group of toothed wheels 7. The casing 9 protects the drive. The band heating elements 6 are placed on the subsequent bearing bushes 4. Immovable sleeves 1, 2 are supported by elements 11, which are fixed on insulating plates 12. The sealing is performed by o-rings 5.

In Figures 4 and 5 the rotational barrel segment is shown in an axonometric view and in the longitudinal section.

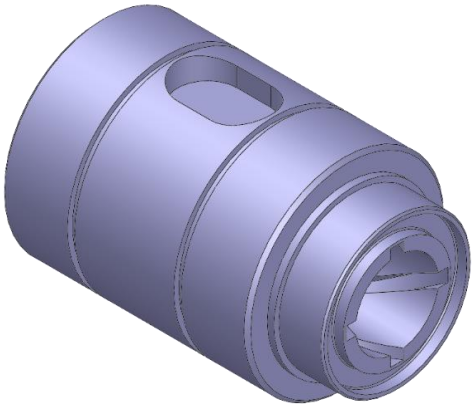

Fig. 4. Conceptual model No 1. Rotational barrel segment

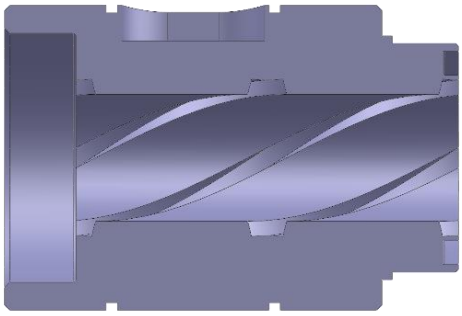

Fig. 5. Conceptual model No 1. Rotational barrel segment. Longitudinal section

1.2 Conception No 2

The most important feature of functioning of the rotational barrel segment, presented in conception No 2, is using divided bearing bushes. This enables an easy assembly of the whole set at the simultaneous mounting of the barrel. In Figure 6 an axonometric view of the conceptual model is shown, while in Figure 7 the visualisation of the longitudinal section of the extruder barrel is presented. The particular elements are also visualised in the assembly Figure – exploded view (Fig. 8).

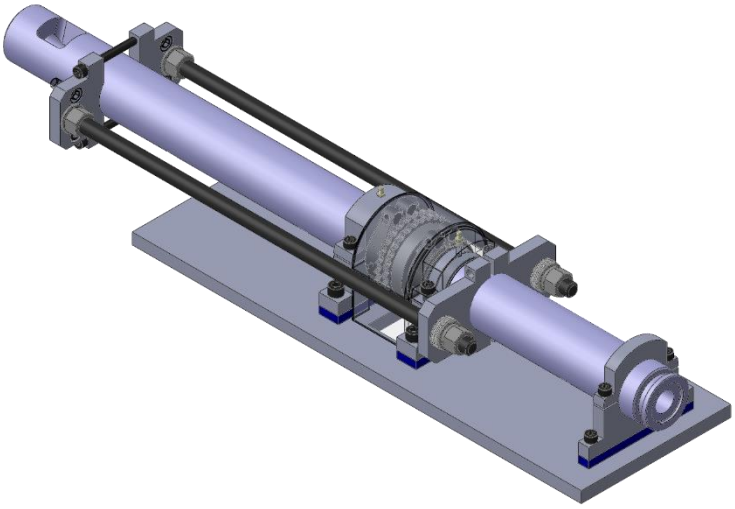

Fig. 6. Conceptual model No 2. Assembly view

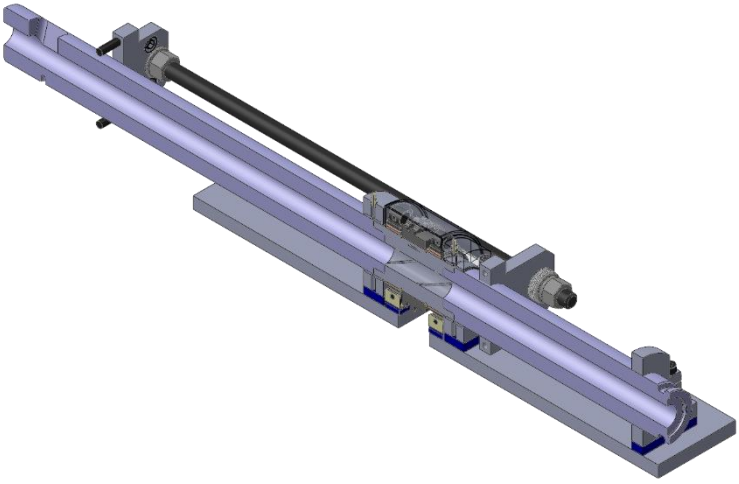

Fig. 7. Conceptual model No 2. Longitudinal section – assembly view

The rotational barrel segment 3 is mounted on bearing bushes 4. The rotation of the segment is made possible by a group of toothed wheels 6. The casing 8 protects the drive. The band heating elements 5 are placed on the subsequent bearing bushes 4. Immovable sleeves 1, 2 are supported by divided bearing bushes 4, which are fixed on support 10 and insulating plates 11. The sealing is performed by o-rings 5.

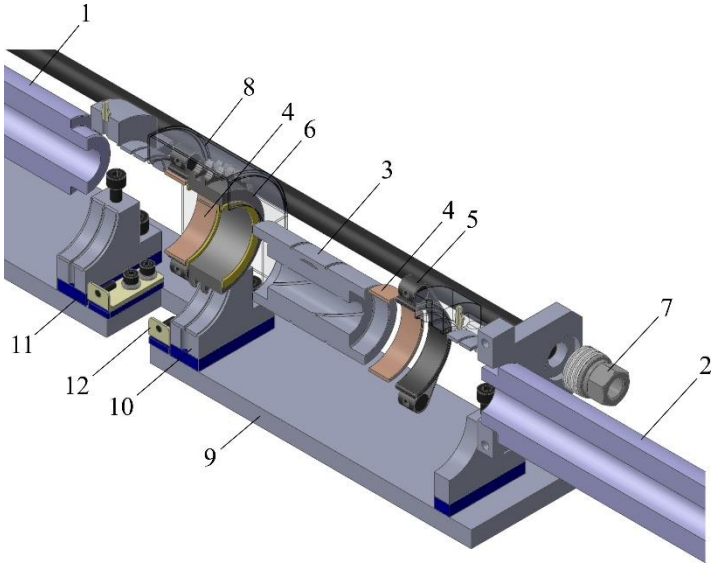

Fig. 8. Conceptual model No 2. Longitudinal section – exploded view: 1 – initial sleeve, 2 – final sleeve, 3 – rotational barrel segment, 4 – bearing bushes, 5 – band heating elements, 6 – toothed wheel, 7 – fixing screw, 8 – casing, 9 – supporting plate, 10 – mounting of the barrel, 11 – insulator, 12 – mounting of the heating element

In Figures 9 and 10 the rotational barrel segment is shown in an axonometric view and in the longitudinal section.

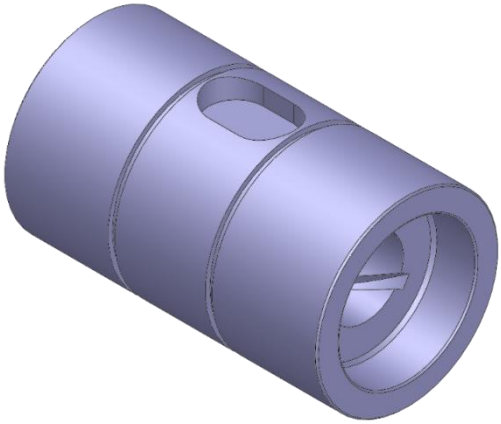

Fig. 9. Conceptual model of the rotational barrel segment No 2

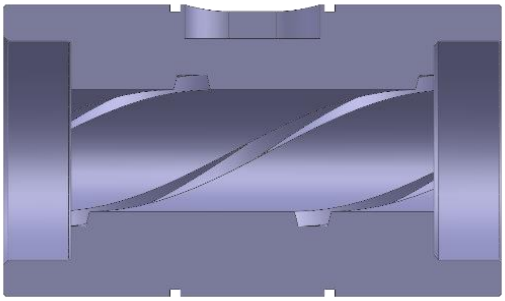

Fig. 10. Conceptual model of the rotational barrel segment No 2. Longitudinal section

1.3 Conception No 3

The third option is characterised by using rolling bearings and a conical inner tip of the sleeve. Such bearings decrease the friction resistance but slightly limit maximum temperature to 280°C or (while keeping the temperature) limit maximum rotations to 115 rev/min. Such bearings also force the elongation of the segment. Divided elements supporting immovable barrels enable an easy assembly of the whole set. In Figure 11 an axonometric view of the conceptual model is presented. In Figure 12 the visualisation of the longitudinal section of the extruder barrel is shown. The particular elements are also visualised in the assembly Figure – exploded view (Fig. 13).

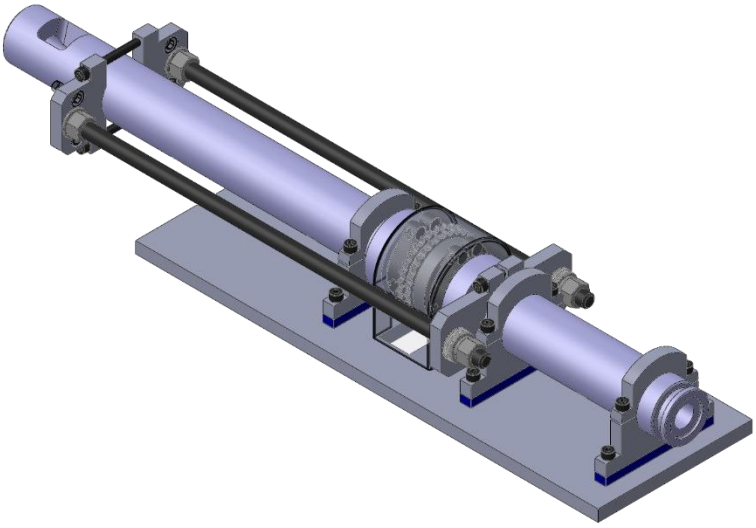

Fig. 11. Conceptual model No 3. Assembly view

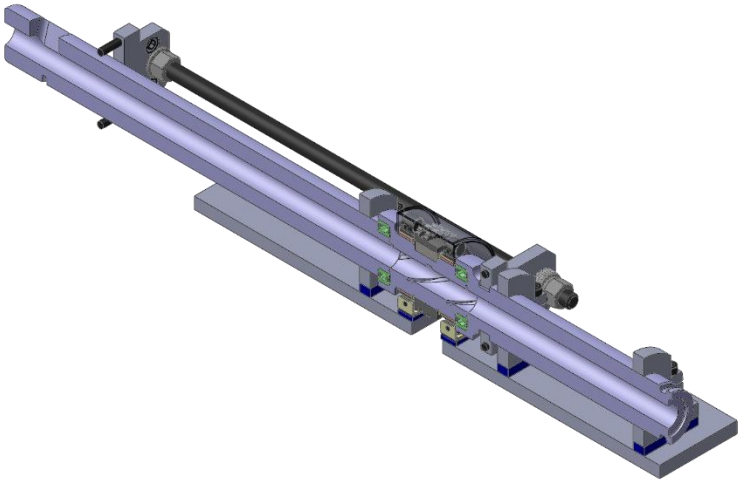

Fig. 12. Conceptual model No 3. Longitudinal section - assembly view

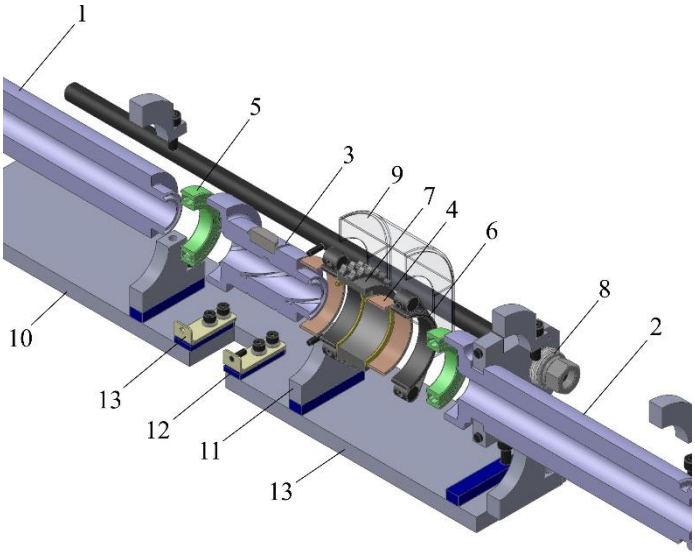

Fig. 13. Conceptual model No 3. Longitudinal section – exploded view: 1 – initial sleeve, 2 – final sleeve, 3 – rotational barrel segment, 4 – bearing bushes, 5 – bearings, 6 – band heating elements, 7 – toothed wheel, 8 – fixing screw, 9 – casing, 10 – supporting plate, 11 – mounting of the barrel, 12 – insulator, 13 – mounting of the heating element

Rotational barrel segment 3 is mounted on rolling bearings 5. The rotation of the segment is made possible by a group of toothed wheels 7. Casing 9 protects the drive. The band heating elements 6 are placed on the subsequent bearing bushes 4.

Immovable sleeves 1, 2 are supported by elements 11, which are fixed on insulating plates 12.

In Figures 14 and 15 the rotational barrel segment is shown in an axonometric view and in the longitudinal section.

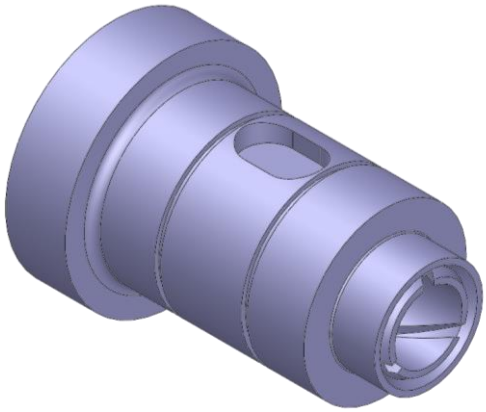

Fig. 14. Conceptual model of the rotational barrel segment No 3

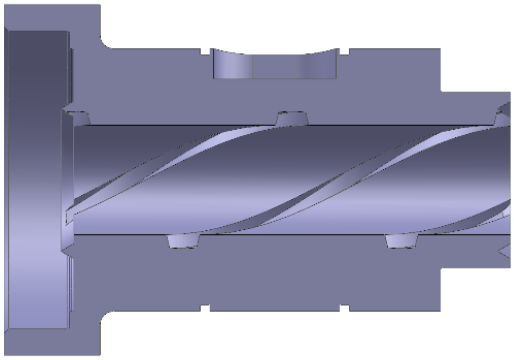

Fig. 15. Conceptual model of the rotational barrel segment No 3. Longitudinal section

The subsequent models do not take into account the possibility of mounting, and the preliminary assumptions of the presented visualisations are the following:

- presented 3D models were made in Solid Edge programme and constitute a conception outline of different constructional solutions of plasticizing systems with rotational barrel elements,
- in order to make the construction descriptions clear, the focus is on presenting the processing screw and the rotational barrel elements cooperating with it,

- in the models, such constructional elements as sealing, drive transmission from the engine, drive transmission between the particular rotational barrel parts, were neglected.

All presented CAD models were made in such a way as they could constitute the modification of W-25 single-screw extruder, and all of them present a classic or modified screw placed in the barrel plasticizing system, so screw diameter D equals 25 mm. The joint length of rotational barrel elements equals 4D (100 mm – for a construction with a number of rotational elements) or 3D (75 mm – for a construction with a single rotational element). The main reason for using such constructional solutions is the intensification of the mixing process and the increase of homogenization of the processed polymer, filled polymer or a composite. The intensity of mixing is increased due to the usage of special constructional elements, which lead to cutting, breaking, rotating and returning of the flowing stream of the processed polymer.

1.4 Conception No 4

The figures below (Fig. 16, Fig. 17) present the plasticizing system with a classic screw and four rotational elements. One of the rotational elements is driven by the engine, while others are driven by appropriate transmission gears forwarding the torque from the one driven by the engine. The rotation directions of the neighbouring rotational elements are opposite. The geometry of rotational elements in the cross-section can be described as circles with six grooves placed every 60 degrees in the shape of the triangle of the height 2 mm and the tip angle 55 degrees. The geometry of grooves is an example and can be different, e.g. square, oval, crescent, elliptic, etc.

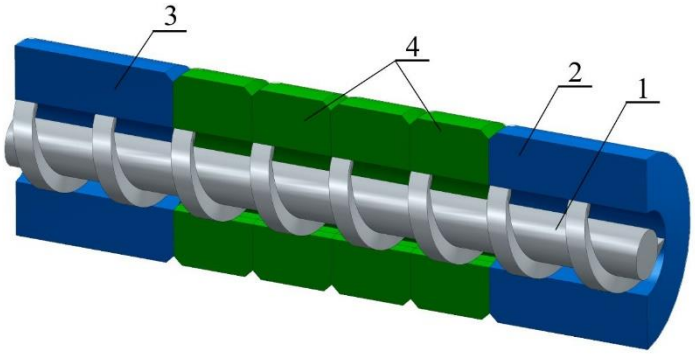

Fig. 16. Longitudinal section of the plasticizing system with a classic screw equipped with four rotational barrel elements: 1 – screw, 2 and 3 – immovable barrel parts, 4 – rotational barrel elements with a grooved inner surface

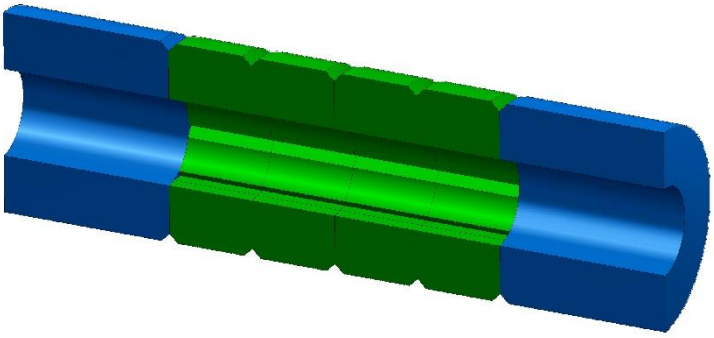

Fig. 17. Longitudinal section of the plasticizing system equipped with four rotational barrel elements with a grooved inner surface, without a screw

Figure 18 shows the cross-section of the considered constructional solution of the rotational barrel segment.

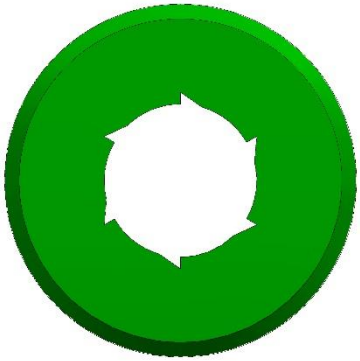

Fig. 18. Cross-section of the rotational barrel segment with six grooves placed every 60 degrees in the shape of the triangle

1.5 Conception No 5

The second conception, presented in Figures 19 and 20 is similar to the first one in regard to the geometry of the screw, number of rotational elements, the method of their drive and the direction of rotation. The difference is in the shape of rotational elements in the cross-section, whose holes are in the shape of equilateral triangle of the height 37.5 mm and rounded tips.

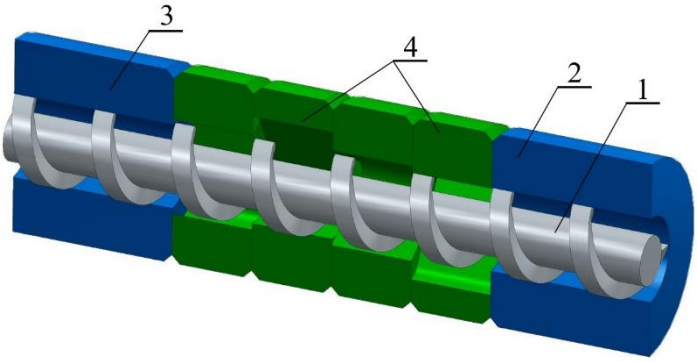

Fig. 19. Longitudinal section of the plasticizing system with a classic screw equipped with four rotational barrel elements: 1 – screw, 2 and 3 – immovable barrel parts, 4 – rotational barrel elements with a hole in the shape of equilateral triangle

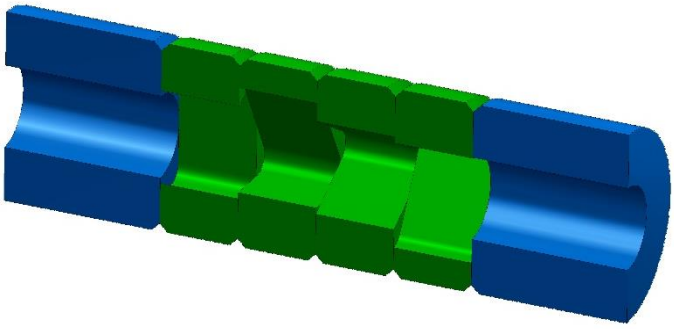

Fig. 20. Longitudinal section of the plasticizing system equipped with four rotational barrel elements with a hole in the shape of equilateral triangle, without a screw

Figure 21 shows the cross-section of the considered constructional solution of the rotational barrel segment.

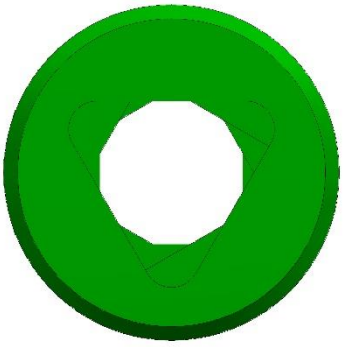

Fig. 21. Cross-section of the rotational barrel segment with the hole in the shape of equilateral triangle with rounded tips

The first modification of the second conception consists in the fact that the plasticizing unit has a classic screw and four rotational elements, which have holes in the shape of equilateral triangles with rounded tips (Fig. 22), and the difference is that the holes are torsional along the axis of the plasticizing system by the angle of 15 degrees, which results in creating a helical channel of a triangular section (Fig. 23). Each rotational element, however, rotates in an opposite direction, which causes turbulence in polymer flow at the point of contact of rotational elements, simultaneously intensifying the process of mixing.

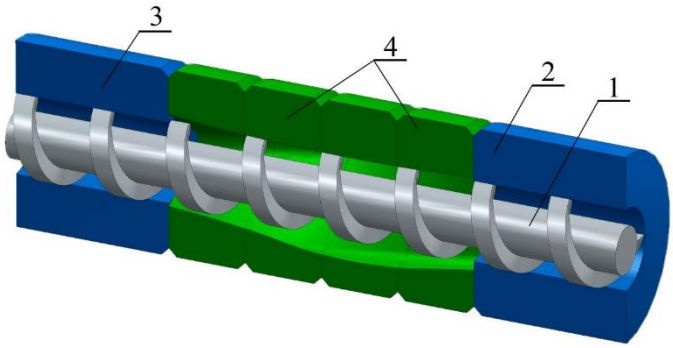

Fig. 22. Longitudinal section of the plasticizing system with a classic screw equipped with four rotational barrel elements: 1 – screw, 2 and 3 – immovable barrel parts, 4 – rotational barrel elements with a torsional hole in the shape of a triangle

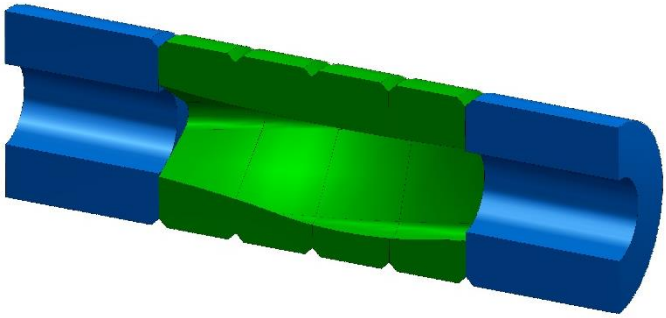

Fig. 23. Longitudinal section of the plasticizing system equipped with four rotational barrel elements with a torsional hole in the shape of a triangle, without a screw

Figure 24 shows the cross-section of the considered constructional solution of the rotational barrel segment.

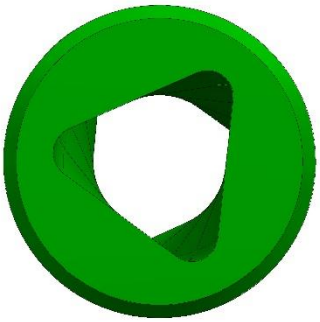

Fig. 24. Cross-section of the rotational barrel segment with helical channel (triangular shape)

The second modification of the second conception presents a constructional solution, in which four rotational elements were used with the hole in the shape of equilateral triangle with rounded tips but the rotational elements are rotated against each other by 30 degrees and joined rigidly creating one big rotational element (Fig. 25 and Fig. 26). The rigid joint makes all the rotational elements move in the same direction with the same speed and the elements can make the rotational movement in the compatible or opposite direction in relation to the rotation direction of the screw.

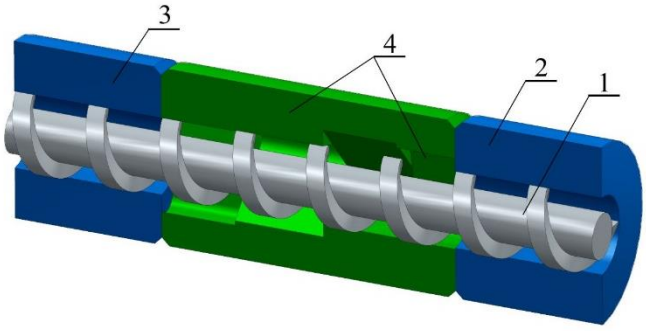

Fig. 25. Longitudinal section of the plasticizing system with a classic screw equipped with four rotational barrel elements: 1 – screw, 2 and 3 – immovable barrel parts, 4 – rigidly joint rotational barrel elements with a hole in the shape of a triangle

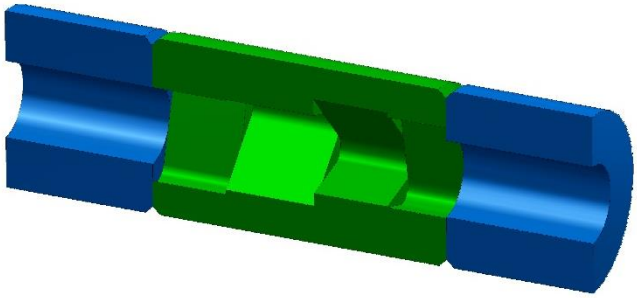

Fig. 26. Longitudinal section of the plasticizing system equipped with four rotational barrel elements with a hole in the shape of a triangle, without a screw

Figure 27 shows the cross-section of the considered constructional solution of the rotational barrel segment.

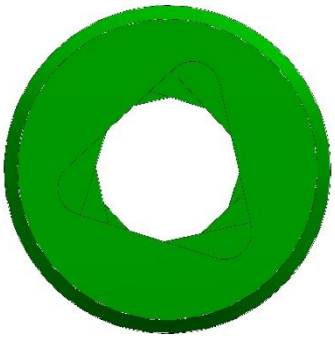

Fig. 27. Cross-section of the rotational barrel segment with the hole of triangular shape, in which elements are rotated against each other by 30 degrees

1.6 Conception No 6

The third conception presents a plasticizing system equipped with a classic screw and one rotational element of the length 4D, which has a hole in the shape of equilateral triangle of the height 37.5 mm, and the hole is additionally torsional by 30 degrees in relation to the axis of the plasticizing system (Fig. 28 and Fig. 29). The rotational element can rotate in the compatible or opposite direction in relation to the rotation direction of the screw.

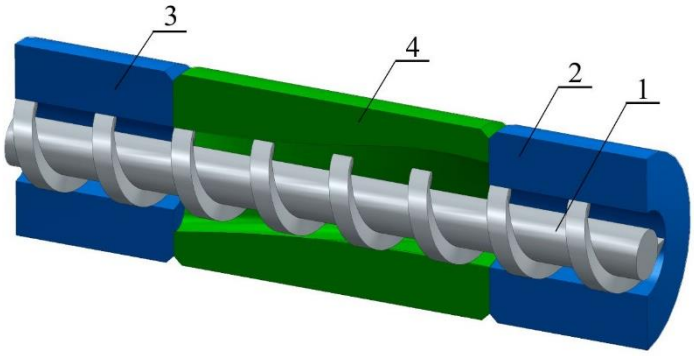

Fig. 28. Longitudinal section of the plasticizing system with a classic screw equipped with a rotational barrel element: 1 – screw, 2 and 3 – immovable barrel parts, 4 – rotational barrel element with a torsional hole in the shape of a triangle

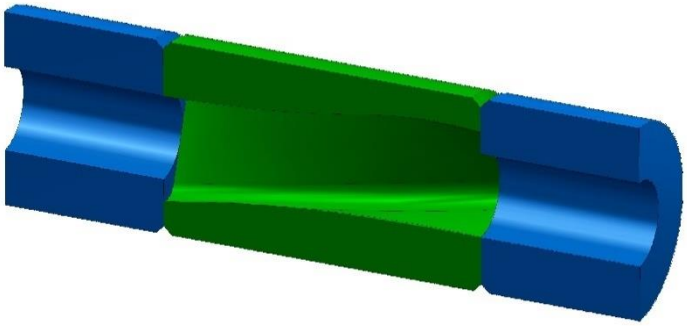

Fig. 29. Longitudinal section of the plasticizing system equipped with a rotational barrel element with a torsional hole in the shape of a triangle, without a screw

Figure 30 shows the cross-section of the considered constructional solution of the rotational barrel segment.

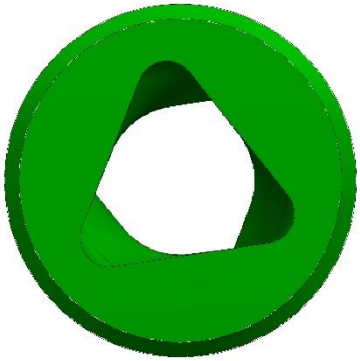

Fig. 30. Cross-section of the rotational barrel segment with the torsional hole in the shape of a triangle

1.7 Conception No 7

The next constructional solution presents the plasticizing system with four rotational elements (Fig. 31 and Fig. 32), and each of them in the cross-section has three longitudinal pins situated every 120 degrees. The pins are of the width equalling half of the width of the rotational element and are situated in the middle of it. Between the rotational elements there is a space for the rotation of specially designed screw parts consisting of three longitudinal pins situated every 120 degrees (Fig. 31). The particular rotational elements are driven analogically to those in Conception No 1.

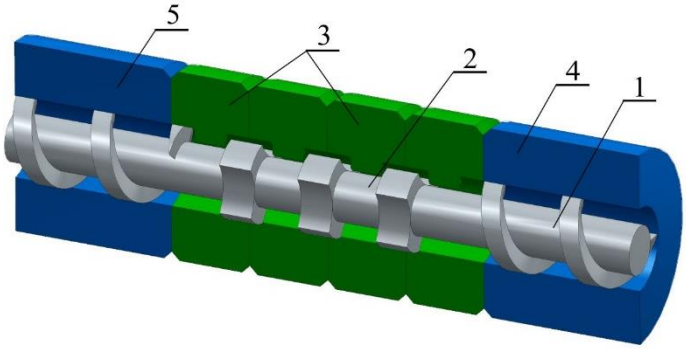

Fig. 31. Longitudinal section of the plasticizing system with a screw with a specially designed part cooperating with four rotational elements: 1 – screw, 2 – modified part of the screw, 3 – rotational elements with a round hole with longitudinal pins, 4 and 5 – immovable parts of the barrel

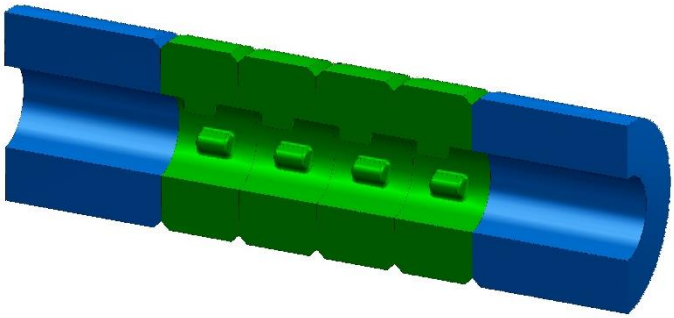

Fig. 32. Longitudinal section of the plasticizing system without a screw with four rotational elements with a round hole with longitudinal pins, without a screw

Figure 33 shows the cross-section of the considered constructional solution of the rotational barrel segment.

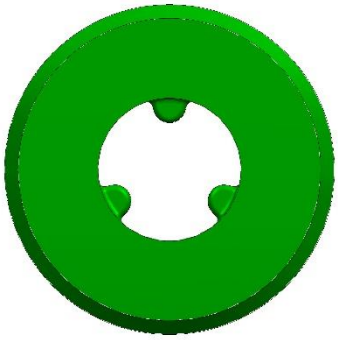

Fig. 33. Cross-section of the rotational barrel segment with the hole with three longitudinal pins situated every 120 degrees

1.8 Conception No 8

The next constructional solution has a non-standard screw with a part specially designed for cooperating with a rotational segment equipped with eight cylindrical pins situated at the circumference every 45 degrees (Fig. 34 and Fig. 35). The thickness of the layer of polymer stream flowing through the plasticizing system decreases at the thickened part of the screw. Directly behind it, the diameter of the root decreases as well as the pressure and flow rate of polymer, which is intensively mixed by the pins on the inner surface of the rotational segment.

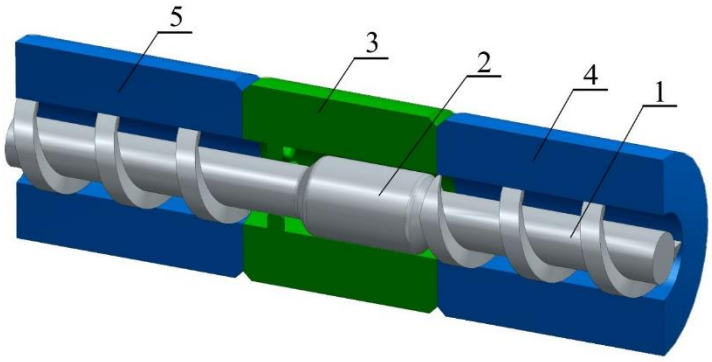

Fig. 34. Longitudinal section of the plasticizing system with a rotational segment and a modified screw equipped with a part deprived of flights and of the increased diameter of the root: 1 – screw, 2 – part of the screw of increased diameter of the root, 3 – rotational segment, 4 and 5 – immovable barrel elements

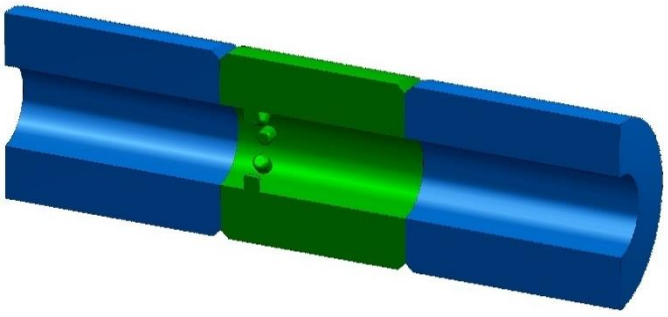

Fig. 35. Longitudinal section of the plasticizing system with a rotational segment, without a screw

Figure 36 shows the cross-section of the considered constructional solution of the rotational barrel segment.

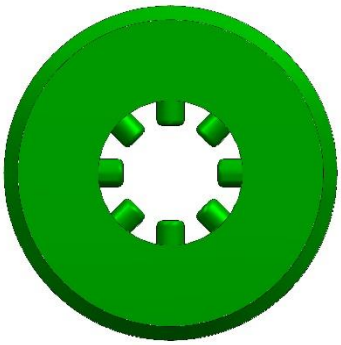

Fig. 36. Cross-section of the rotational barrel segment with the hole with eight cylindrical pins

1.9 Conception No 9

Figures 37 and 38 present a constructional solution of the plasticizing system, which comprises a rotational segment and a screw with a part, which is deprived of flights and has an increased diameter of the root. The length of this part corresponds to the length of the rotational barrel segment. On the inner surface of the rotational segment there are semi-circular pins of the diameter 3 mm situated alternately in 12 rows, which during the rotation cause cutting and mixing of the parallel polymer streams flowing through the screw element with the increased diameter of the root.

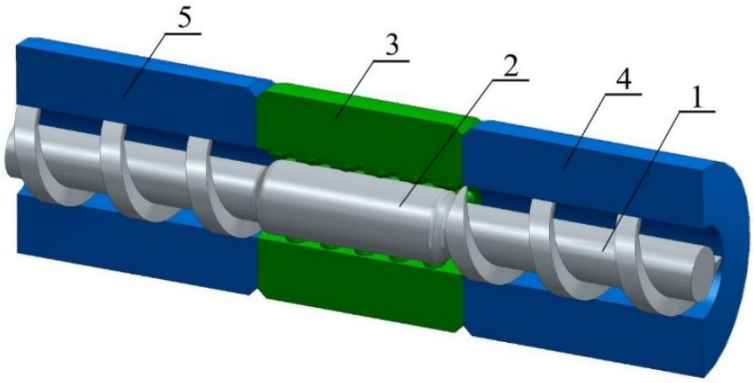

Fig. 37. Longitudinal section of the plasticizing system with a rotational segment and a modified screw: 1 – screw, 2 – part of the screw with increased diameter of the root, 3 – rotational barrel segment, 4 and 5 – immovable parts of the barrel

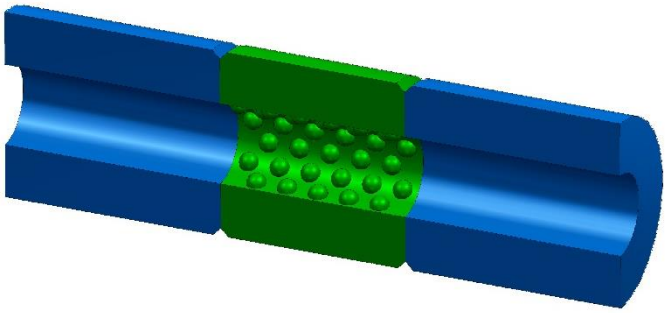

Fig. 38. Longitudinal section of the plasticizing system with a rotational barrel segment, without the screw

Figure 39 shows the cross-section of the considered constructional solution of the rotational barrel segment.

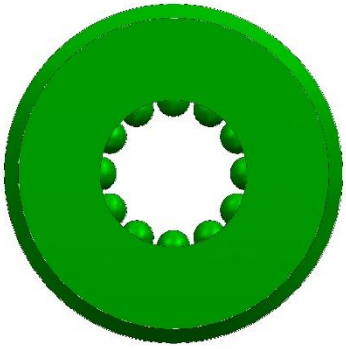

Fig. 39. Cross-section of the rotational barrel segment with the hole with semicircular pins situated alternately in 12 rows

1.10 Conception No 10

The next conception is presented in Figures 40 and 41. It shows a plasticizing system with a classic screw and a rotational barrel segment, and on the inner surface of the latter there is a flight of the direction opposite to the screw flight. This is aimed to lead to the returning of the polymer layer directly at the barrel surface and mixing it with polymer stream entering the area of the rotational barrel segment.

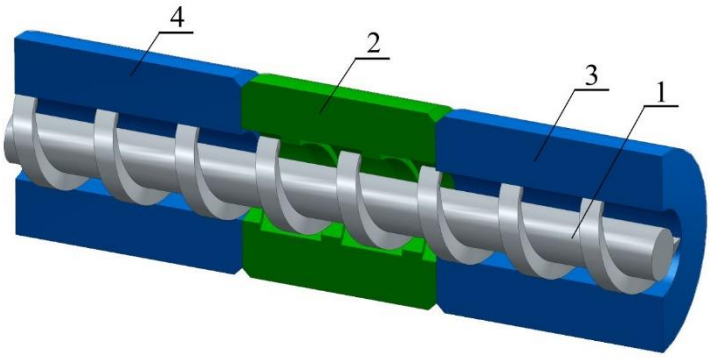

Fig. 40. Longitudinal section of the plasticizing system with a classic screw equipped with a rotational barrel segment: 1 – screw, 2 – rotational barrel segment with a flight on the inner surface of the direction opposite to the screw flight, 3 and 4 – immovable parts of the barrel

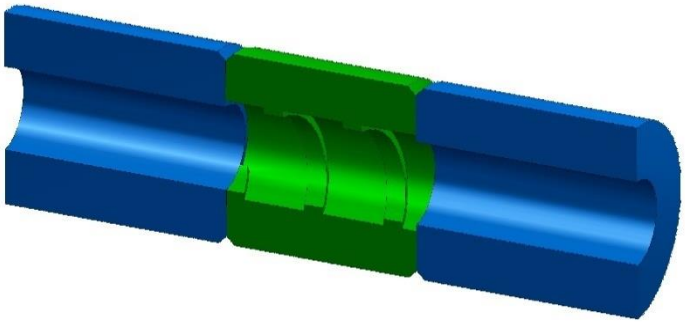

Fig. 41. Longitudinal section of the plasticizing system equipped with a rotational barrel segment, without a screw

Figure 42 shows the cross-section of the considered constructional solution of the rotational barrel segment.

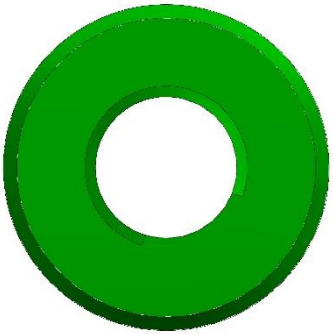

Fig. 42. Cross-section of the rotational barrel segment with the flight on the inner surface

1.11 Conception No 11

The next conception of the rotational barrel segment is presented in Figures 43 and 44. This conception concerns the plasticizing system with the screw without flights or with slight irregularities of the surface on the length of cooperation with the rotational barrel segment. The segment has flights on its inner surface, the same as on the screw. Due to the efficiency of the plasticizing system, the rotational barrel segment can rotate with different speeds in the direction compatible with the direction of screw rotation. The difference in the speeds of barrel segment and the screw influences the degree of polymer mixing and the efficiency of the system.

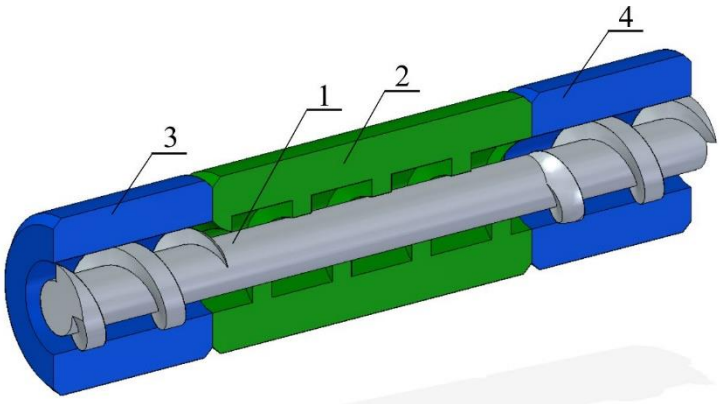

Fig. 43. Longitudinal section of the plasticizing system with a rotational barrel segment and a screw without a flight on the length of the segment: 1 – screw, 2 – rotational barrel segment with a flight on the inner surface, 3 and 4 – immovable parts of the barrel

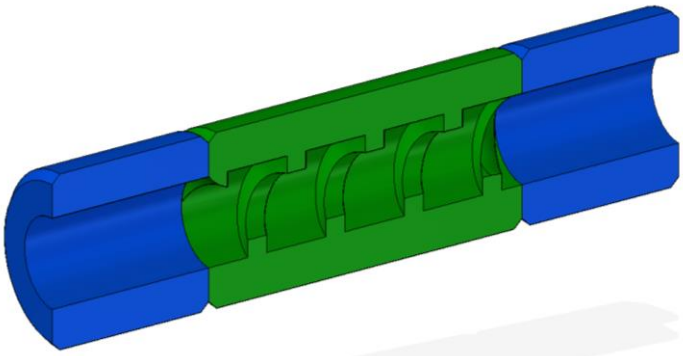

Fig. 44. Longitudinal section of the plasticizing system equipped with a rotational barrel segment, without a screw

Figure 45 shows the cross-section of the considered constructional solution of the rotational barrel segment.

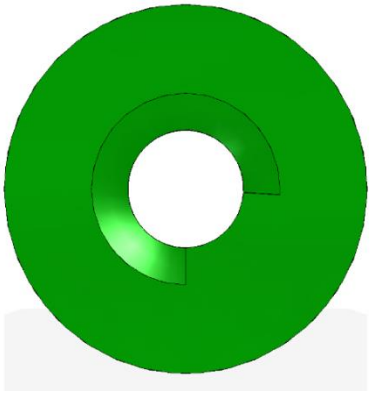

Fig. 45. Cross-section of the rotational barrel segment with a flight on the inner surface

The construction of the plasticizing system in accordance with the conceptions described above can cause some difficulties. The biggest one will probably be providing the required tightness at the contact point of the rotational elements and at the contact point of immovable barrel parts and the rotational elements – especially between the elements rotating in opposite directions. It will be favourable in this case to use sealings made of material with a higher coefficient of thermal expansion than the material, which are used to make the rotational elements. This will allow to maintain the tightness at variable temperatures. An important feature of the sealing is also a small coefficient of friction so that the tribological wear is not fast.

Another difficulty can be the drive transmission in the conceptions with a number of rotational elements. In this case it is favourable to use the transfer of the torque from the motor to one of the rotational elements, and the other ones shall be driven by

transferring the torque from the previous rotational elements by means of appropriate gear.

Because of the complicated construction of the particular solutions, it may be favourable to use the screw consisting of a few parts, which will be connected by means of a thread. It can significantly simplify the assembly of the screw and of the rotational elements.

2. Objective and scope of numerical calculations

The aim of the conducted numerical calculations was to analyse the strength of the new construction of the rotational barrel segment of a single-screw extruder. Three constructional solutions were analysed. The numerical simulation was made on the basis of assembling of the construction elements made in SolidEdge and SolidWorks programmes, a method of finished elements ABAQUS® implemented to the programme. Geometrical models accepted for numerical calculations of the analysed constructions are presented in Figures from 46 to 48.

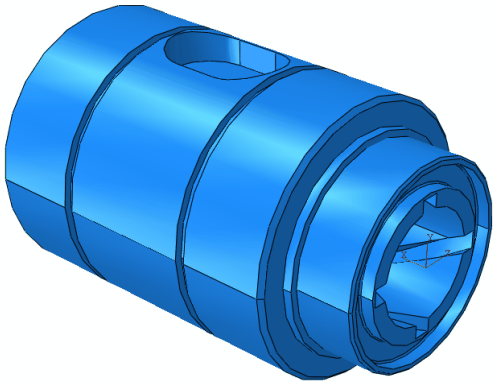

Fig. 46. Model of the rotational barrel segment with 4 helical grooves – variant 1

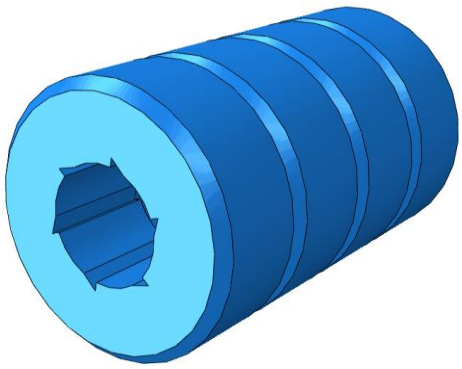

Fig. 47. Model of the rotational barrel segment with 6 longitudinal grooves – variant 2

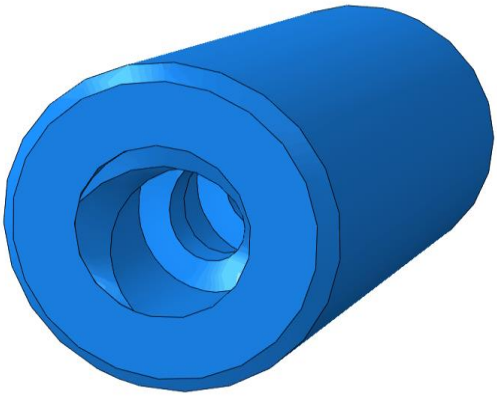

Fig. 48. Model of the rotational barrel segment with a flight on the inner surface – variant 3

The range of the conducted numerical analyses included calculations concerning the estimation of the strength of construction elements exposed to the pressure caused by the transfer of polymer and action of centrifugal force as well as thermal calculations enabling to receive the temperature distribution in the wall and surface of the rotational barrel segment because of polymer friction against the inner surfaces of the segment and heating the rotational segment from the external side. Within the numerical calculations, the following tasks were carried out:

- developing discrete models enabling the numerical analysis using the method of finished elements,
- determining material models and limiting cases of loading the construction,
- conducting numerical simulations enabling to determine the distribution of reduced stress and nodal displacement of construction,
- evaluation of stiffness and strength of construction on the basis of the received results of numerical analysis,
- estimation of temperature distribution in the elements of construction during the exploitation of the rotational barrel segment,
- conclusions of the conducted numerical analysis, presenting the evaluation of the proposed constructional solutions.

3. Construction of a discrete model

3.1 Discretization of construction

Numerical calculations were conducted using the method of finished elements. As a calculating tool ABAQUS® programme was used. The construction of discrete models was made on the basis of the developed geometrical models of analysed constructions.

The discretization of a geometrical model was made using tetragonal solid elements, type C3D4T, which constitute 4-nodal elements with the shape function of

the first order and full integration to enable to take into account in a numerical analysis a thermal degree of freedom. In all variants it was accepted that elements of construction – rotational barrel segment - are made of steel marked 40HM.

In strength calculations, a bilinear model of material was accepted, of elastic-plastic characteristics, for which the following material properties were accepted (Table 1):

Table 1. *Mechanical properties of steel 40HM*

Material property – steel 40HM	
Young modulus E [Pa]	$2.1 \cdot 10^{11}$
Poisson number [-]	0.3
Yield strength R_e [Pa]	$8.8 \cdot 10^{+11}$
Strength limit R_m [Pa]	$1.03 \cdot 10^{12}$
Elongation at break [%]	10

In thermal calculations, a bilinear model of material was accepted, of elastic-plastic characteristics, for which the following thermal properties were accepted (Table 2):

Table 2. *Material properties for thermal calculations*

Material property – steel 40HM	
Density ρ [kg/m^3]	7860
Linear expansion coefficient [1/K]	$1.2 \cdot 10^{-5}$
Heat conduction coefficient λ [W/(m·K)]	58
Specific heat [J/(kg·K)	450

A discrete model of the rotational barrel segment developed for variant 1 is presented in Figure 49.

A discrete model of the rotational barrel segment developed for variant 2 is presented in Figure 50.

Discrete model of the rotational barrel segment developed for variant 3 is presented in Figure 51.

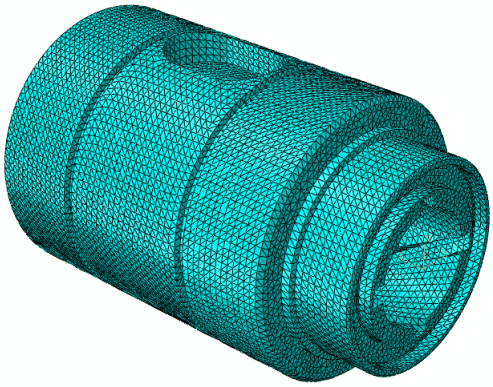

Fig. 49. Discrete model of the rotational barrel segment of the construction - variant 1

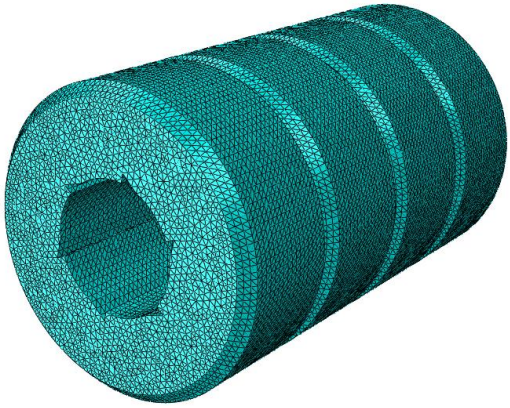

Fig. 50. Discrete model of the rotational barrel segment of the construction - variant 2

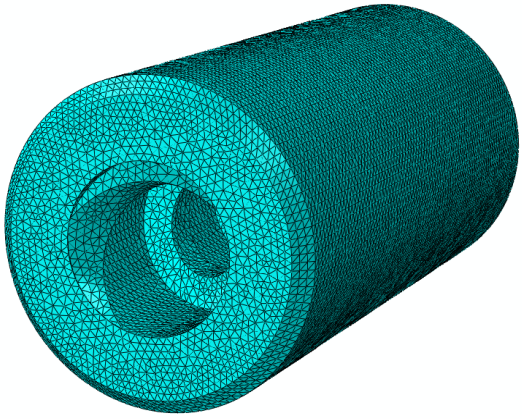

Fig. 51. Discrete model of the rotational barrel segment of the construction - variant 3

3.2 Boundary conditions and loading of construction

The definition of boundary conditions in particular numerical models was carried out by fixing nodes placed on the surfaces of mounting the segment (Fig. 52), on the front edges of the segment (Fig. 53 and Fig. 54) blocking the possibility of their displacement (translational degrees of freedom of nodes placed on these surfaces) in three directions X, Y and Z. Exemplary boundary conditions with marked fixing surfaces for variant 1, 2 and 3 are presented in Figure 52, Figure 53 and Figure 54.

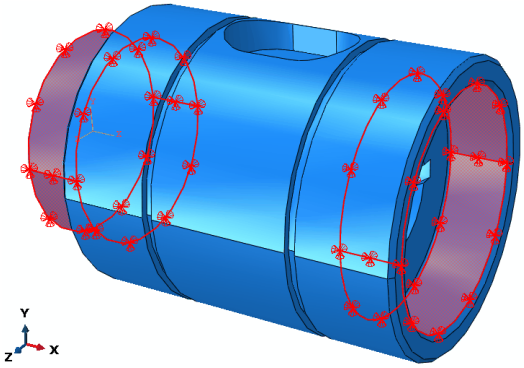

Fig. 52. Boundary conditions of the model – variant No 1

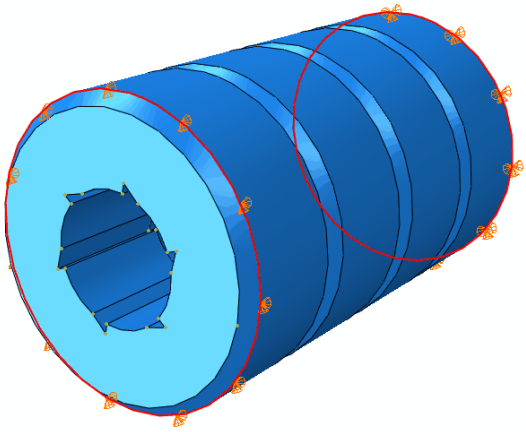

Fig. 53. Boundary conditions of the model – variant No 2

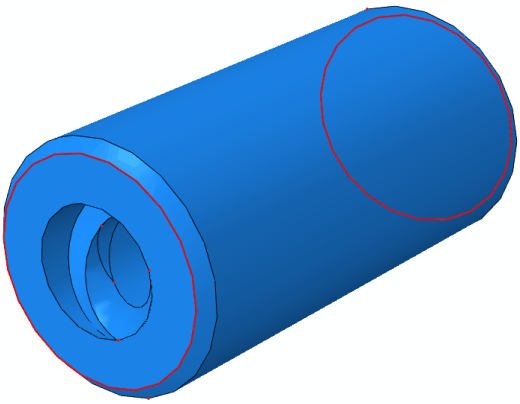

Fig. 54. Boundary conditions of the model – variant No 3

In the analysed numerical models, the following loading of construction was used:

- mechanical load:
  a) internal pressure on the walls of the rotational barrel segment p = 50 MPa (Fig. 55, Fig. 56, Fig. 57).
  b) rotation of the segment with the speed n = 150 rev/min (Fig. 58, Fig. 59, Fig. 60).

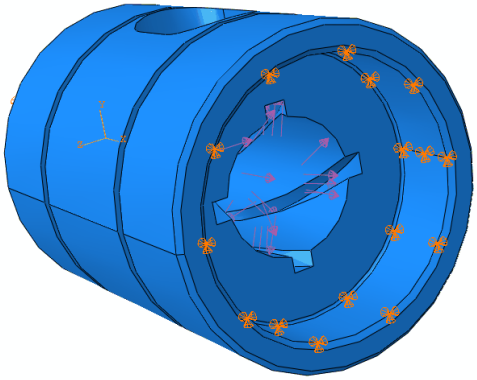

Fig. 55. Loading internal surfaces of the rotational barrel segment with pressure – variant 1

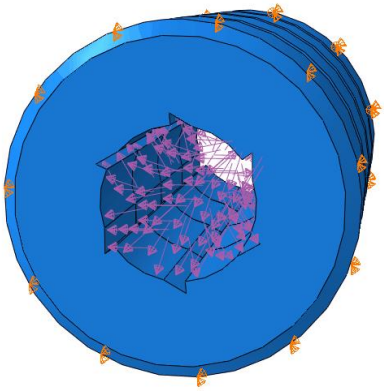

Fig. 56. Loading internal surfaces of the rotational barrel segment with pressure – variant 2

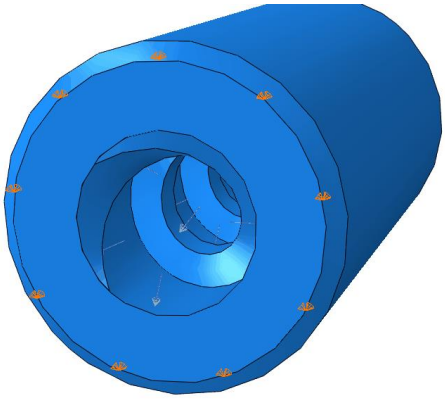

Fig. 57. Loading internal surfaces of the rotational barrel segment with pressure – variant 3

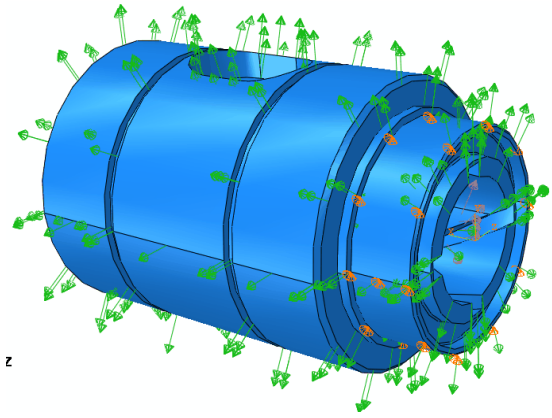

Fig. 58. Loading the model with centrifugal force – variant 1

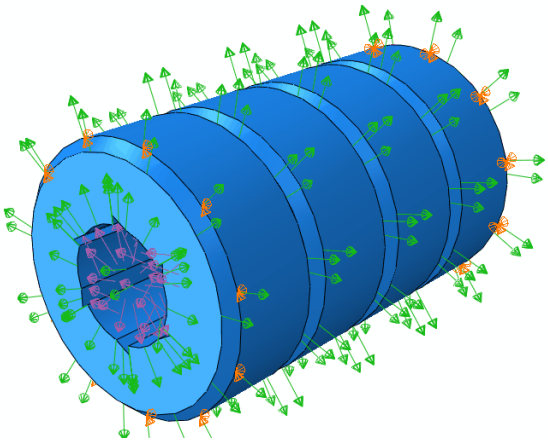

Fig. 59. Loading the model with centrifugal force – variant 2

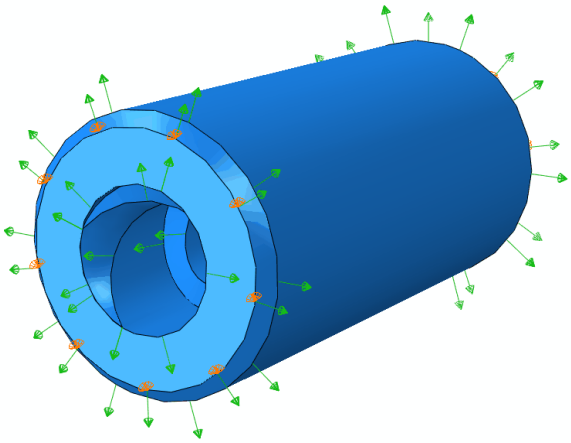

Fig. 60. Loading the model with centrifugal force – variant 3

c) thermal loading:

1) in thermal analysis the loading was the polymer temperature arising as a result of friction and heating by heaters, equalling T = 150°C, applied to the internal surface of the rotational barrel segment,
2) additionally, thermal loading was the temperature coming from heating the external surface of the segment, equalling T = 150°C,
3) initial temperature of the numerical model was accepted as T_0 = 22°C.

The scheme of introducing loading with temperature into the construction of rotational barrel segments is presented in Figures 61, 62 and 63.

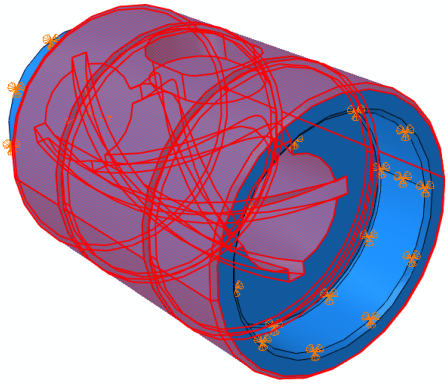

Fig. 61. Loading the rotational barrel segment with temperature – variant 1

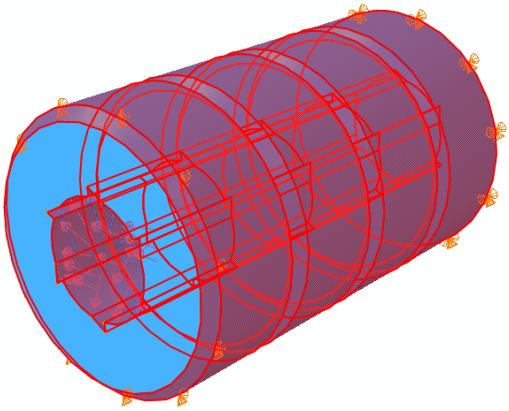

Fig. 62. Loading the rotational barrel segment with temperature – variant 2

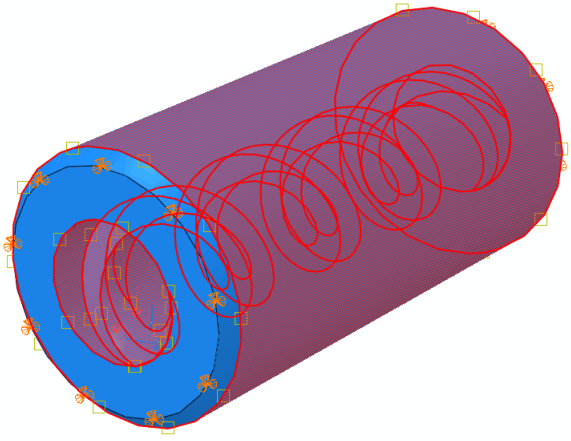

Fig. 63. Loading the rotational barrel segment with temperature – variant 3

4. Results of numerical calculations

A numerical analysis of the construction of the rotational barrel segment was conducted in the range of static calculations, taking into account a geometrically non-linear issue (big displacement and deflection). In order to solve a non-linear system of equations, Newton-Raphson increment-iterative method was used. A strength and stiffness analysis of particular construction elements was conducted on the basis of the distributions of reduced tension, determined in accordance with Huber-Mises-Hencky strength hypothysis in the area of analysed construction and displacement of nodes of its particular elements. The accepted hypothesis is the basic hypothysis used in engineering calculations in relation to elements made of materials of isotropic properties. In thermal calculations, the temperature distribution was determined in the area of analysed constructions, in the state corresponding to 18 000s (5 hours) of constant operation of the machine.

Distributions of tension, displacements and temperature are presented in the form of colourful contour maps against the background of the deflected model, in which the red colour indicates maximum values, while the blue colour minimum values.

4.1 Variant 1 of the construction of the rotational barrel segment

a) Strength calculations

As a result of numerical calculations, total reduced tension in the construction of the rotational segment was determined. The results in the form of the map of reduced tension are shown in Figures from 64 to 66. The presented values of tension are expressed in [Pa].

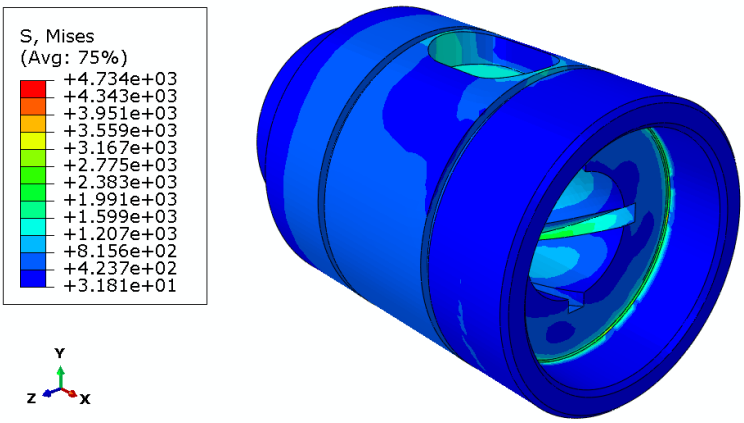

Fig. 64. Distribution of total reduced tension H-M-H resulting from loading with centrifugal force

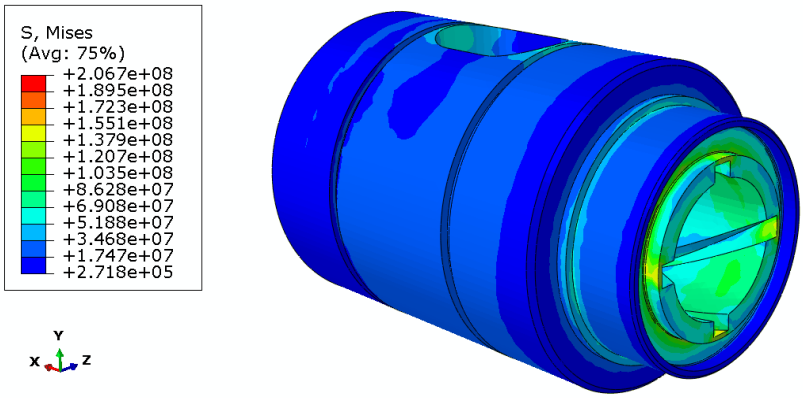

Fig. 65. Distribution of total reduced tension H-M-H resulting from loading with centrifugal force and internal pressure

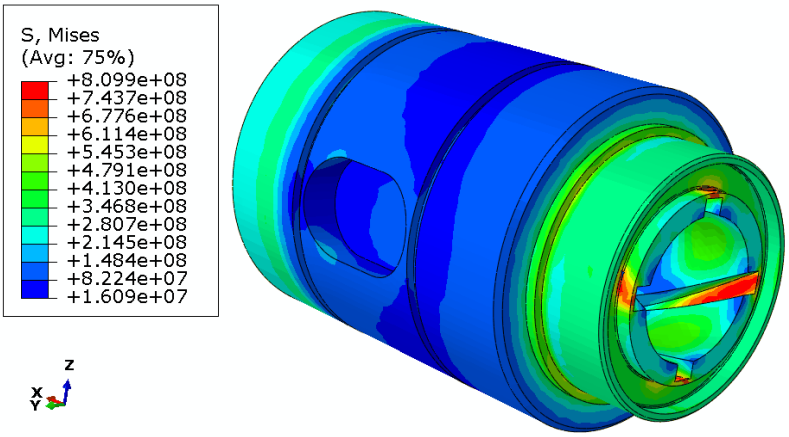

Fig. 66. Distribution of total reduced tension H-M-H resulting from loading with centrifugal force, internal pressure and temperature

The presented maps of reduced tension for the particular states of loading enable to estimate the influence of the given loading on the degree of tension of the material construction. From Figure 64 it turns out that reduced tension coming from the segment rotating with the speed n = 150 rev/min practically does not load the segment because its maximum value is $\sigma_z \approx 0.0047$ MPa. In the case of loading the rotating segment with the internal pressure p = 50 MPa (Fig. 11) the value of tension reaches the level of $\sigma_z \approx 206{,}7$ MPa. A significant increase of the tension level is caused by the operation of a segment with an additional accounting for the conditions of thermal loading, corresponding to the continuous operation of a construction in the time t = 18000 s (5 hours). Maximum reduced tension in the elements of construction reaches

the level of $\sigma_z \approx 809$ MPa. The value of the received tension is not higher than the value of the yield point, which according to the accepted material properties for steel 40HM equals $R_e = 880$ MPa. It means, **that the level of reduced tension appearing in the construction for the considered case of loading does not threaten the safe operation of the construction.**

In Figure 67 the total displacement of nodes of the numerical model of the rotational barrel segment expressed in [m] is presented.

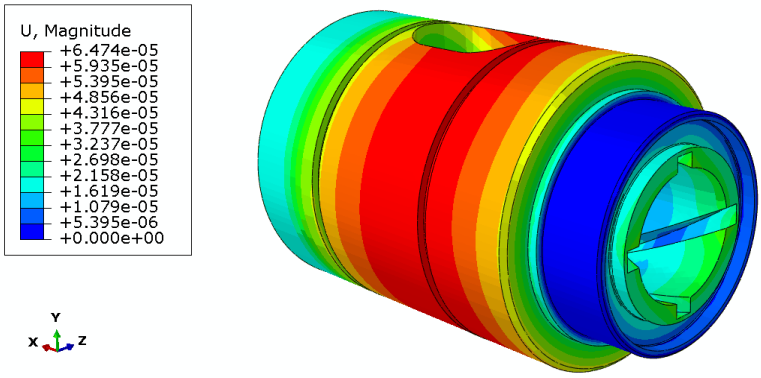

Fig. 67. Map of nodes displacement of the model

The received values of nodes displacement equal 0.004 mm, which constitutes a very small value, not threatening the correct operation of the developed construction. This confirms a high stiffness of the construction.

b) Thermal calculations

As a result of thermal calculations, a fixed state of construction operation was received, consisting in reaching the temperature T = 150°C by the whole segment, which corresponds to the temperature of loading the construction from the outside and inside – Figure 68.

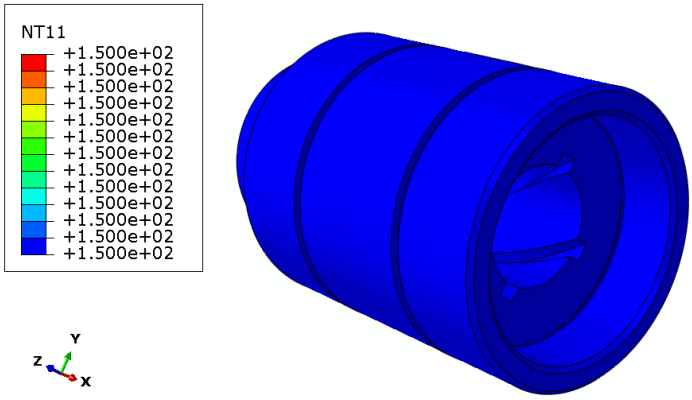

Fig. 68. Temperature distribution in the model of variant 1 of rotational barrel segment

4.2. Variant 2 of the construction of the rotational barrel segment

a) Strength calculations

As a result of numerical calculations the total reduced tension in the construction of the rotational segment was determined. The results in the form of the map of the reduced tension are presented in Figures from 69 to 71. The presented values of tension are expressed in [Pa].

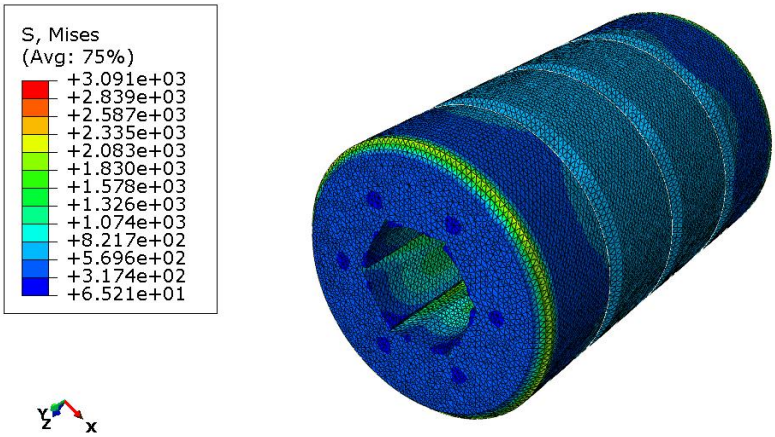

Fig. 69. Distribution of reduced tension H-M-H resulting from loading with centrifugal force

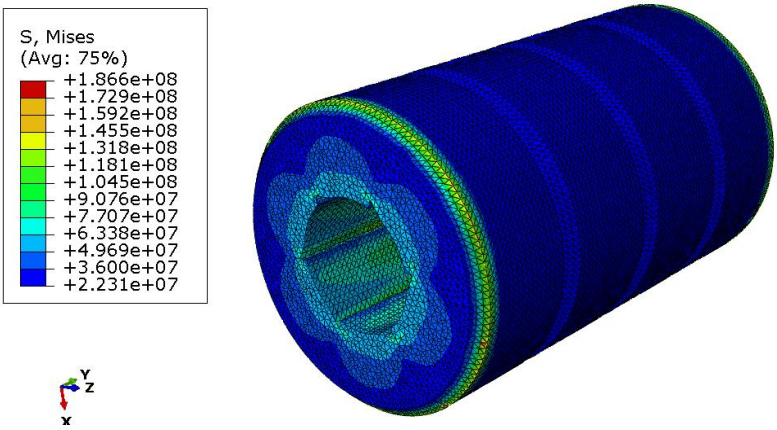

Fig. 70. Distribution of reduced tension H-M-H resulting from loading with centrifugal force and internal pressure

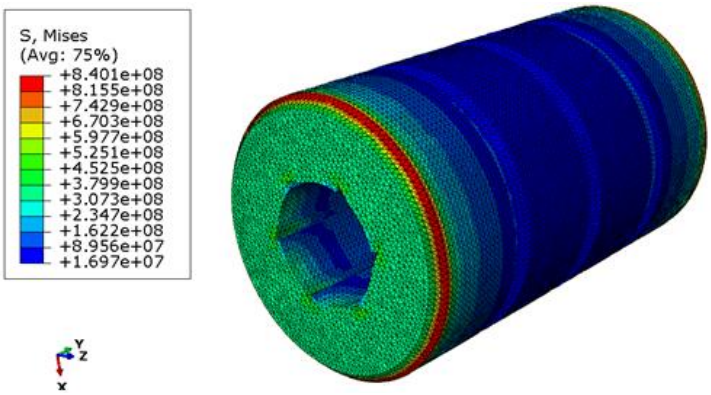

Fig. 71. Distribution of total reduced tension H-M-H resulting from loading with centrifugal force, internal pressure and temperature

The presented maps of reduced tension for the particular states of loading enable to estimate the influence of the given loading on the degree of tension of the material construction. From Figure 69 it turns out that reduced tension coming from the segment rotating with the speed n = 150 r/min practically does not load the segment because its maximum value is $\sigma_z \approx 0.0069$ MPa. In the case of loading the rotating segment with the internal pressure p = 50 MPa (Fig. 70) the value of tension reaches the level of $\sigma_z \approx 187$ MPa. A significant increase of the tension level is caused by the operation of a segment with an additional accounting for the conditions of thermal loading, corresponding to the continuous operation of a construction in the time t = 18000 s (5 hours). Maximum reduced tension in the elements of construction reaches the level of $\sigma_z \approx 840$ MPa. The value of the received tension is not higher than the value of the yield point, which according to the accepted material properties for steel 40HM equals R_e = 880 MPa. It means, that **the level of reduced tension appearing in the construction for the considered case of loading does not threaten the safe operation of the construction.**

Figure 72 presents total displacement of nodes of the numerical model closing element with a group of inlets expressed in [m].

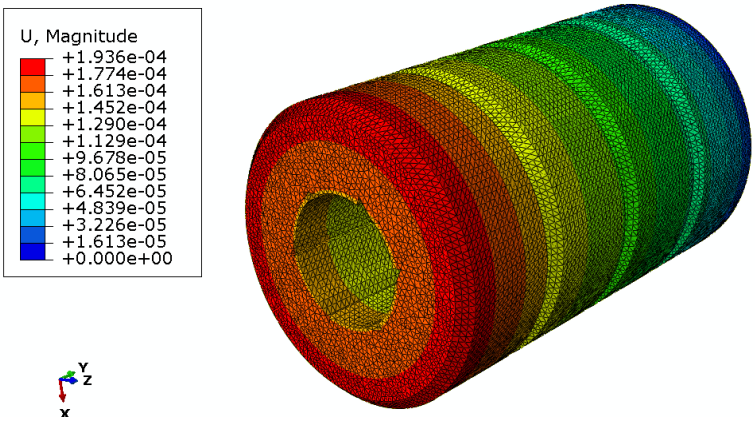

Fig. 72. Map of nodes displacements of the model

The received values of nodes displacement equal 0.045 mm, which constitutes a very small value, not threatening the correct operation of the construction.

b) Thermal calculations

As a result of thermal calculations, a fixed state of construction operation was received, consisting in reaching the temperature T = 150°C by the whole segment, which corresponds to the temperature of loading the construction from the outside and inside – Figure 73.

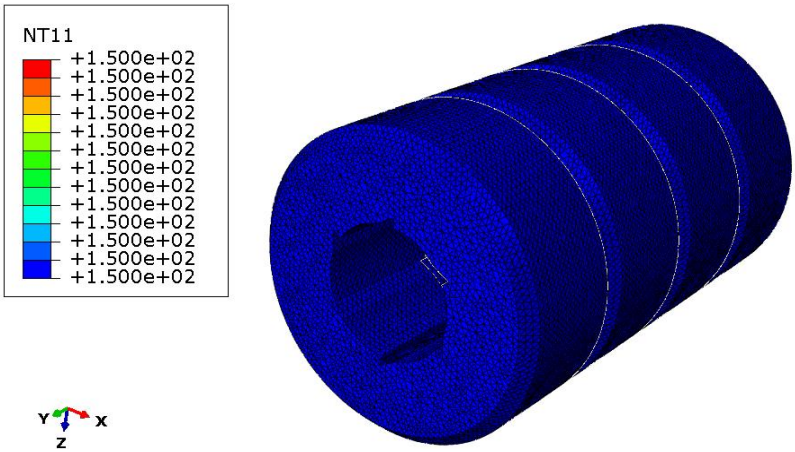

Fig. 73. Temperature distribution in the model of variant 2 of the rotational barrel segment

4.3. Variant 3 of the construction of the rotational barrel segment

a) Strength calculations

As a result of numerical calculations the total reduced tension in the construction of the rotational segment was determined. The results in the form of the map of the

reduced tension are presented in Figures from 74 to 76. The presented values of tension are expressed in [Pa].

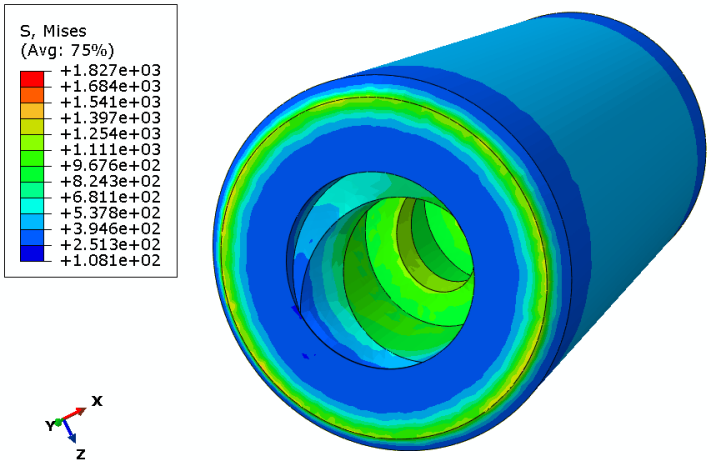

Fig. 72. Distribution of reduced tension H-M-H resulting from loading with centrifugal force

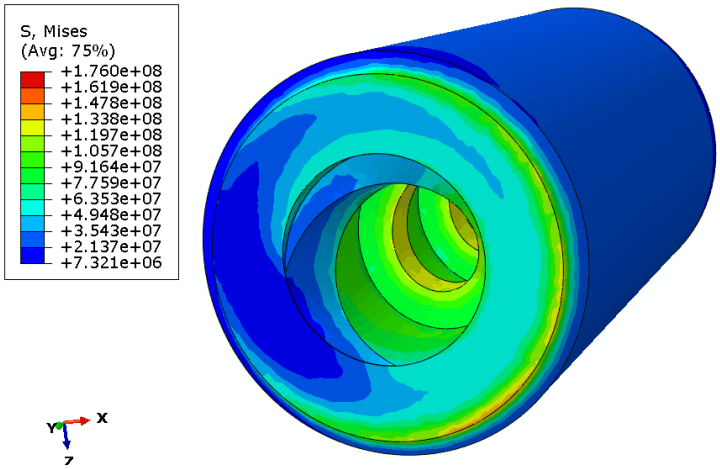

Fig. 73. Distribution of reduced tension H-M-H resulting from loading with centrifugal force and internal pressure

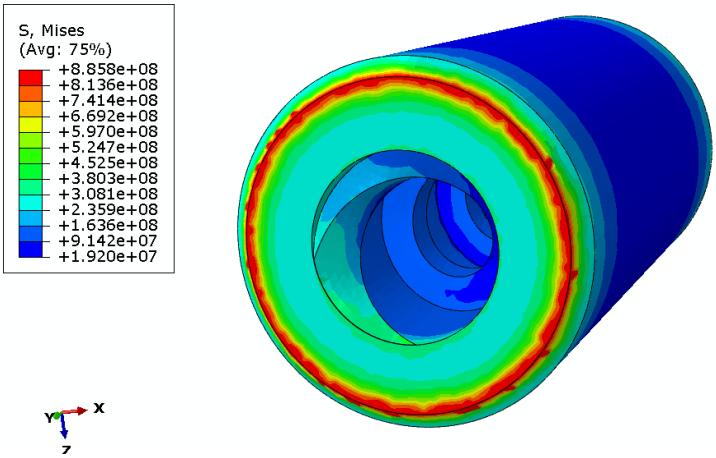

Fig. 74. Distribution of total reduced tension H-M-H resulting from loading with centrifugal force, internal pressure and temperature

The presented maps of reduced tension for the particular states of loading enable to estimate the influence of the given loading on the degree of tension of the material construction. From Figure 74 it turns out that reduced tension coming from the segment rotating with the speed n = 150 r/min practically does not load the segment because its maximum value is $\sigma_z \approx 0.0018$ MPa. In the case of loading the rotating segment with the internal pressure p = 50 MPa (Fig. 75) the value of tension reaches the level of $\sigma_z \approx 176$ MPa. A significant increase of the tension level is caused by the operation of a segment with an additional accounting for the conditions of thermal loading, corresponding to the continuous operation of a construction in the time t = 18000 s (5 hours). Maximum reduced tension in the elements of construction reaches the level of $\sigma_z \approx 885$ MPa. However, the received value results from the way of fixing the model, which, in this case, causes a significant increase of the value of reduced tension. Taking into account this fact, it can be stated that **the level of reduced tension appearing in the construction for the considered case of loading does not threaten the safe operation of the construction.**

Figure 77 presents total displacement of nodes of the numerical model closing element with a group of inlets expressed in [m].

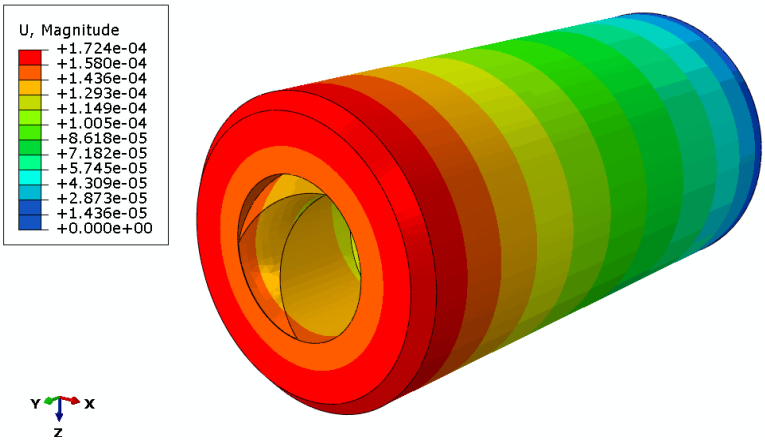

Fig. 77. Map of nodes displacements of the model

The received values of nodes displacement equal 0.017 mm, which constitutes a very small value, not threatening the correct operation of the construction.

b) Thermal calculations

As a result of thermal calculations, a fixed state of construction operation was received, consisting in reaching the temperature T = 150°C by the whole segment, which corresponds to the temperature of loading the construction from the outside and inside – Figure 78.

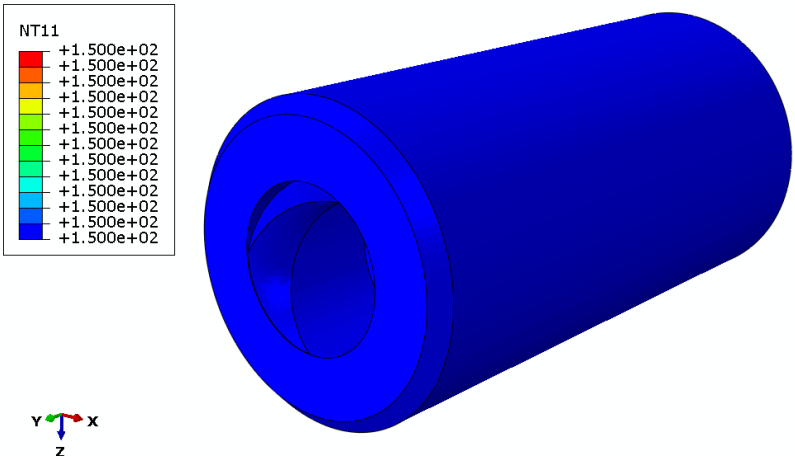

Fig. 78. Temperature distribution in the model of variant 3 of the rotational barrel segment

5. Conclusions

The conducted numerical analysis using the method of finished elements enables to formulate conclusions concerning the strength and thermal estimation of the

analyzed variants of the extruder rotational barrel segment. On the basis of the received results of numerical calculations it was stated that the designed construction operates within a safe range. This is confirmed by the values of tension in the elements of construction, which are not higher than the values of the yield point 880 MPa. Moreover, the received temperature distributions in the construction area, corresponding to 5 hours of the continuous operation of the unit, confirm a stable operation of the segment in the temperature T = 150°C in the whole area of the segment.

Acknowledgement

This project has received funding from the European Union's Horizon 2020 research and innovation programme under the Marie Skłodowska-Curie grant agreement No 734205-H2020-MSCA-RISE-2016.

Ivan Gajdoš[1], Janusz Sikora[2], Emil Spišák[1], František Greškovič[1]

SIMULATION ANALYSIS OF SINGLE SCREW EXTRUDER IN ANSYS POLYFLOW

Abstract: *As the technology of polymer extrusion becomes more sophisticated, demand on possibility to accurate simulate extrusion process in full 3D rises. Significant. This paper deals with steps necessary to carry out successful simulation. Description and analysis of ANSYS Polyflow package and available mesh types is presented in the work. Theoretical background of calculation and adoption of Mesh Superposition Technique is described. In practical part a preprocessing setup for calculations is presented with subsequent evaluation of results in ANSYS CFD-Post.*
Keywords: *Ansys Polyflow, extrusion, numerical calculation.*

1. Introduction

The single screw extruder (SSE) is one of the most widely used tools, not only in the plastics and rubber industry but also in other areas such as food processing. Almost in every technology processing the raw materials (injection molding, extrusion, blow molding, etc.), SSE are involved to melt, convey, compress and mix the different compounds and those steps can affect considerably the quality of the process.

This wide application can explain the intensive research focused on SSE analysis in the literature and, the numerous attempts to model SSEs through numerical simulations. However, the problem and challenges coupled in such simulations (moving parts, thermal behavior, difficult meshing and remeshing tasks, partial filling, to mention just a few) led to many simplifications of the problem. Several approaches have been applied by researchers. 1D models [1, 2] provide a global vision of average values along the flow direction (pressure, temperature, etc.) based on some simplifying assumptions. 1D models do not permit the calculation of detailed flow field's which are of great importance, among others, to the mixing analysis. 2 D & 2 1/2D models [3] provide one of the major popular, less restrictive, simplifications which can offer somewhat more precise local information of the flow field behavior in SSE analysis. Simulation with 3D FEM models allow for a more accurate representation of the flow field. To solve the 3D time-dependent motion of the screws rotating about their axe, an approach with simulating a sequence of several instantaneous positions can be used. These "slides"' are combined to reconstruct the overall effect of the screws motion on

[1)] *Technical University of Košice, Department of CAx Technologies, Mäsiarska 74, 040-01, Košice, Slovak Republic, e-mail: ivan.gajdos@tuke.sk*
[2)] *Lublin University of Technology, Department of Technology and Polymer Processing, ul. Nadbystrzycka 36, 20-618 Lublin, Poland*

the polymer flow. This method requires a considerable effort and lot of resources in the meshing of each individual relative position of the screw body.

The boundary elements method (BEM) has been used [4] to offer an alternative to the large meshing effort. But the basic advantage of the BEM is almost totally lost as soon as non-linearities are introduced in the simulation (including realistic features such as shear-thinning fluids, non-isothermal cases, viscous heating, etc.).

The most proper technique has to combine the power of FEM to deal with strong non-linearities with the simplicity of the mesh generation and absence of remeshing of the BEM. In order to simplify the setup of a 3D unsteady SSE simulation and to avoid the use of a remeshing algorithm, two techniques referred to as the mesh superposition technique [5] and sliding mesh technique have been implemented in the ANSYS POLYFLOW® software. This robust technique dramatically simplifies the meshing of the geometric entities, avoids the use of any remeshing algorithms and does not present the complexities and limitations of the sliding meshes technique.

2. ANSYS POLYFLOW

ANSYS Polyflow® (APF) is a finite-element computational fluid dynamics (CFD) program designed primarily for simulating applications where viscous and viscoelastic flows play an important role. The flows can be isothermal or nonisothermal, two- or three-dimensional, steady-state or time-dependent. APF is used primarily to solve flow problems in polymer and rubber processing, food rheology, glasswork furnaces, and many other rheological applications. The calculation of such flows is based on non-Newtonian fluid mechanics, characterized by a wide variety of fluid models and strong nonlinearities.

It is possible to detect contact during APF simulations. This capability makes APF useful for blow molding, thermoforming, and compression molding simulations. A major advantage is that access to a library of non-Newtonian materials is maintained for all contact problems. APF also provides additional capabilities for glass furnaces, such as bubbling, radiative correction, and electrical heating. APF can perform a number of complex calculations such as multidomain simulations, co-extrusion of several fluids, three-dimensional extrusion, and implicit and time-dependent calculation of free surfaces.

The ANSYS Polyflow package includes the following products and modules (Fig. 1):

- ANSYS Polyflow, the solver,
- ANSYS Polydata, the preprocessor for problem definition,
- GAMBIT, the preprocessor for geometry modeling and mesh generation,
- ANSYS Polymat, the preprocessor for material data specification,
- ANSYS Polystat, the statistical postprocessor for quantitative comparison of flows,
- CFD-Post, the graphical postprocessor for examining results,

- filters (translators) for import of meshes from CAD/CAE packages such as PATRAN and I-deas, and export of meshes and results to these and other programs.

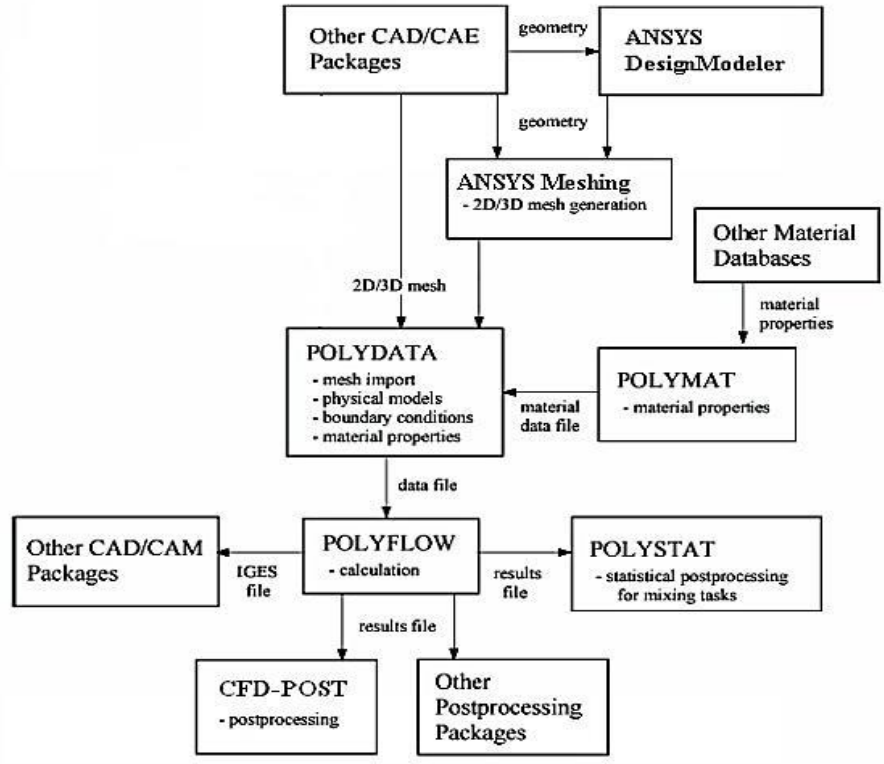

Fig. 1. Structure of ANSYS Polyflow modules

2.1 Mesh topologies supported in Polyflow

Since APF is an unstructured solver, it uses internal data structures to assign an order to the elements, faces, and mesh points in a mesh and to maintain contact between adjacent elements. It does not, therefore, require i, j, k indexing to locate neighboring elements. This gives you the flexibility to use the mesh topology that is best for your problem, since the solver does not force an overall structure or topology on the mesh. In 2D, quadrilateral and triangular elements are accepted, and in 3D, hexahedral, tetrahedral, pyramid, and wedge elements can be used (Fig. 2). Hybrid meshes containing quadrilateral and triangular elements or hexahedral, tetrahedral, pyramid, and wedge elements are also acceptable.

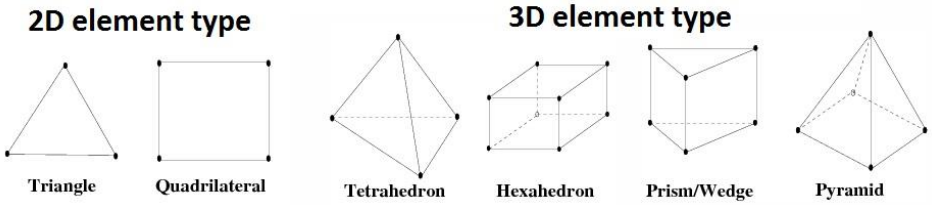

Fig. 2. Types of mesh elements supported in ANSYS Polyflow

3. FLOW SIMULATION WITH MOVING PARTS

APF incorporates techniques known as mesh superposition technique (MST) and sliding mesh technique (SMT). Both techniques have their advantages and limitations in solving simulation of SSE.

3.1 Sliding mesh technique

APF incorporates a sliding mesh technique, which can be used in a similar manner to the (MST) to simulate transient flows with internal moving parts. The applications include industrial processes such as stirring tanks, single screw extruders, and non-intermeshing batch mixers. The advantages of using a sliding mesh over MST are:

- sliding mesh technique is more accurate,
- it does not make any approximation on the shape of moving part. In MST, the shape of moving part depends on the mesh discretization of the flow region.

With SMT come also some limitations in application of this technique in SSE simulations. Limitations of the SMT can be summarized as follows:

- you can solve only the simple rotation of a moving part around a fixed axis
- it does not allow the intermeshing of moving parts
- in this technique, surround each moving part by a cylinder. These cylinders should neither overlap nor cross boundaries of the flow domain during simulation. In 2D cases, the moving parts must be surrounded by circles
- it is available for Generalized Newtonian fluids (isothermal or nonisothermal) and heat conduction problems. It is not available for viscoelastic fluids and transport of species
- sliding mesh motion is limited to rigid rotation. You can define an angular velocity varying with time, if required. Note that ANSYS Polydata will not check if the angular velocity of the sliding mesh is compatible with the boundary condition imposed along the internal boundary of sliding mesh.
- the mixing task is not compatible with the flow fields obtained with sliding mesh techniques. As the node positions of the sliding mesh change with time, the mesh of the flow domain becomes variable. This is a major limitation of the algorithm implemented to track particle paths in ANSYS Polyflow

- while the residence time distribution is calculated for most flow problems, this option is not available when sliding meshes are defined.

When using the sliding mesh technique, decomposing of the SSE flow domain into two parts, as this can be seen in Fig. 3 is necessary: the first one, attached to the barrel wall, is fixed. The second one, attached to the screw surface, will rotate with the same angular rotation than the screw itself. The volume of the screw is not meshed (contrary to the MST). In order to get accurate results with the SMT, it must be pay attention to the two boundaries that are tangential: the inner cylinder of the "fixed" domain and the outer cylinder of the "rotating" domain.

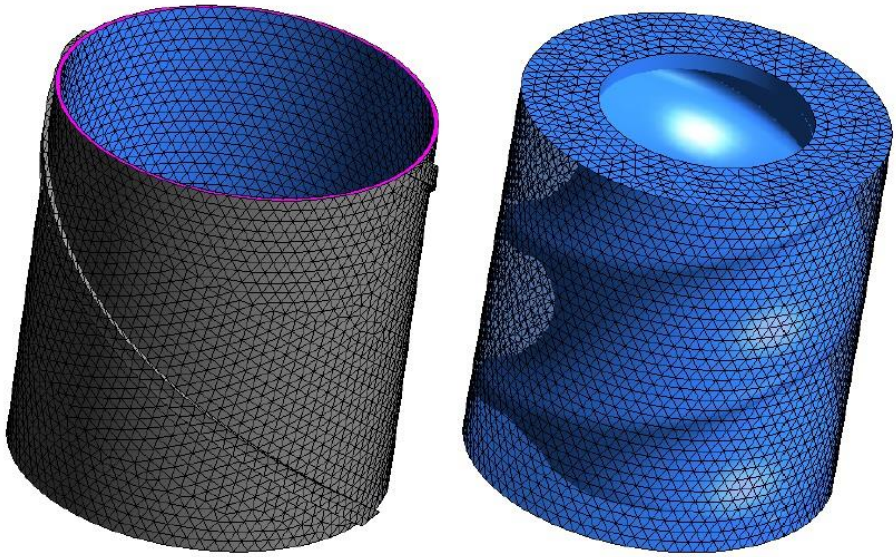

Fig. 3. Segment of SSE meshed for simulation with SMT

Those two boundaries will be connected so that fluid flowing out of one boundary will be flowing in the other boundary. It is desirable and recommended to mesh in the same way (same sizes and same element types) these two boundaries. Moreover, as the mesh attached to the screw is rotating , the time step must be selected so that the displacement per time step of a node on the outer cylinder is smaller or equal to the element size. The SMT is only available for generalized Newtonian fluids and for heat conduction problems in transient tasks.

3.2 Mesh Superposition Technique

Another approach that can be applied for 3D simulation of SSE is mesh superposition technique. The mesh superposition technique has three major advantages:

- mesh generation is much simpler since no complex intermeshing region must be generated,

- it is possible to define a library of moving parts, and to combine them with ANSYS Polyfuse to generate new meshes for new simulations,
- the method is robust, since no remeshing algorithms are needed,
- supports in APF up to 10 moving parts.

The mesh superposition technique also has several limitations:

- it can be used only for 2D planar and 3D models,
- it can be applied only to generalized Newtonian flow,
- the detailed variation of the velocity in the neighborhood of the moving part is not well resolved,
- as the physical boundaries do not match finite-element limits, the mass conservation equation cannot be satisfied in every element; as a result, you may see some limited fluid leakage.

The modeling of internal moving parts requires the modification of the **Navier-Stokes** equations, the mass conservation equation, and possibly the energy equation. The Navier-Stokes equations used in APF to compute a MST task are modified:

$$H(\mathbf{v}-\overline{\mathbf{v}})+(1-H)(-\nabla p+\nabla\cdot\mathbf{T}+\rho\mathbf{g}-\rho\mathbf{a})=\mathbf{0} \tag{1}$$

where: H is a step function
$\mathbf{v}$ is the velocity
$\overline{\mathbf{v}}$ is the local velocity of the moving part
p is the pressure
$\mathbf{T}$ is the extra-stress tensor
$\rho\mathbf{g}$ is the volume force
$\rho\mathbf{a}$ is the acceleration term

For a generalized Newtonian fluid, the extra-stress tensor is defined to be:

$$\mathbf{T}=2\eta(\dot{\gamma},T)\mathbf{D} \tag{2}$$

where: η is the viscosity
$\dot{\gamma}$ is the shear rate
T is the temperature
$\mathbf{D}$ is the rate-deformation tensor

Equation 1 is discretized for each node of the velocity field. For node ***i*** (at location ***x***), if it is outside the moving part, then ***H*** is equal to 0 and the usual Navier-Stokes equations are used. Otherwise, ***H*** is set to 1, and equation 1 degenerates into

$$\overline{\mathbf{v}} = \mathbf{v} \tag{3}$$

in order to impose the local velocity $\overline{\mathbf{v}}(\mathbf{x})$ of the moving part.

More specifically, before solving the Navier-Stokes equations, the “inside" field ***H*** is calculated for the flow domain. This field varies between 0 and 1. A subelement that is overlapped by the moving part has a value of ***H*** = 1, and a subelement outside the

moving part has a value of $\boldsymbol{H}$ = 0. A node $\boldsymbol{i}$ (at location $\boldsymbol{x}$) is considered to be inside the moving part (that is, $\boldsymbol{H}$ = 1) if $\boldsymbol{H}$(x) is greater than a threshold value. The threshold value is usually equal to 0.6, which indicates that more than half of the subelements neighboring the node are overlapped by the moving part. Figure 4 shows a 2D finite element divided into 4 subelements. The subelements that are overlapped by the moving part are marked with a 1, and those that are outside the moving part are marked with a 0. The nodes for which $\boldsymbol{H}$=1 are indicated by filled-in circles.

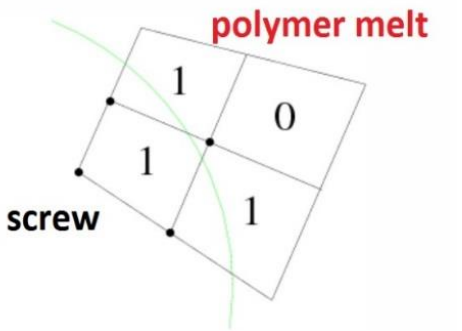

Fig. 4. Presentation of "Inside" Field for a 2D Finite Element

The application of the Navier-Stokes equation (1) in MST assumes a full stick condition along the borders of the moving part. In Polyflow it is possible to enable the option of the slip condition along the borders of the moving part. Nevertheless, because the moving part is represented by means of a domain that overlaps the fluid region, the fluid region will experience only an approximation of the actual boundary of the solid moving part. Because of this approximation, the slipping condition is handled by bounding the local value of the shear stress. In other words, the slipping behavior will obey a mechanism that resembles the asymptotic law. More precisely, if the local value of the shear stress is specified value, the material will be treated as if it is sticking to the wall of the moving part; otherwise, the maximum slipping stress will be applied.

In order to be able to calculate a physically meaningful pressure even in the zones where geometrical penetration occurs, the **mass conservation** equation is modified to become

$$\nabla \cdot \mathbf{v} + \frac{\beta}{\eta} \Delta p = 0 \tag{4}$$

where $\boldsymbol{\beta}$ is a relative compression factor, and $\boldsymbol{\eta}$ is the local viscosity. The relative compression factor $\boldsymbol{\beta}$ is a key aspect of the mesh superposition technique. If there are pressure peaks in regions where a large number of geometrical constraints exist, then the fluid cannot be considered incompressible. To prevent these pressure peaks, the

mass conservation equation has been modified so that the fluid is slightly compressible.

The loss or gain of fluid volume per unit time is linked to the Laplacian of the pressure through the relative compression factor. It is absolutely essential to select the value of this factor carefully. If this factor is too small, pressure peaks will appear in tiny contact regions, especially when the mesh is so coarse that one element exists between the boundary and contact regions. When the factor is too large, the fluid is unphysically compressible and all pressure gradients will be smoothed out, leading to an unphysically low pressure prediction. In ANSYS Polydata, the default value of 0.01 has been shown to be the best choice for this factor when stick conditions are considered along the moving parts. When slipping is considered along the moving parts, a lower value may be needed: it can be acceptable to select a value as low as 10^{-5} or 10^{-6} in order to satisfy the mass conservation. Since a constant pressure per element is assumed, Equation 4 is discretized for each element of the flow domain.

The motion of the moving parts can be both transient and complex. Any type of complex motion can be specified using a user-defined function. Using the specified translational and angular velocities, ANSYS Polyflow integrates the translational and angular positions with an implicit Euler scheme. At each time step, the new position is computed by a displacement (translation and rotation) of the moving part in its reference configuration.

Some other preconditions must be fulfilled when preparing the mesh for MST calculation in APF. The meshes for the flow domain and the moving parts should contain elements of about the same size. It is important that the mesh be fine enough in regions of small geometrical details; otherwise, the coarse mesh will smooth out the details. For the clearance between a screw and its barrel, at least two elements are recommended in the thickness direction (Fig. 5) elements between a screw and its barrel). Pressure and velocity peaks can also be computed due to a coarse mesh in the angular direction. Areas covered by moving parts that are never in the real fluid region do not have to be meshed.

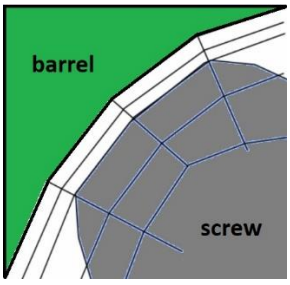

Fig. 5. Meshing the flow domain between barrel wall and screw flight

If case where internal boundaries are overlapped by moving parts, it is necessary to check whether the boundary conditions are compatible with the motion of the

moving parts. Some boundary conditions can easily become incompatible with rotating screw constraints. This may be the case when a screw is rotating and touching the entry/exit sections where an outflow or inflow condition (which implies a zero tangential velocity) is imposed. In this case, it is necessary extend the flow domain, as shown in Figure 6, or apply zero force conditions instead of outflow or inflow conditions.

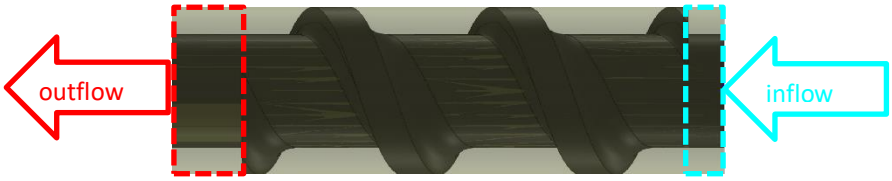

Fig. 6. Extension of the flow domain to prevent incompatibilities in boundary conditions

4. SIMULATION PRE-PROCESSING

Based on assumption mentioned above that APF can handle meshes consisting from various elements, various software solution can be used to mesh prepared CAD data. Usually APF can handle meshes from created in GAMBIT, ANSYS ICEM CFD, ANSYS Meshing, Ansys FLUENT MESH, POLYMESH. It is also possible to mesh fluid domain and moving part domain in different software and join them in one mesh. As the flow domain in single screw extruder has simple cylindrical shape, the best option to mesh the domain is use the hexahedron elements. Using hexahedron elements allow to obtain clean mesh suitable for accurate CFD calculations.

In this example a segment of extruder screw was investigated with screw diameter 25mm, pitch 20mm and 3 revolutions. An 5mm long inflow region with removed flight (Fig. 6) was added. On the outflow section an 10mm region on screw was added. Subsequently the inside of the screw was hollowed out to reduce the number of mesh elements (Fig. 7).

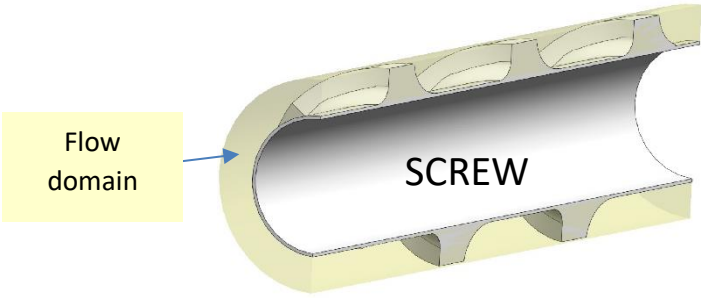

Fig. 7. Cross section of final CAD model of the flow domain and the screw

The hexahedron mesh of flow domain consists of 264 966 elements and the screw mesh consists of 989 393 tetrahedron elements. As the meshes of flow domain and the screw were prepared separately, it was necessary to join them in Ansys Fluent Mesh (Fig. 8).

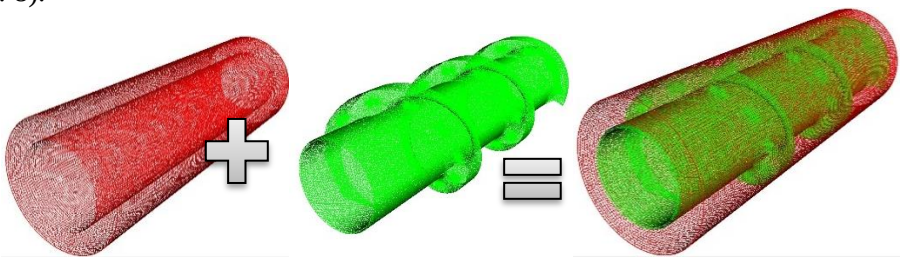

Fig. 8. Combination of the flow domain mesh and the screw mesh

As mentioned before, to capture the actions in the gap between the screw flight and the barrel it was necessary to make flow domain mesh in this area finer. The inflation function was adopted and three elements through the gap were fitted in the flow domain mesh (Fig. 9).

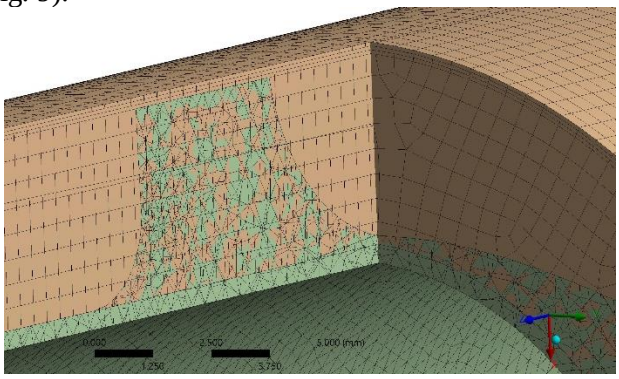

Fig. 9. Layer of elements generated with inflation function

4.1 Boundary conditions

The simulation for this task was calculated as isothermal Newtonian steady state. Final scheme of the computational problem is shown in Figure 10. Flow boundary conditions on the mesh at selected boundaries (BS) were applied:

- BS1 – inflow (Q = 3.0kg/h),
- BS2 – normal forces and tangential velocities vanish (fn & vs) = (0, 0),
- BS3 – cartesian velocities imposed (vx & vy & vz) = 10,472 rad.s^{-1} (100 rpm, direction see Fig. 10),
- BS4 – normal and tangential velocities imposed (vn & vs) = (0, 0).

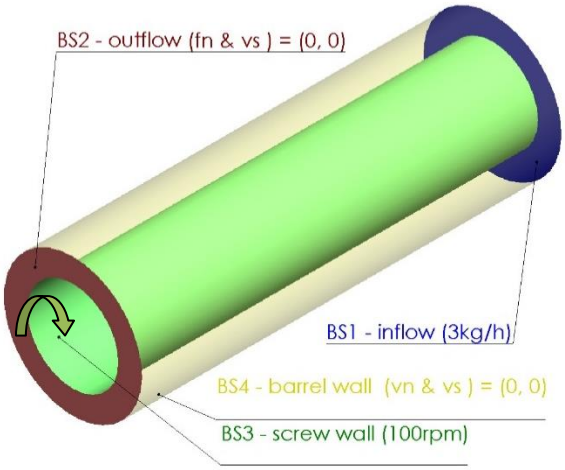

Fig. 10. Numerical boundary conditions

The first two boundary conditions, BS1 and BS2, imply that pressure may be generated along the screw. The pressure at the end of the flow domain is unknown, so we calculate the pressure gradient, which is relative to the zero pressure at the flow domain exit. We have used the power-law rheological model for the material from the APF database Extrusion_HDPE_isoth_463K flowing material.

5. RESULTS AND DISCUSSION

Results postprocessing was performed in Ansys CDF-Post 2019 R2®. Some selected results are presented in Figures 11, 12 and 13. Output fields from APF (in calculated example) are available for values of pressure, viscosity, velocity and shear-rate. Other values if necessary, can be calculated in Ansys CDF-Post, basing on simulation results.

Values of local shear rate are presented on screw axis plane in Figure 11. Distribution of velocity in flow domain is shown in Figure 12 in form of vectors. Velocity streamlines are presented in Figure 13.

It is very challenging to simulate and analyze polymer melt flow inside extruder barrel. These challenges can be solved with 3D FEM CFD simulation, which provides access to local data (velocity, shear rate) with virtually no limited geometry shape of rotating parts. However, to handle the simulation pre-processing requires knowledge of CAD modelling, mesh generation and boundary conditions setting.

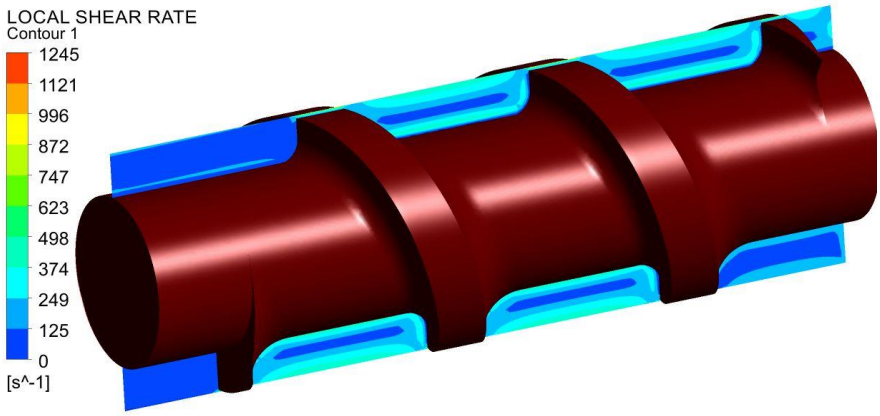

Fig. 11. Local shear rate

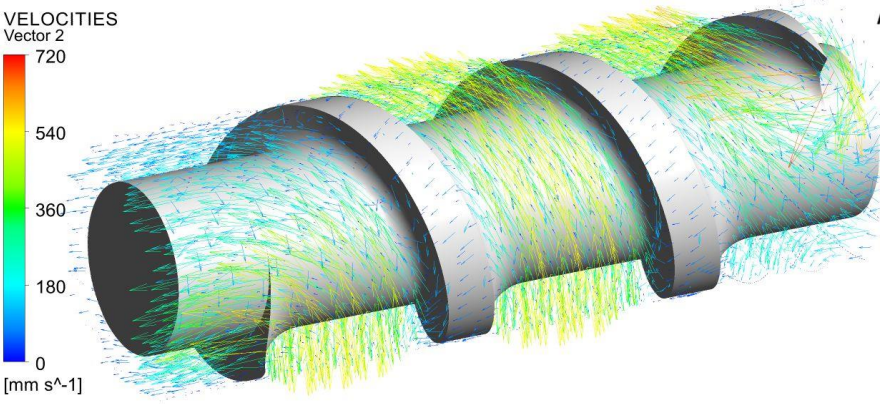

Fig.12 – Velocities vectors through flow domain

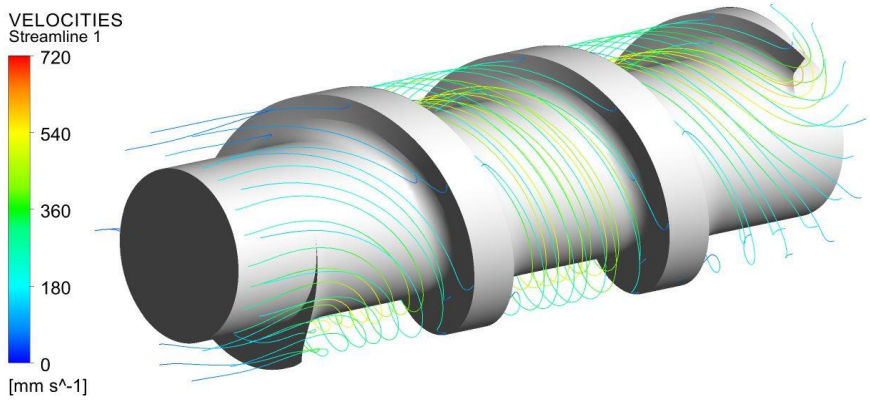

Fig. 13. Flow streamlines with mapped velocities values

Acknowledgements

The project leading to this application has received funding from the European Union's Horizon 2020 research and innovation program under the Marie Skłodowska-Curie grant agreement No 734205-H2020-MSCA-RISE-2016.

References

[1] Bang, D.S., White, J.L., Intern. Polym. Process. 12, p. 278 (1997).
[2] Vergnes, B., Della Valle, G., Delamare, L., Polymer Engineering and Science, 11, p. 1781 (1998).
[3] Potente, H., Flecke, J., SPE Antec Tech. Papers 1, p. 110 (1997).
[4] Rios, A.C., Gramman, P.J., Stan®eld, E., Osswald, T.A., SPE Antec Tech. Papers 1, p. 222 (1998).
[5] Avalosse, T., Macromol. Symp. 112, p. 91 (1996).
[6] ANSYS Polyflow 2019 R2® online help - http://ansyshelp.ansys.com.

Ján Varga[1], Ľudmila Dulebová[1], Janusz Sikora[2]

SELECTED PROPERTIES OF POLYMER COMPOSITE AFTER RADIATION CROSS-LINKING

Abstract: *This article deals with the influence of electron-beam radiation on the micro-mechanical, thermo-mechanical, and structural properties of selected polymers. In the search for the desired improvement of polymers, it is possible to use, inter alia, one particular possible modification namely, crosslinking. This is a process during which macromolecular chains start to connect to each other and, thus, create the spatial network in the structure. In the course of the treatment of the ionizing radiation, two actions can occur: crosslinking and scission of macromolecules, or degradation. Both these processes run in parallel. Using the crosslinking technology, standard and technical polymers can acquire the more "expensive" high-tech polymeric material properties and, thus, replace these materials in many applications. The polymers that were tested were selected from across the whole spectra of thermoplastics, ranging from commodity polymers, technical polymers, as well as high-performance polymers. These polymers were irradiated by different doses of beta radiation (15,33 and 50 kGy).*
Keywords*: plastics, irradiation, crosslinking, mechanical properties, radiation dose.*

1. Introduction

Plastic processing shows an increasing trend on an annual basis [1]. Polymers especially thermoplastics, are used in all industrial fields, and in a wide variety of applications including packaging materials, household products, sports and leisure activities, medical products, and the automotive, aviation, and electro-technical and electronics fields [2].

Material modification is needed in order to obtain better material properties as required in the plastics industry. One of many ways of how to modify polymers is beta radiation crosslinking. In most cases, crosslinked polymers offer better mechanical and thermal properties. The beta radiation sources for the industrial crosslinking of polymers are electron beam accelerators, which allow one to obtain high-radiation doses in a short time [3]. Ionizing radiation (electron beam radiation) can change the macroscopic properties and the molecular structure of polymeric materials [4].

The cross-linking of rubbers and thermoplastic polymers is a well-proven process for the improvement of thermal properties. The chemical cross-linking or rubber vulcanization is normally induced by the effect of heating after processing with the

[1)] *Technical University of Kosice, Faculty of Mechanical Engineering, Department of Engineering Technologies and Materials, Mäsiarska 74, 040 01 Kosice, Slovakia, jan.varga@tuke.sk*

[2)] *Lublin University of Technology, Department of Technology and Polymer Processing, ul. Nadbystrzycka 36, 20-618 Lublin, Poland, j.sikora@pollub.pl*

presence of a curing agent. The cross-linking process for thermosets is very similar. In thermosets, the polymer molecules are also chemically linked due to heat after processing [5].

Radiation technical is a very convenient tool for the improvement or modification of polymer materials through crosslinking, grafting or degradation. Among them, radiation crosslinking is a key technology in the field of radiation processing [6].

Radiation cross-linked-based engineering plastics offers OEM and end users in many branches of industry both technical and economical advantages in comparison with high-performances plastics. They constitute a technical and economical compromise between engineering plastics that failed and high-performances plastic, often over-tailored and expensive [7].

Cross-linking of plastics is a term that we meet in many areas and outside the field of technology too. Radiation cross-linking basically improves plastics in three different ways: it gives them better thermal stability, better abrasion resistance and better resistance to chemical and mechanical influences [8].

A polymer network can be envisioned as a polymer molecule with an infinite molecular weight. Crosslinking is a physical or chemical route by which polymers with branched or crosslinked structures are produced [9].

Crosslinking can be accomplished chemically or by irradiation. Chemical crosslinking with rubber material is called Vulcanization. It is accomplished by a heat induced reaction between the polymers and a crosslinking agent [10]. The effects that polymer crosslinking provides summarizes Fig. 1.

1. Higher tensile strength
2. Improved abrasion/cut through
3. Better crush resistance
4. Solder iron resistance
5. Better over load characteristics
6. Resistance to stress cracking
7. Improved fluid resistance
8. Slightly better flame resistance
9. No change of electricals
10. Negligible change in thermal stability
11. Decrease in flexibility
12. Improved high temperature mechanicals

Fig. 1. Crosslinking Provides

In general, mechanical characteristics are improved, especially at higher temperatures. It results in improved resistance to stress cracking and better fluid resistance [10].

For most plastic materials, equivalent properties may be obtained by the use of irradiation crosslinking, but irradiation may have the following advantages:

1. Irradiation has no lower limit on physical size, smaller conductor sizes, and thin insulation walls may be provided.

2. Irradiation does not use high temperature or pressure. Separator tapes are not required to prevent thin wall insulations from being forced into the conductor strand surface.
3. Irradiation offers the insulation compounder design freedom. Compound additives may be chosen without regard to their reaction to high temperatures and to moisture [10].

The cross-linking of plastics is a chemical process, in which particular molecules of plastics are connected together. In an ideal case, all the molecules will be integrated into the above mentioned grid and the process can be activated by radiation in case of many plastics.

Cross linking will be initiated by irradiating with high energy electron beams or gamma rays. The energy resulting from the irradiation is absorbed by the plastic. The main difference between beta and gamma rays lies in their abilities of penetrating the irradiated material [11]. Gamma rays have a high penetration capacity.

The penetration capacity of electron rays depends on the energy of the accelerated electrons. The process takes place at room temperature and under normal pressure. Irradiation takes place after the moulding process. In this way, the processing advantages of thermoplastics are combined with the properties of duroplastic systems. Parameters can be flexibly adapted to individual requirements in each case. Radiation cross-linking makes thermoplastic polymers stable over a wide temperature range. The most important properties of cross-linking systems are tensibility and elasticity, which also remain under long-time temperature and mechanical loading [11].

Radiation processing with an electron beam offers several distinct advantages when compared with other radiation sources, particularly γ-rays and x-rays. The process is very fast, clean and can be controlled with much precision. The electron beam radiation process is practically free of waste products and therefore is no serious environmental hazard. The cross-linking level can be adjusted by the irradiation dosage. The absorbed dosage means the value of energy of ionizing radiation absorbed by a unit of mass of the processed material. The unit of absorbed dose is 1 Gray (1 Gy = 1J/kg). The main difference between beta and gamma rays is in their different abilities to penetrate the irradiated material [5].

Gamma rays have a high penetration capacity. The penetration capacity of electron rays depends on the energy of the accelerated electrons. Due to electron accelerators, there quired dosage can be applied within seconds, whereas several hours are required in the gamma radiation plant Fig. 2 [12].

Beta and gamma rays can be used for the irradiation of polyolefins, polyesters, halogen polymers and polyamides from the thermoplastics group, elastomers and thermoplastic elastomers. Some of them need the addition of a cross-linking agent. Polymers can be classified into two groups according to their response to ionizing radiation. One group exhibits predominant cross-linking, the other predominant chain scission [5].

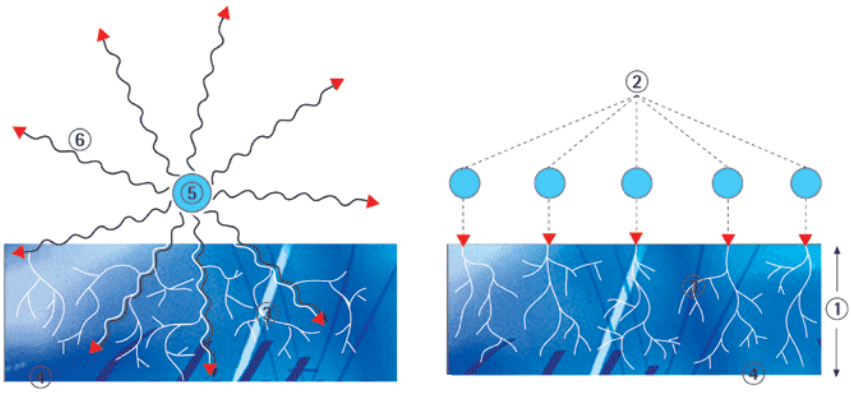

Fig. 2. Design of Gamma Rays (a) and Electron Rays (b): 1 – Penetration depth of an electron, 2 – Primary electron, 3 – Secondary electron, 4 – Irradiated material, 5 – Encapsulated Co – 60 Radiation source, 6 – Gamma Rays

The majority of industrial applications of radiation processing are cross-linking of wire and cable insulations, tube, heat shrink cables, composites, moulded products for automotive and electrical industry etc. [12, 13].

Irradiation cross-linking of thermoplastic materials deals with creation of a cross-link among the macromolecular strings. Intermolecular forces are replaced by a covalent bond. As a result, we can optimise properties of standard and engineering polymers and impart them the properties of high-performance polymers (Fig. 3).

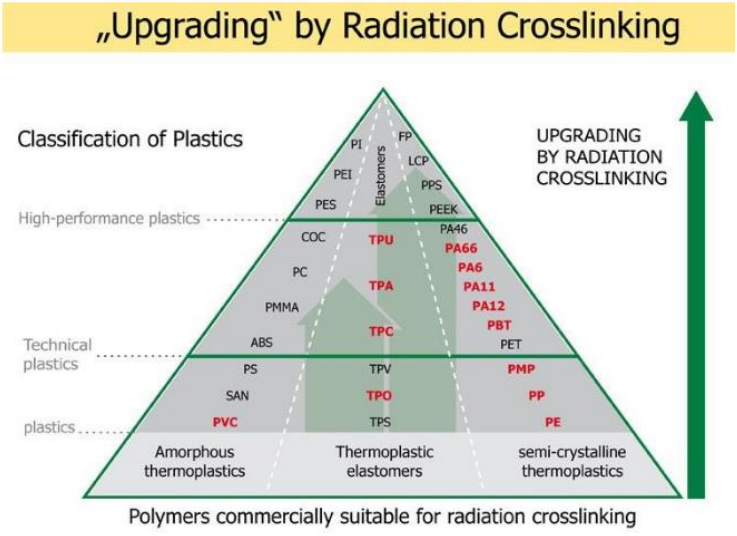

Fig. 3. Pyramid of Polymers for radiation cross-linking

Radiation cross-linking usually improves strength, reduces creep, contributes to chemical resistance improvement and in many cases improves tribological properties. Effect of radiation cross-linking significantly improves temperature stability. Because of that, materials which belong to group of standard polymers can be used in applications, which would be in term of temperature stability intended only to constructive thermoplastic polymers [1].

Polymers can be irradiated in many forms, such as pellets and powder, films, extruded and molded parts or as wire and cable insulation [1]. Plastic parts suitable for radiation cross-linking are extruded products like tubes, pipes and profiles as well as injection moulded parts.

The irradiation cross-linking of thermoplastic materials via electron beam or cobalt 60 (gamma rays) is performed separately, after processing. Generally, ionizing radiation includes accelerated electrons, gamma rays and X-rays [1].

2. Experimental work

Material tested in this work was PP Hostacom CR 250 F G61330. The choice of material was made in view application by plastic parts product for automotive industry.

Polypropylene (PP) is a stereospecific polymer prepared by polymerization using an organometallic catalyst system. Commercial polypropylenes have up to 95% isotactic content, which means that pendant methyl groups are almost all on the same side of the chain. When polypropylene is exposed to ionizing radiation, free radicals are formed and these cause chemical changes [12].

Material PP Hostacom CR 250 F G61330 – is a material, which is filled by 15 % mineral filler – talc. Its good mechanical properties, good scratch resistance and can be processing by different of technology – injection moulding, blow moulding, or extrusion. The using find in automotive, electronics, engineering and consumer industries [14, 15].

Some types of plastics need cross-linking activators in order to obtain effective levels of cross-linking. To prepare of test samples for the irradiation was necessary to mix granulate materials with different cross-linking agent [14]. It was the type of cross-linking agent. TAIC - Tryallyloxy-1,3,5-triazine. The manufacturer is a company Sigma Aldrich.

Test samples enriched by cross-linking agent and test samples without cross-linking agent have been produced by injection moulding technology and were used injection mould with replaceable mould boards Fig. 6. The processing conditions during the injection moulding were according to the recommendation of the producers. For the production injection mold machine DEMAG Ergotech Pro 25-80 (Fig. 4) was used.

Fig. 4. Injection molding machine

Produced test samples were irradiated by gamma radiation in the company BGS Beta-Gamma-Service GmbH, Saala d. Donau, Germany by irradiation dose: 15 kGy and 50 kGy.

Radiation doses were chosen based on the utilization of material in the production of plastics parts in the automotive industry.

After irradiation were carried out selected mechanical properties:

- tensile test,
- Charpy impact test.

Figure 5 and Figure 6 shows replaceable mould inserts used for tensile test and Charpy Impact test.

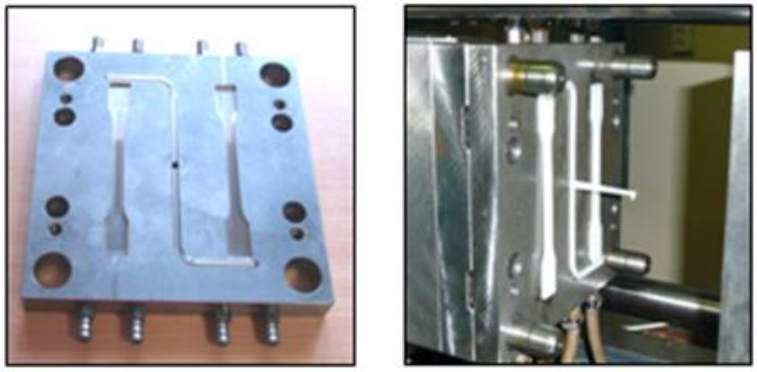

Fig. 5. Repleceablemould inserts for tensile test

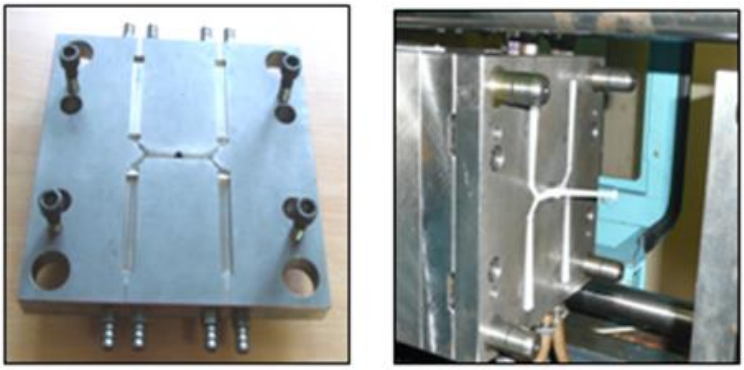

Fig. 6. Repleceable mould inserts for Charpy impact test

The test samples were controlled after injection moulding process and after the conditioning time. For evaluation of tensile properties of plastics was made according to STN EN ISO 527-1, 2 and was used sample type 1A for testing. Tensile test was carried out on tensile machine TIRA- test 2300. It was tested in 5 samples of each type of materials in standard ambient and after UV exposure chamber.

For evaluation of impact resistance of plastics was made according to STN EN ISO 179 – 1. It was tested in 10 samples of each type of materials in standard ambient and after UV exposure chamber. The test samples were subjected to the tests without notch. Impact strength test was carried out on Charpy hammer type PSW 60/500.

The artificial aging test by fluorescent UV lamps were made in the UV chamber according to STN EN ISO 4892-3, exposure time 28 days at 12 hour cycles for all test materials. The test samples after removal of UV chambers were conditioned according to ISO 291:2008. Afterwards, was performed tensile test and impact strength test by Charpy to detect changes in the properties of the materials after artificial aging by UV fluorescent lamps according to above-mentioned methodology [16].

3. Results

3.1 Tensile Test

In evaluating of experiments was compared the influence of a dose of gamma radiation on the mechanical properties of materials.

The graphic dependence of the measured average values of the tensile test of test samples - yield strength σ_Y of test samples in a standard ambient and degradation in UV chambers Figure 7.

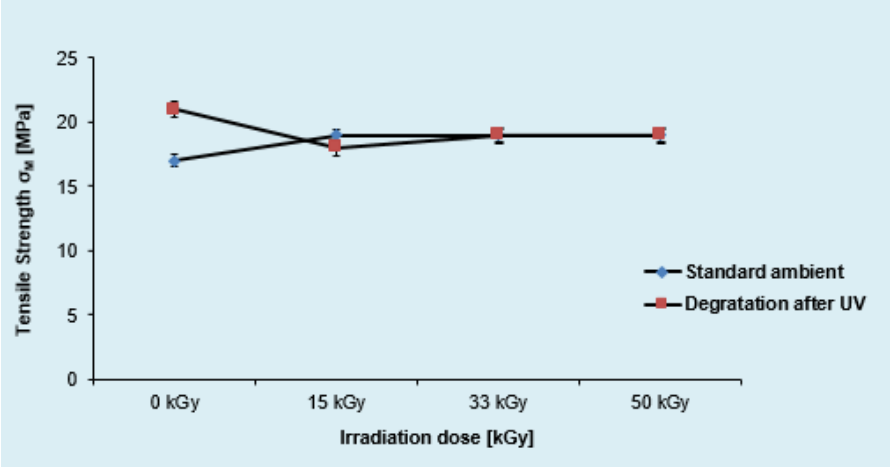

Fig. 7. Tensile strength of test samples with different irradiation dose

The graphic dependence of the measured average values of relativeelongation of test samples in a standard ambient and degradation in UV chamber (Fig. 8).

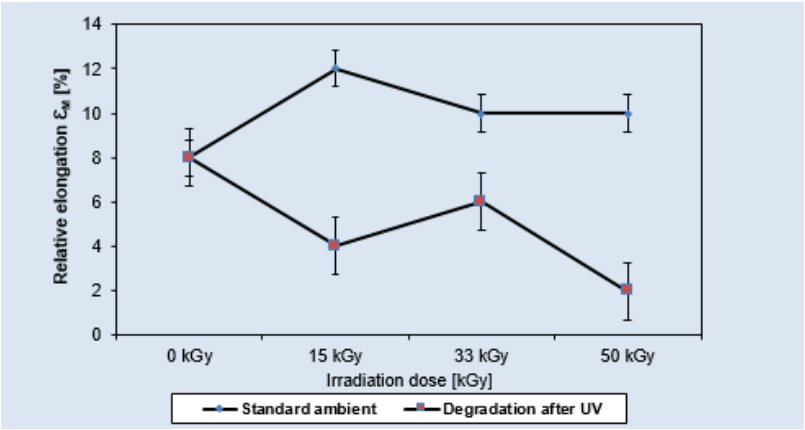

Fig. 8. Relative elongation of test samples with different irradiation dose

3.2 Charpy Impact test

The test samples were controlled after injection molding process and after the conditioning time. It was tested in 10 samples of each type of materials in standard ambient and after UV exposure chamber. The test samples were subjected to the tests without notch. The graphic dependence of the impact resistance a_{cU} of test samples with different irradiation dose (Fig. 9).

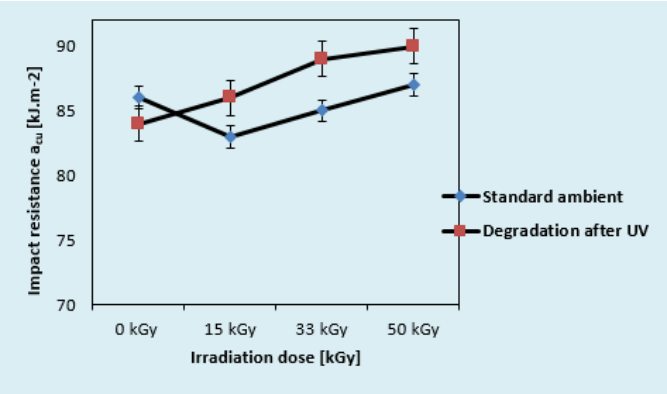

Fig. 9. Impact resistance of test samples with different irradiation dose

The fracture areas of test samples after tensile test without exposure and were observed on scanning electron microscope JEOL JSM - 7000F, Japan.The fracture areas of test samples of non-irradiated and irradiated materials with different of radiation dose in standard ambient after tensile test were compared, Figure 10.

a)

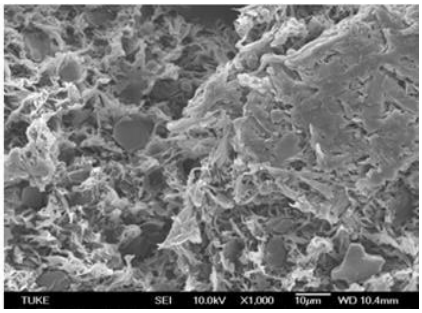

b)

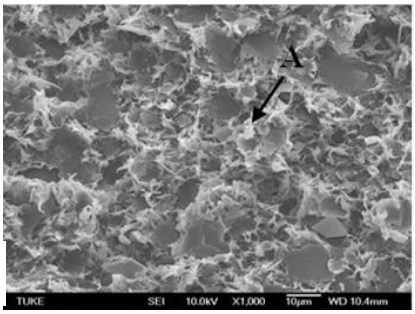

c)

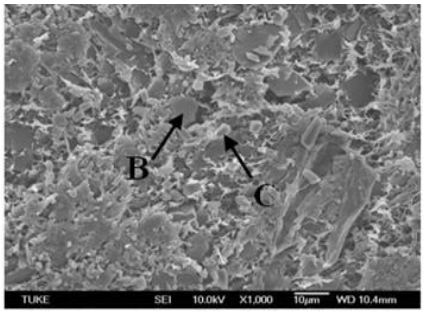

Fig. 10. The fracture areas of test samples irradiated by different radiation dose: a) test sample non irradiated, b) test sample – 15 kGy, c) test sample – 50 kGy

By the influence of cross-linking was observed increasing density of cross-linking, It was created a sufficient number of networked sites. For all test samples there has been a brittle fracture of testing samples. The spectrum of the chemical composition is shown in Figure 11 confirmed on scanning images of test samples in standard ambient the presence of chemical elements. These were the elements of the polymer – A label, the elements of filler – B label and the elements of cross-linking agent (TAIC) – label C.

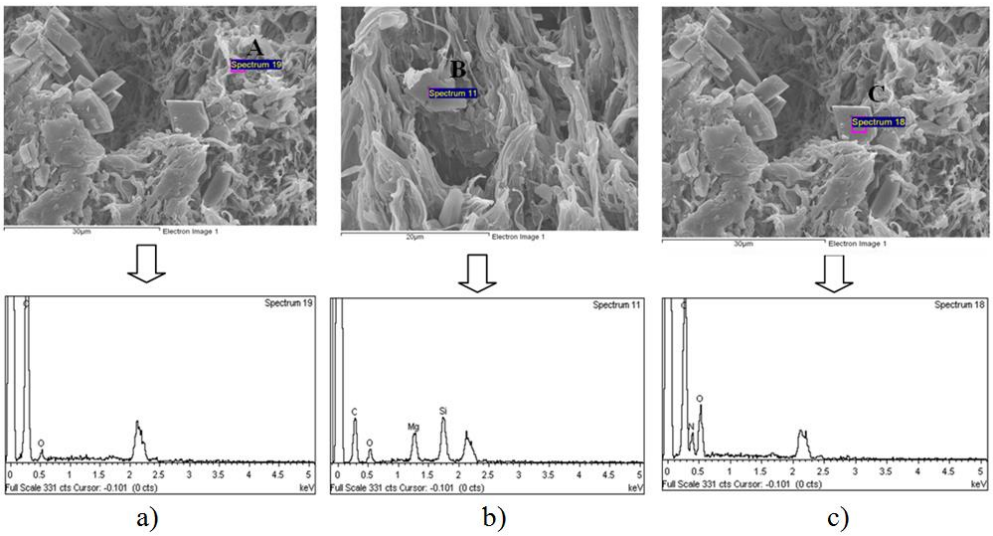

Fig. 11. The spectrum of the chemical composition of tested material in standard ambient: a) test sample non irradiated, b) test sample – 15 kGy, c) test sample – 50 kGy

4. Conclusions

On the basis of the experimental results of mechanical tests the following conclusions could be formulated:

- After tensile test with material Hostacom CR G61330 250 F G61330 by test samples in standard ambient was found increasing tendency of tensile strength and relation elongation.

We can state, that the values of tensile strength and relation elongation were influenced by irradiation dose – Figure 9, 10.

- The value of tensile strength achieved increasing tendency by irradiated test samples in standard ambient against the base material about 10%. By irradiated test samples after degradation in UV chamber were achieved the values of tensile strength decreasing tendency. These values were influenced by irradiation dose about 10–15%.

Irradiated test samples in standard ambient had against non-irradiated material progressive tendency of relative elongation. These values were influenced by

irradiation dose about 25–50%. Irradiated test samples after degradation in UV chamber had against non-irradiated material decreasing tendency of relative elongation. These values were influenced by irradiation dose about 25–75%.

On the basis of the experimental results of mechanical tests the following conclusions could be formulated:

- At the material Hostacom CR G61330 250 F G61330 is not explicit influence of radiation dose to the impact resistance.
- The increasing tendency of value a_{cU} was recorded in irradiated test samples after degradation in UV chamber.
- By non – irradiated and irradiated test samples in standard ambient was recorded decreasing tendency by irradiation dose 15 and 33 kGy and marginal increase by irradiation dose 50 kGy.
- The highest values of parameter a_{cU} of irradiated test samples were evaluated at 50 kGy radiation dose.

Acknowledgement

This project has received funding from the European Union's Horizon 2020 research and innovation programme under the Marie Skłodowska-Curie grant agreement No 734205-H2020-MSCA-RISE-2016.

References

[1] Manas, D., et all., The High-Density Polyethylene Composite with Recycled Radiation Cross-Linked Filler of rHDPEx, Polymers 2018, 10, 12, 1361.

[2] Hubo S., Leite L., Martins C., Ragaert K., Evaluation of post-industrial and post-consumer polyolefin-based polymer waste streams for injection moulding; Proceedings of the 6th Polymers & Mould Innovations International Conference; University of Minho, Guimarães, Portugal. 10–12 September 2014; pp. 201–206.

[3] Khonakdar, H.A., Jafari, S.H., Wagenkecht, U., Jehnichen, D., Effect of electron-irradiation on cross-link density and crystalline structure of low- and high-density polyethylene. Radiat. Phys. Chem. 2006, 75, 78–86.

[4] Manas, D. et all.,The Effect of Irradiation on Mechanical and Thermal Properties of Selected Types of Polymers, Polymers 2018, 10, 2, 158–166.

[5] Mizera, A. et all., Properties of Polymers after Radiation Cross-linking, International journal of mathematics and computers in simulation 2012, 6, 592–599.

[6] Yoshii, F., Radiation Crosslinking of Polymer Materials, Takasaki Radiation Chemistry Research Establishment, JAERI, Jaeri – Conf 2004-007, 83–91.

[7] Ionisos, Z.I., Radiation cross-linked plastics: a versatile material solution for packaging, automotive, Electrotechnic and Electronics, Radiation Physics and Chemistry, Volume 71, Issues 1–2, September–October 2004, 527–530.

[8] Brocka, Z., Strahlenvernetzte Kunstoffe Verarbeitung, Eigenschaften, Anwendung, Springer VDI Verlag, Düsseldorf. 2006, pp. 1–30.
[9] Ortiz, J., Lima, E., Handbook of Polymer Synthesis, Characterization, and Processing, February 2013, ISBN: 9781118480793.
[10] http://www.marmon-ad.com/polymer-cross-linking, cit.
[11] Greškovič, F., Varga, J., Dulebová, Ľ., The utilize of gamma radiation in the examination of mechanical properties of polymeric materials. Metalurgija 2012, 51, 2, 245–248.
[12] Drobny, J.G., Radiation Technology for Polymers, Boca Raton: CRC Press, 2003.
[13] BGS – Beta Gama Service. [online]. www: http://bgs.eu.
[14] Bussink J., Engineering Plastics. In: Lemstra P.J., Kleintjens L.A. (eds) Integration of Fundamental Polymer Science and Technology-3. Springer, Dordrecht, (1989), 43-50.
[15] Shukushima, H., Radiation Physics and Chemistry, 2001, 60, 4–5, 489–493.
[16] Varga, J., The influence of radiation crosslinking on mechanical properties of plastic parts, PhD thesis, Košice, 2009, pp. 100–140.

António Gaspar-Cunha[1]

COMPUTATIONAL ASSESSMENT OF THE ROTATIONAL BARREL SEGMENT LOCATED ON THE MEETERING ZONE OF AN EXTRUDER

Abstract: *The development of new extruders able to process polymer nanocomposites is of a primordial importance given the new developments in the plastics industry. For that purpose, these machines must take into account two different aspects: they must be able to extrude the material at a given rate and, simultaneously, must be able to mix the incorporated nanofillers in the polymer matrix in an efficient way. These are two main objectives that are in conflict and, thus, a compromise solution must be considered. For that purpose, in this work, is proposed the use of modelling software's to assess the behavior of a rotational barrel segment located in the metering zone of the extruder. The aim being to compute the performance of different geometries, considering the two objectives referred above. The results obtained allows to conclude about the better operating conditions to use when a rotational barrel segment is used.*
Keywords*: rotational barrel segment, computer modelling, extrusion.*

1. Introduction

The main aim of this work is to assess the performance of a rotational barrel element located in the metering region of the extruder, *i.e.*, when the polymer is totally melted. This section corresponds to the second geometrical element developed within the project NEWEX. Its performance will be evaluated through the use of modelling software.

This area of development is concerned with a rotational barrel segment (RBS) rotating in the same or opposite direction as the screw. The rotational barrel segment, fitted with intensifying grooves of torsional angle and torsional direction, is a vital element of plasticizing system of a new extruder developed in the framework of the NEWEX project and will be mounted in the metering zone. It is a complete novelty that has not been described in literature or used in the existing extruders, except in some work developed by the team [1, 2, 3, 4, 5].

Changing the rotational speed of the grooved barrel segment as well as the direction of its rotation during the extrusion process will enable to influence the thermal, rheological, kinematic and dynamic conditions in the plasticizing system of the new extruder. Due to that behaviour, it will be possible to efficiently control the extrusion process and to improve the quality of the products obtained because enhancing the above processes will result in the homogenization of the thermal and mechanical properties of materials and the structure of the products, without the need to use additional, expensive devices such as the gear pump and static mixer. This will be of

[1)] *IPC – Institute of Polymers and Composites, Department of Polymer Engineering, University of Minho, Campus de Azurém, Guimarães, Portugal. agc@dep.uminho.pt.*

utmost importance for polymer processing industry, as well as for food, cosmetics and pharmaceutical industries.

For the calculations, the modelling program described in [6] was used. For that purpose, various velocities, in both directions, of the rotational barrel segment were tested. The results are discussed, and some conclusions are proposed.

2. Presentation and discussion of results

2.1. Extruder, material and operating conditions

The extruder used has a square pitch screw with a diameter (D_{screw}) of 25 mm and a *L/D* ratio equal to 25 (Fig. 1). It was fitted with a conventional screw with the lengths of the feed, compression and metering zones equal to 8D, 8D and 9D, respectively. The internal screw diameter is 16.6 mm and 22.0 mm, respectively for the feed (D_{i1}) and metering (D_{i3}) zones, and the total length of the grooves zone (L_g) is 100 mm. The rotational barrel segment was located at 16D and two lengths being tested, 1D and 3D.

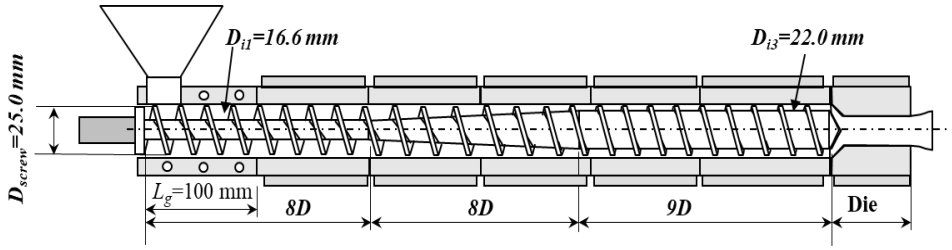

Fig. 1. Extruder geometry

Figure 2 shows the three different situations that can occur when an RBS is implemented in an extruder: a) the velocity of the RBS (N_b) is nil; b) the velocity of the RBS has the same direction than that of the screw (Ns) and c) the velocity of the RBS has a different direction than that of the screw.

In the first case the relative barrel velocity (V_b) results by transforming the rotational screw speed (N_s) in a linear velocity near the interior barrel velocity (see reference [6]), this is: $V_b = \pi N_s D$ (where D is the external screw diameter). In the second case the resulting (V'_b) velocity is reduced, while in the third the resulting velocity increases.

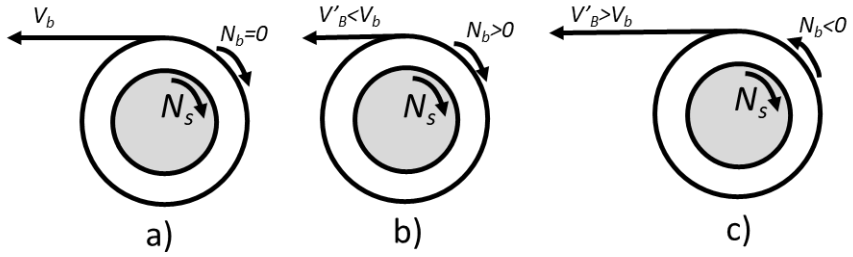

Fig. 2. Definition of the relative barrel velocity (V'_b)

Table 1 shows the relevant properties of the polymer used in the calculations, a High-Density Polyethylene, Malen E FGAN 18-D003 from Basell. The viscosity was obtained experimentally using a capillary rheometer being the data fitted using the power law model as follows. See also Figure 3.

In all calculations, the operating conditions were fixed. The screw speed was 120 rpm and the barrel temperature profile in the solids zone varies linearly between 30ºC and 70ºC in the first 5 turns (the solids conveying zone) and is constant and equal to 170ºC in the remainder of the barrel and die.

$$\eta = \eta_0 \, \gamma^{(n-1)} e^{-a(T-T_0)} \tag{1}$$

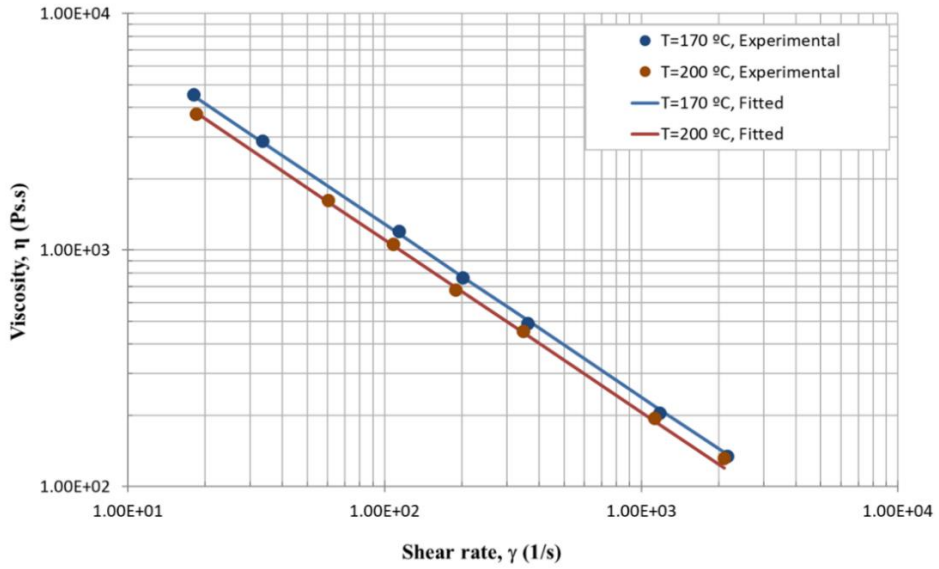

Fig. 3. Rheological data

Table 1. *Properties for LDPE (Malen E FGAN 18-D003)*

Properties			**LDPE**	**Unit**
Density	*Apparent*	ρ_0	495.0	kg/m^3
	Solid	ρ_s	921.0	kg/m^3
	Melt	ρ_m	854.4	kg/m^3
Friction coefficients	*Internal*		0.67	---
	Hopper		0.30	---
	Barrel		0.40	---
	Screw		0.20	---
Thermal conductivity	*Solid*	k_s	0.141	W/m ºC
	Melt	k_m	0.078	W/m ·ºC
Specific Heat	*Solid*	C_s	3160.0	J/kg
	Melt	C_m	2682.0	J/kg
Melting heat		h	1.03 x 10^6	J/kg
Melting temperature		T_m	113.0	ºC
Viscosity: Power law		n	0.27	---
		η_0	3.7e4	Pa/s
		a	0.005	1/°C
		T_0	170.0	°C

2.2. Results and discussion

Figure 4 shows the results of the solid bed profile obtained to assure that the rotational barrel segment is located in a region were the polymer is totally melted. In this situation the melting occurs before the length of 15*L/D*.

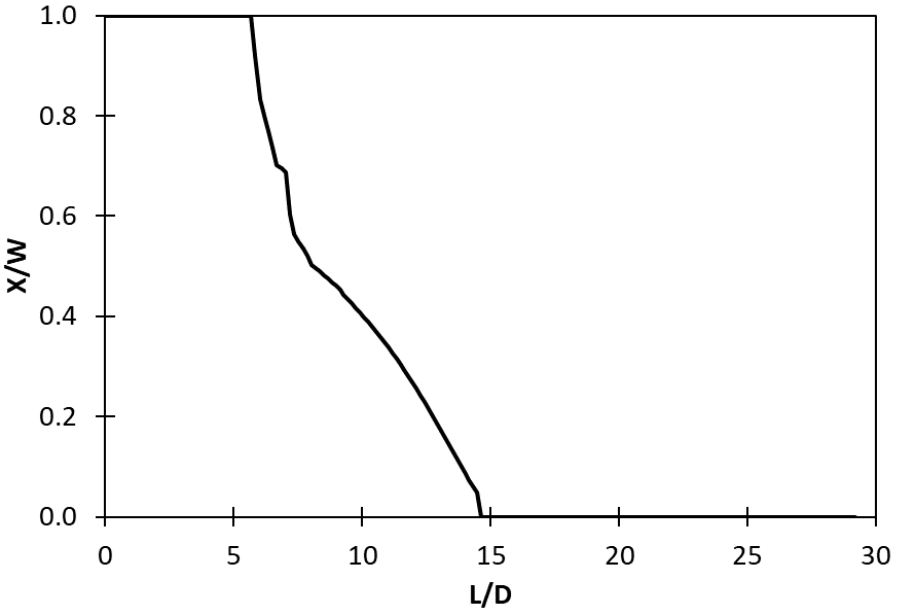

Fig. 4. Solid bed profile when the velocity of the RBS is nil

Case 1 - L_b = 1D: $L/D \in$ [16, 17]

In this case the length of the rotational barrel (L_b) is 1D. As can be seen in Table 2, eight screw speeds of the RBS (N_b) were teste. First, it was considered a situation where this speed is nil. The Table presents the different values necessary to analyse the performance of the RBS. The most important aim been to maximize the mixing, quantified here by WATS, while little changes must be obtained in the remaining criteria, *i.e.*, output, melt temperature at die exist (T_{melt}), mechanical power consumption (*Power*), length of screw required for melting ($L_{melting}$) and viscous dissipation.

Negative RBS speeds mean that the RBS is rotating in the opposite direction of the screw. Since the screw speed was fixed at 120 rpm, when the RBS speed is -120 rpm the biggest differences for WATS are obtained, while the other characteristics does not change significantly, except the output, which decreases (see Table 2).

Also, when the pressure profiles are considered (Figures 5 and 6), it is possible to see that the high performance in the mixing degree (WATS) occurs when pressure decreases, which influences the output undesirably.

Table 2. *Influence of Rotational Barrel Section (L_b = 1D: L/D ∈ [16; 17])*

N_b (rpm)	Output (kg/hr)	T_{melt} (°C)	Power (W)	$L_{melting}$ (m)	WATS	Viscous Dissipation
0.0	5.3	188.9	2278	14.6	308.0	1.46
-20.0	5.4	189.0	2295	14.8	334.2	1.46
-40.0	5.5	189.2	2331	14.8	328.4	1.46
-80.0	5.5	189.3	2383	14.8	317.3	1.46
-120.0	5.7	189.8	2397	15.1	307.9	1.44
20.0	5.3	188.8	2283	14.3	339.2	1.47
40.0	5.2	188.8	2238	14.4	347.5	1.47
80.0	4.9	188.8	2214	14.2	358.0	1.48
120.0	4.9	189.0	2185	14.0	366.0	1.48

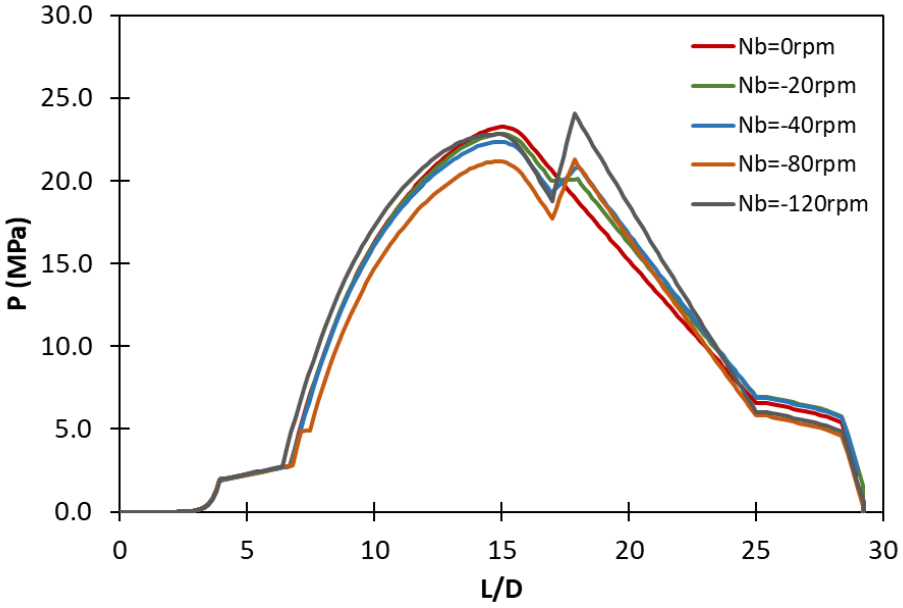

Fig. 5. Pressure profile for <u>case 1</u> with the RBS velocity in the opposite direction of the screw

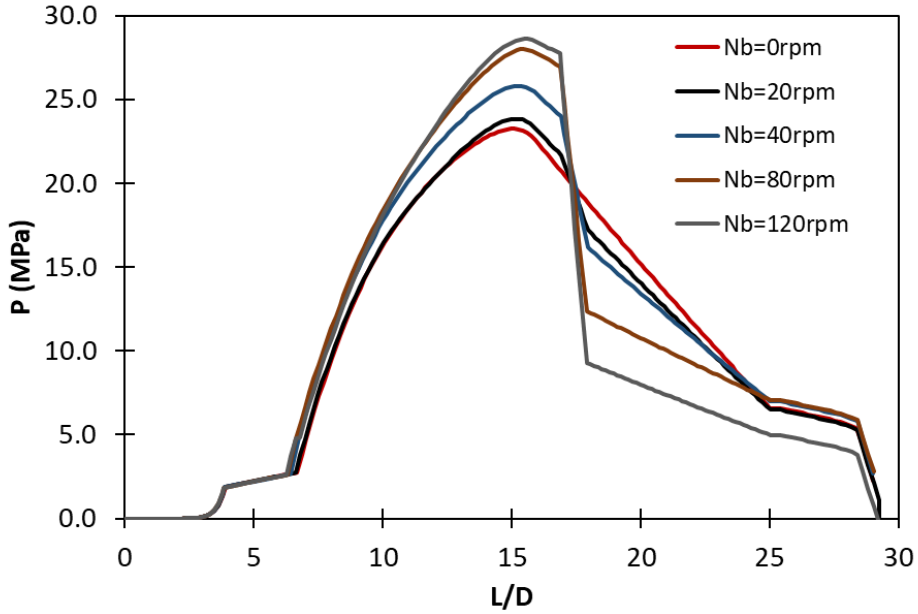

Fig. 6. Pressure profile for case 1 with the RBS velocity in the same direction of the screw

Case 2 - L_b = 3D: $L/D \in [16, 19]$

Table 3 and Figures 7 and 8 presents the same type of results as those for case 1 above, but now considering the length of the RBS equal to 3D (case 2). The conclusion is the same as previously discussed.

However, in this case, it is important to note that the best performance for the mixing is obtained in situations that the pressure decreases below zero, this is the case when N_b is equal to 80 and 120 rpm (Fig. 8). In practice this cannot occur. This is the advantage of analysing the different geometries and operating conditions using computer programs.

Taking this into account, a possible solution is to increase the pressure before to the extruder have the capacity of overcome this limitation in pressure. This can be done by implementing a barrel with grooves in the solids conveying zone. This is done in case 3 below.

Table 3. *Influence of Rotational Barrel Section (L_b = 3D: L/D ∈ [16; 19])*

N_b (rpm)	Output (kg/hr)	T_{melt} (°C)	Power (W)	$L_{melting}$ (m)	WATS	Viscous Dissipation
0.0	5.3	188.9	2278	14.6	308.0	1.46
-20.0	5.5	189.3	2358	14.8	383.3	1.46
-40.0	5.8	190.1	2395	15.5	376.4	1.45
-80.0	6.1	191.1	2583	15.6	339.9	1.44
-120.0	6.4	192.2	2834	15.8	315.6	1.43
20.0	5.1	188.5	2241	14.1	405.1	1.47
40.0	4.8	188.2	2163	14.0	422.9	1.48
80.0	4.0	187.7	2195	12.8	451.0	1.50
120.0	3.7	187.8	2100	12.2	484.1	1.51

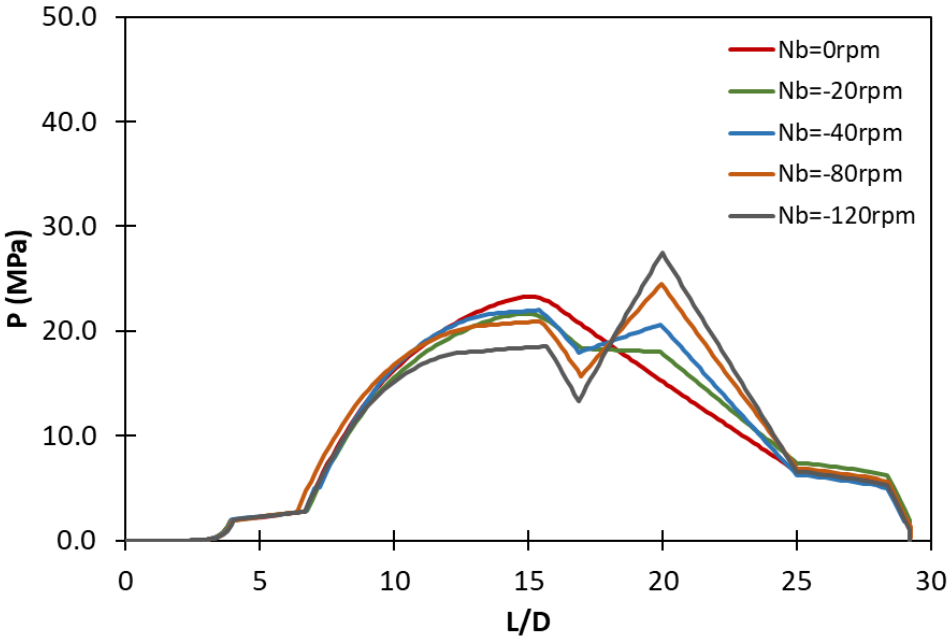

Fig. 7. Pressure profile for <u>case 2</u> with the RBS velocity in the opposite direction of the screw

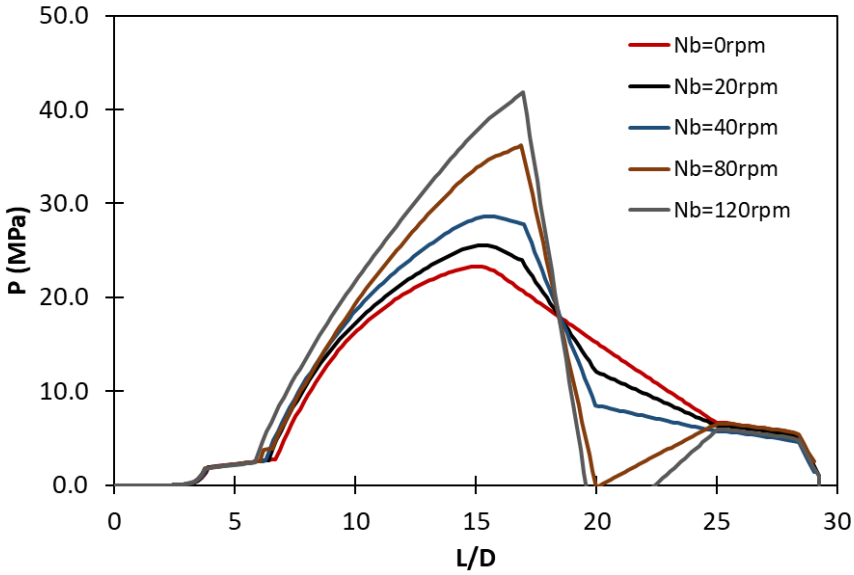

Fig. 8. Pressure profile for <u>case 2</u> with the RBS velocity in the same direction of the screw

<u>Case 3 - L_b = 3D: $L/D \in [16; 19]$; with grooves</u>

The analysis of Table 4 and Figures 9 and 10 is possible to see that the existence of grooves in the solids conveying zone helps in solving the zero-pressure problem in some cases, such for example when the RBS speed is 80 rpm. For this situation is possible to obtain a good mixing behaviour. However, in all cases a balance between the mixing and output must be done.

Table 4. *Influence of Rotational Barrel Section (L_b = 3D: $L/D \in [16; 19]$; with grooves)*

N_b (rpm)	Output (kg/hr)	T_{melt} (°C)	Power (W)	$L_{melting}$ (m)	WATS	Viscous Dissipation
0.0	5.3	188.9	2278	14.6	308.0	1.46
-20.0	5.7	188.4	2975	14.4	372.1	1.13
-40.0	5.8	188.9	3077	14.6	358.0	1.11
-80.0	6.1	189.7	3306	15.0	330.2	1.12
-120.0	6.4	191.1	3488	15.0	304.6	1.13
20.0	5.3	187.7	2798	14.0	398.4	1.10
40.0	5.0	187.6	2714	13.6	411.6	1.21
80.0	4.3	187.6	2767	11.7	430.0	1.30
120.0	3.9	188.0	2771	6.1	482.4	1.28

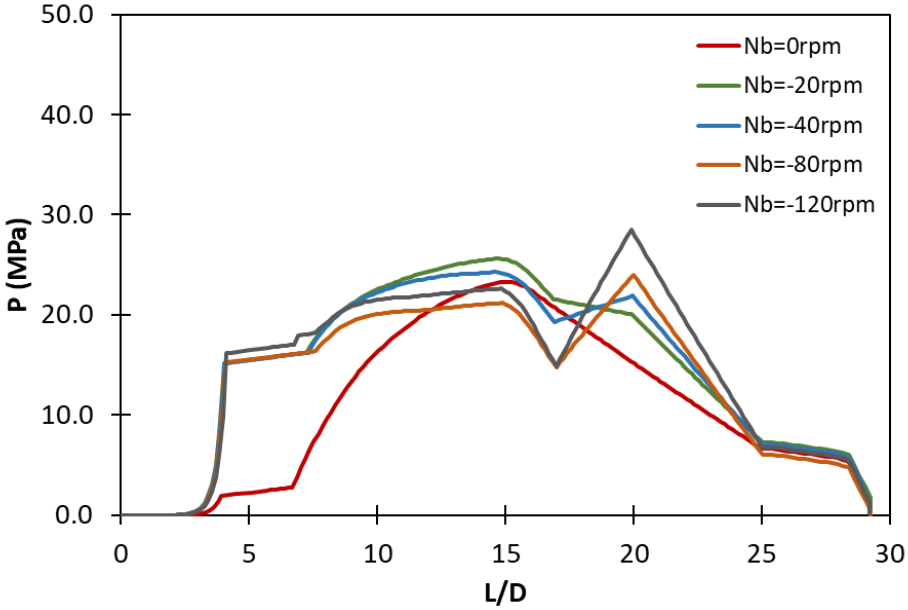

Fig. 9. Pressure profile for case 3 with the RBS velocity in the opposite direction of the screw

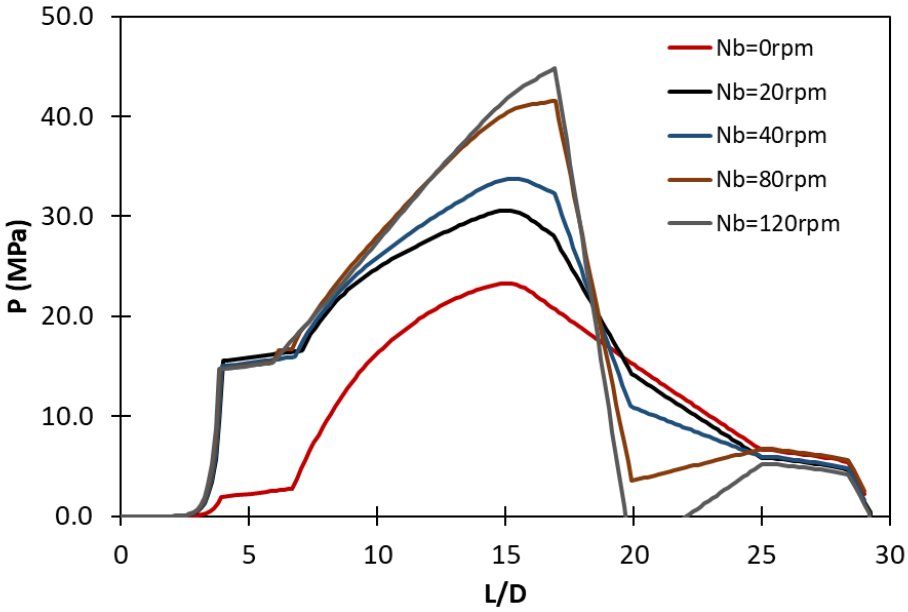

Fig. 10. Pressure profile for case 3 with the RBS velocity in the same direction of the screw

5. Conclusions

The main conclusion that can drawn in this computational study, in which the influence of the length and the velocity of the RBS were assessed, is related with the balance between the output of the extruder and the mixing degree that can be accomplished by the RBS, but taking into consideration, simultaneously, the pressure profile along the extruder.

The better balance is can be obtained when a barrel section with grooves is used in the solids conveying zone.

Further study considering the specific flow inside the different geometries proposed for the RBS must be done experimentally. This will complete the assessment of the RBS geometries proposed.

Acknowledgements

This Project has received funding from the European Union's Horizon 2020 research and innovation programme under the Marie Skłodowska-Curie grant agreement No 734205-H2020-MSCA-RISE-2016.

References

[1] Sikora J. W., Sasimowski E., Verfahrenseinheit mit rotierendem Zylinderbereich. Kunststoffe 2006, 96, 7, p. 104.

[2] Sikora J. W., Sasimowski E., Processing Unit with Rotating Cylinder Segment. Kunststoffe International 2006, 9, p. 1.

[3] Sikora R., Sikora J. W., Barrel of an extruder. Polish Patent No 185728.

[4] Sasimowski E.,Characteristics of an extrusion process with a rotating sleeve of the barrel. Polimery 2008, 53, 1, p. 47.

[5] Sasimowski E., Sikora J.W., Królikowski B., Effectiveness of polyethylene extrusion in a single-screw grooved feed extruder. Polimery 2014, 59, 6, p. 505–510.

[6] Gaspar-Cunha, A., "Modelling and Optimisation of Single Screw Extrusion Using Multi-Objective Evolutionary Algorithms", Lambert Academic Publishing, Koln, 2009.

António Gaspar-Cunha[1]

GLOBAL EXTRUDER MODELLING: ACTIVE GROOVED FEED SECTION, ROTATIONAL BARREL SEGMENT AND SPECIAL SCREWS

Abstract: *The use of modelling and optimization computer programs in the design of extrusion machines is of primordial importance as it avoids a process of trial-and-error and the intensive use of experimental results. The aim of this work is to present the results obtained when designing a single screw extruder machine for the processing of nanocomposites. This extruder comprehends the use of grooves in the feed zone of the barrel, a rotational barrel segment in the metering zone and a special screw. The results obtained allows to conclude about the performance of the extruder developed and the better operating condition s to use. It is important to note that only when a sufficient pressure is generated in the feed zone, by the use of the grooves, the rotation barrel segment have the best performance concerning mixing.*
Keywords*: single-screw extruder, numerical modelling, screw design.*

1. Introduction

The aim of this chapter is to present the results concerning the global modelling of the extrusion process taking into account the new geometrical devices developed within the NEWEX project: i) active grooved feed sections, ii) rotational barrel segments and iii) special screws. Each one of these devices were studied individually before. The results obtained in the present chapter take into account the conclusions drawn in those individual studies.

The first dealt with the active grooved feed section. In the last forty years numerous theoretical and experimental studies have been performed using extruders with grooves in the barrel [1–9]. From these studies it can be verified that there are two main methods of approaching the problem, the first considers that the coefficient of friction polymer-barrel with grooves can be replaced by an average friction coefficient, the second considers the existence of the flow of granules throughout the grooves. For the calculation of the average coefficient of friction, four models were implemented in computer, for which some simulations were carried out in order to verify their suitability and their sensitivity to changes in the system geometry.

The main conclusion to be taken from the assessment of the Solution Models proposed is that the existence of grooves in the solids conveying zone it is an effective way of improving the performance of the extruder. This performance depends on both the depth and the total width of the grooves. The existence of the helicoidal grooves with a channel implemented in the direction of the screw channel enables the auto-

[1)] *IPC – Institute of Polymers and Composites, Department of Polymer Engineering, University of Minho, Campus de Azurém, Guimarães, Portugal. agc@dep.uminho.pt.*

cleaning of the grooves without deteriorating the performance. However, this can be also accomplished in the case of Solution Model 1, given that the depth is decreasing to zero at the end of the grooves zone, subsequently the polymer will does not accumulate in the grooves.

From these assumptions, the Solution Model chosen to be implemented in the prototype machine is Solution Model 1 due to its versatility concerning changes in both the depth and total width of the grooves and the good capacity of auto-cleaning.

Then, in the second study the aim was to present the modelling results concerning the rotational barrel segment located in the metering region of the extruder, *i.e.*, when the polymer is totally melted. This second area of development is concerned with a rotational barrel segment (RBS) rotating in the same or opposite direction as the screw. The rotational barrel segment, fitted with intensifying grooves of torsional angle and torsional direction, is a vital element of plasticizing system of a new extruder and will be mounted in the metering zone. It is a complete novelty that has not been described in literature or used in the existing extruders, except in some work developed by the team [10–14].

Changing the rotational speed of the grooved barrel segment as well as the direction of its rotation during the extrusion process will enable to influence the thermal, rheological, kinematic and dynamic conditions in the plasticizing system of the new extruder. Due to that behaviour, it will be possible to efficiently control the extrusion process and to improve the quality of the products obtained because enhancing the above processes will result in the homogenization of the thermal and mechanical properties of materials and the structure of the products, without the need to use additional, expensive devices such as the gear pump and static mixer. This will be of utmost importance for polymer processing industry, as well as for food, cosmetics and pharmaceutical industries. For the calculations, the modelling program described in [15] was used. For that purpose, various velocities, in both directions, of the rotational barrel segment were tested. The results are discussed, and some conclusions were proposed.

The main conclusion that can be drawn in this computational study, in which the influence of the length and the velocity of the RBS were assessed, is related with the balance between the output of the extruder and the mixing degree that can be accomplished by the RBS, but taking into consideration, simultaneously, the pressure profile along the extruder. The better balance is can be obtained when a barrel section with grooves is used in the solids conveying zone.

Finally, in the third study, the modelling results concerning the different screws proposed was presented. The screws developed within the project have a complex geometry that was not possible to take into account by the modelling software, which is only able to compute conventional screw geometries, grooved barrels and barrier screws. However, the calculations made using the conventional screws similar to those proposed within the project show that some important differences are accomplished. For the calculations, the modelling program described in [15] was used. For that

purpose, various velocities od the screw were tested. The results are discussed, and some conclusions are proposed.

The main conclusion that can take from these results is that the choice of a screw cannot be independent of the use, it must be made taking into account simultaneously the other geometries developed within the project**,** namely, the use of a barrel with grooves in the feed zone and/or a rotational barrel in the pumping zone.

Therefore, considering the conclusions above, the active grooved feed section Model 1, developed within the project, was tested for different for different velocities and geometry of the rotational barrel segment and for different screw geometries, as described in the next section.

2. Case studies

2.1 Standard extruder geometry

The extruder used has a square pitch screw with a diameter (D_{screw}) of 25 mm and a *L/D* ratio equal to 25 (Fig. 1). It was fitted with a conventional screw with the lengths of the feed, compression and metering zones equal to 8D, 8D and 9D, respectively. The internal screw diameter is 16.6 mm and 22.0 mm, respectively for the feed (D_{i1}) and metering (D_{i3}) zones. The total length of the grooves zone (L_g) is 100 mm and the rotational barrel segment was located at 16D with length of 3D.

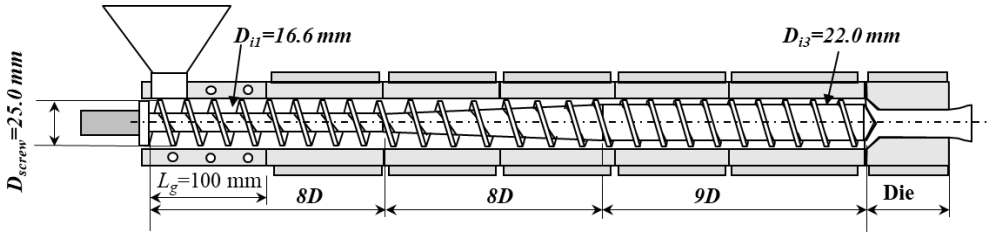

Fig. 1. Extruder geometry

2.2 Grooves geometry

The main objective of the grooves is to increase the coefficient of friction between the solid polymer granules and the inner wall of the cylinder, which is known to increase the throughput capacity of the extruder. The grooves can be longitudinal or helical (Fig. 2).

In the extruder presented above there is the possibility of including sections with different geometry of grooves with the length of 4D (100 mm) and where the depth varies linearly from a maximum value at the beginning of the grooves, until it cancels out. Table 1 shows the various configurations used for the grooves.

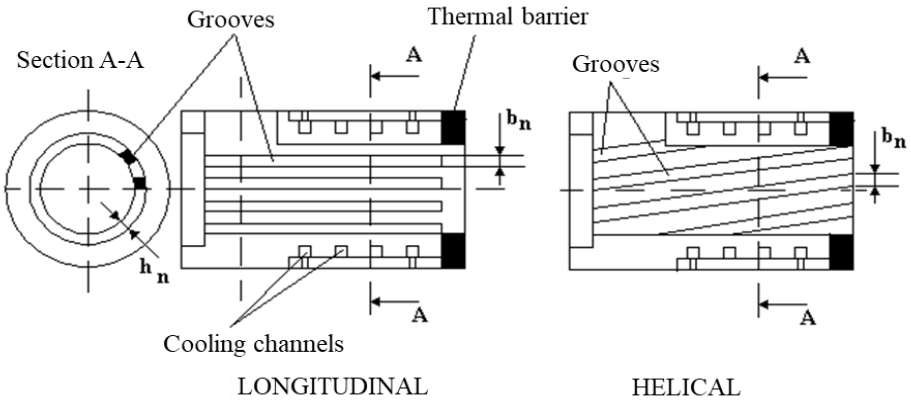

Fig. 2. Longitudinal and helical grooves in the barrel

Figures 3 and 4 characterizes the geometry defined by Solution Model 1 for the grooves. Model 1a, shown in Figure 3, represents the grooves device designated by Newex 3 with the device totally open, i.e., when the grooves have the maximum value for the initial depth (h_{N0}), while in Figure 4 is shown Model 1d, the case when this depth is nil.

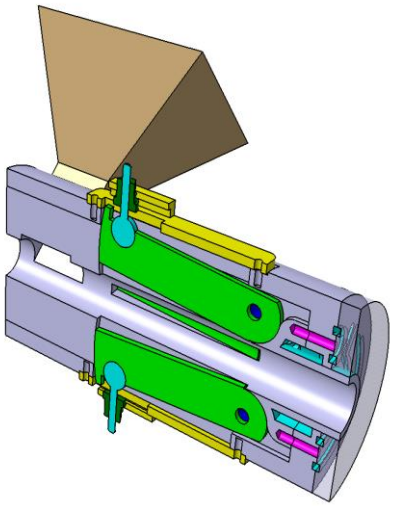

Fig. 3. Solution Model 1a: Newex 3 totally open

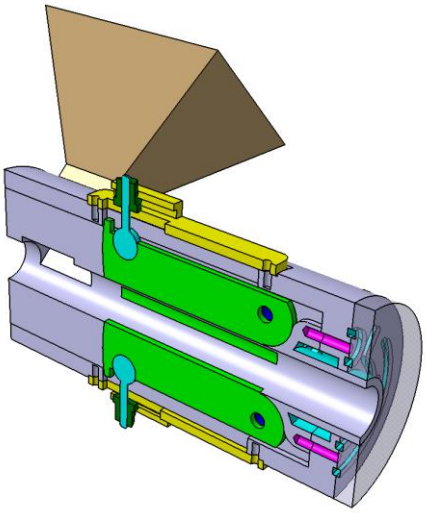

Fig. 4. Solution Model 1d: Newex 3 totally closed

Table 1. *Grooves geometry for the Solution Models 1 (Model 1: N_N=4; Model 2: N_N=5)*

Solution Models	b_N **(mm)**	h_{N0} **(mm)**	N_N	L **(mm)**	$B = N_N * b_N$ **(mm)**	**Type**
Model 1	6.0	6.0	4	100.0	24	L
Model 2	6.0	6.0	5	100.0	30	L

2.3 Rotational barrel segment geometry

Figure 5 shows the three different situations that can occur when an RBS is implemented in an extruder: a) the velocity of the RBS (N_b) is nil; b) the velocity of the RBS has the same direction than that of the screw (N_s) and c) the velocity of the RBS has a different direction than that of the screw. In the first case the relative barrel velocity (V_b) results by transforming the rotational screw speed (N_s) in a linear velocity near the interior barrel velocity (see reference [6]), this is: $V_b = \pi N_s D$ (where D is the external screw diameter). In the second case the resulting ($V_{'b}$) velocity is reduced, while in the third the resulting velocity increases.

In the present study rotational barrel segment was located at 16D with a length of 3D and four different rotational barrel segment velocities (Nb) were tested: -80 rpm, -120 rpm, 80 rpm and 100 rpm.

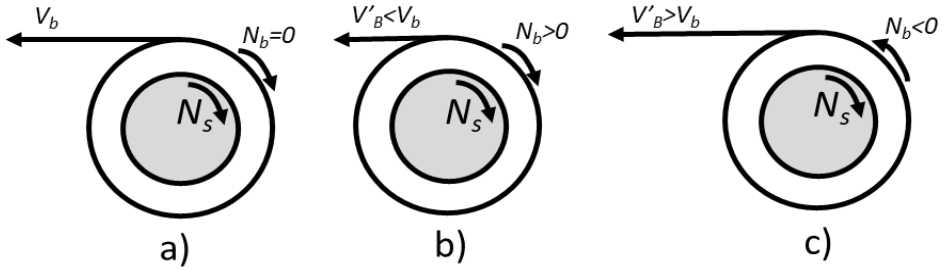

Fig. 5. Definition of the relative barrel velocity (V'b)

2.4 Special screws geometry

Different screws geometries were tested, using three different internal diameters in the metering zone (D_{i3}), i.e., Screw 1 with 22 mm, Screw 2 with 21 mm and Screw 3 with 20 mm. The screw speed was fixed in 120 rpm. Screw 2 (22 mm) was also tested for three different pitch in all screw extension, 23, 25 and 27 mm.

2.5 Material properties

Table 2 shows the relevant properties of the polymer used in the calculations, a High-Density Polyethylene, Malen E FGAN 18-D003 from Basell. The viscosity was obtained experimentally using a capillary rheometer being the data fitted using the power law model as follows. See also Figure 6.

$$\eta = \eta_0 \, \gamma^{(n-1)} e^{-a(T-T_0)} \tag{1}$$

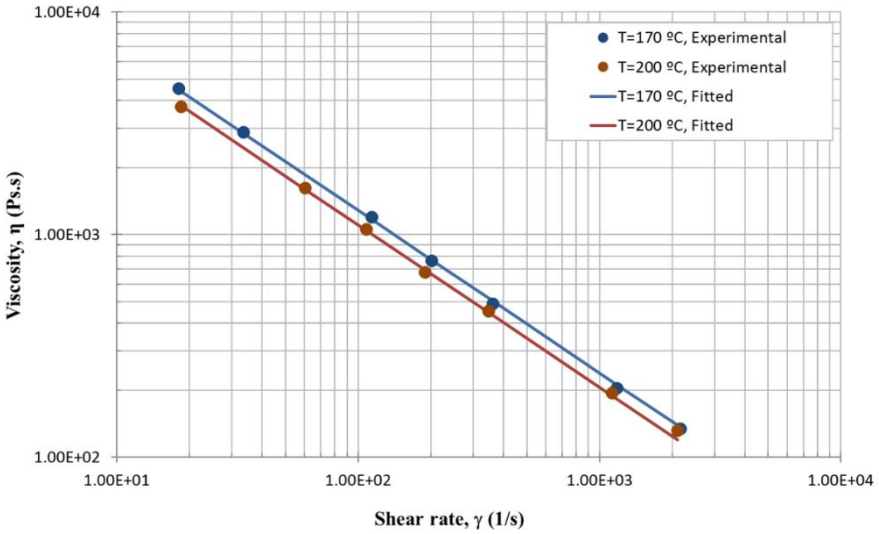

Fig. 6. Rheological data

***Table 2**. Properties for LDPE (Malen E FGAN 18-D003)*

Properties			**LDPE**	**Unit**
Density	*Apparent*	ρ_0	495.0	kg/m^3
	Solid	ρ_s	921.0	kg/m^3
	Melt	ρ_m	854.4	kg/m^3
Friction coefficients	*Internal*		0.67	---
	Hopper		0.30	---
	Barrel		0.40	---
	Screw		0.20	---
Thermal conductivity	*Solid*	k_s	0.141	W/m ºC
	Melt	k_m	0.078	W/m ºC
Specific Heat	*Solid*	C_s	3160.0	J/kg
	Melt	C_m	2682.0	J/kg
Melting heat		h	1.03 x 10^6	J/kg
Melting temperature		T_m	113.0	ºC
Viscosity: Power law		n	0.27	---
		η_0	3.7e4	Pa/s
		a	0.005	1/°C
		T_0	170.0	°C

In all calculations, the operating conditions were fixed. The screw speed was 120 rpm and the barrel temperature profile in the solids zone varies linearly between 30ºC and 70ºC in the first 5 turns (the solids conveying zone) and is constant and equal to 170ºC in the remainder of the barrel and die. Table 3 presents the calculations made taking into account the conclusions taken before.

Therefore, the grooved Model 1 was chosen and, then, the better rotational barrel segment rotational screw speeds were used (i.e., -80, -120, 80 and 100 rpm) and all different geometries of the screw were tested.

Table 3. *Cases study (N_N – number of grooves; N_b – rotational barrel segment velocity; D_i – internal screw diameter; P – pitch)*

Case study	Grooved Model 1 N_N	Rotational Barrel Segment N_b (rpm)	Screw Geometry	
			D_i (mm)	P (mm)
1	5	-80	23.0	25.0
2			22.0	25.0
3			20.5	25.0
4	5	-120	23.0	25.0
5			22.0	25.0
6			20.5	25.0
7	5	80	23.0	25.0
8			22.0	25.0
9			20.5	25.0
10	5	100	23.0	25.0
11			22.0	25.0
12			20.5	25.0
13	4	-120	23.0	25.0
14			22.0	25.0
15			20.5	25.0
16	5	-120	22.0	23.0
17			22.0	25.0
18			22.0	27.0

3. Presentation and discussion of results

3.1 Influence of rotational barrel segment velocity

Figures 7 and 8 and Table 3 shows the most important results for cases study 1, 2 and 3 (Table 3). The better results obtained are in bold in Table 4, *i.e.*, when the internal diameter of the screw in the metering zone is 22 mm. This conclusion results from a balance between all the parameters considered, including the fact that when the diameter is 23 mm the solid bed profile does not behave correctly, also, in this case, the mixing (WATS) accomplished is not satisfactory.

Table 4. *Results for case studies 1, 2, and 3 (N_b = -80rpm, L_b = 3D: $L/D \in [16; 19]$)*

D_i (mm)	N_b (rpm)	Output (kg/hr)	T_{melt} (°C)	Power (W)	$L_{melting}$ (m)	WATS	Viscous Dissipation
23.0	-80	4.371	186.6	3378	12.692	480.8	1.28
22.0	**-80**	**6.302**	**188.8**	**3865**	**15.58**	**464.5**	**1.11**
20.5	-80	9.108	185.7	4451	15.06	316.0	1.09

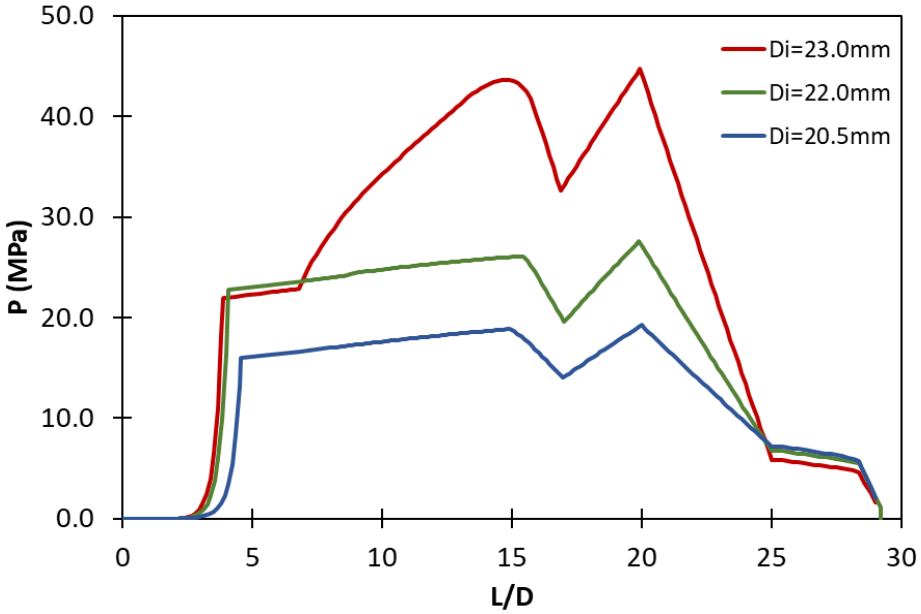

Fig. 7. Pressure profile for cases study 1, 2 and 3

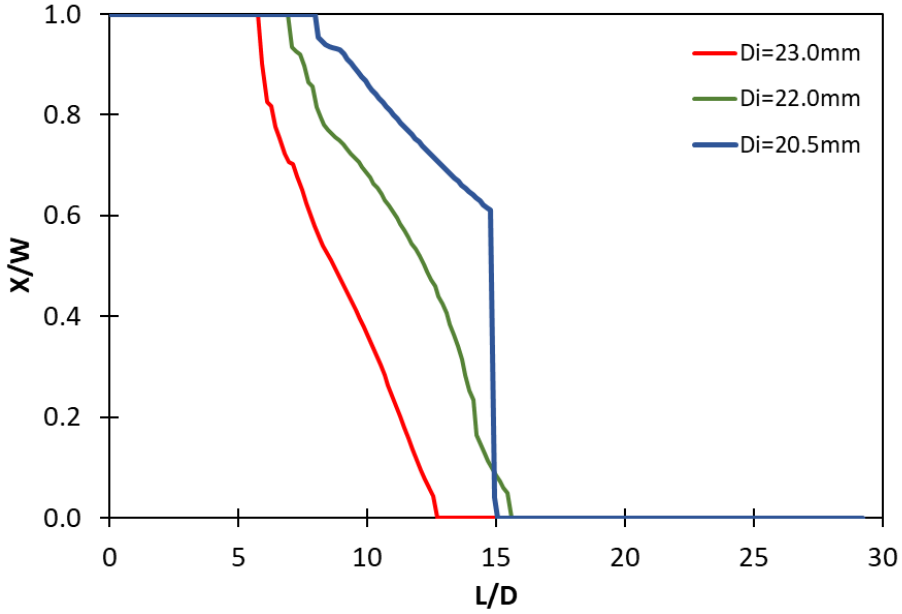

Fig. 8. Solid bed profile for cases study 1, 2 and 3

For case studies 4, 5 and 6, presented in Table 5 and Figure 9, but now for N_b = -120rpm, the better results are obtained again when Di is 22 mm. In this case, an analysis of the pressure profile shows that the results for case study 6 were not good.

However, in some cases signalled in red in the tables, it is important to note that the pressure decreases below zero. In practice this cannot occur. This is the advantage of analysing the different geometries and operating conditions using computer programs.

Table 5. *Results for cases study 4, 5 and 6 (N_b = -120rpm, L_b = 3D: L/D ∈ [16; 19])*

D_i (mm)	N_b (rpm)	Output (kg/hr)	T_{melt} (°C)	Power (W)	$L_{melting}$ (m)	WATS	Viscous Dissipation
23.0	-120	4.525	187.4	3576	12.904	512.0	1.26
22.0	**-120**	**6.602**	**189.6**	**4301**	**15.52**	**486.3**	**1.12**
20.5	-120	8.890	185.1	3941	19.49	331.5	1.09

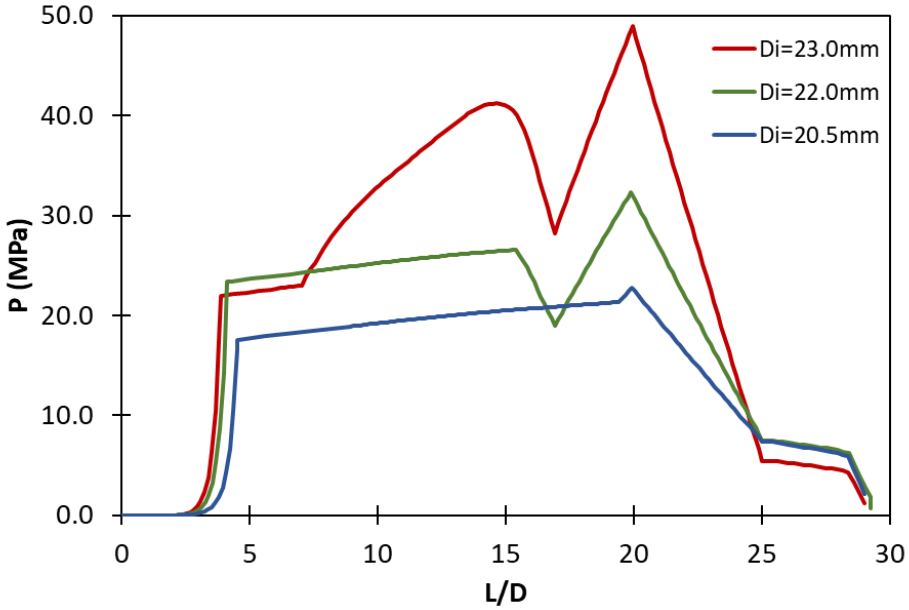

Fig. 9. Pressure profile for cases study 4, 5 and 6

Again, for cases study 7, 8 and 9, the better results are obtained for a screw with an internal diameter of 22 mm, as can be seen in Table 6 and Figure 10. The same happen for cases study 10, 11 and 12, presented in Table 7 and Figure 11, and for cases study 13, 14 and 15, presented in Table 7 and Figure 11.

Table 6. *Cases study 7, 8 and 9 (N_b = 80rpm, L_b = 3D: L/D ∈ [16; 19])*

D_i (mm)	N_b (rpm)	Output (kg/hr)	T_{melt} (°C)	Power (W)	$L_{melting}$ (m)	WATS	Viscous Dissipation
23.0	80	2.872	184.4	3003	10.152	407.3	1.41
22.0	**80**	**4.547**	**187.5**	**2903**	**12.72**	**308.2**	**1.29**
20.5	80	8.079	181.6	3766	17.85	155.7	1.07

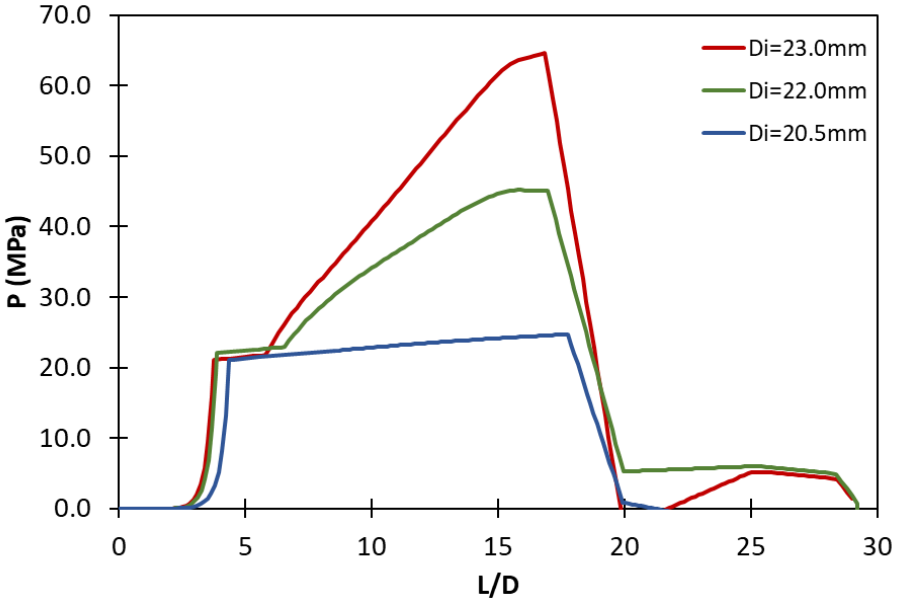

Fig. 10. Pressure profile for cases study 7, 8 and 9

Table 7. *Cases study 10, 11 and 12 (N_b = 100rpm, L_b = 3D: L/D ∈ [16; 19])*

D_i (mm)	N_b (rpm)	Output (kg/hr)	T_{melt} (°C)	Power (W)	$L_{melting}$ (m)	WATS	Viscous Dissipation
23.0	100	2.956	185.1	3556	7.584	390.0	1.41
22.0	**100**	**4.355**	**187.7**	**2932**	**12.79**	**325.1**	**1.31**
20.5	100	6.067	186.6	3181	15.86	243.6	1.10

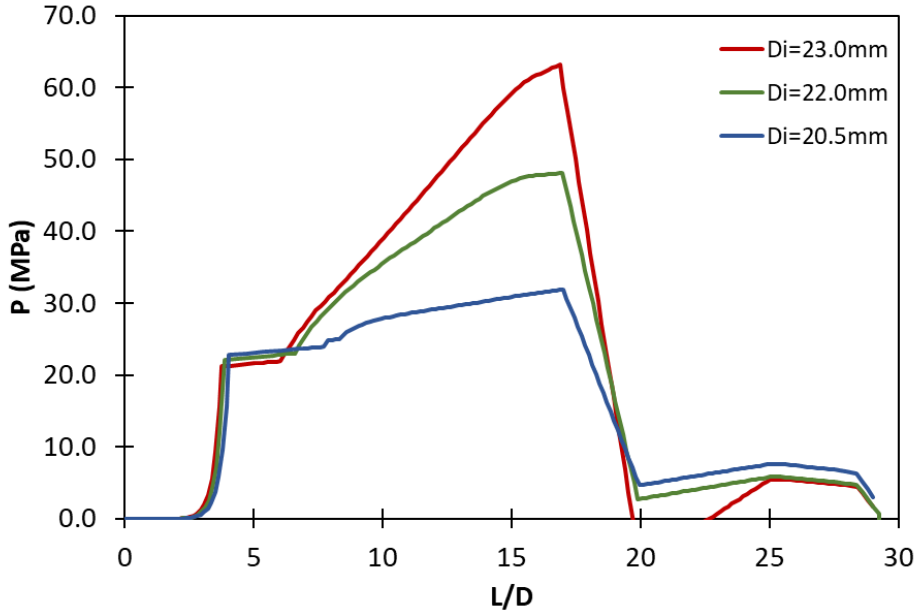

Fig. 11. Pressure profile for cases study 10, 11 and 12

Table 8. *Influence of Rotational Barrel Section (N_b = -120rpm, L_b = 3D: L/D ∈ [16; 19])*

D_i (mm)	N_b (rpm)	Output (kg/hr)	T_{melt} (°C)	Power (W)	$L_{melting}$ (m)	WATS	Viscous Dissipation
23.0	-120	4.502	187.4	3565	12.812	508.8	1.18
22.0	**-120**	**6.576**	**189.8**	**4341**	**14.76**	**461.2**	**1.12**
20.5	-120	8.798	186.0	3635	18.78	356.3	1.09

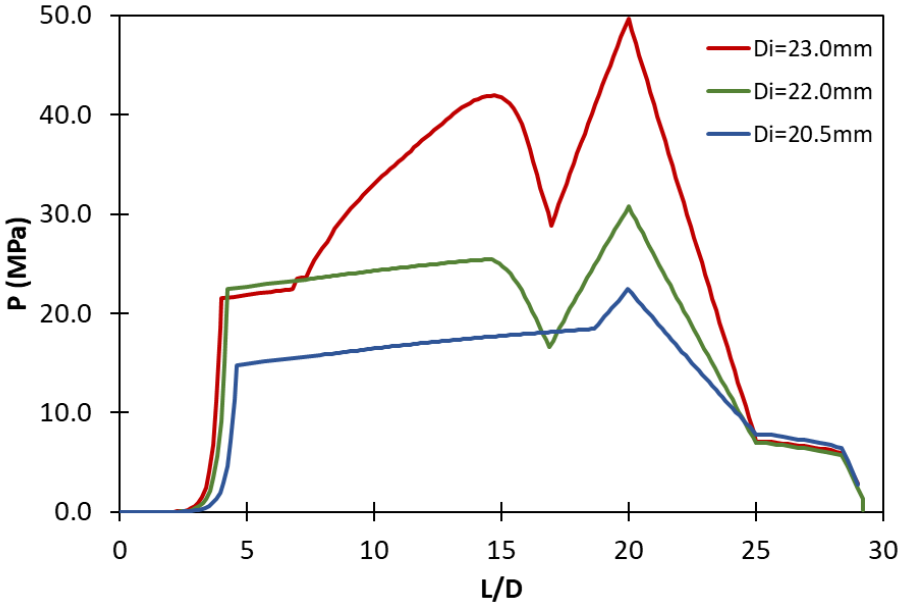

Fig. 12. Pressure profile for cases study 13, 14 and 15

3.2 Influence of screw geometry

Table 9 and Figure 13 show the results for cases study 16, 17 and 18, when the pitch of the screw varies. In this case the velocity of the rotational barrel was fixed in -120 rpm (as in this case the output is higher). The better results were obtained when the pitch is 27 mm, but the results for the other cases were not very different.

Table 9. *Results for cases study 16, 17 and 18 (N_b = -120rpm, L_b = 3D: L/D ∈ [16; 19])*

P **(mm)**	N_b **(rpm)**	**Output (kg/hr)**	T_{melt} **(°C)**	**Power (W)**	$L_{melting}$ **(m)**	**WATS**	**Viscous Dissipation**
23.0	-120	6.637	189.6	4756	14.880	473.6	1.12
25.0	-120	6.602	189.6	4301	15.52	486.3	1.12
27.0	-120	6.654	190.6	3860	15.76	486.3	1.12

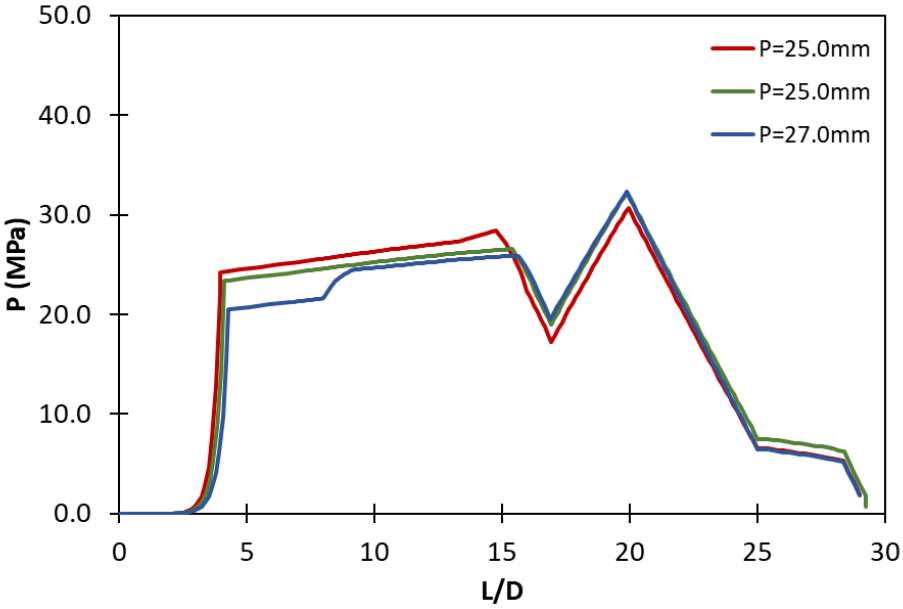

Fig. 10. Pressure profile for cases study 16, 17 and 18

6. Conclusions

Considering the results obtained, the best screw to be used is the one with a square pitch, this is, with the pitch equal to the external screw diameter, in this case equal to 25 mm. Simultaneously, the better rotational speed of the rotational barrel segment is -120 rpm.

From this, the results obtained in all the reports recommend the use of the grooved barrel segment Model 1, a rotational speed of the rotational barrel segment of -120 rpm and a screw with a square pitch and an internal diameter in the metering zone of 22 mm.

Acknowledgements

This project has received funding from the European Union's Horizon 2020 research and innovation programme under the Marie Skłodowska-Curie grant agreement No 734205–H2020-MSCA-RISE-2016.

References

[1] Boes, D., Krämer, A., Lohrbäccher, V., Scheneiders, A., Kunststoffe Germ. Plast., 80, 6, 659, 1990
[2] Potente, H., Kunststoffe Germ. Plast., 75, 7, 439, 1985
[3] Rautenbach, R., Peiffer, H., Kunststoffe Germ. Plast., 72, 3, 137, 1982
[4] Rautenbach, R., Peiffer, H., Kunststoffe Germ. Plast., 72, 5, 262, 1982
[5] Grünschloss, E., Kunsttoffe Germ. Plast., 74, 7, 405, 1984
[6] Rawendaal, C., Polymer Extrusion, Hanser Publishers, Munich, 1986
[7] Potente, H., Kunststoffe Germ. Plast., 78, 4, 355, 1988
[8] Potente, H., Koch, M., Intern. Polym. Process., 4, 4, 288, 1989
[9] Goldacker, E., Diss. RWTH Aachen, 1971
[10] Sikora J. W., Sasimowski E., Verfahrenseinheit mit rotierendem Zylinderbereich. Kunststoffe 2006, 96, 7, p. 104.
[11] Sikora J. W., Sasimowski E., Processing Unit with Rotating Cylinder Segment. Kunststoffe International 2006, 9, p. 1.
[12] Sikora R., Sikora J. W., Barrel of an extruder. Polish Patent No 185728.
[13] Sasimowski E.,Characteristics of an extrusion process with a rotating sleeve of the barrel. Polimery 2008, 53, 1, p. 47.
[14] Sasimowski E., Sikora J.W., Królikowski B., Effectiveness of polyethylene extrusion in a single-screw grooved feed extruder. Polimery 2014, 59, 6, p. 505–510.
[15] Gaspar-Cunha, A., "Modelling and Optimisation of Single Screw Extrusion Using Multi-Objective Evolutionary Algorithms", Lambert Academic Publishing, Koln, 2009

Lino A. Costa[1], Renê S. Pinto[2], António Gaspar-Cunha[2]

INTRODUCTION TO EVOLUTIONARY MULTIOBJECTIVE OPTIMIZATION

Abstract: *Most real-world problems are intrinsically multiobjective in nature. The simultaneous optimization of multiple conflicting objectives leads to the existence of different trade-offs between the objectives. Different approaches can be considered in solving multiobjective problems: scalarization methods, in which the scalarized function is solved, and evolutionary algorithms, which simultaneously seek to find several compromise solutions. Evolutionary Algorithms, inspired by the natural evolution of species, emerged as a powerful alternative for solving multiobjective optimization problems. The outcome of these algorithms is a set of incomparable optimal solutions that permits the decision maker to perceive the compromises and select the preferable alternatives. In this chapter a brief overview on Evolutionary Multiobjective Optimization is presented.*
Keywords: *optimization, algorithms, scalarization methods.*

1. Introduction

Most engineering optimization problems involve multiple conflicting objectives or criteria. If they are formulated as a single objective problem, it is not possible to capture the multiple, conflicting and incommensurate axes evaluation of the merits of potential solutions. In fact, there is no single solution that simultaneously optimizes all criteria, but a set of solutions that represent different trade-offs among them. Thus, it is advantageous to consider multiobjective optimization approaches that deal with more than one objective and can provide crucial knowledge to assist the decision-making process [1].

2. Multiobjective optimization

Generally, an optimization problem can be simply described as the problem of finding an optimal solution, *i.e.*, the best solution from all feasible solutions. However, in a multiobjective optimization problem that deals with more than one objective, there exists a set of optimal solutions that are incomparable. Since none of these solutions can be considered to be superior to other in this set, they are all optimal. So, the notion of optimality is different in multiobjective optimization. In the next sections, the mathematical formulation, basic concepts such as dominance and optimality, and the main multiobjective optimization approaches are addressed.

[1)] *ALGORITMI Center, University of Minho, Campus de Azurém, Guimarães, Portugal*
[2)] *Department of Polymer Engineering, Institute for Polymer and Composites, University of Minho, Campus de Azurém, Guimarães, Portugal, agc@dep.uminho.pt.*

2.1 Problem formulation

A multiobjective optimization problem (MOP) with m objectives and n decision variables can be formulated as follows [2]:

$$\min_{x \in \Omega} \quad \boldsymbol{f}(\boldsymbol{x}) \equiv (f_1(\boldsymbol{x}), \dots, f_m(\boldsymbol{x}))$$

$$\text{subject to} \quad g_i(\boldsymbol{x}) \leq 0, i \in \{1, \dots, p\}$$
$$h_j(\boldsymbol{x}) = 0, j \in \{1, \dots, q\}$$

where $\boldsymbol{x}$ is the decision vector, *i.e.*, $\boldsymbol{x} \in \Omega \subseteq R^n$ with $\Omega = \{x \in R^n : \boldsymbol{l} \leq \boldsymbol{x} \leq \boldsymbol{u}\}$, $\boldsymbol{f}$ is the objective vector of m objective functions, *i.e.*, $\boldsymbol{f} \in \phi \subseteq R^m$, $g_i : R^n \to R$ are p inequality constraint functions and $h_j : R^n \to R$ are q equality constraint functions, and $\boldsymbol{l}$ and $\boldsymbol{u}$ are the vectors of the lower and upper bounds on decision variables, respectively. Mathematically, any maximization objective can be converted as a minimization one since $\max f_i(x)$ is equivalent to $-\min(-f_i(x))$ for $i \in \{1, \dots, m\}$. The objective vector $\boldsymbol{f} : R^n \to R^m$ maps the n-dimensional decision space into the m-dimensional objective space. Each solution in the decision space has a unique image in the objective space (but, the inverse may be not unique). Figure 1 illustrates the mapping between the two multidimensional spaces.

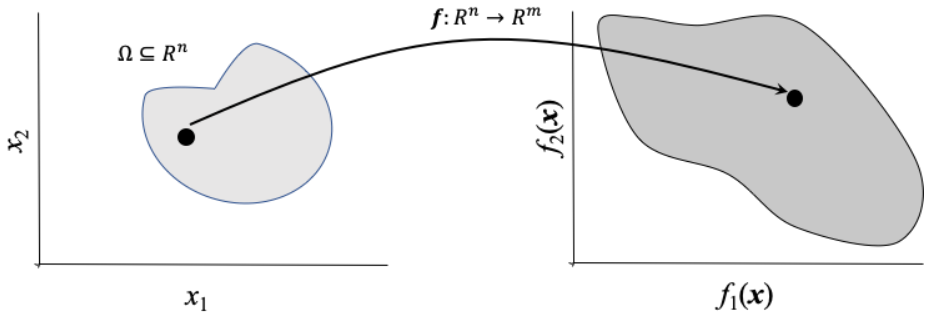

Fig. 1. Decision variable space and objective function space

2.2 General concepts

In a MOP, the goal is to minimize all objectives simultaneously, *i.e.*, to find feasible solutions where every objective function is minimized. If all objectives do not conflict with each other, *i.e.*, there exist a unique solution that minimizes all the objectives. In practice, this situation is unlikely to occur with most of the engineering optimization problems. The existence of multiple conflicting objectives gives rise to a set of optimal solutions, instead of a single optimal solution. The solutions in this set represent different compromises or trade-offs between the objectives. These solutions are incomparable each other since none of these solutions can be said to be better than others. In this case, the objective space is partially ordered and the dominance concept allows to compare solutions as follows:

Definition 1 (dominance): Given two solutions $\boldsymbol{x} \in \Omega$ and $\boldsymbol{y} \in \Omega$, the solution $\boldsymbol{x}$ is said to dominate the solution $\boldsymbol{y}$, denoted by $\boldsymbol{x} \prec \boldsymbol{y}$, if and only if $f_i(\boldsymbol{x}) \leq f_i(\boldsymbol{y})$, for all $i \in \{1, \ldots, m\}$ and $f_j(\boldsymbol{x}) < f_j(\boldsymbol{y})$ for at least one $j \in \{1, \ldots, m\}$.

In multi-objective optimization, the aim is to find the non-dominated solutions that approximate the optimal trade-offs between the objectives. This leads to the concepts of Pareto optimality as follows:

Definition 2 (Pareto optimality): Let $\boldsymbol{x}^* \in \Omega$ be a feasible solution, $\boldsymbol{x}^*$ is Pareto optimal if and only if there is no other solution $\boldsymbol{y} \in \Omega, \boldsymbol{y} \neq \boldsymbol{x}^*$, that $\boldsymbol{y} \prec \boldsymbol{x}^*$.

The set of all *non-dominated solutions* is called the *Pareto optimal set*:

Definition 3 (Pareto optimal set): For a given MOP, the Pareto optimal set is defined as $PS = \{\boldsymbol{x}^* \in \Omega | \nexists\, \boldsymbol{y} \in \Omega: \boldsymbol{y} \prec \boldsymbol{x}^*\}$.

The set of the images of the non-dominated solutions in the *Pareto optimal set* is the *Pareto optimal front*:

Definition 4 (Pareto optimal front): For a given MOP and Pareto optimal set PS, the Pareto optimal front is defined as $PF = \{\boldsymbol{f}(\boldsymbol{x}^*) \in R^m | \boldsymbol{x}^* \in PS\}$.

Figure 2 illustrates the mapping between the Pareto optimal set and Pareto optimal front. The Pareto optimal front is composed of non-dominated vectors that correspond to incomparable solutions.

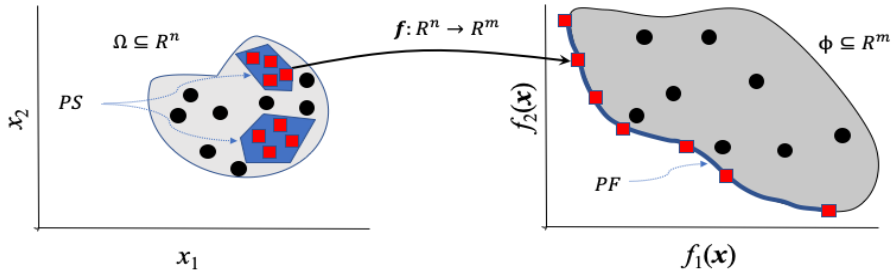

Fig. 2. Pareto optimal set and Pareto optimal front

In a MOP, the objective functions may have different scales and magnitude. Thus, it is important to normalize their values in order to facilitate the search and decision-making processes. Normalization can be done by using some special points defined in the objective space. These points define the range of the entire Pareto optimal front. The *ideal vector* is constituted by the lower bounds of all objectives:

Definition 5 (ideal vector): For a given MOP, the vector $\boldsymbol{z}^*$ that minimizes each of all objective functions is the ideal vector $\boldsymbol{z}^* \in R^m$.

The components of the ideal vector can be obtained by minimizing separately each one of the objective functions of the MOP. Unlike the ideal vector $\boldsymbol{z}^*$, which represents the lower bound of each objective in the entire feasible objective space, the nadir vector $\boldsymbol{z}^{\boldsymbol{nad}}$, represents the upper bound of each objective in the entire Pareto optimal front. It should be noted that the nadir vector is not the vector with the worst feasible

function values. In order to approximate the nadir vector, critical points are computed, *i.e.*, the points with the worst objective function values among all Pareto optimal solutions:

Definition 6 (critical point): For a given MOP, a point $\boldsymbol{c}^{(i)}$ is a critical point with respect with the i-th objective function, if it is the worst value of f_i among all Pareto optimal solutions, *i.e.*, $\boldsymbol{c}^{(i)} = \{\boldsymbol{f}(\boldsymbol{x}) | \boldsymbol{x} = \underset{\boldsymbol{x}^* \epsilon PS}{\operatorname{argmax}} f_i(\boldsymbol{x}^*)\}$.

The elements of the *nadir vector* are obtained from the components of the critical points of all objectives.

Definition 7 (nadir vector): For a given MOP, the nadir vector $\boldsymbol{z}^{\boldsymbol{nad}}$ is the vector which the j-th component is the j-th component of the corresponding critical point, *i.e.*, $\boldsymbol{z}^{\boldsymbol{nad}} = (c_1^{(1)}, c_2^{(2)}, \ldots, c_m^{(m)})$.

Figure 3 represents the ideal vector, nadir vector and critical points for a MOP.

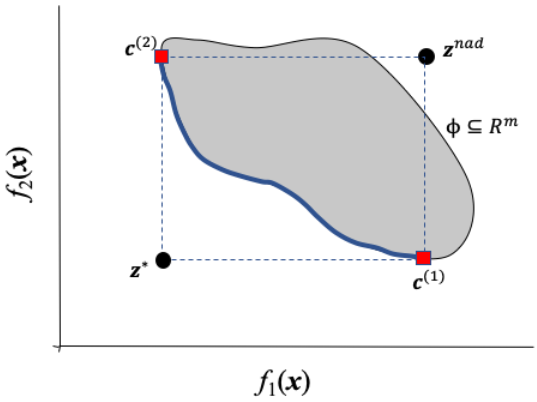

Fig. 3. Ideal vector, nadir vector and critical points for a MOP

The ideal vector and the nadir vector can be used to normalize objectives functions to the same order of magnitude in the interval [0,1]. The normalized objective function f_i^{norm} for the i-th objective function is computed by

$$f_i^{norm} = \frac{f_i - z_i^*}{z_i^{nad} - z_i^*}$$

Normalization is an important issue that facilitates the decision-making process by the identification of trade-offs between Pareto optimal solutions in the normalized objective space.

2.3 Multiobjective optimization approaches

There is a large variety of approaches to solve MOPs that can be classified in according to different criteria. A general and probably most commonly categorization of these approaches is to classify the approaches according to the participation of the

decision maker (DM) in the process [2]: no-preference, a priori, interactive and a posteriori methods. In the no-preference methods, no articulation of the DM preference information is used. In a priori methods, the DM provides preference information before the search of compromise solutions. However, in practice, often the DMs preferences are not reliably captured and reflected in the search process. In interactive methods, DM preference information is progressively articulated with the search of solutions. Finally, in a posteriori methods, the search of a set of compromise solutions is performed before the decision-making process. In this case, DMs can select the most suitable solution from this set according to their preferences. It should be stressed that in this approach, it is required an approximation as close and diverse as possible to the true Pareto optimal set. Moreover, a whole range of optimal solutions provides valuable information about the underlying problems, in particular the trade-offs at stake in different regions that can be crucial for effective decision-making. Another common classification is to distinguish between the so-called classical or traditional methods and multi-objective evolutionary algorithms. Such classification is mainly based on the working principles to search for Pareto optimal solutions for a MOP.

Most classical or traditional methods [2] are known as scalarization methods. In these methods, scalarization functions are used to reformulate the MOP as a single objective optimization problem. One advantage of the scalarization methods is that the scalarized problems can be solved using single objective optimization algorithms. Nevertheless, usually, scalarization functions involve several parameters. By varying the parameter values, different Pareto optimal solutions can be approximated. Therefore, approximating the entire Pareto optimal set can be computationally expensive since requires multiple runs with different parameters values. Nevertheless, these methods have some drawbacks such as the necessity of defining appropriate sets of values for the parameters that are dependent on the problem. The weighted sum method is an example of such methods, consisting in the minimization of the weighted sum of the objectives. For MOPs with convex Pareto fronts, this method guarantees that all Pareto optimal solutions can be achieved by a particular combination of the weights. However, Pareto optimal solutions in non-convex regions of the Pareto front are not obtained. Other scalarization methods, such the ε-constraint method or the weighted Tchebycheff method can approximate solution in non-convex regions of the Pareto optimal front.

Multiobjective evolutionary algorithms (MOEAs) work with a population of candidate solutions, which approximate the Pareto optimal set in a single run, instead of having to perform multiple runs with different parameter settings as in the case of the majority of classical methods for multiobjective optimization. In MOPs, solutions are compared against multiple objectives. Therefore, the notion of a better solution is not straightforward as it is in single-objective optimization. The performance of any MOEA is strongly related to the efficacy of its selection mechanism that guides the

search in the objective space, balancing convergence and diversity. A common approach to simulate natural selection in MOEAs consists in assigning fitness values to individuals in the population that measure the individuals' quality. Accordingly, most modern MOEAs can be classified into three different types: dominance-, scalarizing- and indicator-based algorithms.

Dominance-based approaches calculate an individual's fitness on the basis of the Pareto dominance relation [3] or according to different criteria [4]. Scalarizing-based approaches [5] incorporate traditional mathematical techniques based on the aggregation of multiple objectives into a single parameterized function. Indicator-based approaches use performance indicators for fitness assignment; pairs of individuals are compared using some quality measure (usually the epsilon or hypervolume indicator) [6]. The fitness value reflects the loss in quality if a given solution is removed [7].

2.4 Performance measures

In MOPs with multiple conflicting objectives, the outcome of an optimization algorithm is a set of incomparable solutions that approximates the Pareto optimal set. Therefore, there is a significant difference concerning the performance assessment of multiobjective algorithms that is related with the produced outcome. In single objective optimization, for instance, the outcome is a solution that minimizes the objective function. So, the quality of the outcome can be defined by means of the objective function value: the smaller the value, the better performance (assuming minimization). In multiobjective optimization, the outcome of the optimization algorithm is usually an approximation set constituted by incomparable solutions. There are two distinct goals in multiobjective optimization that can be expressed in terms of the approximation set obtained (a posteriori approach): (i) it should be as close as possible to the true Pareto optimal front, and (ii) it should be as diverse as possible. So, it is not straightforward to compare multi-objective optimization algorithms performance. In Figure 4, the first approximation set is better in terms of convergence and worst in terms of diversity, the opposite occurs with the second approximation set.

Different performance measures for assessing the quality of approximation sets have been proposed to compare multiobjective optimization algorithms. Some of them measure the convergence of an approximation set to the Pareto optimal front. Others capture the diversity of an approximation set. Eventually, some performance measures are able to measure the convergence to the true Pareto optimal front as well as the diversity of solutions in an approximation set. Examples of such performance measures are the hypervolume indicator [8] and the Inverted generational distance (IGD) indicator [9].

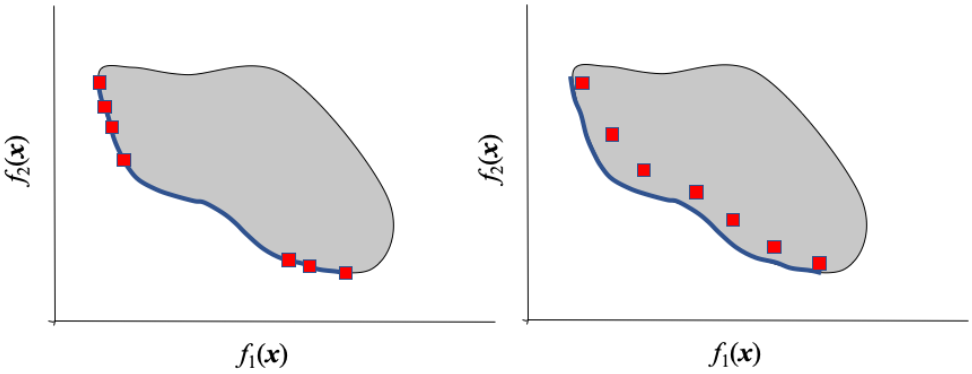

Fig. 4. Performance assessment of approximations to the Pareto optimal front

The hypervolume indicator measures the volume of the dominated region of the objective space relative to a reference set. IGD indicator computes the average distance from each point in a reference set to the closest solution in the approximation set. These performance indicators can be also used to guide the search of multi-objectives algorithms towards the Pareto optimal set.

3. Multiobjective Evolutionary Algorithms

The biological evolution, introduced in the outstanding Charles Darwin's book *On the Origin of Species*, describes the process by how a population of individuals of some specie evolves over generations. Through the *Natural Selection* process, only the individuals most adapted to the environment will survive over time and therefore will reproduce and become more common in the population. Disruptive differences in the phenotype of the individuals are performed partly by random mutations that might occur in the genome of the organisms. Eventually, a mutation occurred in some individual will produce a characteristic that is good (or even essential) to the organism survive in its natural environment. In the course of time, only the most adapted individuals will remain in the population. Basically, this process is done through two mechanisms: Selection and Variation.

In 1975 John Holland published a formal study [10] proposing a metaheuristic inspired by the natural selection process in order to develop algorithms for operations research and adaptive systems in computational environments, which was the foundation of genetic and evolutionary algorithms.

In a Genetic Algorithm (GA) a population is formed by a set of individuals, each representing a candidate solution for a given problem. All properties of each solution are encoded in a chromosome structure, which might be a string or numeric vector, for instance. This type of representation should allow the application of operators to perform modifications (mutations) in the properties in order to generate offspring solutions. Starting from an initial population of different individuals, an iterative

process is performed using the operators to generate new individuals and evolve the population towards better solutions to the given problem. To make evolution possible, there must be a metric to evaluate the quality of each solution and a mechanism to select only the best solutions in order to produce future generations. In optimization problems, the fitness metric can be the objective function, so the problem becomes evolve an initial population of solutions in order to find the best solutions (individuals) which minimizes (or maximizes) the objective function.

3.1 Structure of Genetic Algorithms

Inspired by the biological process, GAs processes a population of individuals, each representing a possible solution to a given problem. Using the mechanisms related to the natural selection process to variate and generate new individuals from the initial population, the main goal is to develop an evolutionary process throughout successive iterations in order to achieve a set of good (or optimal) solutions to the problem in the final population. In this context, the main components of a GA are:

- **Individual**: Is a feasible solution to a given problem. For example, if the problem to be solved is the minimization of the function $f \in \mathbb{R}: f(x) = x^2 + 2x$, an individual might by any real number;
- **Population**: is a set of individuals, *i.e.*, a set of possible solutions to the given problem. The size of the population depends on the nature of the problem. It might contain since dozens or hundreds up to several thousands of possible solutions. In general, the initial population is randomly generated;
- **Fitness function**: Is the problem to be solved. It might be a numerical function to be optimized, a complex mathematical model, or even a black box system with well-known inputs and outputs variables. An important requirement is the ability to evaluate the quality of each solution in order to allow the identification of the best individuals in the population;
- **Selection**: Is the mechanism which allows to identify and select the best individuals in the population to breed a new generation. There are different methods which can be used for this purpose, some of them are based only in the value of fitness function, others can also use stochastic models to sample the population;
- **Variation**: Once the best individuals were selected from the current population, the variation process will be performed by using genetic operators, mainly recombination (crossover) and mutation. The idea behind these algorithms is exactly the same in nature, produce a new individual (child) from a pair of individuals (parents) preserving the characteristics of its parents. Eventually, solutions that are better than its parents will emerge from this process;
- **Termination condition**: Is (are) the predefined condition(s) that will stop the iterative evolution process. It might be a fixed number of generations that was reached or a minimal (or maximal) fitness value that was found, for instance.

Figure 5 shows the general structure of a GA. The algorithm starts by generating the initial population randomly. A predefined population or even a combination of both can also be used. The iterative process comprises in calculate the fitness function for each individual and check for the termination conditions. If such conditions were satisfied, the algorithm is done and the final population will be composed by a set of individuals which are supposed to be the best (or optimal) solutions to the given problem. Otherwise, the process continues by applying selection and variation process in order to select the best individuals from the current population and generate an offspring using genetic operators, such as recombination and mutation. This process is repeated until the termination conditions are reached.

Four main components needs to be defined in order to develop and apply a GA to a given problem: the fitness function(s), selection method, genetic operators and the representation of each individual (solution) in a genetic structure (chromosome) where the variation operator(s) can be applied. The classical Knapsack problem can be used to illustrate this process.

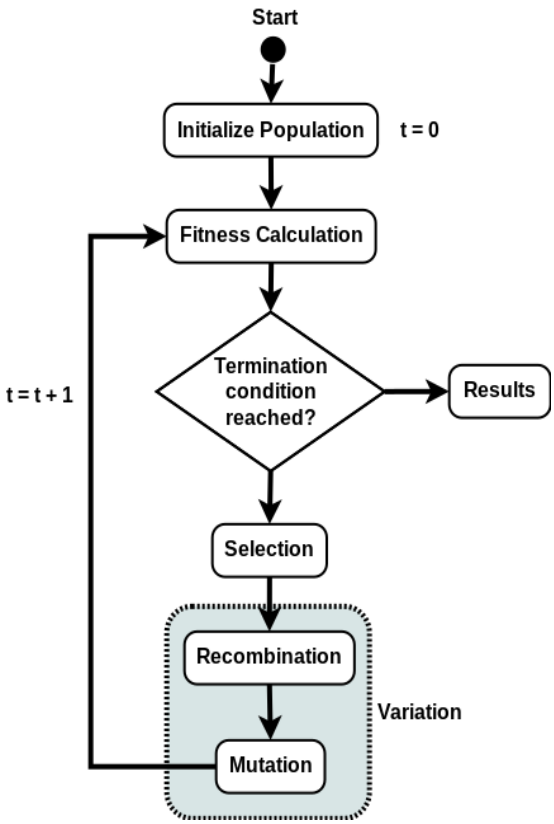

Fig. 5. General structure of a Genetic Algorithm

3.2. Application of Genetic Algorithms

The *0-1 Knapsack problem* (KSP) is a classic example in combinatorial optimization. For a given set of items, each with a specific value and weight, the problem becomes determine the best combination of items that fits into a bag (with a maximum weight restriction) maximizing the total value of all items. A formal definition is: for a given set *S* with *N* items, each with weight w_i and value v_i, $i = 1, \ldots, N$, there is a bag with maximum capacity $W > 0$. The main goal is to find a subset of items which satisfies the following conditions:

$$\text{maximize } \sum_{i=1}^{N} x_i \times v_i$$
$$\text{subject to } \sum_{i=1}^{N} x_i \times w_i \leq W \text{ and } x_i \in \{0,1\}$$

($x_i = 1$ means that the object its inside the bag. Otherwise, $x_i = 0$.)

Suppose a set of eight items described in Table 1. Concerning the problem formulation, each solution can be represented by a binary chromosome structure, which is a string of bits 0's and 1's representing the x_i value, *i.e.*, 1 if the item is inside the bag or 0, otherwise. Figure 6 shows the structure of a chromosome representing a feasible solution where the items 1, 2 and 5 are inside the bag. By representing the individuals using the binary chromosome structure, genetic operators such as crossover (recombination) and mutation can be easily applied to generate new individuals.

Table 1. *Items considered by the example*

	O_1	O_2	O_3	O_4	O_5	O_6	O_7	O_8
Weight	12	3	17	5	9	20	7	4
Value	10	8	12	9	4	11	3	5

O_1	O_2	O_3	O_4	O_5	O_6	O_7	O_8
1	1	0	0	1	0	0	0

Fig. 6. Chromosome for a feasible solution

Concerning fitness function, it should be noted that in the KSP problem it's possible to find a combination of items which maximizes the total value but it violates the maximum weight restriction. This kind of solution is not feasible, so the fitness function should take into account the feasibility of each solution concerning all restrictions imposed by the problem. A simple mechanism to handle the restrictions is to penalize invalid solutions. For a given solution *S* to the KSP problem, the following fitness function can be defined:

$$f(S) = \sum_{i=1}^{N} x_i \times v_i - Pen(S)$$

where $Pen(S)$ is a penalty function, defined by:

$$Pen(S) = \begin{cases} 0, & if\ S\ is\ feasible \\ \rho \times \left(\sum_{i=1}^{N} x_i \times w_i - W \right), & otherwise \end{cases}$$

If the solution is feasible, *i.e.*, the total weight of the items in the set does not exceed the maximum weight supported by the bag, the penalty value is 0. Otherwise, a linear value will be given. The value ρ is defined by:

$$\rho = max_{i=1,\ldots,N} \frac{v_i}{w_i}$$

Once the fitness function and the representation (chromosome) for each individual are specified, the Selection and Variation methods need to be defined. In this example, the *Tournament* selection method will be used. In this method, few individuals are chosen at random from population and several "tournaments" are run among them. For each tournament, the winner is the one with the best fitness value, therefore will be selected to breed next population after variation method is applied. Selection pressure is a probabilistic measure of how better individuals will be favoured in the process. At one hand, higher selection pressure will cause just a few better individuals to be selected, which can take the algorithm to a premature convergence. On the other hand, lower values will cause the individuals to have approximately the same chance to be selected, decreasing the chances to find good solutions or convergence in the search space. Using the tournament method, the selection pressure can be adjusted by changing the tournament size, where higher values will make weak individuals to have lower chances to be selected. For a given size *k*, the tournament selection algorithm is straightforward, as can be seen in Figure 7.

Tournament Selection with size k
1: Choose *k* individuals from current population at random 2: Select the best of the *k* individuals as progenitor

Fig. 7. Tournament selection algorithm

Suppose an initial population of ten individuals, created at random and listed in Table 2. A binary tournament selection can be applied, which means that two individuals (randomly selected from the population) will compete with each other. The winner will be selected as progenitor to produce new offspring. Table 3 lists ten binary tournaments applied to the initial population.

Table 2. *Initial population randomly generated*

Solution	Chromosome	Total Value	Total Weight	Quality
S_1	01001001	17	16	17
S_2	00010010	12	12	12
S_3	00010000	9	5	9
S_4	00011000	13	14	13
S_5	00110000	21	22	21
S_6	01000011	16	14	16
S_7	11000000	18	15	18
S_8	00000010	3	7	3
S_9	01000000	8	3	8
S_{10}	10000010	13	19	13

Table 3. *Tournament selection*

Tournament	Competitors	Winner
1	S_7 x S_3	S_7
2	S_6 x S_9	S_6
3	S_5 x S_4	S_5
4	S_4 x S_8	S_4
5	S_9 x S_5	S_5
6	S_5 x S_7	S_5
7	S_2 x S_4	S_4
8	S_2 x S_4	S_4
9	S_2 x S_3	S_2
10	S_6 x S_3	S_6

Once the best individuals were selected from the population, the Variation process can be applied to progenitors in order to produce the next offspring. Crossover (recombination) is a genetic operator that can be used to produce descendants from progenitors. Figure 8 illustrates the process. First, a crossover point is randomly chosen (indicated by the dotted line in the Figure). All bits to the right of this point will be swapped between the two parent chromosomes. Considering S_1 = {10110010} and S_2 = {10001110}, after the crossover process, two descendants will be generated: S'_1 = {10110110} and S'_2 = {10001010} resulting from the recombination of both parents. This method is called Single-point crossover. There are several different variants of crossover operator. For more information, see [11]. Table 4 lists each

descendant generated through crossover using the selected individuals (from previous tournament selection) arranged by pairs.

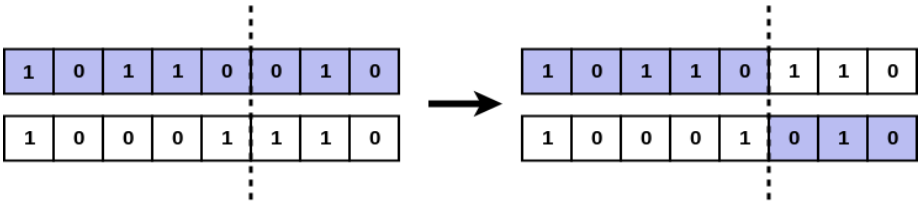

Fig. 8. Crossover process

Table 4. *Crossover operator applied selected individuals by pairs*

Progenitors	Descendants
110000|00 010000|11	110000|11 010000|00
0|0110000 0|0011000	0|0110000 0|0011000
001|10000 001|10000	001|10000 001|10000
00011|000 00010|010	00011|010 00010|000
0|0010010 0|1000011	0|0010010 0|1000011

Table 5. *Mutation operator applied to each individual*

Before	After
1100001**1**	11000010
01000000	10000000
00110000	00110000
0**0**0**1**10**0**0	01001010
0**0**110000	01110000
0011**0**000	00111000
000**11**010	00000010
0**0**010000**0**	01010001
0001**0**0**1**0	00011000
01000**011**	01001100

Although crossover process is able to produce different descendants from its progenitors, it can be hard to achieve diversity among the individuals. Thus, mutation is the other genetic operator important to complete the variation process. It acts on each individual introducing minimal modification in order to produce diversity. These modifications are made at random and can follow a distribution (uniform or Gaussian, for instance). Concerning binary chromosomes, the mutation operator will change some of the bits to produce the modifications, *i.e.*, bit 0 it's changed to 1 and vice-versa. Usually, the probability to make a modification in the chromosome is very small; otherwise it can lead to random individuals. The main goal of mutation is introduce diversity to avoid individuals become too similar to each other, which can stop the evolution process or reach local minima. Table 5 lists the individuals resulted from the crossover operation before and after the application of mutation operator. A higher mutation rate was used just to illustrate the process. Original bits that were changed are highlighted. Table 6 evaluates all individuals resulted from the mutation process.

Table 6. *Evaluation of the new offspring*

Individual	Total Value	Total Weight	Quality
11000010	21	22	21
10000000	10	12	10
00110000	21	22	21
01001010	15	19	15
01110000	29	25	27
00111000	25	31	20
00000010	3	7	3
01010001	22	12	22
00011000	13	14	13
01001100	23	32	17

As shown in Figure 5, all described processes (Fitness Calculation, Selection and Variation) are repeated iteratively until the termination conditions are reached. Considering the KSP example and the initial population listed in Table 2, the GA was applied through 20000 iterations. Five feasible solutions remained in the final population, which are listed in Table 7.

Since in the KSP example it was considered only eight items, there are 2^8 (256) possible solutions, which can be easily generated and evaluated. For the imposed weight restriction, there are only 44 feasible solutions (from 256) and the optimal (best) solution is 11010000. This solution was found by the GA and is listed in the first line in Table 7. Although this example has a small search space, it can illustrate

the capabilities, the theory and methods behind Genetic Algorithms, which has been applied on several areas to solve different kinds of complex problems.

Table 7. *Feasible solutions in the final population (after 20000 iterations)*

Individual	Total Value	Total Weight	Quality
11010000	27	20	27
01010001	22	12	22
00011001	18	18	18
10000001	15	16	15
01001000	12	12	12

3.3 Appling evolutionary algorithms to the multiobjective optimization

In addition to Genetic Algorithms, there are several other techniques inspired in the natural evolutionary process, providing different genotype representations, evolution strategies or fitness determination. All these methods belong to a class of Evolutionary Algorithms (EAs). Before the development of these kinds of algorithms, there were traditional approaches to tackle multiobjective optimization problems that were adapted from single-objective optimization [11], such as scalarization. Another approach is treat one objective function as the fitness and the others as restriction functions to the problem. However, in multiobjective problems the objectives conflict with each other. Thus, there is no single optimal solution; all solutions from the Pareto Front provide different trade-offs between the objectives. In this context, EAs are able to evolve a set of candidate solutions to the problem concerning all objective functions at the same time. There are other advantages:

- EAs are able to work with problems involving multimodal equations, which can be hard to handle by the majority of traditional optimization algorithms,
- The computational time can be controlled fixing a maximum number of iterations, which can be useful for complex problems with huge search space,
- In general, EAs are not too difficult to implement,
- Other techniques can be combined with EAs, such as local search or other metaheuristics,
- Since the evolutionary mechanisms are separate from the problem representation, EAs can be easily adapted to several different problems.

Evolutionary Multiobjective Optimization Algorithms (EMOAs) are genetic algorithms developed to solve multiobjective optimization problems. In principle, it has the same structure of GAs as shown in Figure 5. However, there are special mechanisms to work with multiobjective functions, especially to evaluate the fitness of multiple objectives. In this context, there are several EMOA available on the literature: Vector-Evaluated Genetic Algorithm (VEGA) [8], Strength Pareto

Evolutionary Algorithm (SPEA) [3], Pareto Archived Evolution Strategy (PAES) [12] and Non-dominated Sorting Genetic Algorithm (NSGA) [4], for instance.

In general, an EMOA comprises the following operations:

- Initialization: Generation of the initial population composed by a set of solutions, often generated at random,
- Fitness calculation: the fitness value for each solution should take into account the dominance relationship between the individuals. Non-dominated must have better quality than dominated solutions. If a dominance relationship cannot be defined, the fitness value should take into account the Pareto set to favour the solutions of the front,
- Selection: Based on the fitness value, the best individuals (solutions) are selected to breed the next generation,
- Variation: Using genetic operators, the selected individuals are combined and/or modified to provide variation in the individuals of the population,
- The whole process is repeated iteratively in order to achieve a final population of individuals that comprises a Pareto front, *i.e.*, with all (or the majority) individuals composed by non-dominated solutions.

Several studies concerning EMOAs has been published over the years which represents not only an important research field, but also a relevant set of methods and tools to solve complex problems with multiple objective functions, commonly found in real-world problems.

4. Conclusions

This chapter presented a brief overview on Evolutionary Multiobjective Optimization. Many real-world problems comprises multiple objectives that are conflicting in nature, which means that there is no single optimal solution, but a set of solutions giving different trade-offs between the objectives. These kind of problems are generally difficult (or even impossible) to solve using exact methods within a feasible computational time, especially when the search space is huge. In this context, EMO methods provide powerful tools to find good (or optimal) solutions to multiobjective problems. The evolutionary approach are flexible regarding the problem formulation and operate on a set of possible solutions (population), being excellent to achieve Pareto set approximations. Also, it can outperform a merely random strategy, where points in the search space are randomly generated without explore the similarities between the solutions. Several studies on the literature have been use EMO to tackle highly complex problems with success and there is a continuous research work on new algorithms to improve the technique.

Acknowledgement

This project has received funding from the European Union's Horizon 2020 research and innovation programme under the Marie Skłodowska-Curie grant agreement No 734205-H2020-MSCA-RISE-2016.

References

[1] Deb, K., Multi-objective Optimization using Evolutionary Algorithms, John Wiley & Sons, Inc., 2001.

[2] Miettinen, K., Nonlinear multiobjective optimization, vol. 12, Springer Science & Business Media, 2012.

[3] Zitzler, E., Laumanns, M., Thiele, L., "SPEA2: Improving the strength Pareto evolutionary algorithm," TIK-report, vol. 103, 2001.

[4] K. Deb, A. Pratap, S. Agarwal and T. A. M. T. Meyarivan, "A fast and elitist multiobjective genetic algorithm: NSGA-II," *IEEE transactions on evolutionary computation*, vol. 6, pp. 182–197, 2002.

[5] Li, H., Zhang, Q., Multiobjective optimization problems with complicated Pareto sets, MOEA/D and NSGA-II, IEEE transactions on evolutionary computation, vol. 13, pp. 284–302, 2009.

[6] Zitzler, E., Künzli, S., Indicator-based selection in multiobjective search, International Conference on Parallel Problem Solving from Nature, 2004.

[7] Zitzler, E., Thiele, L. Bader, J., On set-based multiobjective optimization, IEEE Transactions on Evolutionary Computation, vol. 14, pp. 58–79, 2009.

[8] Zitzler, E., Thiele, L., Multiobjective optimization using evolutionary algorithms - a comparative case study, International conference on parallel problem solving from nature, 1998.

[9] Bosman, P. A. N. , Thierens, D., The balance between proximity and diversity in multiobjective evolutionary algorithms, IEEE transactions on evolutionary computation, vol. 7, pp. 174–188, 2003.

[10] Holland, J. H. et all., Adaptation in natural and artificial systems: an introductory analysis with applications to biology, control, and artificial intelligence, MIT press, 1975.

[11] Gaspar-Cunha, A., Takahashi, R., Antunes, C. H. Manual de computação evolutiva e metaheurística, Imprensa da Universidade de Coimbra/Coimbra University Press, 2012.

[12] Knowles, J., Corne, D., The pareto archived evolution strategy: A new baseline algorithm for pareto multiobjective optimisation, Congress on Evolutionary Computation (CEC99), 1999.

Janusz W. Sikora[1], Paweł Wysmulski[2], Jan Varga[3]

NEW CONCEPTS OF A SPECIAL SCREW FOR A NEW GENERATION EXTRUDER

Abstract: *The work presents various design concepts of a special screw, geometrically adapted to the constructionally changed rotary barrel element. Eight different design solutions of special screws were presented in the form of CAD models. Next, numerical calculations were carried out aiming at strength and heat analysis of selected models. Numerical calculations were conducted using the method of finished elements. As a calculating tool ABAQUS® program was used. The special screw was loaded with the torque, the pressure, the torgue and the pressure, as well as with the temperature. Calculations have shown that the proposed special screw designs are correct, under load they operate in a safe range of stresses, and their operation at a higher temperature is stable.*

Keywords: *special screw, CAD, MES, thermal and strength analysis*

1. CAD Models

The CAD models developed for the special screws are conceptual designs that describe the basic functionalities, geometrical features and dimensions of the screws adapted to the altered geometrical features of the newly designed barrels. In particular, these screws will be adapted to the geometrical features of the rotational barrel segment and will constitute a basic validation of its design. The conceptual designs presented below have been prepared using Solid Edge software; they allow to create physical models or early prototypes using techniques such as 3D printing.

The assumptions and requirements that must be met by the special screw are dictated by the geometrical features and dimensions of the screw that has been used in studies of extrusion of polyethylene filled with a nanofiller. These studies were conducted as part of the tasks completed in WP1. The geometrical features and dimensions of the screw used in the standard extruder are shown in Figure 1.

[1)] *Lublin University of Technology, Faculty of Mechanical Engineering, Department of Technology and Polymer Processing, ul. Nadbystrzycka 36, 20-618 Lublin, Poland, janusz.sikora@pollub.pl*

[2)] *Lublin University of Technology, Faculty of Mechanical Engineering, Department of Machine Design and Mechatronics, ul. Nadbystrzycka 36, 20-618 Lublin, Poland, p.wysmulski@pollub.pl*

[3)] *Technical University of Kosice, Faculty of Mechanical Engineering, Department of Engineering Technologies and Materials, Masiarska 74, 040 01 Kosice, Slovakia, jan.varga@tuke.sk*

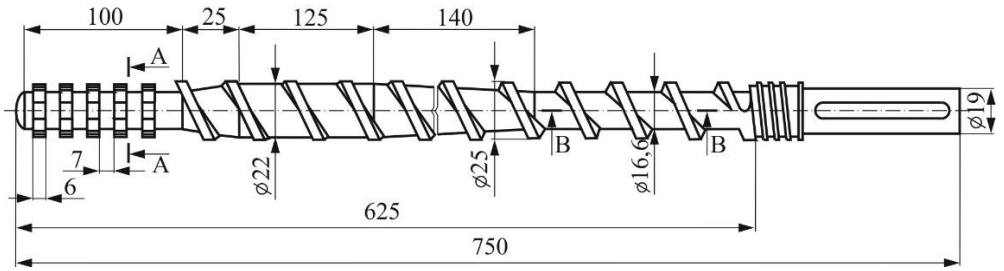

Fig. 1. Screw geometry used in the extrusion process

The description of each conceptual model will, therefore, begin with a short characterization of the geometry and dimensions of the screw, followed by a presentation of views of the screw. The metering section, containing five annular shear-mixing elements, will not be changed. Other elements that must remain unaltered include screw length, both total and (especially) working length, screw diameter, and the number of flights.

Eight different design solutions of special screws were presented in the form of CAD models. They are the result of brainstorming sessions held by the participants of the Newex project, as well as reflections and consultations with specialists in this area – engineers who design plasticizing systems, including screws.

1.1 Concept No 1

The design concept of the rotational barrel segment requires that the screw have a smooth, flightless section that will cooperate with the flights formed on the inner surface of the barrel segment. Concept no. 1 (Fig. 2) assumes that the working length of the screw is 625 mm and its total length is 750 mm. The screw is a single-flight

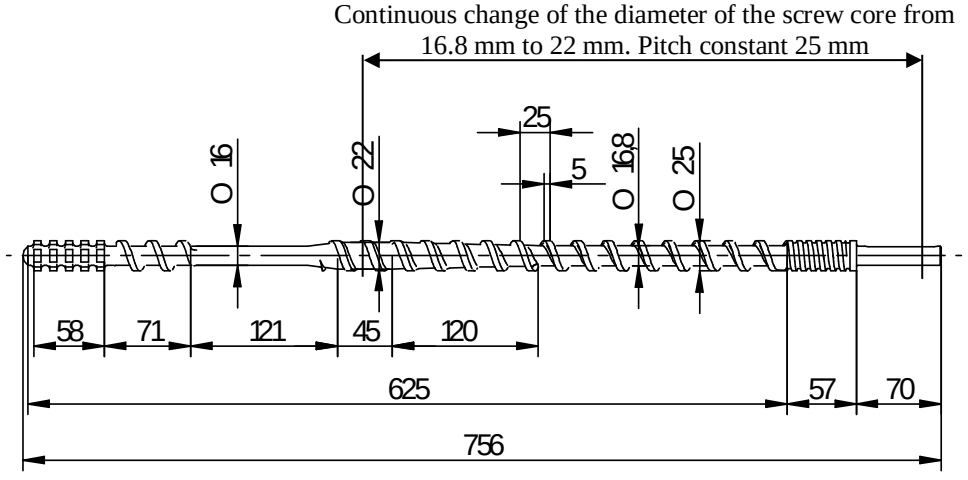

Fig. 2. Special screw and its basic dimensions – Concept No 1

screw; in the part in which the screw channel is continuous, screw diameter increases from 16.8 mm to 22 mm, but a constant pitch of 25 mm is maintained. Then, in the smooth part, the diameter of the screw decreases to 16 mm. In the final part of the screw, there are three screw flights extending over a length of 71 mm; the screw ends in 5 elements for intensive mixing and shearing. The compression ratio of the screw is 2.09. The compression ratio is calculated as the ratio of the volume of the screw channel at the beginning of the feeding zone to the volume of the screw channel upstream of the smooth part of the screw. Figure 2 gives the dimensions of the screw.

Figure 3 shows a Solid Edge 3D model of the screw.

Fig. 3. Conceptual model No 1 of the special screw

1.2. Concept No 2

In this concept, only the diameter of the smooth part of the screw is increased to 22 mm. The remaining geometric parameters are the same as in the special screw described in Concept No 1. The compression ratio of the screw is 2.09. Concept No 2 of the special screw and its dimensions are shown in Figure 4.

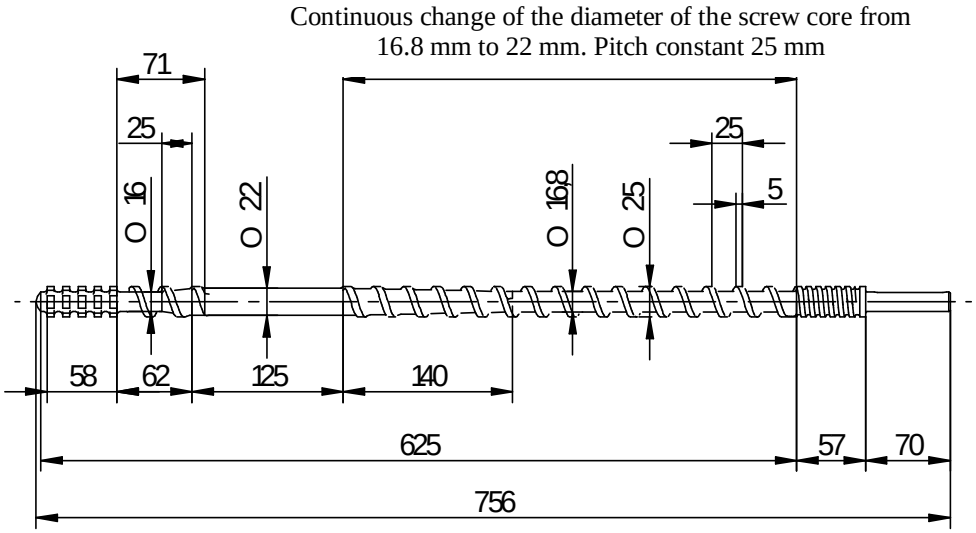

Fig. 4. Special screw and its basic dimensions – Concept 2

Figure 5 shows a Solid Edge 3D model of the screw.

Fig. 5. Conceptual model No 2 of the special screw

1.3. Concept No 3

Concept No 3 of the special screw has a modified geometry over a length of 165 mm upstream of the smooth screw section. The change consists in reducing the pitch of the screw from 25 mm to 11 mm, while maintaining a constant diameter of the screw core of 16.8 mm – in other words, only the width of the screw channel is reduced. This modification ensures a compression ratio of 2.27. A schematic of the screw proposed in Concept No 3 with basic dimensions marked in it is shown in Figure 6.

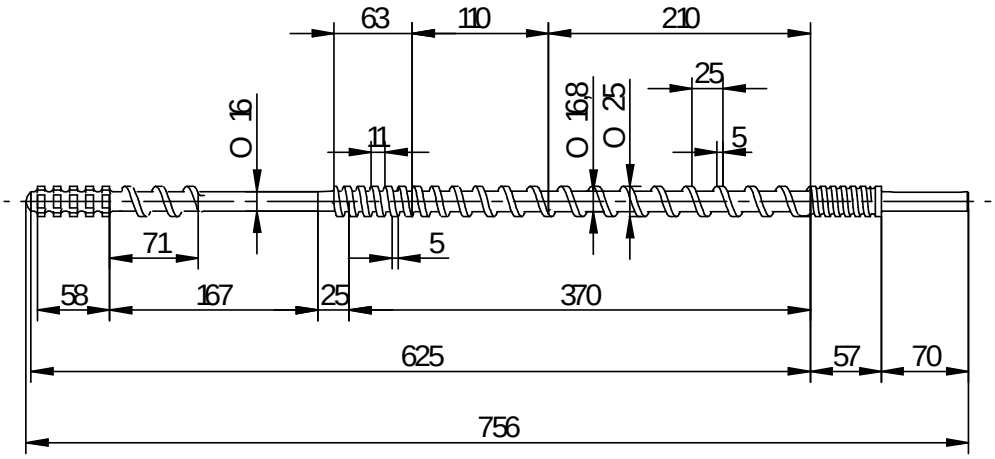

Fig. 6. Special screw and its basic dimensions – Concept 3

Figure 7 shows a Solid Edge 3D model of this screw.

Fig. 7. Conceptual model No 3 of the special screw

1.4. Concept No 4

Concept No 4 of the special screw has a modified geometry over a length of 165 mm upstream of the smooth section of the screw. The change consists in reducing the pitch of the screw from 25 mm to 15 mm, while also changing the diameter of the screw core from 22 mm to 20 mm; in other words, the depth of the channel is increased and its width is decreased. This design solution provides a compression ratio of 2.43. Concept No. 4 of the screw with its basic dimensions is shown in Figure 8.

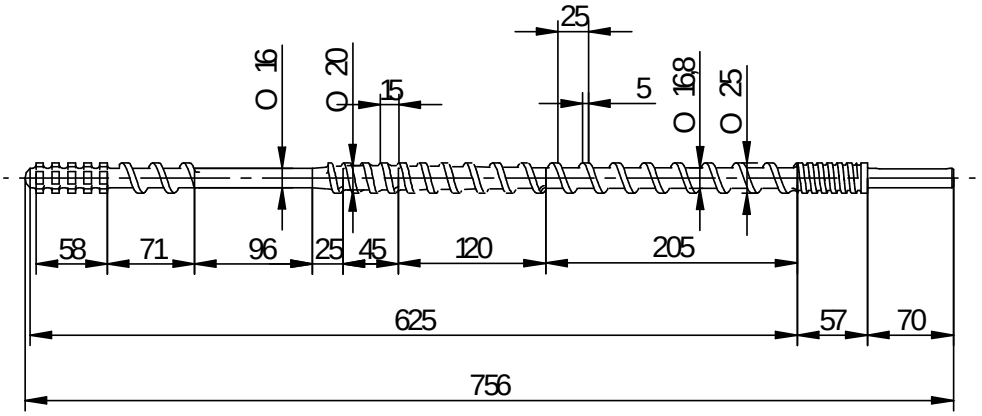

Fig. 8. Special screw and its basic dimensions – Concept 4

Figure 9 shows a Solid Edge 3D model of this screw.

Fig. 9. Conceptual model No 4 of the special screw

1.5. Concept No 5

Concept No 5 of the special screw has a modified geometry on a length before of the smooth section of the screw. The change consists in continous increase in screw diameter from 16.8 mm to 22 mm with unchanged 25 mm pitch of the screw flight. Therefore, only the depth of the screw channel is reduced. This design solution provides a compression ratio of 2.41. Concept No 5 of the screw with its basic dimensions is shown in Figure 10.

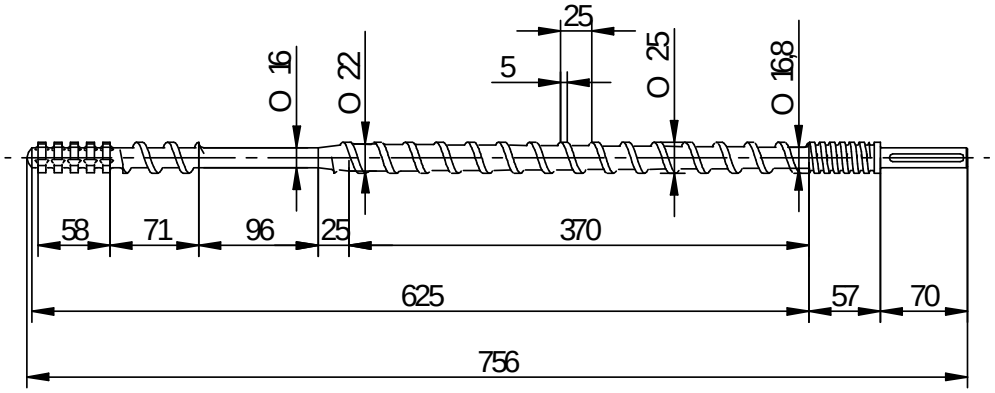

Fig. 10. Special screw and its basic dimensions - Concept 5

Figure 11 shows a Solid Edge 3D model of this screw.

Fig. 11. Conceptual model No 5 of the special screw

1.6. Concept No 6

In this concept, screw has a modified geometry along its length before the smooth section of the screw. The change consists in a continuous increase in the screw diameter from 15 mm to 22.2 mm and a continuous increase in the screw pitch from 23 mm to 26 mm. Thus, the depth of the screw channel decreases and at the same time its width is reduced. This ensures a compression ratio of 2.15. The screw according to the concept No 6, with the basic dimensions marked out, is shown in Figure 12.

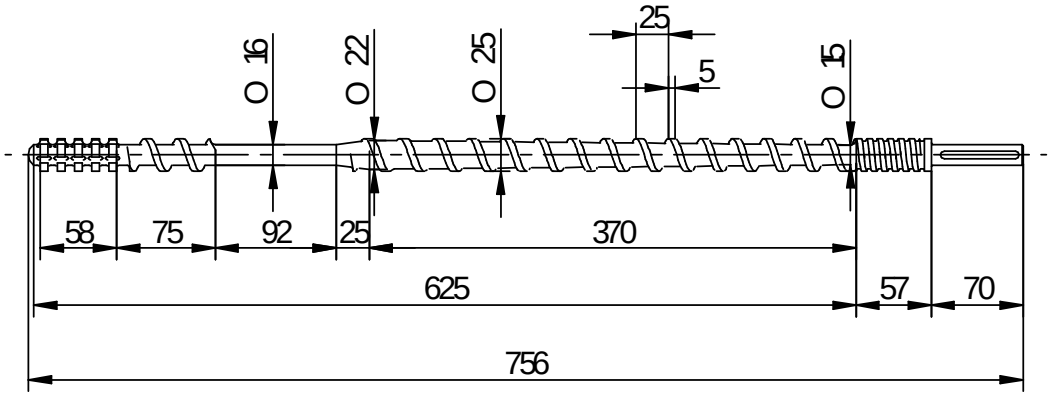

Fig. 12. Special screw and its basic dimensions – Concept 6

Figure 13 shows a Solid Edge 3D model of this screw.

Fig. 13. Conceptual model No 6 of the special screw

1.7. Concept No 7

The concept No 7 of a special screw is characterized by an increased diameter of the smooth section of the screw up to 19 mm. The other geometrical elements are immutable (compared to the screw concept no 1). This ensures a compression ratio of 2.09.

The screw according to concept No 7, with the basic dimensions marked out, is presented in Figure 14.

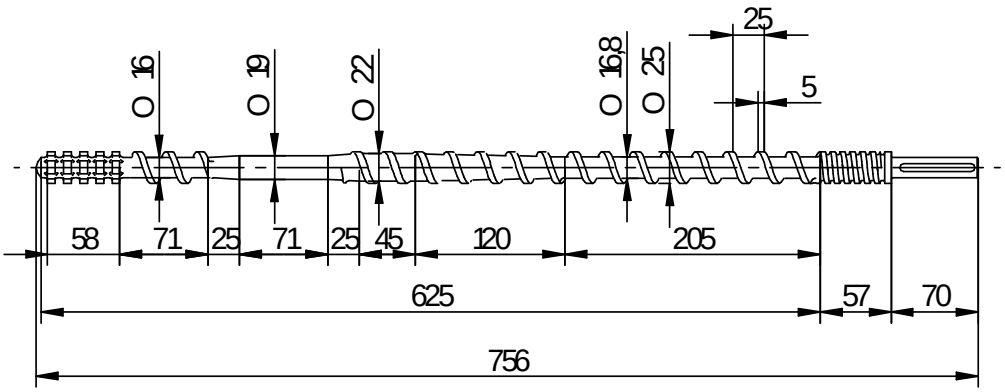

Fig. 14. Special screw and its basic dimensions – Concept 7

Figure 15 shows a Solid Edge 3D model of this screw.

Fig. 15. Conceptual model No 7 of the special screw

1.8. Concept No 8

According to this concept, the screw has the first two pitch unchanged, then the width of the flight is reduced from 5 mm to 3 mm, while the 25 mm screw pitch is maintained, then 165 mm is followed by a continuous change of the screw diameter from 16.8 mm to 20 mm and change screw pitch from 25 mm to 15 mm. The other part of the screw is immutable in geometric terms, i.e. such as in screw 4 and 1. This provides a compression ratio of 2.29.

Concept No. 8 of the screw with its basic dimensions is shown in Figure 16.

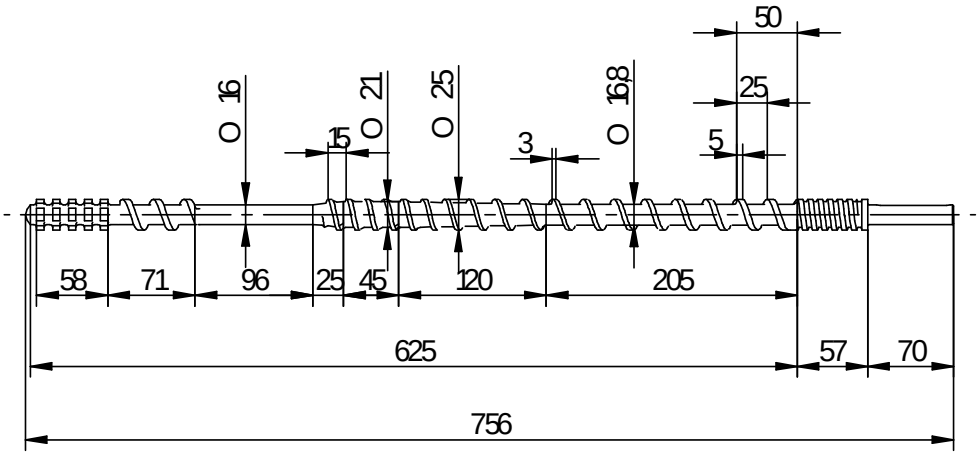

Fig. 16. Special screw and its basic dimensions – Concept 8

Figure 17 shows a Solid Edge 3D model of this screw.

Fig. 17. Conceptual model No 8 of the special screw

2. Objective and scope of numerical calculations

The aim of the conducted numerical calculations was to analyse the strength of the new constructions of the special screws of a new single-screw extruder, constructionally matched with the changes introduced in the barrel, mainly in the rotational barrel segment. The numerical simulation was made on the basis of assembling of the construction elements made in SolidEdge programme, a method of finished elements ABAQUS® implemented to the programme. Three constructional solutions of special screws were analysed, which were chosen during the discussion among the members of the research team and consultation with specialists in the field. The analysed models of the screws were characterised with the diameter Ø25 mm, the smallest core diameter 16 mm and the total working length 755 mm. General geometrical models of special screws accepted for numerical calculations of the analysed constructions are presented in Figure 2, Figure 4 and Figure 6. In Figures 3, 5 and 7 the enlarged screw is shown in order to focus on the constructional details. The geometrical features of each model were presented in a previous paragraph.

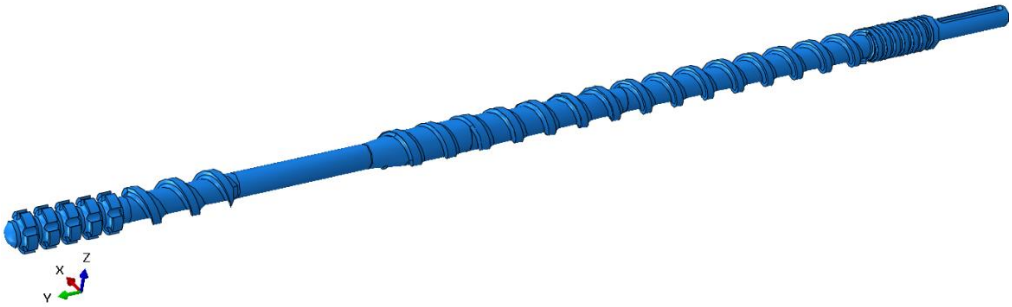

Fig. 18. A special screw model with increasing diameter before RBS – variant 1 (concept no 1 – Fig. 2)

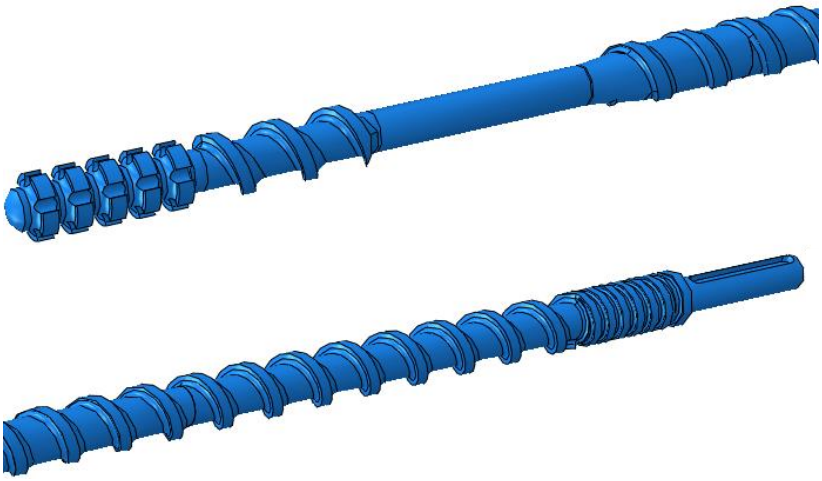

Fig. 19. Enlargement of the special screw with increasing diameter before RBS, with visible constructional details

Fig. 20. A special screw model with increasing diameter and decreasing pitch before RBS – variant 2 (concept no 4 – Fig. 9)

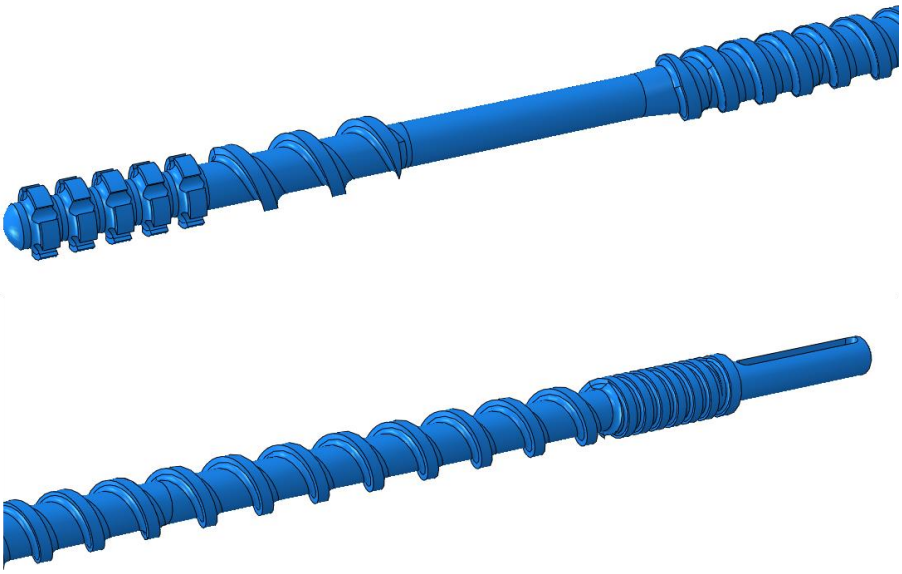

Fig. 21. Enlargement of the special screw with increasing diameter and decreasing pitch before RBS, with visible constructional details

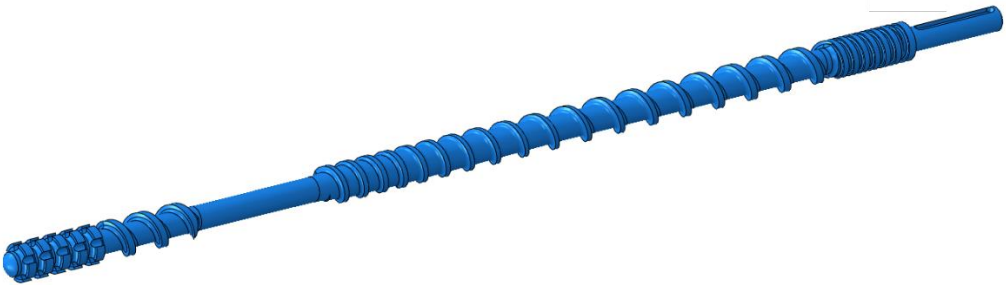

Fig. 22. Model of a special screw – variant 3 (concept no 8 – Fig. 17)

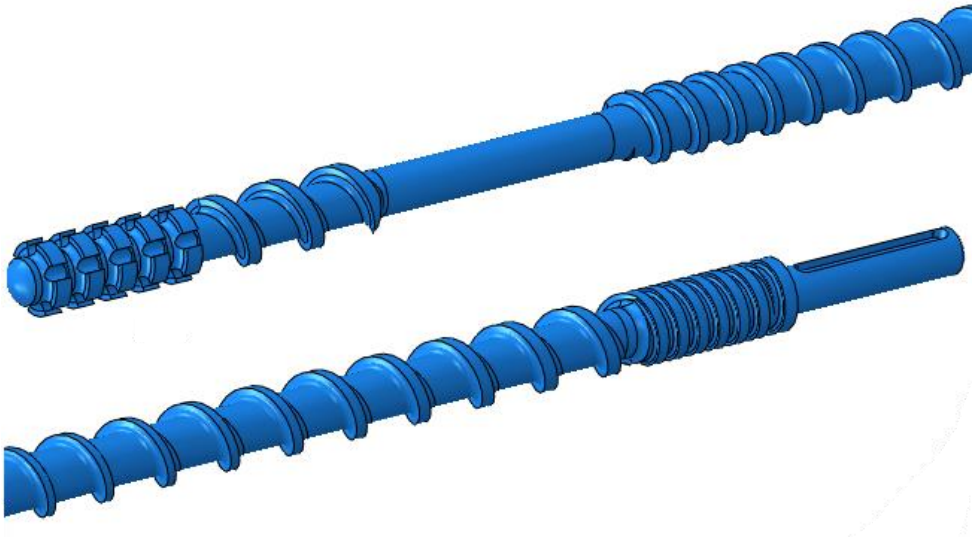

Fig. 23. Enlargement of the special screw decrease of width flight, increase diameter of the screw and decrease pitch of the screw with visible constructional details

The range of the conducted numerical analyses included calculations concerning the estimation of the strength of special screws exposed to the pressure caused by the transfer of polymer, torque from the screw drive as well as thermal calculations enabling to receive the temperature distribution on the surface of the extruder screw because of polymer friction against the inner surfaces of the screw and heating the screw from the external side. Within the numerical calculations, the following tasks were carried out:

– developing discrete models enabling the numerical analysis using the method of finished elements,
– determining material models and limiting cases of loading the construction,
– conducting numerical simulations enabling to determine the distribution of reduced stress and nodal displacement of construction,
– evaluation of stiffness and strength of construction on the basis of the received results of numerical analysis,
– estimation of temperature distribution in the elements of construction during the exploitation of the extruder screw,
– conclusions of the conducted numerical analysis, presenting the evaluation of the proposed constructional solutions.

2.1. Discretization of construction

Numerical calculations were conducted using the method of finished elements. As a calculating tool ABAQUS® programme was used. The construction of discrete

models was made on the basis of the developed geometrical models of analysed constructions, presented in the previous point.

The discretization of a geometrical model was made using tetragonal solid elements, type C3D4T, which constitute 4-nodal elements with the shape function of the first order and full integration to enable to take into account in a numerical analysis a thermal degree of freedom. In all variants it was accepted that elements of construction – special screws of the extruder - are made of steel marked 40HM.

In strength calculations, a bilinear model of material was accepted, of elastic-plastic characteristics, for which the following material properties were accepted (Table 1):

Table 1. *Mechanical properties of steel 40HM*

Material property – steel 40HM	
Young modulus E [MPa]	$2.1 \cdot 10^5$
Poisson number [-]	0.3
Yield strength R_e [MPa]	$8.8 \cdot 10^2$
Strength limit R_m [MPa]	$1.03 \cdot 10^3$
Elongation at break [%]	10

In thermal calculations, a bilinear model of material was accepted, of elastic-plastic characteristics, for which the following thermal properties were accepted (Table 2):

Table 2. *Material properties for thermal calculations*

Material property – steel 40HM	
Density ρ [kg/m^3]	7860
Linear expansion coefficient [1/K]	$1.2 \cdot 10^{-5}$
Heat conduction coefficient λ [W/(m·K)]	58
Specific heat [J/(kg·K)	450

A discrete model of the special screw developed for variant 1 is presented in Figure 24.

Fig. 24. Discrete model of the special screw – variant 1

A discrete model of the special screw developed for variant 2 is presented in Figure 25.

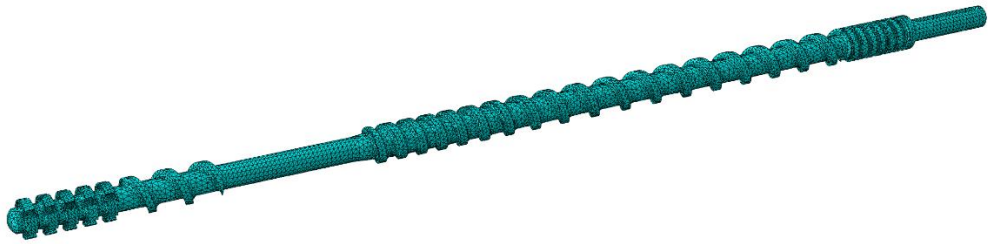

Fig. 25. Discrete model of the special screw – variant 2

A discrete model of the special screw developed for variant 3 is presented in Figure 26.

Fig. 26. Discrete model of the special screw – variant 3

2.2. Boundary conditions and loading of construction

The numerical analysis of the adopted special extruder screws were carried out for four loading cases:

– case I: the screw loaded with the torque M_c = 200 Nm;
– case II: the screw loaded with the pressure p_{max} = 25MPa;
– case III: the screw loaded with the torque Mc = 200Nm and the pressure p_{max} = 25MPa;

- case IV: the screw heated to the temperature t_{max} = 190°C paralelly loaded with the torque Mc = 200Nm and the pressure p_{max} = 25MPa.

a) Boundary conditions and loading of construction – case I

The definition of boundary conditions in a numerical model for case I of calculations was carried out by fixing nodes placed on the surfaces of mounting the special screw (Fig. 27), blocking the possibility of their displacement (translational degrees of freedom of nodes placed on these surfaces) in three directions X, Y and Z. The torque Mc = 200 Nm was applied to the drive shaft of the screw. Exemplary boundary conditions and the loading of the special screw for selected variants 1, 2 and 3 are presented in Figures 27, 28 and 29.

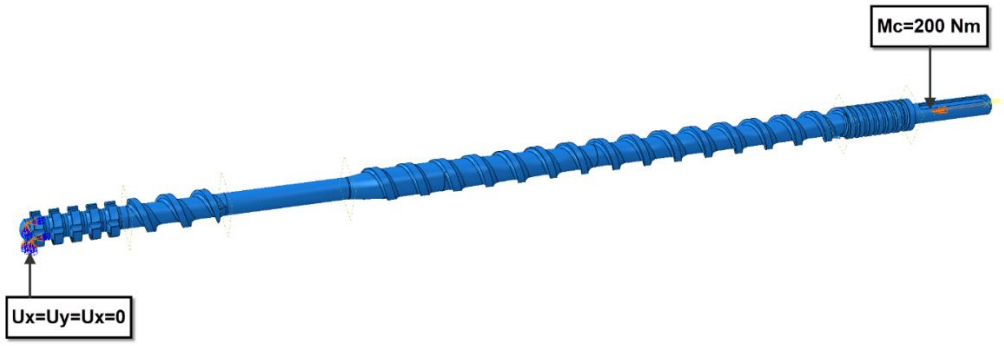

Fig. 27. Boundary conditions and loading of numerical model of the special screw - variant I

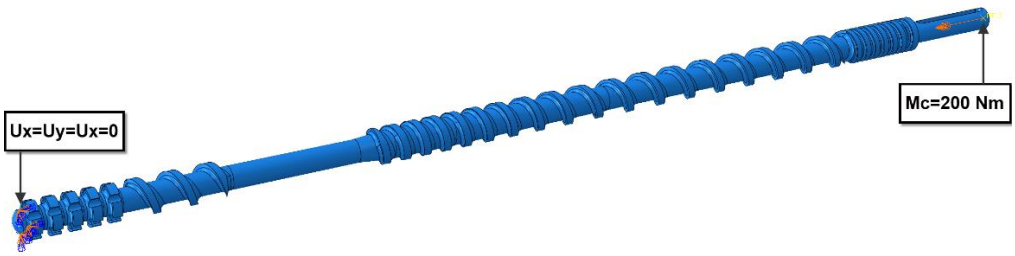

Fig. 28. Boundary conditions and loading of numerical model of the special screw – variant II

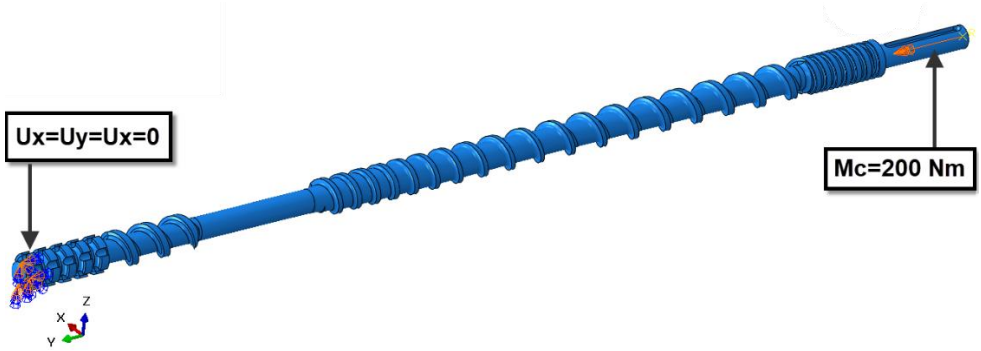

Fig. 29. Boundary conditions and loading of numerical model of the special screw – variant III

b) Boundary conditions and loading of construction – case II

The definition of boundary conditions in a numerical model for case II of calculations was carried out by fixing nodes placed on the surfaces of mounting the special screw (Fig. 30), blocking the possibility of their displacement (translational degrees of freedom of nodes placed on these surfaces) in three directions X, Y and Z. The pressure resulting from the pressures exerted by the transported material was applied by means of mathematical functions reaching the maximum pressure p_{max} = 25 MPa in the area of the largest diameter of the screw core. Exemplary boundary conditions and the loading of the special screw for selected variants 1, 2 and 3 are presented in Figures 30, 31 and 32.

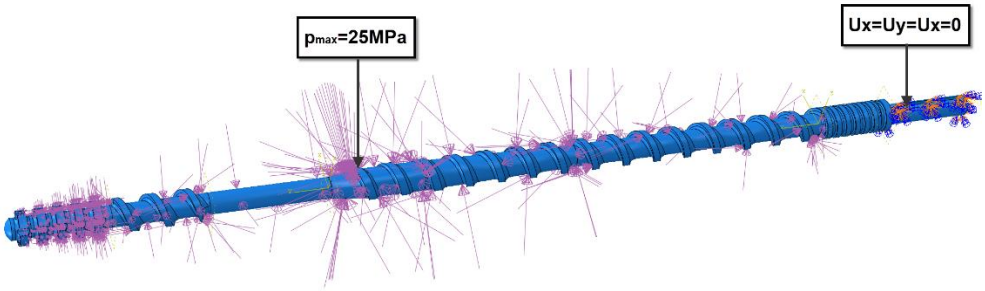

Fig. 30. Boundary conditions and loading of numerical model of the special screw – variant I

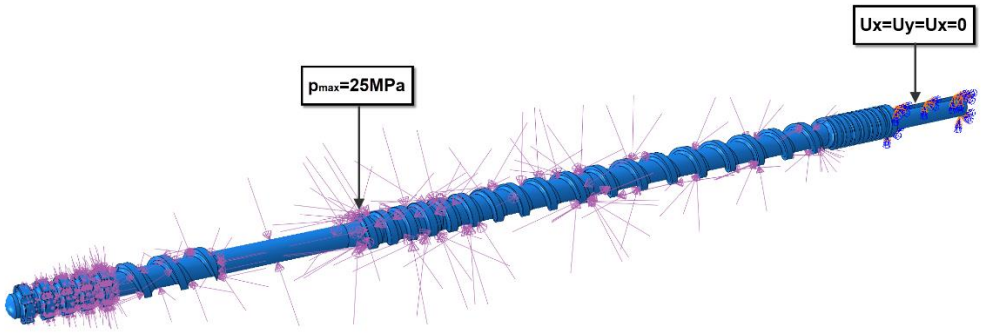

Fig. 31. Boundary conditions and loading of numerical model of the special screw – variant II

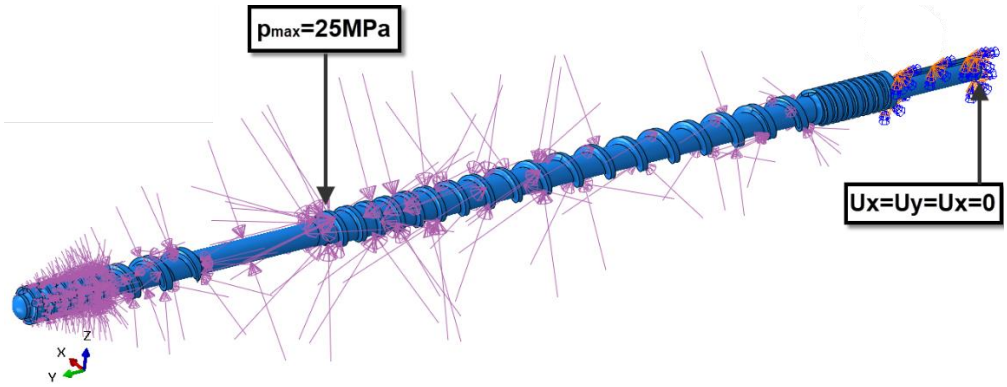

Fig. 32. Boundary conditions and loading of numerical model of the special screw – variant III

c) Boundary conditions and loading of construction – case III

The definition of boundary conditions in a numerical model for case III of calculations was carried out by fixing nodes placed on the surfaces of mounting the special screw (Fig. 33), blocking the possibility of their displacement (translational degrees of freedom of nodes placed on these surfaces) in three directions X, Y and Z. The torque Mc = 200 Nm was applied to the drive shaft of the screw. The pressure resulting from the pressures exerted by the transported material was applied by means of mathematical functions reaching the maximum pressure p_{max} = 25 MPa in the area of the largest diameter of the screw core. Exemplary boundary conditions and the loading of the special screw for selected variants 1, 2 and 3 are presented in Figures 33, 34 and 35.

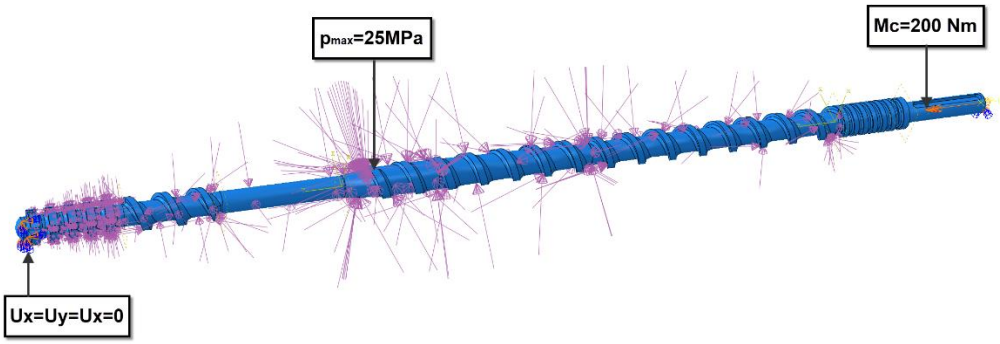

Fig. 33. Boundary conditions and loading of numerical model of the special screw – variant I

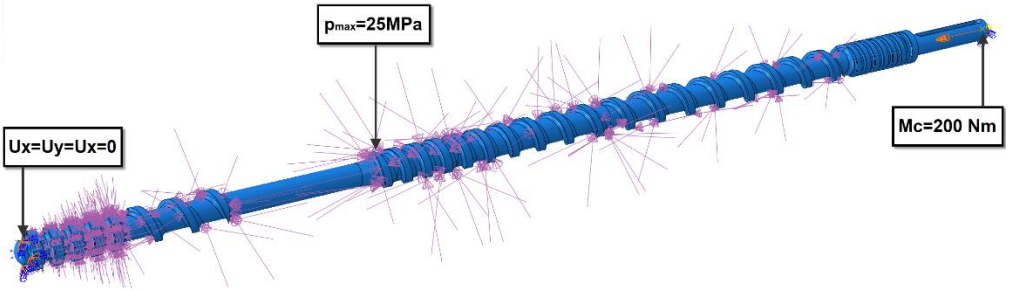

Fig. 34. Boundary conditions and loading of numerical model of the special screw – variant II

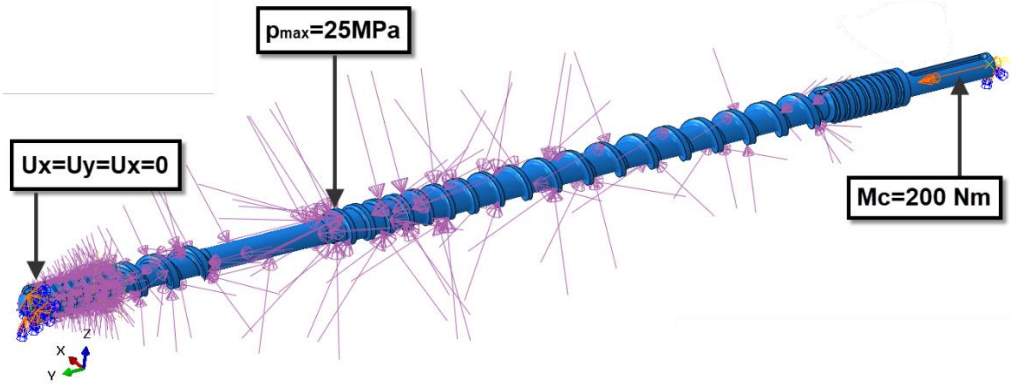

Fig. 35. Boundary conditions and loading of numerical model of the special screw – variant III

d) Boundary conditions and loading of construction – case IV

The definition of boundary conditions in a numerical model for case IV of calculations was carried out by fixing nodes placed on the surfaces of mounting the special screw (Fig. 33), blocking the possibility of their displacement (translational degrees of freedom of nodes placed on these surfaces) in three directions X, Y and Z. The torque Mc = 200 Nm was applied to the drive shaft of the screw. The pressure resulting from the pressures exerted by the transported material was applied by means of mathematical functions reaching the maximum pressure p_{max} = 25 MPa in the area of the largest diameter of the screw core. Additionally, the screw was heated by means of a defined mathematical function in order to reflect the physical behaviour of the screw during the polymer extrusion process, the maximum value of the temperature of the screw was accepted T ≈ 190°C (Fig. 36). The initial temperature of the numerical model was accepted as T_0 = 22°C. Exemplary boundary conditions and the loading of the special screw for selected variants 1, 2 and 3 are presented in Figures 36, 37 and 38.

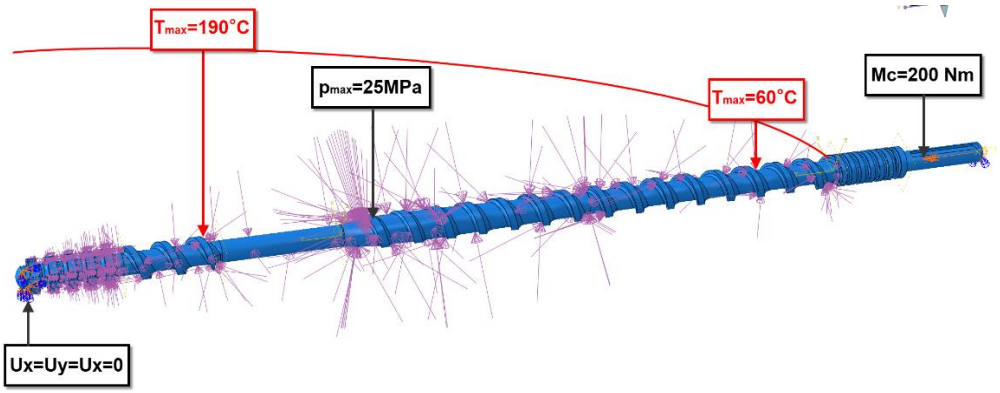

Fig. 36. Boundary conditions and loading of numerical model of the special screw – variant 1

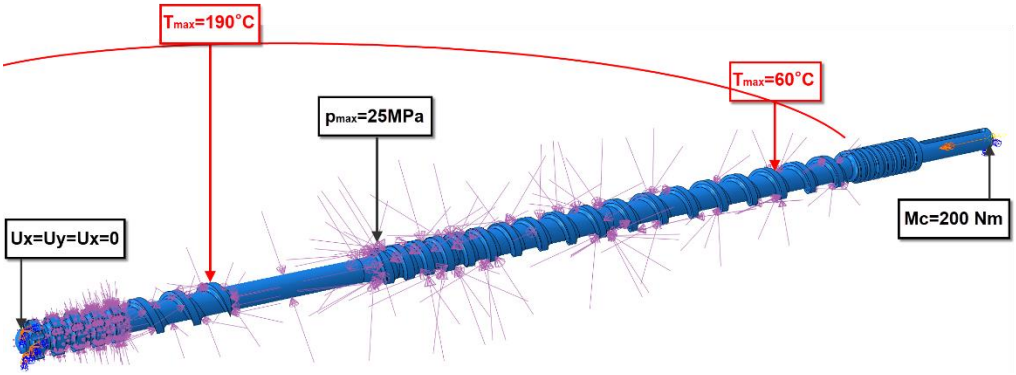

Fig. 37. Boundary conditions and loading of numerical model of the special screw – variant 2

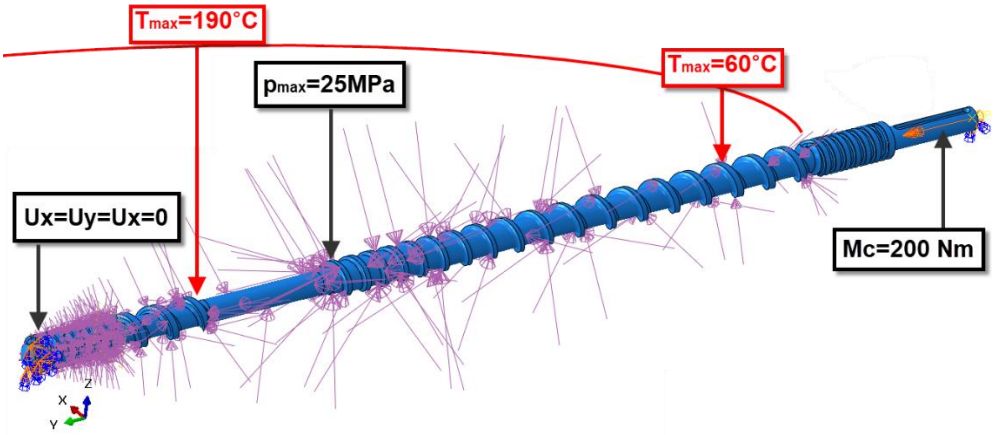

Fig. 38. Boundary conditions and loading of numerical model of the special screw – variant 3

3. Results of numerical calculations

A numerical analysis of the construction of the special screw was conducted in the range of static calculations, taking into account a geometrically non-linear issue (big displacement and deflection). In order to solve a non-linear system of equations, Newton-Raphson increment-iterative method was used. A strength and stiffness analysis of particular construction elements was conducted on the basis of the distributions of reduced tension, determined in accordance with Huber-Mises-Hencky strength hypothysis in the area of analysed construction and displacement of nodes of its particular elements. The accepted hypothesis is the basic hypothysis used in engineering calculations in relation to elements made of materials of isotropic properties. In thermal calculations, the temperature distribution was determined in the area of analysed constructions, in the state corresponding to 18 000s (5 hours) of constant operation of the special screw.

Distributions of tension, displacements and temperature are presented in the form of colourful contour maps against the background of the deflected model, in which the red colour indicates maximum values, while the blue colour minimum values.

3.1. Variant 1 of the construction of the special screw

a) Strength calculations

As a result of numerical calculations, total reduced tension in the construction of the special screw was determined. The results in the form of the map of reduced tension are shown in Figures from 39 to 41. The presented values of tension are expressed in MPa.

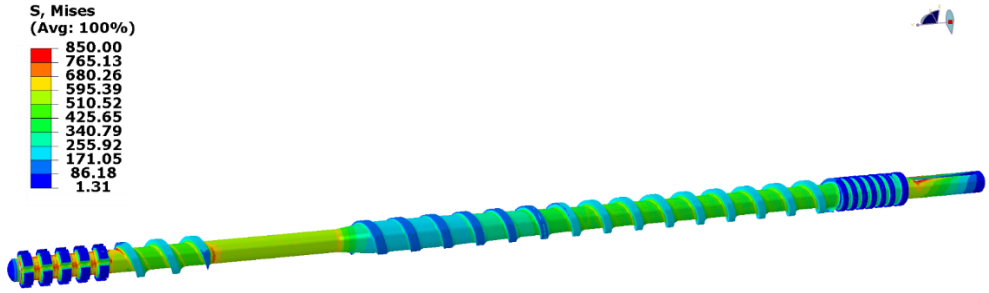

Fig. 39. *Distribution of reduced tension H-M-H in the special screw under total torque load* – case I

The presented maps of reduced tension for the particular states of loading enable to estimate the influence of the given loading on the degree of tension of the material construction. From Figure 39 it turns out that reduced tension resulting only from the torque of the drive shaft of the special screw equalling Mc = 200000 Nmm approach the yield strength of the studied material $\sigma_z \approx 850$ MPa. The analysis of the case when only pressure of $p_{max} = 25$ MPa is applied to the surface of the screw showed the

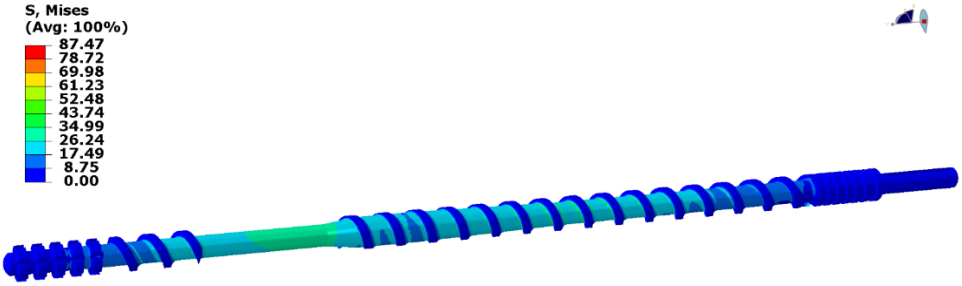

Fig. 40. *Distribution of reduced tension H-M-H in the special screw under total torque load* – case II

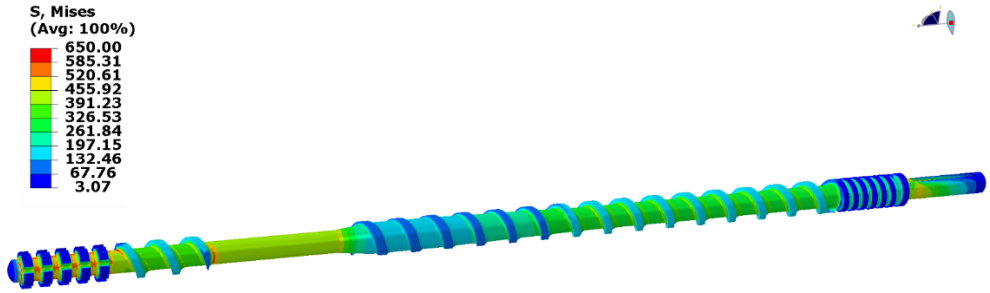

Fig. 41. *Distribution of reduced tension H-M-H in the special screw under total torque load* – case III

generation of tension of about $\sigma_z \approx 87{,}47$ MPa - Figure 40. Case III consisted in taking into account the loading of the screw with the torque Mc = 200000 Nmm and pressure of pmax = 25 MPa applied to the screw. In this case of loading (case III) the value of tension reaches $\sigma_z \approx 650$ MPa (Fig. 41). A decisive drop in tension is caused by the operation of the screw with regard to loading the screw only with pressure.

b) Thermal calculations

The next stage of the analysis was connected with calculations including the thermal analysis of the special screw. Initially, the screw was heated to the room temperature $T_0 = 22°C$. Case IV of the screw load was extended with parameters corresponding to the continuous operation of this element in time t = 18000s (5 hours) in temperature $T \approx 190°C$ - Figure 42.

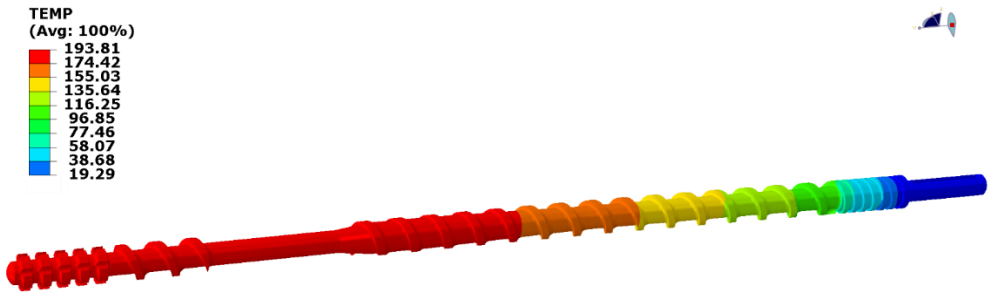

Fig. 42. Temperature distribution in the model of the special screw – variant 1

The maximum reduced tension in the special screw model is in this case at the level of $\sigma_z \approx 879{,}33$ MPa. The areas in which maximum tension is generated are marked in red, they occur in this part of the screw in which the drive was applied and in the final part of the extruder screw - Figure 43. The value of the received pressure is high but does not exceed the yield point value, which, in accordance with the accepted material properties for steel 40HM, equals $R_e = 880$ MPa. It means that the level of reduced tension occurring in the construction for the considered case of loading (loading with torque, with pressure of exponential distribution at the length of the model and with temperature of exponential distribution at the length of the screw) does not threaten the safe operation of the developed construction of the special screw.

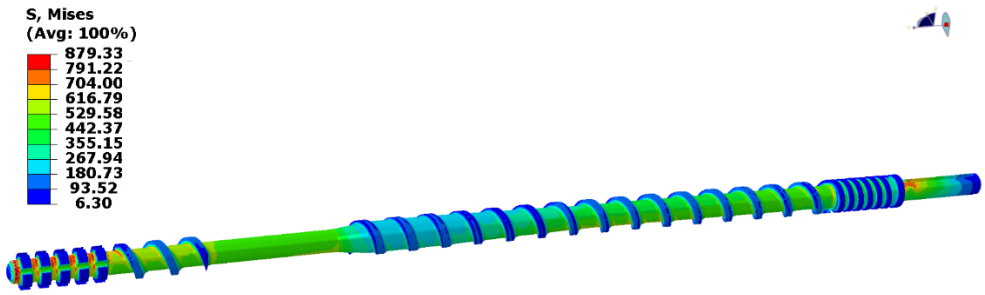

Fig. 43. Strength analysis including thermal parameters of the special screw – variant 1

3.2. Variant 2 of the construction of the special screw

a) Strength calculations

As a result of numerical calculations, total reduced tension in the construction of the special screw was determined. The results in the form of the map of reduced tension are shown in Figures from 44 to 46. The presented values of tension are expressed in [MPa].

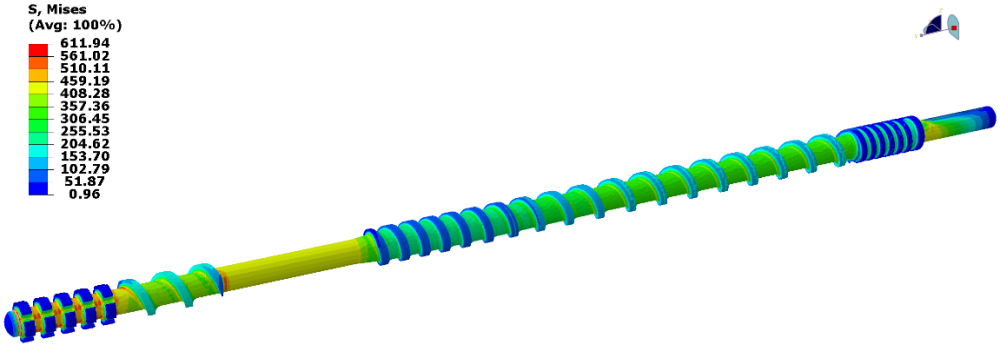

Fig. 44. Distribution of reduced tension H-M-H in the special screw under total torque load – case I

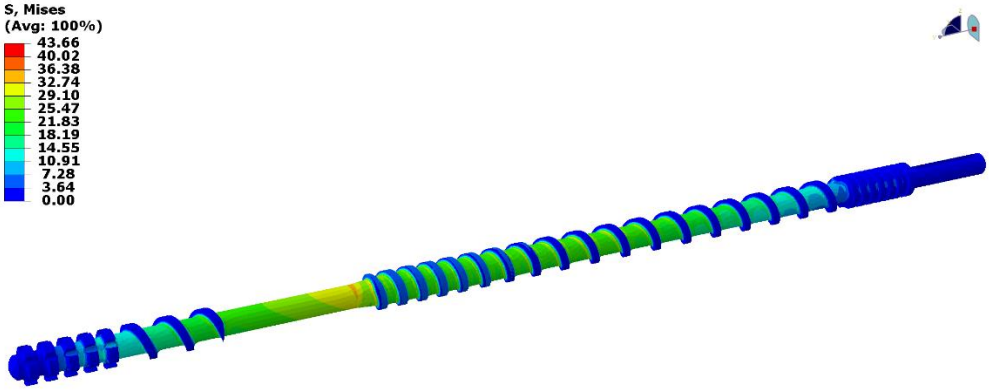

Fig. 45. Distribution of reduced tension H-M-H in the special screw under total torque load – case II

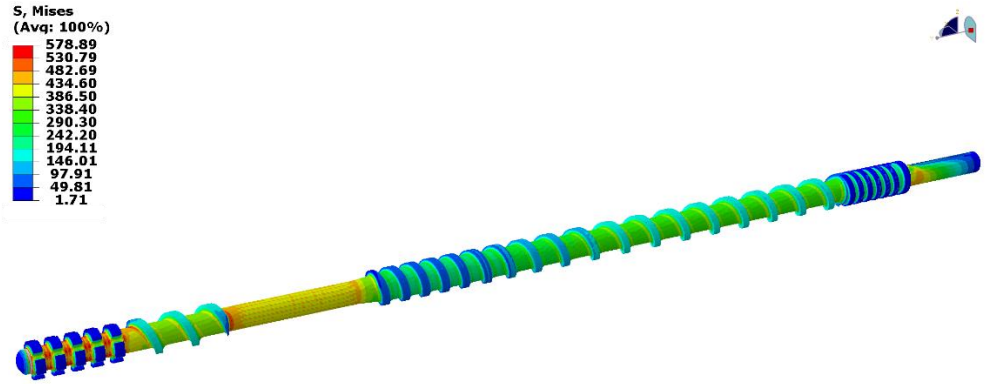

Fig. 46. Distribution of reduced tension H-M-H in the special screw under total torque load – case III

From Figure 44 it turns out that reduced tension resulting only from the torque of the drive shaft of the special screw equalling Mc = 200000 Nmm approach the yield strength of the studied material $\sigma_z \approx$ 611,94 MPa. The analysis of the case when only pressure of pmax = 25 MPa is applied to the surface of the screw showed the generation of tension of about $\sigma_z \approx$ 43,667 MPa – Figure 45. Case III consisted in taking into account the loading of the screw with the torque Mc = 200000 Nmm and pressure of pmax = 25 MPa applied to the screw. In this case of loading (case III) the value of tension reaches $\sigma_z \approx$ 578,89 MPa (Fig. 46). A decisive drop in tension is caused by the operation of the screw with regard to loading the screw only with pressure.

b) Thermal calculations

The next stage of the analysis was connected with calculations including the thermal analysis of the special screw. Initially, the screw was heated to the room

temperature T_0 = 22°C. Case IV of the screw load was extended with parameters corresponding to the continuous operation of this element in time t = 18000s (5 hours) in temperature T ≈ 190°C – Figure 47.

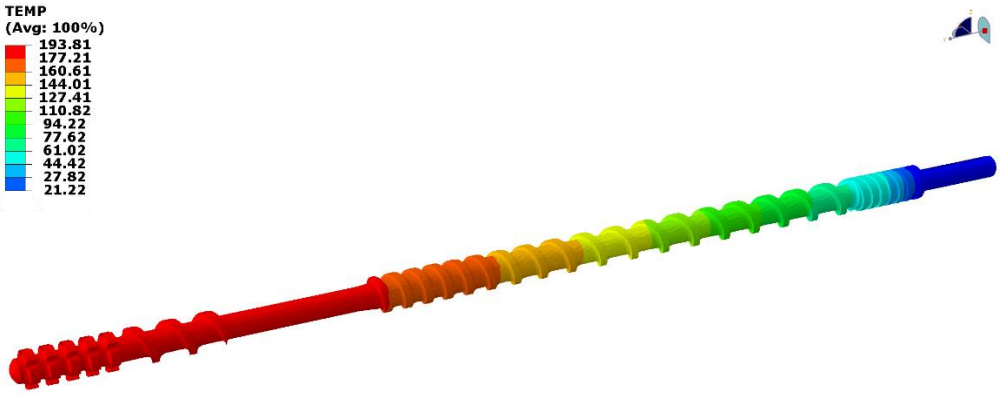

Fig. 47. Temperature distribution in the model of the special screw – variant 2

The maximum reduced tension in the special screw model is in this case at the level of $\sigma_z \approx 875{,}12$ MPa. The areas in which maximum tension is generated are marked in red, they occur in this part of the screw in which the drive was applied and in the final part of the extruder screw – Figure 48. The value of the received pressure is high but does not exceed the yield point value, which, in accordance with the accepted material properties for steel 40HM, equals R_e = 880 MPa. It means that the level of reduced tension occurring in the construction for the considered case of loading (loading with torque, with pressure of exponential distribution at the length of the model and with temperature of exponential distribution at the length of the screw) does not threaten the safe operation of the developed construction of the special screw.

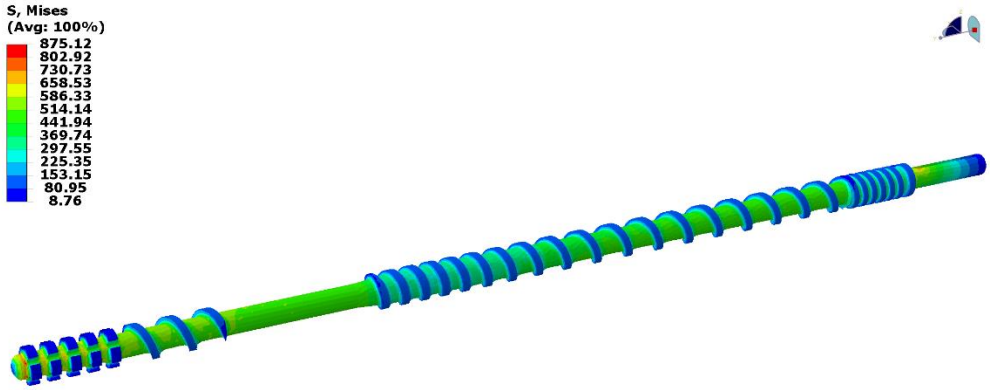

Fig. 48. Strength analysis including thermal parameters of the special screw – variant 2

3.3. Variant 3 of the construction of the special screw

a) Strength calculations

As a result of numerical calculations, total reduced tension in the construction of the special screw was determined. The results in the form of the map of reduced tension are shown in Figures from 49 to 51. The presented values of tension are expressed in [MPa].

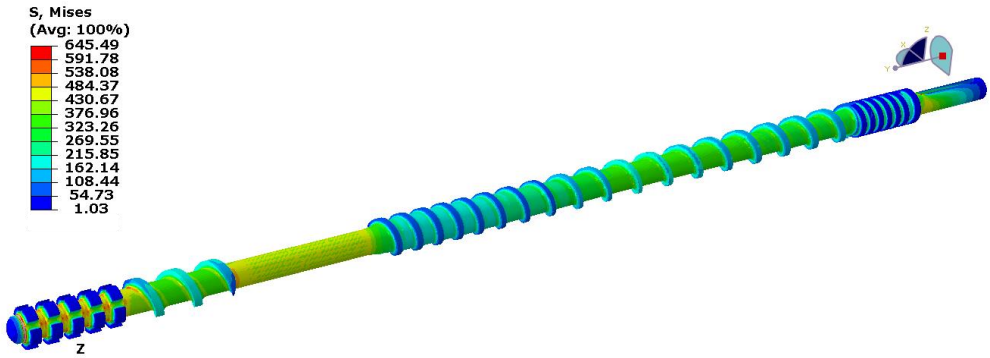

Fig. 49. Distribution of reduced tension H-M-H in the special screw under total torque load – case I

From Figure 49 it turns out that reduced tension ($\sigma_z \approx 645{,}49$MPa) resulting only from the torque of the drive shaft of the special screw equalling Mc = 200000 Nmm are safe and does not threaten the safe operation of the developed construction of the special screw. The analysis of the case when only pressure of pmax = 25 MPa is applied to the surface of the screw showed the generation of tension of about $\sigma_z \approx 46{,}26$ MPa – Figure 50. Case III consisted in taking into account the loading of the screw with

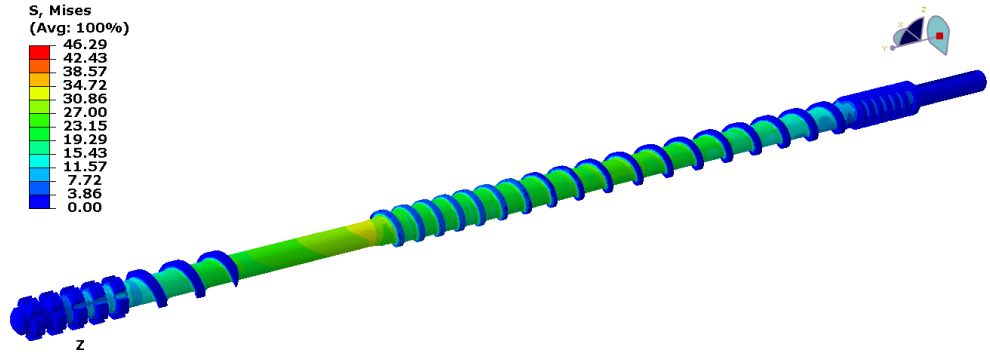

Fig. 50. Distribution of reduced tension H-M-H in the special screw under total torque load – case II

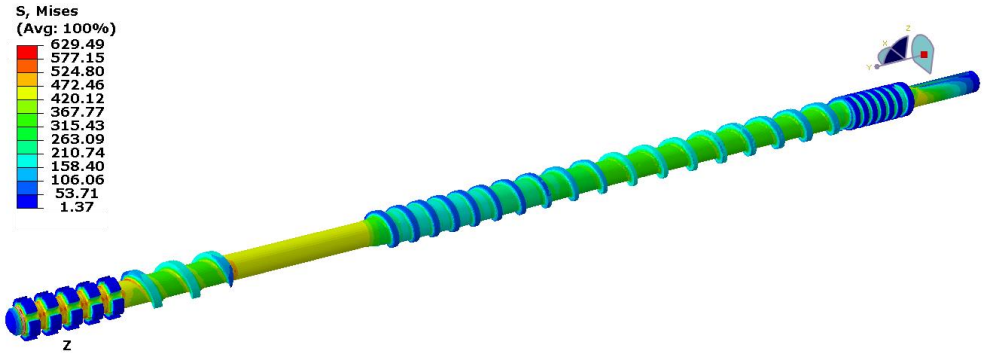

Fig. 51. Distribution of reduced tension H-M-H in the special screw under total torque load – case III

the torque Mc = 200000 Nmm and pressure of pmax = 25 MPa applied to the screw. In this case of loading (case III) the value of tension reaches $\sigma_z \approx$ 629,49 MPa (Fig. 51). A decisive drop in tension is caused by the operation of the screw with regard to loading the screw only with pressure.

b) Thermal calculations

The next stage of the analysis was connected with calculations including the thermal analysis of the special screw. Initially, the screw was heated to the room temperature T_0 = 22°C. Case IV of the screw load was extended with parameters corresponding to the continuous operation of this element in time t = 18000s (5 hours) in temperature T ≈ 190°C – Figure 52.

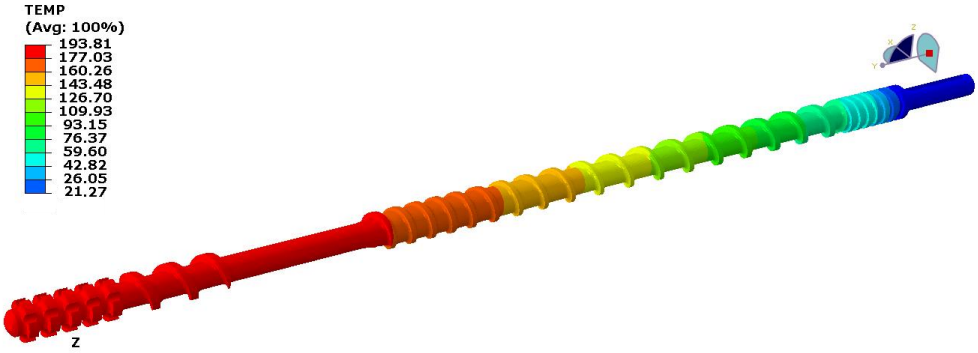

Fig. 52. Temperature distribution in the model of the special screw – variant 3

The maximum reduced tension in the special screw model is in this case at the level of $\sigma_z \approx$ 878,42 MPa. The areas in which maximum tension is generated are marked in red, they occur in this part of the screw in which the drive was applied and in the final

part of the extruder screw – Figure 53. The value of the received pressure is high but does not exceed the yield point value, which, in accordance with the accepted material properties for steel 40HM, equals R_e = 880 MPa. It means that the level of reduced tension occurring in the construction for the considered case of loading (loading with torque, with pressure of exponential distribution at the length of the model and with temperature of exponential distribution at the length of the screw) does not threaten the safe operation of the developed construction of the special screw.

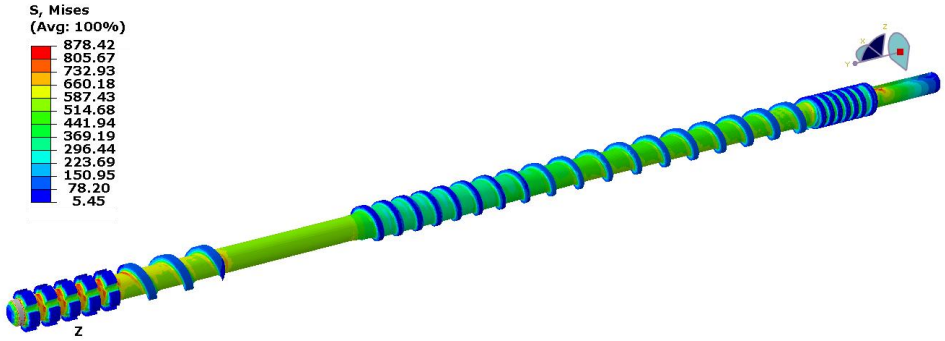

Fig. 53. Strength analysis including thermal parameters of the special screw – variant 3

6. Conclusion

The conducted numerical analysis using the method of finished elements enables to formulate conclusions concerning the strength and thermal estimation of the analysed variants of the special screw of the new extruder. On the basis of the received results of numerical calculations it was stated that the designed models of the special screws (variant 1, variant 2 and variant 3) under total load (with torque, pressure and temperature of the defined values) operate within a safe range. This is confirmed by the tension values in the elements of construction which do not exceed the value of the yield point R_e = 880 MPa for the accepted steel 40HM. Moreover, the received temperature distributions in the area of the screw, corresponding to the state of 5 hours of the continuous operation of the construction, confirm the stable work of the screws in temperature T = 190^{o}C in the whole area of an element. It means that the accepted construction of all models of the special screws of the extruder is designed correctly – it is sufficiently strong and can operate correctly under the required load.

It is worth paying attention to variant 1 of the special screw, whose construction enables more stable thermal operation.

Acknowledgements

This Project has received funding from the Union's Horizon 2020 research and innovation programme under the Marie Skłodowska-Curie grant agreement No 734205-H2020-MSCA-RISE-2016.

Oleh Suberlyak[1], Volodymyr Krasinskyi[1], Victoria Zemke[1], Natalia Chopyk[1]

IMPACT OF POLYOLEFIN RATIO ON THE PROCESSABILITY OF RAW MATERIAL IN EXTRUSION PROCESSES

***Abstract**: A comparative analysis of the influence of blends composition based on the different polyethylenes, as well as polypropylene on the rheological and technological properties has been carried out. It was proposed the optimal composition of polyethylenes blend which possess sufficient technological ability to be processed by the extrusion. The technological and physical-mechanical properties of extrusion raw materials for pipes production on the basis of blends of different polyethylene brands are investigated.*

***Keywords**: polyolefins, melt flow index, tensile curves, extrusion, a blend of polymers, rheological properties.*

1. Introduction

Composition compound is the most important factor of effect on the processability of production process and quality of polymer pipes. The complex of physical and chemical properties of polyolefins makes it possible to be widely used for being processed into consumer products of many industrial fields.

The most common of these are the injection molding and extrusion. The necessary condition for the technological process of extrusion is the ability of polyolefins under certain conditions of processing to obtain products with stable parameters.

The domestic branch of polyethylene pipes production works exclusively on imported raw materials which affects the quality and production cost. Volumes of imported polyethylene for the pipe production are formed by the activity of the domestic construction market. We usually get raw materials from Europe, Russian Federation and the Asian region.

The largest share is made up of polyethylene from European producers, accounting for 58% of the total amount of imported raw materials. The main suppliers are: Basell, Unipetrol Group, Sabic (European segment) and Borealis [1].

The polyethylene applied in Ukraine in the volume of 39% is being produced at the Kazanorgsintez (COS), LUKOIL Oil (Stavrolin) and Nizhnekamsk-Neftekhim, and Prikarpatnaftokhim LLC plants.

Polyethylene which is produced in the countries of southeast Asia accounts for 3% of the total supply [2].

The largest group of industrial thermoplastics are polyolefins which are the basis of many blends [3]. Authors have previously studied the rheological and technological properties of polyolefins blends, in particular polyethylene of high and low density

[1)] *Lviv Polytechnic National University, Department of Chemical Technology of Plastics, 12, Bandera Str., Lviv, 79013, Ukraine, e-mail: vkrasinsky82@gmail.com*

with ultrahigh-molecular linear polyethylene manufactured by LLC "Prykarpatnaftokhim" (Ukraine) [4].

By the mixing in the melt of various polyolefins the materials of specific properties that impossible to obtain during the synthesis of a particular type are produced.

The use of ultra-high molecular weight linear polyethylene (UHMWPE) in polymer blends is caused by the complex of properties: high impact strength, physical and mechanical properties, non-toxicity and high resistance to aggressive media. At the same time, it should be noted that the processing by such methods as injection molding and extrusion of PE is complicated due to the low melt flow index (its high viscosity). In previous papers, the authors obtained the blends of ultra-high molecular polyethylene with polyolefins as well as filled compositions via the different mixing mechanisms [4]. The resulting composites are characterized by significant structural changes compared to the raw material, due to different affinity components. As a result, it is difficult to achieve sufficient homogeneity of the melt of such compositions, and, hence their processability [5].

Compositions based on blends of high and low density polyethylene are characterized by excellent physical and mechanical properties and have the same chemical structure. At the same time, they are characterized by sufficient processing capacity for processing by such high-performance methods as injection molding and extrusion [6].

Blends based on ultra-high molecular weight polyethylene with industrial polyolefins have sufficient technological capacity, but the operational properties of pipes on its basis, in particular, mechanical strength are insufficient.

Study purpose. The purpose of the work was to research the influence of the composition of polyethylene blends on its rheological behavior and to create a mixture with optimal technological parameters adapted for pipe extrusion.

Therefore, the task of improving the processability of blends based on polyolefins, suitable for processing by extrusion method is relevant.

During the work it was necessary to conduct the following studies:

- to determine the influence of composition of blends on the basic technological and physical and mechanical properties of polyethylene;
- study of technological and physical-mechanical properties of extrusion raw materials for pipes on the basis of blends of different types of polyethylenes.

Object of research: polymer blends based on polyolefins.

Subject of research: the study of influence of polyolefins on the raw materials processability.

2. Initial substances and research methods

We used high density extrusion polyethylene of two brands: LITEN PL-10 (analogue PE-80) (Unipetrol, Czech Republic) and PE2LP11-9 (analogue PE-100) (Kazanorgsintez, Russia).

The main indicators of initial raw materials are presented in Table 1.

Table 1. *Basic indicators of raw materials*

Parameter	PE2LP11-9	LITEN PL-10
MFI $_{190\,^\circ C\,/\,5{,}0\,kg}$, g/10 min	0.08 – 0.1	0.43
Soot content,%	2.0 – 2.5	2.25
Density, kg/m^3	956-962	952
Relative elongation at tensile,%	≥ 500	≥ 500
Boundary of fluidity at tensile, MPa	21	18.0-20.1

The flow curves (dependences of the shear stress τ on the shear rate $\dot{\gamma}$) of the polymer melts were obtained applying a capillary viscosimeter with a set of capillaries of different lengths but of the same diameter [7, 8]. The flow curves were obtained using a capillary with a diameter of 2,095±0,005 mm and a length of 8 mm at the different loads and at three temperatures: 190, 210, 230°C.

The melt flow index determination (MFI) of the initial polymers and its blends was conducted using the IIRT device in accordance with the standard method (GOST 11645–73) [8].

In order to increase the melt flow, the polyethylene of PE2LP 11-9 brand was mixed with polyethylene of LITEN PL-10 brand in amounts of 20, 30, 70 and 80% by weight. The blends were prepared as follows: the components were first blended mechanically, then co-melted for 15 minutes applying a plunger-capillary plasticiser. The melt was extruded through a nozzle of a diameter 2,095±0,005 mm at a temperature of 190°C at a load of 5 kg and received strands that were crushed with a rotary knife crusher. The obtained agglomerate was processed applying a Kuasy 32/25 thermosetting machine and samples were obtained for physical and mechanical studies in the form of standard blades for the following parameters: temperature in the zones of the injection cylinder 200, 220, 240°C, plastification time 90 s, screw velocity 100 rev/min, the temperature of the form 20°C, the pressure of casting 100 MPa, the holding under pressure 15 seconds, cooling time 20 seconds.

In this work the UHMWPE and blends on its base with polymers homologues (HDPE, LDPE and PP) were researched. Some examples of blends are given in Table 2.

Table 2. *Properties of initial polymers and blends*

Indicators	UHMWPE	LDPE	HDPE	PP	UHMWPE/ PP=20:80	UHMWPE/ HDPE=80:20
MFI g/10 min	0.24	1.97	6.4	12.52	5	0.4
Relative elongation at break,%	100	160	105	18	13	120
Boundary of fluidity a tensile, MPa	18	6.8	19	27	31.2	17

Physical and mechanical properties, the boundary of fluidity, the destructive tension at stretching, the maximum tensile stress, the relative elongation at the yield strength, the relative elongation at break were determined in accordance with the standard (GOST 11262-76) [9]. Physical and mechanical properties were determined applying bursting machine of type Kao Tieh – Kimura 050/RT – 601U (Japan, range of tensile speeds of 50–500 mm/min, tensile strengths of 500 and 1000 kg, measuring range from 05 to 5000 mV/cm, step 0.01 mm).

3. Results and discussion

The task of research is the creation of polyolefin blends, in particular, blends based on ultra-high molecular weight polyethylene which would be suitable for processing by injection molding and extrusion and could be used in various industries.

The authors, in the course of research were established the dependence of the change in fluidity of UHMWPE blends on the additives content – industrial polyolefins: polyethylene of low density (MFI = 1.97 g/10min), high density polyethylene (MFI = 6.4 g/10min) and polypropylene (MFI = 12.52 g/10min.). The abnormal behavior of blends including those close in structure, such as high molecular weight polyethylene and high density polyethylene was revealed. It has been determined that by matching the correspondent additives and adjusting their content and mixing conditions, it is possible to achieve the required processability of the blends with a melt flow index in the range from 0.4 to 5 g/10 min (component content 75–90% by weight) [4]. The influence of LDPE, HDPE and PP additives and conditions of mixing with UHMWPE on the main properties of its blends was researched and it was confirmed that short-term mixing in absence of shear stresses causes a noticeable reduction in the strength of composites and significantly affects the rheological behavior of blends. Studying the behavior of polymer melt in a wide range of changes in the parameters of the formation allows predicting the nature of the change in the properties of the melt reflected by the flow curves (Fig. 1).

Research of the nature of change in flow curves in the range of 10^0–10^3 s^{-1} shear rates and basing on the results of fluidity evaluation and its blends concerning to the processing conditions it was possible to make a prediction of the suitability for recycling [10]. In this range the stress increases which can indicate the relaxation transitions in macromolecules of long length, which affects the rheological behavior of the studied blends, and, consequently, the conditions for the processing of these blends.

The nature of the flow curves is rectilinear only the pure UHMWPE has a variable character of the curve and at the shear rate $\approx 10^2$ s^{-1} there is a jump-like change in the slope of the curves, which can be explained by the relaxation transitions between the macromolecules in the fluctuation grid. As a result, a chaotic mixing of the polymer occurs and the material is slid along the channel walls, which, in turn affects the rheological behavior of the investigated blends. In the case of mixing UHMWPE with additives used in the work the nature of the curves $\tau = f(\gamma)$ for the initial UHMWPE

in the blends is changed (Fig. 1b). The values of the shear stress are reduced in relation to the initial UHMWPE and the nature of the curves varies in a straight line.

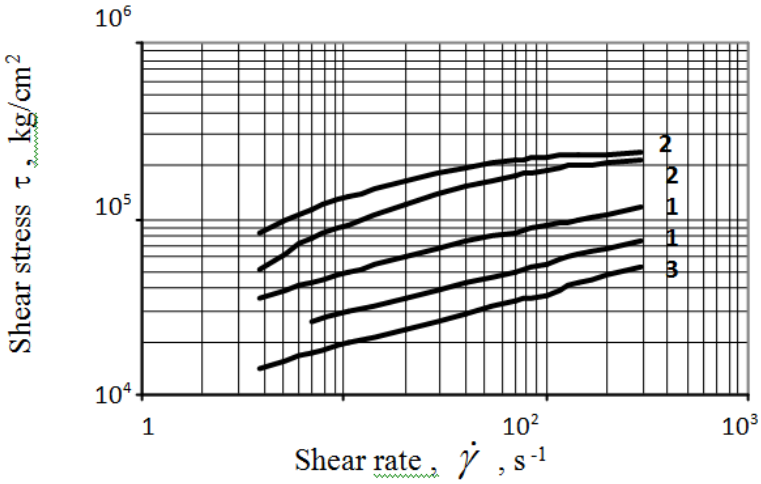

a)

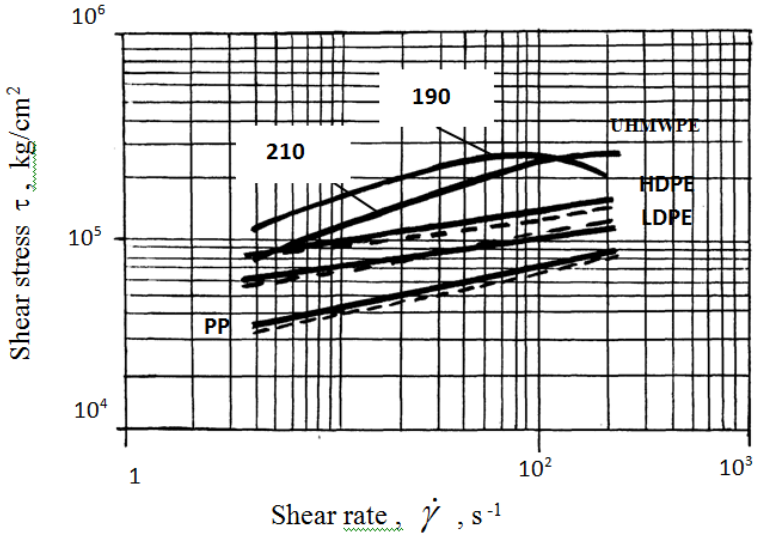

b)

Fig. 1. Flow curves: a – blends based on UHMWPE with HDPE (1), LDPE (2) and PP (3); b – initial polymers (UHMWPE, PP, LDPE, HDPE); - - - – literary data; – - experimental data at T = 190°C.

It was determined, simultaneously, the possibility of filling the blends based on ultra-high molecular polyethylene and its influence on the rheological and technological behavior of polyolefin blends [11] was studied.
It has been determined that the initial polymer system (UHMWPE:HDPE = 20:80) and composites filled with mineral filler with calcium carbonate ($CaCO_3$) provide linear dependences between shear stresses τ and shear rate in the investigated interval of shear stresses $\dot{\gamma}$ (Fig. 2) [13] corresponding to general rheological notions.

At the same time, it can be noted that with the filling of $CaCO_3$ the shear stress increases significantly, especially for the flow at a lower temperature (T = 150°C). An increase in the content of the filler in the composite up to 30% by weight causes ability of melting to the non-Newtonian character of the flow in a relatively narrow range of changes in the shear stress. A change in the angle of inclination is manifested and in this case the effect is manifested more to the contrary at the elevated temperature. In previous studies [12, 13] for the improvement of the flow of polymer blends, the treating of the $CaCO_3$ surface with lubricants (stearin, oleic acid, etc.) was carried out. If for the filling of the polymer system a treated $CaCO_3$ was used, for example by stearic acid, a curvature shift (curve 4) was observed in the direction of increasing the shear rate and decreasing the angle of inclination of the curve indicating a significant decrease in the viscosity of the system at 200°C (Fig. 2).

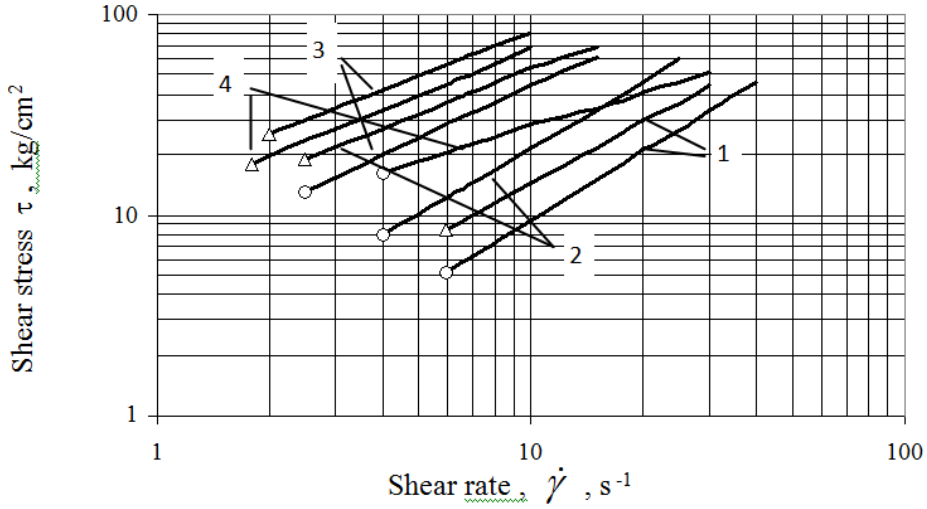

Fig. 2. The melt flow curves based on a blend of UHMWPE: HDPE. Content of treated $CaCO_3$,%: 1–0; 2–20; 3–30; 4–30 Temperature, °C: o–200, Δ–150

On the basis of the obtained data it was determined that within the content of the filler 20% by weight. the particles of $CaCO_3$ form a relatively ordered heterogeneous grid in a matrix of a polymer melt which is being indicated by a change in the slope

of the curve with increasing of the shear rate. Such changes may indicate an improved processing ability of the obtained composites.

Mixing of UHMWPE with polyolefins via the different mechanisms contributes to the formation of compositions with various structural modifications due to different affinity of components.

Homogeneity of polymer blends depends on the affinity of individual components, mixing conditions and its ratio. On the other hand, homogeneity affects the physical and mechanical properties.

In order to follow changes in the properties of the initial polymers and their blends the effect of the ratio of components on the physical and mechanical properties under standard conditions and after heat treatment at different temperatures was carried out [14, 15]. Different ratios of components of the composition of UHMWPE / additive (80/20; 50/50; 20/80) were chosen.

Table 3 summarizes the results of physico-mechanical studies of blends based on UHMWPE depending on the nature and content of additive and obtained at injection molding.

The obtained samples were divided into three parts: one of which was examined for tensile under normal conditions, and the other two before the research were subjected to heat treatment at a temperature of 60 and 120°C accordingly.

Table 3. *Physical and mechanical properties of the blends based on UHMWPE [15]*

Compositions	Content,%	σ_{el} , MPa	ε_{el} , %	σ_b , MPa	ε_b , %
UHMWPE	–	19/26	30/19	11/11	100/90
LDPE	–	10/10.5	34/20	13/14	160/138
HDPE	–	13.5/21	40/22	14.7/10	105/132
PP	–	25/42	11/16	24/38	18/24
UHMWPE:PP	80/20	17.7/24.8	5/7	14/25	9/13
	50/50	29.5/28	6/8	25/27	10/11
	20/80	31.2/33	8/6	27.2/32.8	13/34
UHMWPE: LDPE	80/20	18.2/20	20/20	15/17.5	126/96
	50/50	11.7/23.4	11/23	17/14.6	148/110
	20/80	12/25	22/23	13/11	149/250
UHMWPE: HDPE	80/20	17/27	27/19	16/26.4	120/40
	50/50	18/16	32/21	15/19.4	115/118
	20/80	19/34	37/5	17.5/33	176/30

– heat treatment of compositions at T = 120°C.

The maximum value of σ_{el} is being achieved for different composition of blends depending on the nature of additive. So for PP the maximum reaches with its content up to 20% by weight. For such blend σ_{el} increases by almost 50% compared to the initial polymer. At the same time, for the HDPE the maximum of σ_{el} is achieved already at 80% of its content in the blend, and for LDPE the growth of σ_{el} is manifested

in all blends almost equally [16]. However, in general for both polyethylene with an increase in the content of additive there is some deterioration of the physical and mechanical parameters. At the same time, with an increase in the content of PE additive in blend the main factor is the content of PP – 20 and 80% by weight.

Heat treatment of the blends at T = 60°C leads to a partial increase in the values of maximum stress at break, in particular, for blends containing PP it was 1–5%. For the UHMWPE with LDPE blends the growth of σ_{el} is observed only for the content of additive of 20% by weight and the deformability of the blend decreases in comparison with the initial blends. In blends containing HDPE the growth of σ_{el} in stretching being observed only at 80% by weight, although in the latter case there is a sharp deterioration of deformability of the sample.

For all compositions the deformative ability naturally decreases, only for blends with low content of PP there is a slight increase.

For thermo-treated at 120°C of a group of samples, it can be noted that in blends containing PP there is a further growth of σ_b and when the content of PP in the blend is 80% by weight, the growth of ε_b in 2.5 times is occurred. Although compared with heat-treated blends at 60°C no significant changes in σ_b are observed.

In blends containing PE there is a noticeable change in σel when stretching depending on the composition of the blend. The highest values of σ_{el} have the blends with additive content of 80% by weight. In this case, there is a significant decrease in deformability for all blends compositions containing PE. The exception is a blend with the content of LDPE 80% by weight for which elongation at break makes ε_b = 250%. It has been defined that the optimum combination of strength and elasticity (σ_{el}, ε_{el}) is realized in blend of UHMWPE with the content of LDPE 20% by weight, HDPE -10-20% by weight and PP – 5–10% by weight.

Using the value of melt flow index, you can set the method for processing of the polymer, as well as blends. For example, for the injection molding there are conditionally recommended polymers with MFI ≥ 3÷7 g/10 min; for coating – 20 g/10 min.; for extrusion – 0,3÷2 g/10 minutes [10].

Thus, according to the initial values, the polyethylene PE2LP11-9 has an extremely low flow index making it difficult to process it even by extrusion.

In work, the comparative analysis of melt flow index (MFI) as for separate types and for blends of polyethylenes have been conducted (Table 4).

The maximum homogeneity of the blends is being achieved when the components of the blend are characterized by close values of the melt flow index, which is important for regulating the physical and mechanical properties of the products, and as a consequence, affects the processability of the blends during the processing by extrusion.

For the study, the blends which were mechanically mixed in the ratio of 20 and 30% by weight of LITEN PL-10 polyethylene up to 80÷70% by weight and PE2LP11-9 polyethylene were prepared.

Table 4. *The melt flow index of composites based on blend of polyethylenes*

Material	Composite content, % wt.	MFI $_{190/5,}$ g/10 min
PE2LP 11-9	100	0.08
LITEN PL-10	100	0.25
PE2LP 11-9 / LITEN PL-10	80/20	0.14
	70/30	0.22
	30/70	0.40
	20/80	0.39
UHMWPE	100	0.24
UHMWPE / HDPE	80/20	0.4
	60/40	0.62
	20/80	1.4

The polyethylene of the PE2LP11-9 brand is characterized by very low value of the melt flow index. In order to create a suitable raw material for extrusion, it was blended with a more fluid LITEN PL-10 polyethylene in amounts of 20 and 30% by weight.

As the content of PE LITEN PL-10 in blend containing PE2LP 11-9 increases, the MFI of the obtained blends increases significantly. At the content of LITEN PL-10 in blend of 70% by weight. the MFI of composite is 0.40 g/10min, which significantly exceeds the MFI of the initial PE2LP 11-9 and also the LITEN PL-10. It can be explained by the inversion of the phases during the melt flow of the newly created blend which is not thermodynamically compatible. Blends based on PE2LP 11-9 with the addition of LITEN PL-10 in an amount from 30 to 70% by weight are technological by the fluidity for extrusion and can be used to produce water pipe. But in this case the physical and mechanical properties of raw materials are important.

Determination of physical and mechanical properties of blends of polyethylenes will allow to analyze the ability of blends for manufacturing of the water pipes. The test results for the polyethylene of LITEN PL-10 brand are shown in Figure 3a, and for polyethylene of PE2NT11-9 brand in Figure 3b**.**

The addition of low-flowing polyethylene (PE2LP 11-9) to polyethylene of LITEN PL-10 brand did not significantly affect the physical and mechanical properties of the blends. The value of the tensile strength is almost the same as the starting values of the LITEN PL-10. However, somewhat higher values of yield strength are characterized the blends of PE2LP 11-9 with the addition of LITEN PL-10, in particular 30% by weight.

Blends based on LITEN PL-10 and PE2LP11-9 with the content of 20 and 30% by weight have satisfactory fluidity, but the physical and mechanical properties are lower in relation to the initial materials.

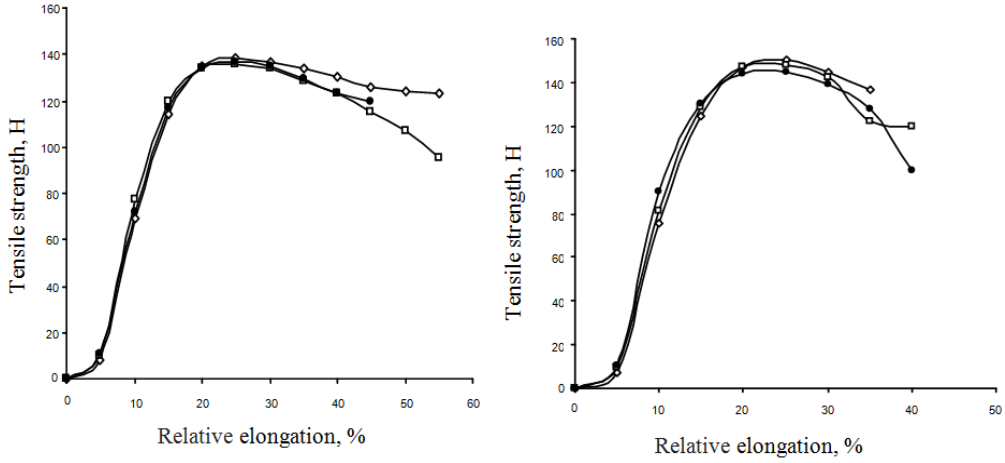

a) b)

Fig. 3. Tension curves of LITEN PL-10 and PE2LP11-9 and its blends:
a) ◊ - polyethylene LITEN PL-10; *b) ◊ - polyethylene PE2LP11-9;*
• - 20% by weight of PE2LP11-9; *• - 20% by weight of LITEN PL-10;*
□ - 30% by weight of PE2LP11-9 *□ - 30% by weight of LITEN PL-10*

Mixing UHMWPE with PE, which has a significantly lower molecular weight allows to obtain homogeneous blend, as evidenced by the dependence [3]:

$$\Delta G_b = \frac{\rho VRT}{M_l}\left\{\frac{M_l}{M}\cdot\left[\phi_A \ln\phi_A + (1-\phi_A)\cdot\ln(1-\phi_A)\right] + 2\phi_A(1-\phi_A)\right\}, \quad (1)$$

where T – temperature of mixing; ϕ_A – volume fraction of the polymer; M_l – limited molecular mass.

We determined the dependence of the shear stress on the shear rate for the initial polyethylenes of PE2NT11-9 and LITEN PL-10 brands, as well as their blends applying a capillary of different lengths but of the same diameter. The influence of temperature on the nature of the flow is determined (Fig. 4).

The flow curves of the initial polymers and its blends were obtained applying a viscosimeter of constant pressure IIRT at the different temperatures. As you can see, all dependencies in logarithmic coordinates are linear. As the shear stress increases, the deformation rate of the melt of polyethylene blends increases, regardless of the composition content and temperature of the experiment. For initial polyethylenes, the dependence of the shear rate on the stress carries another character. For PE2LP 11-9 at 190°C (curve 1, Fig. 4a), there is a significant increase in the shear rate with increasing tension and at temperatures of 210 and 230°C – decreases. It can be explained by the influence of the molecular weight distribution and the peculiarities of the chemical structure of the low-flowing polymer. For the PE of LITEN PL-10

brand there is an opposite dependence – at temperatures of 210 and 230°C the shear rate increases sharply with increasing tension, and at 190°C – decreases. Such changes in the properties of polyethylene blends can be explained by the creation of a fluctuation grid.

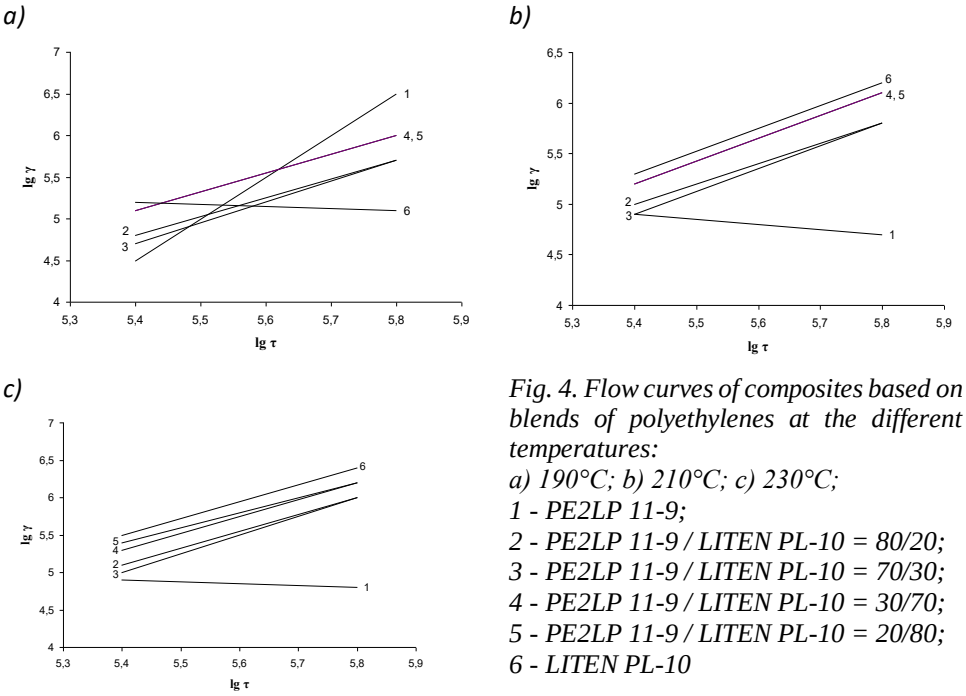

Fig. 4. Flow curves of composites based on blends of polyethylenes at the different temperatures:
a) 190°C; b) 210°C; c) 230°C;
1 - PE2LP 11-9;
2 - PE2LP 11-9 / LITEN PL-10 = 80/20;
3 - PE2LP 11-9 / LITEN PL-10 = 70/30;
4 - PE2LP 11-9 / LITEN PL-10 = 30/70;
5 - PE2LP 11-9 / LITEN PL-10 = 20/80;
6 - LITEN PL-10

Consequently, the composites that have viscosity which siginifically differs from viscosity of the initials polymers were obtained as a result of mixing of two brands of polyethylene with different fluidity.

4. Conclusions

The influence of nature and composition of blends based on UHMWPE with polymer homologues (LDPE, HDPE, PP) on the rheological and physical–mechanical properties is determined. Optimal compositions of technologically homogeneous blends with satisfactory fluidity, processing ability and high physical and mechanical properties are defined.

The possibility of filling the blends based on UHMWPE with mineral filler was found. The introduction of 20% calcium carbonate, treated with Ca stearate improves the processing ability of the obtained composites.

The experimental method has proved the possibility of improving the processability of extrusion polyethylene of PE2LP 11-9 brand of low fluidity by mixing it with the brand of high fluidity polyethylene.

It has been shown that due to the mixing of PE2LP 11-9 with LITEN PL-10 it is possible to significantly increase the fluidity of PE2LP 11-9 without reducing the mechanical properties of material. For extrusion of water pipes the most optimum in terms of strength and fluidity there is blend with the ratio of components PE2LP11-9 to LITEN PL-10 as 70 to 30% by weight. Such a composition possesses the highest homogeneity (the phenomenon of phase inversion during the melt flow through the capillary does not manifest), as well as high strength.

References

[1] Analiz rynka plastykovoi tary i trub (PE i PP) v Ukraine// Plimernye truby-Ukraina: Analitika rynka, 2018 [https://pro-consulting.ua/.../analiz-rynka-plastikovoy-tary-i-trub-pe-i-pp-v-ukraine-20].

[2] Rynok importu trubnogo polietylenu v Ukraini. Plimernye truby - Ukraina: Analitika rynka, 2016 [polypipe.info/analytics/1414-rynok-importy-pe-ykraina].

[3] D. Pol, S. Niumen., Polimernye smesi. Moscow: Mir (v.1), 485, 1981.

[4] Kyrulo M.S., Zemke V.M., Sybeliak O.V., Anomalino velyki vidchilenia vid adytyvnosti v zaleznosti sklad-vlastyvosti v sumishah na osnovi nadvysokomolekuliarnoho polietylenu. Visnyk Natsionalnoho universytetu "Lvivska Politekhnika". Khimiia, tekhnolohiia rechovyn ta yih zastosuvannia, 447 (2002), 74–78.

[5] Andreeva I.I., Veselovskaj E.V., Sverhvusokomolekyljrnuy polietulen vusokoy plotnosti. Moscow: Himij,75, 1980.

[6] Kalinchev E.L., Sakovceva M.B., Svoystva i pererabotka termolastov. L.: Himij, 287, 1983.

[7] Toropceva A.M, Belogorodskaj K.V., Bondarenko V.M., Laboratornuy praktukym po himij i tehnologij vusokomolekyljrnuh soedineniy. L: Himij, 415, 1972.

[8] GOST 11645-73. Plasticheskie masu. Metod opredelenij pokazatelj tekuchosti posplava termoplastov. – vzamen GOST 11645-65; vveden 01.07.74 – M.: Izd-vo standartov, 1973.

[9] GOST 1262-76. Plasticeskie masu. Metodu isputanij na rastjzenie. – vzamen GOST 1162-65; vveden 01.07.77. – M.: Izd-vo standartov, 1976.

[10] Zemke, V., Syberlyak, O., Vplyv pryrody dodanku ta umov zmishuvania na reolohochni vlastivosti shumishei poliolephiniv. Desiata naukova konpherencia „Lvivski chimichni chitania", 2005, PH4.

[11] Suberlyak, O., Kurylo, M., Zemke, V., Melnyk, W.., The improvement of high molecular weight polyethylene processibility. "Materiały polimerowe i ich przetwórstwo", 2000, 65–68.

[12] Ciprin, M.G., Irgen, L.A., Lanno, V.A., Reologicheskie i tehnologicheskie harakteristiki rasplavov polietilena napolnenogo melom i izvestnjkovoj mykoj // Mehanika kompozicionuh materialov, 6, 1992, 829–837.

[13] Zemke, V.M., Kyrulo, M.S., Suberlyak, O.V., Dosldzenia vpluvy mineralngo napovnuvacha na symish NVMPE:PEVG. Kompozicijni polimerni materialy, 2, v. 24 (2002), 123–126.
[14] Zemke, V., Kurylo, M., Suberlyak. O., Processing and compositions properties on the base of ultra high-weight molecular polyethylene. X Seminarium Tworzywa sztuczne w budowie maszyn, 2003, 443–447.
[15] Zemke, V., Suberlyak, O., Sobchak, R., Morpholohichni zminy nadmolekyliarnoi struktury v sumishah poliolephiniv z technolohichnumy vidchodamy nadvysokomolekuliarnoho polietylenu. Polimernuyi zurnal, 1(27), 23–28.

Volodymyr Levytskyi[1], Andrii Masyuk[1], Khrystyna Kysil[1], Bogdan Savchenko[2], Volodymyr Skorokhoda[1]

RHEOLOGY OF MELTS OF POLYAMIDE 6 AND POLYPROPYLENE COMPOSITES WITH MODIFIED SILICATE FILLER

***Abstract**: The rheological properties of composites based on industrial thermoplastics - polypropylene and polyamide 6 and polyvinylpyrrolidone-silicate fillers. The change in the shear stress of composites is studied, depending on the shear rate, the nature of the filler and the temperature have been studied. It is established that the nature of the curves in the Newtonian region of the flow is similar, while the shape of the curves in the course of the development of the anomalous flow is significantly different. It has been found that the increase in temperature leads to an increase in the shear rate, and hence to a decrease in the effective viscosity of the mixtures. The introduction of the filler in polypropylene, regardless of its nature and content and temperature, leads to an increase in viscosity .On the basis of the obtained rheological data, the constants of the rheological equation, the value of the apparent activation energy of the viscous flow and the melt flow index of modified filled thermoplastic composites in the non-Newtonian region of flow are calculated. It has been found that the activation energy of the viscous flow is slightly reduced when the filler is introduced into polypropylene and polyamide 6.It was established that the melt flow index of the obtained materials increases with the introduction of the filler in comparison with the pure thermoplastics. It is found that the filled composites, which include the polyvinylpyrrolidone, are characterized by an increase in the value of the melt flow index with a decrease in the degree of bonding of the polyvinylpyrrolidone with the silicate framework of filler.*

***Keywords:** Rheological properties, flow curves, polyvinylpyrrolidone-silicate filler, polymer composites*

1. Introduction

Polymer composite materials to a large extent satisfy high demands of consumers and compete successfully with various materials of structural and heat engineering purposes. At present, thermoplastic polymers with fillers of various natures, in particular silicates are widely used for their production, since on their basis it is possible to create materials with a complex of new and necessary properties with a small expense [1, 2].

[1)] *National University Lviv Polytechnic, Department of Plastics Engineering, st. S.Bandera, 12, 79013 Lviv, Ukraine, e-mail: vlevytskyj@gmail.com*

[2)] *Kyiv National University of Technologies and Design, Department of Applied Ecology, Technologies of Polymers and Chemical Fibers, st. Nemirovich-Danchenko, 2, 01011 Kyiv, Ukraine.*

It was established [3, 4] that the physico-mechanical, thermophysical and rheological properties of polymer composite materials (PCM) containing silicate fillers are largely determined both by the nature of the filler itself and its technological compatibility with the polymer matrix. In order to improve the technological compatibility with the polymer matrix and to direct the regulation of the technological and operational properties of polymer composite materials, silicate fillers are pre-modify by functional-active compounds [5].

The physicochemical method [6], which is based on the co-precipitation of sodium liquid glass and functional surface-active polymeric modifiers, in particular polyvinylpyrrolidone (PVP) under the action of chloride acid, is effective in the production of modified fillers, which provides a uniform distribution of the modifier on the surface and in the volume of the filler.

During the interaction of the polymer matrix and the filler, the conformational mobility of the polymer chain changes and steric interferences occur, which also has an effect on the nature of the interaction of the components. Thus, a decrease in the relaxation mobility of the polymer chain leads to a change in the glass transition temperature and the melt temperature of the polymer. At the same time, an increase in the degree of filling and reduction of the size of the filler particles, as a rule, leads to an increase in the average time of relaxation of macrochains. The change in the flexibility of the polymer chain leads to changes in the conditions for the crystallization of polymers and the change in the packing density of macromolecules on the surface of the filler.

The filled polymer can be considered as a three-phase system, which consists of filler, a polymer matrix, and a boundary layer, whose properties are different from the properties of the first two components of PCM. The filler particles may also form a grid in the polymer matrix due to the interaction between themselves or through the association of the adsorption layers of the polymer. At the same time, the probability of formation of such a grid increases with increasing content and anisotropy of the filler particles in the polymer matrix [7].

Due to the localization in the inter-structure regions of the polymer, the modifying additions that are not compatible with the polymer matrix contribute to the increase in the overall mobility of the elements of supramolecular structures and the mobility of the chains of macromolecules in disordered zones. In this case, especially in amorphous regions, the amount of residual stresses decreases and the order of the structure of the polymer increases. Due to this, the technological and operational properties of PCM are increased in comparison with the unfilled polymer. At the same time, the introduction of modifiers to polymers not only accelerates the relaxation processes, but also affects the nature of the interaction of a polymer with a filler, which contributes to the formation of more thermodynamically stable structures

During the interaction of a polymer with a filler, the formation of a boundary layer of a polymer near the solid surface is observed and an increase in the content of the filler leads to the fact that a significant part of the polymer is in the interphase layer [8]. The restriction of molecular mobility in the adsorption and surface layers causes

difficulties for the passage of relaxation processes, which leads to an increase in residual (internal) stresses. The tensions that arise in the process of processing composites do not disappear after the removal of thermal or power fields. Such residual stresses cause premature destruction of products, their cracking, change in shape and size, which results in loss of performance properties. Internal stresses can be reduced in the composites by introducing into the polymeric matrix of plasticizers, dopants, surface treatment by surfactants. This increases the mobility of macromolecules at the interface of the phases, but reduces the adhesion of the polymer to the fillers.

Thus, in order to significantly increase the physical, mechanical and thermophysical properties of the thermoplastic composite materials, the material needs to have as affinity between the filler and the polymer. And this is achieved by introducing into the polymer a nanosized (fine dispersed) filler, in the structure of which there are functional active groups that provide effective interaction on the boundary between the phases of the polymer-filler and reducing of internal stresses [9].

At the same time, the mechanism of the specific influence of such fillers and their modifiers on the properties of polymers is not fully investigated, which prevents the wide introduction of such materials in various industries.

The ability of polymers and polymer composite materials to processing, the choice of an optimal method for their processing, and the calculation of process parameters are determined, first and foremost, by their technological properties [10]. The choice of the method of processing and optimization of technological parameters of the process are carried out taking into account such characteristics of raw materials as viscosity and melting flow index (MFI), granulometric composition, moisture and volatile content, bulk density, technological shrinkage. The exact information on the technological properties of the material also allows you to adjust the regimes of its processing, calculate the size of the forms, provide high performance and reduce the amount of raw material waste.

One of the most important properties of polymeric materials which largely determine their ability to reprocess are rheological characteristics. The study of such rheological properties as the activation energy of the viscous flow and the input corrections make it possible to predict the morphological peculiarities of structural constructions in polymer composites both in melt and in solid state, which, in turn, will also affect the operational properties of products on their basis. Understanding the essence of the rheological properties of composite materials is very important for establishing optimal conditions for processing and the selection of equipment and control of mechanical and physical properties of products.

2. Materials and methods

To create polyvinylpyrrolidone-silicate fillers, an aqueous solution of sodium liquid glass (Na-LG) with a concentration of 1 mol/L and a module of n =1,6 and

a functional-active polyvinylpyrrolidone polymer with a molecular weight of 28,000 g/mol was used. Pre-preparing PVP solutions in Na-LG on which were acted by concentrated HCl. After coagulation, the precipitate was filtered, washed thoroughly with distilled water and dried under vacuum. The diameter of the particles is 170–350 nm.

PCM based on industrial thermoplastics with polyvinylpyrrolidon-silicate filler were obtained by mixing in a viscous fluid in a Cellier laboratory extruder equipped with a 700 mm long screw and a diameter of 25 mm. The speed of the screw rotation was 10-100 rpm. The temperature of the extruder zone for mixtures based on PP (Moplen HF501N) was 483–488, 498–503, 513–518 K, for PA-6 composites (PA-6 120/321 OST-6-06-C9-83) – 453–463, 473–483, 493–508 K. The obtained extrudate was chopped on a gear-type crusher. The choice of mixing conditions for components is conditioned by the requirements of the technology of processing plastics [11]. Terms of preparation of PCM are summarized in Table 1.

Table 1. *Basic stages and conditions for the preparation of thermoplastic composite*

No	Basic stages		Conditions oproduction	
			PP	PA-6
1	Powdering by filler the thermoplastic granules in ball mill with subsequent drying of mechanical mixture	$\tau_{Powd.}$,	15-20	
		$T_{Powd.}$, K:	293	
		$T_{dry.}$,	2.0–3.0	8.0–10.0
		$T_{dry.}$, K:	363	
		$P_{dry.}$, kPa:	101.3	2.5
2	Homogenization of components on Cellier laboratory extruder		Temperature zones of the material cylinder K: PP: 483–488, 498–503, 513–518 K; PA-6:453–463, 473–483, 493–503 K	

The formation of the flow curves of melting of polymer composites was carried out on a MFI apparatus "IIRT-M" using capillaries in length 8 and 25 mm and a diameter of 2,095 ± 0,005 mm. The volume flow of material in the capillary [12] was calculated by the formula:

$$Q = \frac{S \cdot \pi \cdot d^2}{4 \cdot t}, \tag{1}$$

where S – displacement of the piston, m;

d – diameter of the piston, m;

t – the time of movement.

Effective rate of displacement in the capillary:

$$\gamma_{ef} = \frac{4 \cdot Q}{\pi \cdot r^3}, \tag{2}$$

where r – radius of capillary, m.

Tensile shear in the capillary:

$$\tau = \frac{\Delta P \cdot r}{2 \cdot L} = \frac{9{,}81 \cdot 4 \cdot r \cdot P}{\pi \cdot d^2 \cdot 2 \cdot L}, \tag{3}$$

where P – weight of cargo, kg; ΔP – pressure drop between the ends of the capillary; L – capillary length, m.

The shear rate, taking into account the correction of Rabinovich [12], was determined by constructing in the logarithmic coordinates the auxiliary curve of the strain stress from the shear rate taking into account the Weissenberg-Rabinovich method [12]. Differentiating of the obtained dependence founded the index of viscosity anomaly due to the tangent of the angle of inclination of the curve. Hence, the shear rate:

$$\gamma = \frac{(3 \cdot n + 1)}{4 \cdot n} \cdot \gamma_{ef}, \tag{4}$$

where n - index of viscosity anomaly (degree of non-Newtonian behavior);

γ is the corrected value of the shear rate, s^{-1}.

The effective maturation viscosity was calculated as the ratio of the displacement stress to the shear rate:

$$\eta = \frac{\tau}{\gamma}, \tag{5}$$

Using the rheological equation (6), its constants were determined:

$$\tau = m_0 \cdot \exp\left(\frac{E}{RT}\right) \cdot \gamma^n, \tag{6}$$

where τ is the displacement stress for this polymer mixture, Pa; η – maturation viscosity, Pa · s; γ is the shear rate, s^{-1}; n – anomaly of viscosity index; E is the imaginary activation energy of the viscous flow, J/mol; m_0 is a constant that depends on the nature of the material, Pa · s.

The activation energy of the viscous flow of melting of polymers and their blends was determined according to the equation:

$$E_a = 2{,}303 \cdot R \cdot \lg \frac{(\eta_{T2} - \eta_{T1})}{(1/T_2 - 1/T_1)}, \tag{7}$$

where $\acute{\eta}_{T1}$ і $\acute{\eta}_{T2}$ – the viscosity of the material at temperatures T_1 and T_2, respectively.

3. Results and discussion

3.1. Rheological properties of thermoplastic composites based on polypropylene and polyamide 6

Products made of polymeric composite materials are preferably produced by injection molding. Therefore, understanding the essence of the rheological properties of composite materials is very important for establishing optimal processing conditions, choosing the design of snap-in and power-strength parameters of the equipment, predicting the mechanical and physical properties of products [7].

As we see, for the PP composites based on precipitated Na-LG and co-precipitated PVP and Na-LG (Fig. 1), the flow curves are shifted to the region of greater shear stress. At the same time, for PA-6, no such regularities are observed (Fig. 2).

The rheological properties of the filled materials substantially depend on the nature of the filler. At the same time, under the influence of the filler in the melt of the thermoplastic, a specific supramolecular structure formed by the macromolecules of the polymer and the particles of the filler is formed. Therefore, the nature of all curves in the Newtonian region of the flow is similar to each other. This, in our opinion, suggests that the process of flow occurs with the particles of the filler, which are covered with adsorption layer of the polymer, resulting in an effective increase in the volume of the dispersed phase. During the flow, such an adsorption layer is capable of being moved as a unit together with the particles of the filler [13].

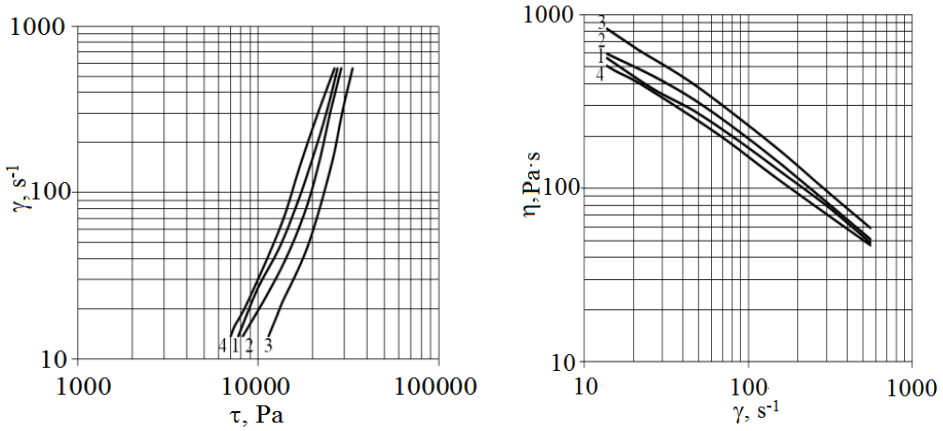

Fig. 1. The flow curves of composite materials based on PP at 473 K. Filler: 1 – without filler; 2 – precipitated Na-LG; 3 – coprecipitated Na-LG with PVP; 4 – physical mixture of precipitated Na-LG and PVP

At the same time, the introduction of a finely dispersed filler into the polymer results in an increase in the effective viscosity values compared to the incomplete thermoplastic (curves 2, 3 − Fig. 1 and 2 − Fig. 2) and obviously does not significantly affect the temperature coefficient in the viscosity in the Newtonian region of the flow.

The mechanism of the flow of such materials is similar between them, and therefore, in our opinion, the gap of bonds between the particles of the filler and the polymer matrix is not observed.

In the case of polypropylene composites (Fig. 1), the introduction of a filler based on a precipitated Na-LG and a coprecipitated PVP with Na-LG, compared with pure PP, contributes to the displacement of anomalous viscosity in the region of lower shear rate. Similar processes are also observed when a precipitated Na-LG is introduced into polyamide 6 (Fig. 2). At the same time, when using as a filler of a physical mixture of PVP and precipitated Na-LG (Fig. 1, 2, curve 4), the values of effective viscosity are significantly lower.

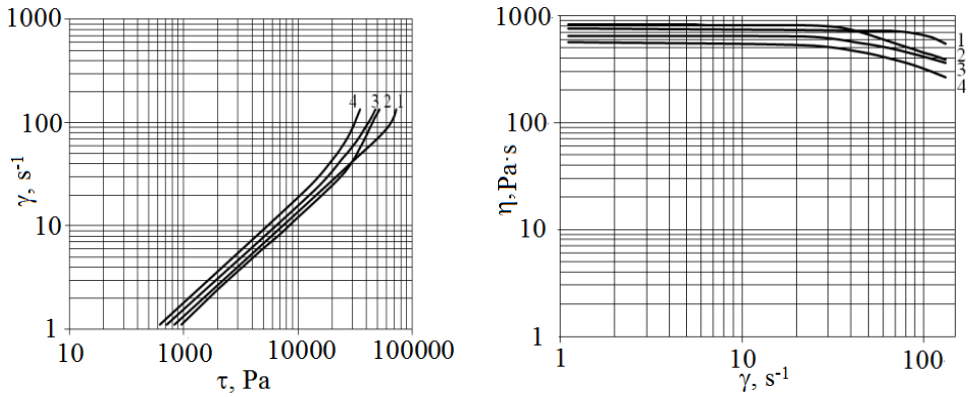

Fig. 2. The flow curves of composite materials based on PA-6 at 498 K
Filler: 1 – without filler; 2 – precipitated Na-LG; 3 – coprecipitated Na-LG with PVP;
4 – physical mixture of precipitated Na-LG and PVP

In general, the rheological properties of PCM essentially depend on the structure formation in the polymer medium of the filler particles (the so-called active filler) and their interaction with each other through the macromolecules of the thermoplastic, adsorbed on the surface of the particles. In this case, the filer particles act as centers of formation of a continuous spatial grid formed under the influence of their force fields. The fixation of the thermoplastic macromolecules on the surface of the filler particles leads to the formation around of such particle the adsorption shell with increased physical and mechanical properties. In this case, the fineness of the filler leads to the formation of a strong spatial structural grid, with the reduction of the particle size, contributes to the reduction of the maximum content of the filler, which is necessary for the formation of such a grid [14].

Changing the viscosity values for the filled materials indicates that the structures formed are thixotropic in nature due to the presence of thin interlayer regions of the dispersed phase in the particle contact areas. Such interlayer areas increase the strength of the system and contribute to a significant increase in plastic flow without significant destruction of its structure.

The large angle of inclination of dependence the effective viscosity on the shear rate for the filled PP (Fig. 1) is obviously due to the decrease in the thickness of the adsorption layer, and may also be explained by the differences in the molecular mobility of the macrocells: the distant macromolecules, in contrast to the macromolecules, connected with the surface of particles, take an active part in the process of flow. In addition, at large values of the shear stress, macromolecules with low mobility, located closer to the surface, are also involved in the flow process. Similarly, one can also explain the decrease in viscosity when temperature rises (Fig. 3).

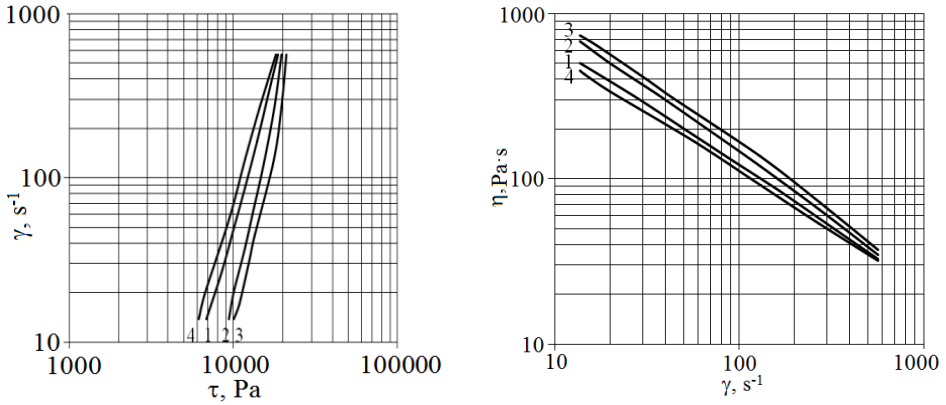

Fig. 3. The flow curves of composite materials based on PP at 503 K
Filler: 1 – without filler; 2 – precipitated Na-LG; 3 – coprecipitated Na-LG with PVP;
4 – physical mixture of precipitated Na-LG and PVP

The difference in the appearance of curves in the non-Newtonian region, depending on the nature of the filler, can also be explained by the fact that with the growth of the shear rate, the hydrogen bonds between the functional groups are destroyed, in the first place, the density of the fluctuation grid decreases, which obviously leads to a decrease effective viscosity of PCM. In addition, due to the clathrate structure of PVP-silicate particles, the strength of hydrogen bonds formed during the introduction of coprecipitated Na-LG and PVP into thermoplastics will be greater compared to thermoplastics filled with physical mixture of PVP and precipitated Na-LG.

The increase in temperature naturally leads to a decrease in the effective viscosity of PCM on the basis of PP and PA-6, and thus does not affect the nature of the curves of flow in the Newtonian region (Fig. 4 and Fig. 5).

It is necessary to note the change in the nature of the curves in the Non-Newtonian region, in which, with increasing temperature, the intensity of the anomalous flow increases, which may be explained by a decrease in the thickness of the adsorption layer with increasing temperature and shear stress stress.

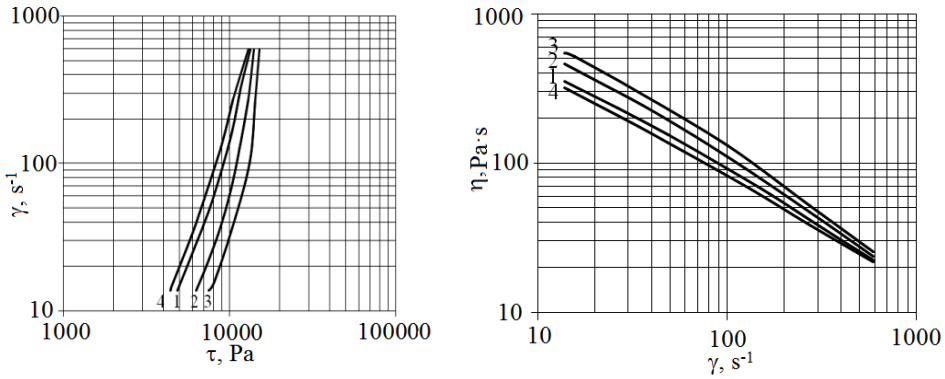

Fig. 4. The flow curves of composite materials based on PP at 533 K. Filler: 1 – without filler; 2 – precipitated Na-LG; 3 – coprecipitated Na-LG with PVP; 4 – physical mixture of precipitated Na-LG and PVP

In addition, the temperature increase leads to an increase in the shear rate at a fixed value of the shear stress, and hence to a decrease in the effective viscosity of PCM. Obviously, this feature is explained by the fact that, with increasing temperature, the strength of bonds between the thermoplastic macromolecules decreases more significantly than the strength of the bonds between the active groups of the filler particles and the macromolecules of PP or PA-6 [15].

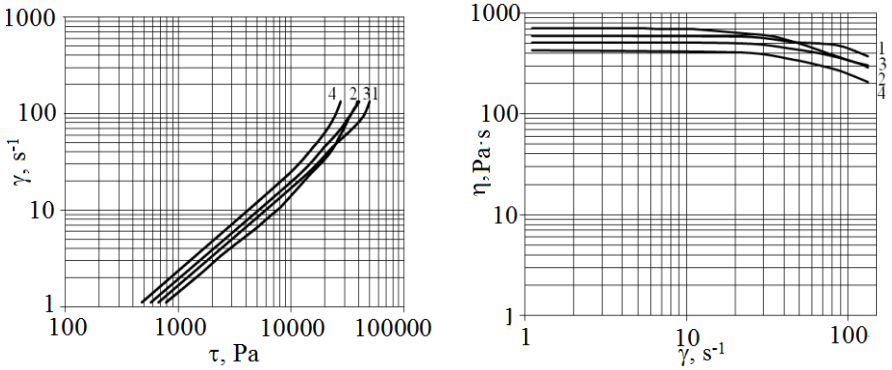

Fig. 5. The flow curves of composite materials based on PA-6 at 513 K. Filler: 1 – without filler; 2 – precipitated Na-LG; 3 – coprecipitated Na-LG with PVP; 4 – physical mixture of precipitated Na-LG and PVP.

Based on dependencies lg(1/η) on τ (Fig. 6 and Fig. 7) it is possible to trace the effect of the nature of the filler on the magnitude of the non-Newtonian viscosity of the melt. As can be seen, the different inclination of the molten viscosity curves depending on the shear stress of the filled PP and PA-6, as compared to the non-filled thermoplastics, indicates the presence of additional interactions between the filler and

the polymer. This character of the curves confirms that the stability of the fluctuation grid, which is formed due to the physical connections between the different groups of nature, essentially depends on both the temperature and the shear rate.

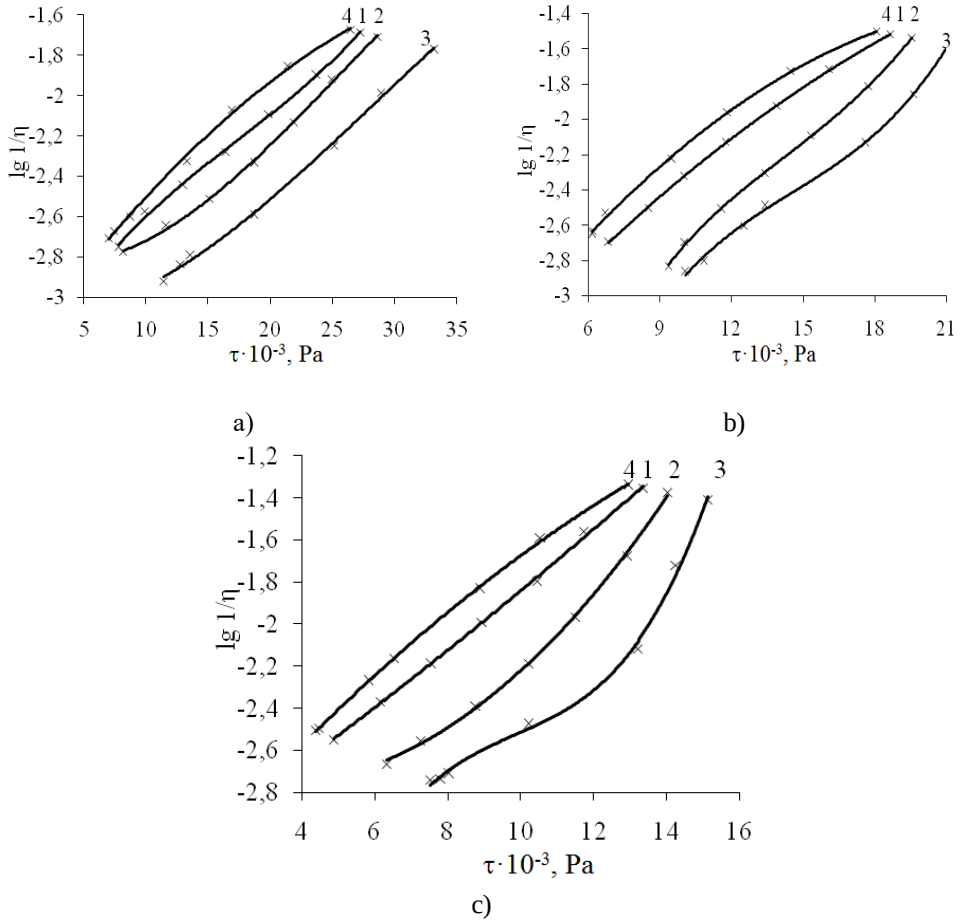

Fig. 6. Dependence of the melt viscosity of PP on shear at different temperatures: a) – 473 K; b) – 503 K; c) – 533 K.
Filler: 1 – without filler; 2 – precipitated Na-LG; 3 – coprecipitated Na-LG with PVP; 4 – physical mixture of precipitated Na-LG and PVP

As we can see, the temperature rise for filled PP and PA-6 composites leads to a decrease in the effective viscosity (Fig. 6 and Fig. 7). In addition, the effect of coprecipitated Na-LG and PVP on the behavior of PCM on the basis of PP, in contrast to PA-6, is characterized by an increase in viscosity throughout the investigated range

of shear stresses, which is consistent with the classical notions of the influence of inactive filler on the viscosity of melting of polymeric systems.

It was established that melts of polyamide 6 materials with fillers containing precipitated Na-LG with non-block functional groups exhibit a higher sensitivity to shear stresses during the flow as evidenced by the greater influence of τ on effective viscosity (Fig. 7). The filler based on the coprecipitated Na-LG and PVP reduces the viscosity of PA-6, but the nature of the viscosity dependence on τ in comparison with the unfilled PA-6 does not change, which is obviously due to the formation of uniform adsorption layers from the segments of polyamide 6 macromolecules on the surface of this filler.

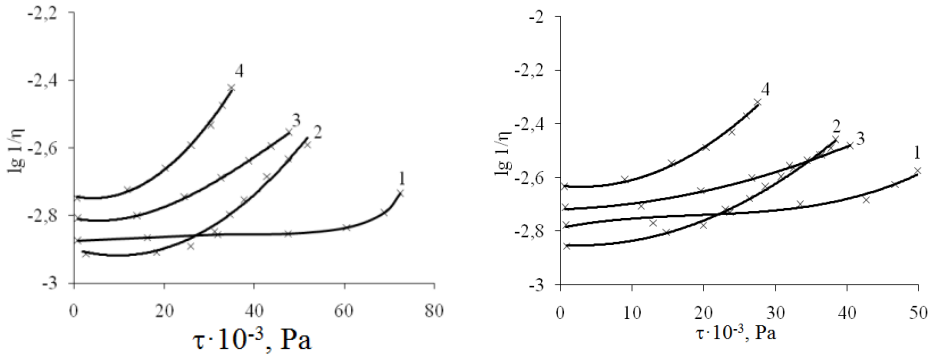

a) b)

Fig. 7. Dependence of the melt viscosity of PA-6 on shear at different temperatures: a) – 498 K; b) – 513 K.
Filler: 1 – without filler; 2 – precipitated Na-LG; 3 – coprecipitated Na-LG with PVP; 4 – physical mixture of precipitated Na-LG and PVP

On the basis of performed rheological researches and according to modern ideas about the mechanism of flow of polymers and corresponding methods of mathematical description [16], the values of the flow index and the imaginary energy of activation of the viscous flow E_a of melts of modified thermoplastics in the non-Newtonian region of the flow were calculated (Table 2).

The different nature of the change of rheological parameters for filled PEs and PA-6s, depending on the nature of the filler, due to different intermolecular interactions between the thermoplastic and the filler (in the case of PP - mainly hydrophobic nature, and for PA-6 - between the functional groups), and in the with this, different influences of the filler on the density of the thermoplastic fluctuation grid.

By the magnitude of the flow index, one can judge the intensity of the development of anomaly of viscosity of the studied composite materials [17].

Table 2. *Influence of the temperature and nature of the filler on the value of the flow index of the melt of thermoplastic composites*

No	Filler	PP		PA-6		
		Temperature, K				
		473	503	533	498	513
1	Without filler	0.39	0.40	0.44	0.57	0.63
2	Precipitated Na-LG	0,38	0.39	0.41	0.46	0.51
3	Coprecipitated Na-LG with PVP	0.36	0.38	0.40	0.54	0.58
4	Physical mixture of precipitated Na-LG and PVP	0.40	0.43	0.45	0.44	0.49

Comparing the value of the flow index to the thermoplastic PVP systems, the silicate filler should be noted that the flow index in the Newtonian region does not depend on the content of the filler and the temperature and is close to 1. At the same time, for the non-Newtonian region, the effect of the filler on the index of flow is more pronounced especially for PP composites at lower temperatures.

The flow index in the non-Newtonian region is the smallest for the materials based on coprecipitated Na-LG-PVP and PP. When another filler is introduced into the PP or by an increase in temperature, it increases throughout the studied range of shear stresses. In addition, an increase in temperature leads to a natural increase in the index of flow of composites on the basis of filled PP and PA-6, since in the region of investigated temperatures (for PCM on the basis of PP - 473–533 K, for PA-6 – 498–513 K), with an increase in unbound PVP there is an increase in the fluidity of molds filled with PP and PA-6 and a decrease in their effective viscosity.

As is known [18], the viscous flow is an activation process, the elementary act of which is to move segments from one equilibrium position to another. In this case, the activation energy of the viscous flow (Ea) is determined by the energy that a segment must obtain due to the fluctuation of thermal energy and which is necessary for separating this segment from the segments surrounding it. The values of the activation energy of the viscous flow of composite melt melts are given in Table 3.

The value of the activation energy of the viscous flow is somewhat reduced when the filler is introduced into PA-6 and slightly increases for PP. The smallest values of Ea, regardless of the nature of the thermoplastic, are observed when using the filler on the basis of the physical mixture of PVP and precipitated Na-LG, which can be explained by the considerable heterophage of the system, as well as the simultaneous plasticization of the components of the filler, which in this case do not form strong intermolecular bonds among themselves and contribute to reducing the density of the fluctuation grid.

Table 3. *The value of the activation energy of the viscous flow (E_a, kJ/mol) melts of composites based on PP and PA-6*

Polymer	Filler			
	Without filler	Precipitated Na-LG	Coprecipitated Na-LG with PVP	Physical mixture of precipitated Na-LG and PVP
PP	20.5	22.8	23.4	19.1
PA-6	54.1	53.5	52.8	51.7

At the same time, the introduction of PVP-silicate fillers on the basis of coprecipitated Na-LG and PVP, as well as precipitated Na-:G in the PP, is accompanied by an increase in the value of the activation energy of the viscous flow of the melt, as compared to pure thermoplastics, which can be explained by changes in the formation interphase layers and a number of specific interactions of hydrophobic nature between the macromolecules of the thermoplastic, PVP and silicate frame.

3.2. Melt flow index of thermoplastic composites based on polypropylene, polyamide 6, and polylactide

Simplest and at the same time, the most common in practice by the method of evaluation of the fluidity of polymer is the study of their melt flow index (MFI). By this indicator it is possible to carry out an initial assessment of the viscosity of polymeric materials and their ability to procesing.

In this regard, studies were carried out on the establishment of MFI PP and PA-6 with different contents of the filler, depending on its nature. The contents of the filler were changed within 0-10% by weight.

In the region of investigated temperatures with an increase in unbound PVP there is an increase in the fluidity of melts. This is also evidenced by the values of melt flow rates depending on the nature and amount of the filler (Fig. 8).

The MFI of the materials obtained depends essentially on the nature of the filler. Thus, in particular, it increases with the introduction of precipitated Na-LG, as compared to the unfilled thermoplastics. An interesting feature is that the PCM, which consists of PVP, is characterized by an increased value of the MFI when the degree of connection of the PVP with the silicate framework of the filler is reduced.

Increasing the values of the MFI, both for PP and for PA-6, is obviously due to the plasticization effect of the filler. At the same time, depending on the amount of filler, there are concentration areas where the MFI changes slightly.

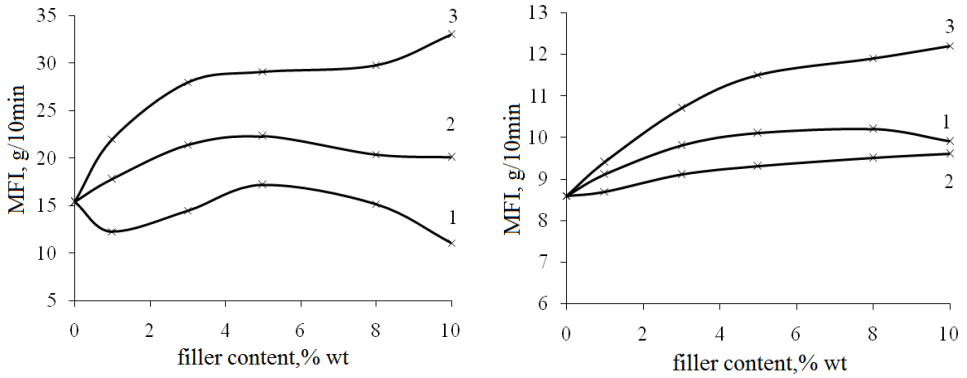

a) *b)*

Fig. 8. Influence of nature and content of filler on MFI: PP (a) and PA-6 (b). Filler: 1 − without filler; 2 − precipitated Na-LG; 3 − coprecipitated Na-LG with PVP; 4 − physical mixture of precipitated Na-LG and PVP

Obviously, in this region, an unaltered fluctuation grid is formed with a roughly constant number of intermolecular adhesions and a uniform phase-layer arises. In this case, the region of the metastable state of the PCM covers the initial interval of the content of the filler and is characterized by a tangible change in properties. It was proved [19] that in such areas the viscosity drop in the melt of polymers. In this case, the content of the filler in the composite corresponds to 4% by weight. It should be noted that for PCM with a filler on the basis of a physical mixture of precipitated Na-LG and PVP, an increase in MFI is observed and with a filler content of more than 5% by weight.

Consequently, the addition of a filler leads to an increase in MFI by 40–80% for PP and 10-30% for PA-6. Melting of polymeric composites with PVP-containing filler is characterized by increased value of MFI with decreasing PVP bonding with a silicate fissile framework.

The introduction of filer based on coprecipitated Na-LG with PVP in the polylactide (INGEO 3001D) leads to a decrease in material fluidity, in particular the value of the melt flow index. Adding 1% by weight of filler reduces the value of the MFI to 21 g/10 min, MFI of unfilled PLA is 22 g/10 min. Further increase in the content of filler to 2, 5, 10 and 20% by wt. naturally reduces the value of MFI of composite to 16.5, 11.8, 8.2 and 6.7 g/10 min, respectively.

The highest values of the MFI filled with PP and PA-6 are observed for PCM thermoplastic-physical mixture of PVP and precipitated Na-LG, which is due to the plasticization of the filler components, which do not form strong intermolecular bonds between themselves and contribute to the reduction of the density of the fluctuation grid. To ensure optimum conditions of interaction in the viscous state of PP or PA-6 with PVP-silicate filler, the PVP content should be ≈ 5% by weight.

4. Conclusions

The results of the studies confirm the significant effect of polyvinylpyrrolidone-silicate filler on the rheological properties of polyamid 6 and polypropylene composites.

The curves of the dependences in the Newtonian region of the flow are found to be similar to each other on the basis of the flow curves of the suppressed thermoplastics, while the appearance of the flow curves during the development of the flow anomalies differ significantly. In addition, it was found that increasing the temperature contributes to an increase in the shear rate at a fixed value of the shear stress, and leeds to a decrease in the effective viscosity of the composite melts.

It is established that the introduction of the modified filler promotes shift of anomalous viscosity of the melt of the composites in the region of lower shear stresses. This is explained by the polar interactions between the active centers of the PVP and the silicate frame with the macromolecules of thermoplastics. The development of anomalous flow for pure polyamide 6 is observed at a shear rate of 100 s^{-1}, while for modified PA-6 at 498 this value is less and is 40 s^{-1}.

Calculated values of the flow index and the apparent activation energy of the viscous flow of polypropylene and polycaproamid melts filled with polyvinylpyrrolidone-silicate fillers.

References

[1] Suprakas, S. R., Masami, O., Polymer/layered silicate nanocomposites: a review from preparation to processing. Progress in Polymer Scienc 2003, 28, 11, 1539–1641.

[2] Yiu-Wing Mai, Zhong-Zhen Yu, Polymer nanocomposites. Cambridge: Woodhead Publishing Limited, 2006. – 608.

[3] García, M., Polymer – Inorganic Nanocomposites, Influence of Colloidal Silica. Enschede: Thesis Univ. of Twente, 2004. – 157.

[4] Levytskyj, V., Kochubei, V., Gancho, A., Influence of the silicate modifier nature on the structure and properties of polycaproamide. Chemistry and Chemical Technology 2013, 7, 2, 169-172.

[5] Mittal, V., Polymer Nanocomposites: Advances in Filler Surface Modifications. Nova Science Publishers: New York, NY, USA, 2009. – 216.

[6] Levytskyi, V. Ye., Masyuk, A.S., Suberlyak, O.V., Preparation and properties of polymer-silicate composites based on hydrophilic polymers. Voprosy Khimii i Khimicheskoi Tekhnologii 2017, 6, 68-74.

[7] John, M., Dealy, K.F., Wissbrun Melt Rheology and Its Role in Plastics Processing: Theory and Applications. Dordrecht: Kluwer Academic Publishers, 1990. – 680.

[8] Brechet, Y., Cavaille, J.Y., Chabert, E., Chazeau, L., Dendievel, R., Flandin, L., Gauthier, C., Polymer based nanocomposites: Effect of filler-filler and filler-matrix interactions. Advanced Engineering Materials 2001, 3, 571-577.

[9] Mittal, V., Polypropylene-layered silicate nanocomposites: Filler matrix interactions and mechanical properties. Journal of Thermoplastic Composite Materials, 2007, 20, 6. 575-599.
[10] Rakesh, K., Gupta Polymer and Composite Rheology. New York: Marcel Dekker, 2000. – 416.
[11] Charles, A., Harper Handbook of plastic processes. Hoboken: John Wiley & Sons, 2006. – 743.
[12] Chang, D. H., Rheology and Processing of Polymeric Materials, Volume 1 Polymer Rheology. New York: Oxford University Press, 2007. – 707.
[13] Braun, D. B., Rosen, M. R., Rheology Modifiers Handbook Practical Use. New York: William Andrew, 1999. – 509.
[14] Lipatov, Y. S., Colloid Chemistry of Polymers. Elsevier Science Ltd. Amsterdam, 1988. – 460.
[15] Levytskyi, V. E., Masyuk, A. S., Bialopiotrowicz, T., Bilyi, L. M., Humenets'kyi T. V., Morphology and properties of thermoplastic composites with modified silicate fillers. Materials Science 2018, 54, 1, 48-54.
[16] Dealy, J.M., Wissbrun K.F., Melt Rheology and Its Role in Plastics Processing: Theory and Applications. Dordrecht: Kluwer Academic Publishers, 1990. – 680.
[17] Gupta, R. K., Kennel, E., Kim, K. J., Polymer Nanocomposites Handbook. Cambridge: CRC Press, 2009. –566.
[18] Koszkul, J., Materiały Polimerowe. Częstochowa: CRTM, 1999.-174.
[19] Vaia, R., Giannelis, E., Polymer melt intercalation in organically-modified layered silicates: model predictions and experiment. Macromolecules 1997, 30, 8000-8009.

Edited by: Prof. Janusz W. Sikora, Ph.D., D.Sc.
Assoc. Prof. Ľudmila Dulebová, Ph.D., D.Sc.

Reviewed: prof. **Janette Brezinová,** Ph.D., D.Sc., Technical University of Košice, Slovakia
Tomasz Rydzkowski, Ph.D., D.Sc., Assoc. Prof., Koszalin University of Technology, Poland

Tittle: **Technological and design aspects of the processing of composites and nanocomposites Volume II**

Publisher: Lublin University of Technology, ul. Nadbystrzycka 38D, 20-618 Lublin, Poland

Print: 100 pieces

Printed by: Lublin University of Technology

ISBN

Scientific-Practical International Workshop under a Project H2020-MSCA-RISE-2016-734205

This project has received funding from the European Union's Horizon 2020 research and innovation programme under the Marie Skłodowska-Curie grant agreement No 734205–H2020-MSCA-RISE-2016

ISBN: 978-83-7947-378-6